Very High-Order CFD Solver on General Unstructured Polygonal Grids

Xiasu Yang

THÈSE DE DOCTORAT DE SORBONNE UNIVERSITÉ

Spécialité : MÉCANIQUE

École doctorale de *Sciences Mécaniques, Acoustique, Électronique et Robotique de Paris*

présentée par :
Xiasu YANG

pour obtenir le grade de :
DOCTEUR DE SORBONNE UNIVERSITÉ

Very High-Order CFD Solver on General Unstructured Polygonal Grids

devant le jury composé de :

M.	AZAIEZ	Prof. Bordeaux INP-ENSCBP	*Rapporteur*
P.	DA COSTA	Prof. Sorbonne Université	*Examinateur*
G.A.	GEROLYMOS	Prof. Sorbonne Université	*Co-Directeur de Thèse*
C.	TENAUD	DR CNRS École CentraleSupélec	*Rapporteur*
I.	VALLET	Dr. HDR MC Sorbonne Université	*Co-Directrice de Thèse*
M.	VISONNEAU	DR CNRS École Centrale de Nantes	*Examinateur*

Sorbonne Université, Institut Jean Le Rond d'Alembert, UMR CNRS 7190
4 Place Jussieu, 75252 Paris Cedex 05

Abstract

An arbitrarily high-order 2D CFD solver is developed in this thesis, which is intended for solving compressible Navier-Stokes equations with Godunov-type Finite-Volume Method on general unstructured polygonal computational grids. High-order accurate spatial discretization is made possible by a polynomial-based constrained least-squares (CLSQ) reconstruction scheme which treats boundary conditions as additional equality constraints in the original least-squares functional, and solves the constrained optimization problem with Lagrange multipliers. The CLSQ scheme achieves scalable spatial order in both interior and boundary regions without the need for ghost cells. The Riemann problem is solved at cell interfaces with an all-Mach corrected approximate-state HLLC Riemann solver, and the steady-state solution is obtained by an implicit dual-time-stepping scheme implemented with a choice of different iterative and approximately factored linear solvers. The new CFD solver is tested on 3 laminar flow test-cases : a NACA0012 airfoil test-case, a zero-thickness flat-plate boundary layer test-case and a backward-facing step with an expansion ratio of 101/52. The solver shows excellent mesh flexibility and the order of accuracy is verified by comprehensive qualitative and quantitative analyses. For the backward-facing step case, the results obtained by the current CFD solver are in excellent agreement with the experimental data and with previous 2D computations. Moreover, the CLSQ reconstruction also demonstrates notable advantages over traditional second-order interpolation-based spatial discretization schemes in predicting separation, reattachment and small vortical structures in the near-wall region.

Contents

Abstract i

List of Figures viii

List of Tables viii

Nomenclature ix

1 Introduction 1
- 1.1 Background . . . 1
- 1.2 Motivation . . . 4
- 1.3 Thesis Outline . . . 5

2 Governing Equations and Computational Methods 6
- 2.1 Governing Equations . . . 6
- 2.2 Overview of Computational Methodology . . . 9
- 2.3 Constrained Least-Squares (CLSQ) Reconstruction . . . 12
  - 2.3.1 Reconstructing Polynomial . . . 12
  - 2.3.2 Dirichlet Type . . . 15
  - 2.3.3 Neumann Type . . . 16
  - 2.3.4 Interior Cell Treatment . . . 18
  - 2.3.5 Existence and Uniqueness Analysis . . . 19
- 2.4 Low-Mach Corrected HLLC Riemann Solver . . . 20
- 2.5 Implicit Time-integration . . . 25
  - 2.5.1 Jacobi Iterative Method . . . 30
  - 2.5.2 Block LU-SGS Iterative Method . . . 31
  - 2.5.3 Approximately Factored LU-SGS Method . . . 32
- 2.6 Grid Reordering Strategy . . . 34
- 2.7 Boundary Conditions . . . 37
  - 2.7.1 Boundary Numerical Flux . . . 37
  - 2.7.2 Adiabatic No-slip Wall . . . 39
  - 2.7.3 Isothermal No-slip Wall . . . 39
  - 2.7.4 Riemann Invariant Inflow and Outflow . . . 40
  - 2.7.5 Reservoir Inflow . . . 42
  - 2.7.6 Pressure Outflow . . . 44

3 Evaluation of Computational Methods **45**
3.1 Evaluation of Implicit Schemes . . . 45
3.1.1 Iterative Error and Reduction . . . 45
3.1.2 Backward-Facing Step at $Re_{u_B,D_h} = 100$ . . . 47
3.1.3 Backward-Facing Step at $Re_{u_B,D_h} = 389$ . . . 48
3.1.4 Backward-Facing Step at $Re_{u_B,D_h} = 1000$ . . . 49
3.1.5 Implicit Scheme for High-order Spatial Discretization . . . 56
3.1.6 Summary on Implicit Scheme Evaluation . . . 58
3.2 Evaluation of Constrained Least-Squares (CLSQ) Reconstruction . . . 60
3.3 Evaluation of Arbitrary Polygonal Grids . . . 65
3.3.1 Zero-thickness FPBL . . . 66
3.3.2 Low-Reynolds NACA 0012 Airfoil . . . 72
3.3.3 Backward-Facing Step (BFS) . . . 80

4 Flow Physics Analyses **88**
4.1 Literature Review on Laminar BFS Flows . . . 88
4.2 Results of Laminar BFS Flows with CLSQ3 . . . 92
4.3 Results with High-order CLSQ schemes . . . 106

5 Conclusions and Perspectives **111**
5.1 Summary . . . 111
5.2 Perspectives . . . 112
5.2.1 Finite-curvature Boundary Edges . . . 112
5.2.2 Turbulence Modeling . . . 113
5.2.3 Unstructured WENO Extension . . . 114

Bibliography **115**

A Existence and Uniqueness of the CLSQ Solution **130**

B Low-Mach Laminar BFS Flow Tests **135**

C Literature Review on Turbulent BFS Flows **139**

D Turbulent Equations and Boundary Conditions **151**
D.1 Favre-Reynolds-averaged Navier-Stokes Equations and GLVY-RSM . . . 151
D.2 Boundary Conditions . . . 152
D.2.1 Adiabatic No-slip Wall . . . 152
D.2.2 Isothermal No-slip Wall . . . 154
D.2.3 Riemann Invariant Inflow and Outflow . . . 155
D.2.4 Reservoir Inflow . . . 156
D.2.5 Pressure Outflow . . . 156

List of Figures

1.1 (a): internal structure of an turbofan aircraft engine made by CFM; (b): tip leakage vortices in a blade cascade. 4

2.1 Schematic representation of a stencil associated with a boundary cell E_0. 12
2.2 Schematic representation of a stencil associated with an interior cell E_0. 18
2.3 HLLC approximate Riemann solver. Four distinct constant regions are delimited by the left, right and contact waves. 20
2.4 Illustration of the current grid reordering procedure on a simplified unstructured grid, starting from a single-cell HP_1. 36
2.5 Boundary treatment in the current study, ⊠ are the Gauss-Legendre quadrature points on the boundary edge. 37

3.1 Convergence history using both Jacobi and BLU-SGS methods with different CFL at $Re_{u_B,D_h} = 100$. 47
3.2 Convergence history using Jacobi method with different ε^* at $Re_{u_B,D_h} = 100$. . . . 49
3.3 Convergence history using BLU-SGS method with different ε^* at $Re_{u_B,D_h} = 100$. . 50
3.4 Convergence history comparison among Jacobi, BLU-SGS and LU-SGS methods at $Re_{u_B,D_h} = 100$. 51
3.5 Comparison history using BLU-SGS method with different CFL at $Re_{u_B,D_h} = 389$. 51
3.6 Convergence history using both Jacobi and BLU-SGS methods with different ε^* at $Re_{u_B,D_h} = 389$. 52
3.7 Convergence history comparison among Jacobi, BLU-SGS and LU-SGS methods at $Re_{u_B,D_h} = 389$. 53
3.8 Convergence history using Jacobi method with different r^* at $Re_{u_B,D_h} = 1000$. . . 53
3.9 Convergence history using BLU-SGS method with different r^* at $Re_{u_B,D_h} = 1000$. 54
3.10 Convergence history using BLU-SGS method with different CFL* with $r^* = -0.5$ at $Re_{u_B,D_h} = 1000$. High CFL$^* = 10^{13}$ does not ensure convergence. 54
3.11 Comparison history using BLU-SGS method with different CFL* for $r^* = -1.0$ at $Re_{u_B,D_h} = 1000$. 55
3.12 Convergence history comparison among Jacobi, BLU-SGS and LU-SGS methods at $Re_{u_B,D_h} = 1000$. 56
3.13 Study on the effects of high-order CLSQ reconstruction on the convergence of implicit scheme using Jacobi method. Reynolds numbers $Re_{u_B,D_h} = 200, 389, 800$ are investigated with CLSQ3, CLSQ4, CLSQ5 and CLSQ6. 57
3.14 Number of m-iterations M_{it} for each n-iteration with Jacobi method using CLSQ4, CLSQ5, CLSQ6 at $Re_{u_B,D_h} = 800$. 58

3.15 BFS Cartesian grid parameters : blue lines correspond to the bounding grid lines, parameters colored in red are independent parameters and the other parameters in black are generated automatically based on them. Parameter values for the current BFS test-case are given in Tab. 3.1. 61
3.16 Grid convergence result of the pressure coefficient C_p and the skin-friction coefficient c_f on the bottom wall plotted against x-coordinate normalized by the step height H. 63
3.17 Grid convergence result of the pressure coefficient C_p and the skin-friction coefficient c_f on the bottom wall plotted against x-coordinate normalized by the step height H. 63
3.18 Evaluation of the observed order of accuracy p for the CLSQ3 scheme on the Backward-Facing Step. The relative error ε and observed order p are plotted against the inverse normalized grid spacing. Results are shown for four primitive variables. 64
3.19 Results of the pressure coefficient C_p and the skin-friction coefficient c_f on the bottom wall plotted against x-coordinate normalized by the step height H. Spatial discretization performed with CLSQ3-CLSQ6. 65
3.20 Results of the pressure coefficient C_p and the skin-friction coefficient c_f on the bottom wall plotted against x-coordinate normalized by the step height H. Results zoomed to the near-step region. Spatial discretization performed with CLSQ3-CLSQ6. 65
3.21 Geometric set-up of the flat-plate boundary layer test-case. (a): global computational domain; (b): near-wall region. 66
3.22 Quad-dominant unstructured grid for zero-thickness flat-plate boundary layer. (a): farfield mesh; (b): interface between farfield and near-wall regions. 67
3.23 Four types of stretched polygonal meshes in the near-wall region. (a): quad-dominant; (b): isosceles triangles; (c): right-angled triangles; (d): hexagons; (e): Cartesian. 68
3.24 Static pressure contour plots obtained on four types of stretched polygonal meshes in the near-wall region. (a): quad-dominant; (b): isosceles triangles; (c): right-angled triangles; (d): hexagons; (e): Cartesian. The flat-plate is represented by the black solid line. Minor unsmoothness issue due to ParaView rendering. 69
3.25 Pressure and skin-friction coefficient distributions (Eqn. 3.9) computed with different stretched near-wall meshes. TriFar-IsoTriNW: triangulated farfield, isosceles triangular near-wall; TriFar-RigTriNW: triangulated farfield, right-angled triangular near-wall; QuadDFar-QuadDNW: quad-dominant farfield, quad-dominant near-wall; QuadDFar-CartNW: quad-dominant farfield, Cartesian near-wall; QuadDFar-HexaNW: quad-dominant farfield, hexagonal near-wall. 70
3.26 Four levels of adaptively refined grids targeting on the leading edge of a zero-thickness flat plate. (a) is the coarsest, (d) is the finest. The flat-plate is represented by the black solid line. 71
3.27 Pressure and skin-friction coefficient distributions in the close vicinity of leading edge, computed using TriFar-IsoTriNW grid with 4 levels of adaptive refinement. . . 72
3.28 Geometric set-up of the low-Reynolds NACA 0012 test-case at $Re_{V_\infty, L_{chord}} = 1000$. The dashed circle corresponds to near-wall region. 73
3.29 Three types of unstructured grids used for the low-Reynolds NACA 0012 airfoil test-case : Quad is the purely quadrilateral grid, QuadD-0 is the baseline quad-dominant grid and QuadD-1 is the quad-dominant grid refined within the separation bubble. All grids are shown for AoA = 17°. 74

3.30 Pressure contours (a, b, c) and pressure coefficient distribution on the upper and lower surfaces of the airfoil (d). AoA = 17°. Minor unsmoothness issue due to ParaView rendering. 75
3.31 Chord-wise pressure coefficient distributions at low and high Reynolds numbers for AoA = 15°. Data source : Ladson *et al.* [138]. 76
3.32 Separation bubbles colored in black containing cells with negative u (a, b, c) and distribution of the skin-friction coefficient on the upper surface of the airfoil (d). AoA = 17°. 77
3.33 Cells with negative u constituting the separation bubble at four different angles of attack AoA = $0°, 5°, 10°, 20°$. Computations performed on Quad grids. 78
3.34 Curves of lift and drag coefficients for $0° \leq$ AoA $\leq 20°$ compared to the time-averaged lift and drag coefficients from the unsteady DNS simulations of Gopalakrishnan Meena *et al.* [98] 79
3.35 Subdivision rules for quadrilateral, triangular, pentagonal and hexagonal cells. Red line segments represent the dividing lines. 80
3.36 Three types of baseline unstructured meshes for the BFS test-case of Armaly *et al.* [13]. 81
3.37 Three levels of adaptive refinement enveloping the primary recirculation zone at $Re_{u_B,D_h} = 100$. The zone colored in red has x-velocity $u > 0$ while the blue region has $u < 0$. 83
3.38 Convergence history comparison among the three types of adaptively refined polygonal grids. 84
3.39 Normalized streamwise velocity profiles. Comparison made among the three baseline unstructured grids without adaptive refinement. 84
3.40 Streamwise velocity profiles on the three adaptively refined unstructured grids. Comparison made among all levels of refinement. (a) : rectangle-dominant, (b) : triangular, (c) : pentagon-hexagon-dominant. 85
3.41 Pressure coefficient C_p and the skin-friction coefficient c_f on the bottom wall plotted against x-coordinate normalized by the step height H. Computed with 4 levels of adaptively refined Cartesian grids. 86
3.42 Pressure coefficient C_p and the skin-friction coefficient c_f on the bottom wall plotted against x-coordinate normalized by the step height H. Computed with 4 levels of adaptively refined Cartesian grids. Results near the step $x = 0$ are shown. 86
3.43 Pressure coefficient C_p and the skin-friction coefficient c_f on the bottom wall plotted against x-coordinate normalized by the step height H. Computed with 3 levels of adaptively refined triangular grids. 87
3.44 Pressure coefficient C_p and the skin-friction coefficient c_f on the bottom wall plotted against x-coordinate normalized by the step height H. Computed with 3 levels of adaptively refined triangular grids. Results near the step $x = 0$ are shown. 87

4.1 Schematic representation of Armaly *et al.* [13] test-case. 93
4.2 fields of x-velocity u scaled by the inlet bulk velocity $u_{B_i} = 45.37$m/s for $Re_{u_B,D_h} = \{100, 389, 1000\}$ of Armaly *et al.* [13] test-case. 95
4.3 Vorticity fields for $Re_{u_B,D_h} = 100, 389, 1000$ of Armaly *et al.* [13] test-case. Minor unsmoothness issue due to ParaView rendering. 96
4.4 Streamlines colored by velocity magnitude scaled by the inlet bulk velocity $u_{B_i} = 45.37$m/s for $Re_{u_B,D_h} = \{100, 389, 1000\}$ of Armaly *et al.* [13] test-case. 97

4.5 Magnified view of corner vortex for $Re_{u_B,D_h} = \{100, 389, 1000\}$ of Armaly *et al.* [13] test-case. . . . 98
4.6 Flow separation and reattachment locations of Armaly *et al.* [13] test-case, comparison with experimental data. . . . 99
4.7 Prediction of flow separation and reattachment locations by linear interpolation between two Gaussian quadrature points denoted by ⊠. . . . 100
4.8 Flow separation and reattachment locations of Armaly *et al.* [13] test-case, comparison with previous 2D computational results. Data sources : Biswas *et al.* [28], Chiang *et al.* [44], Kim and Moin [130]. . . . 101
4.9 Length of corner vortex x_c normalized by step height H for Re_{u_B,D_h} = 100, 200, 291, 389, 500, 800, 1000 of Armaly *et al.* [13] test-case. . . . 102
4.10 Reynolds-scaled pressure drop distribution along channel axis, comparison with Biswas *et al.* [28] results. . . . 102
4.11 Normalized pressure drops and pressure rise in the entire channel plotted against Reynolds number. . . . 103
4.12 Streamwise velocity profiles compared with data from different experimental and numerical studies at Re_{u_B,D_h} = 100, 389, 1000. Data sources : Chiang and Sheu [46], Guerrero and Cotta [101], Armaly *et al.* [13]. . . . 105
4.13 Flow separation and reattachment locations of Armaly *et al.* [13] test-case for Re_{u_B,D_h} = 100, 200, 291, 389, 500, 800, 1000. Comparison made among results obtained by CLSQ3, CLSQ4, CLSQ5 and CLSQ6. . . . 106
4.14 Streamwise velocity profiles of Armaly *et al.* [13] test-case for $Re_{u_B,D_h} = 100, 389, 1000$. Comparison made among results obtained by CLSQ3, CLSQ4, CLSQ5 and CLSQ6. 108
4.15 Magnified view of corner vortex at Re_{u_B,D_h} = 100 of Armaly *et al.* [13] test-case. Comparison made among results obtained by CLSQ3, CLSQ4, CLSQ5 and CLSQ6. 109
4.16 Length of corner vortex x_c normalized by step height H for Re_{u_B,D_h} = 100, 200, 291, 389, 500, 800, 1000 of Armaly *et al.* [13] test-case. Comparison made among results obtained by CLSQ3, CLSQ4, CLSQ5 and CLSQ6. . . . 110
4.17 First appearance of roof vortex at $Re_{u_B,D_h} = 399$, the left end of each line segment represents x_4/H, the right end is x_5/H. Comparison made among results obtained by CLSQ3, CLSQ4, CLSQ5 and CLSQ6. . . . 110

A.1 Schematic representations of two-dimensional natural lattices $\mathcal{X}^m_{\text{nat}}$, where $m = p-1$ is the highest polynomial degree [49]. . . . 132

B.1 Normalized pressure p_{N} field for the Armaly *et al.* [13] test-case at Re_{u_B,D_h} = 100 and $M = 0.01, 0.05, 0.2$. HLLC Riemann solver without low-Mach correction is used for numerical flux computations. . . . 136
B.2 Normalized pressure p_{N} field for the Armaly *et al.* [13] test-case at Re_{u_B,D_h} = 100 and $M = 0.01, 0.05, 0.2$. Low-Mach corrected HLLC Riemann solver AM-HLLC-P [218] is used for numerical flux computations. . . . 137
B.3 Streamwise velocity profiles at Re_{u_B,D_h} = 100 and inlet Mach number $M = 0.01, 0.05, 0.2$ computed with HLLC and AM-HLLC-P Riemann solvers. Experimental data sources : Armaly *et al.* [13]. . . . 138

C.1 Schematic representation of a generic turbulent BFS test-case with front and top views. . . . 140

List of Tables

3.1 Uniformly refined grids used for grid convergence study for the laminar BFS test-case. * denotes the independent parameter given as input, all parameters are shown in Fig. 3.15. Grid 1-3 are generated by successive subdivisions of Grid 0, hence the geometric progression rates are not applicable. 62

4.1 Velocities and lengths used for Reynolds number definitions in the literature of laminar BFS. 88
4.2 Table of pressure data for Armaly *et al.* [13] test-cases at different Reynolds numbers Re_{u_B,D_h} ranging from 100 to 1000. 94
4.3 2D grid comparison between present study and Biswas *et al.* [28] 99

A.1 Number of Gauss-Legendre quadrature points per boundary edge $\bar{N}_{\boxtimes}$ and number of polynomial coefficients N_c for different polynomial orders p [91]. 131

C.1 Velocities and lengths used for Reynolds number definitions in the literature of turbulent BFS. 139
C.2 Turbulent benchmarks cases tested for BFS flows in the literature. 147
C.3 RANS models tested on turbulent BFS flows in the literature. 149
C.4 Published studies on turbulent BFS flows in the literature. 150

Nomenclature

Abbreviations

AM	All-Mach
BC	Boundary Condition
BLU-SGS	Block Lower-Upper Symmetric Gauss-Seidel
CAS	Computer Algebra System
CFD	Computational Fluid Dynamics
CFL	Courant-Friedrichs-Lewy condition
CLSQ	Constrained Least-Squares
DG	Discontinuous Galerkin
DTS	Dual-Time-Stepping
ENO	Essentially Non-Oscillatory
FDM	Finite Element Method
FEM	Finite Difference Method
FVM	Finite Volume Method
GLVY	Gerolymos-Lo-Vallet-Younis
HLLC	Harten-Lax-van Leer-Contact
KKT	Karush–Kuhn–Tucker
LSQ	Least-Squares
LU-SGS	Lower-Upper Symmetric Gauss-Seidel
RANS	Reynolds-averaged Navier–Stokes equations
ROD	Reconstruction of Off-site Data
RSM	Reynolds Stress Model
TVD	Total Variation Diminishing
WENO	Weighted Essentially Non-Oscillatory

Governing Equations (Section 2.1)

δ_{ij}	Kronecker delta	
γ	Heat capacity ratio	
κ	Thermal conductivity	$[\mathrm{W} \cdot \mathrm{m}^{-1} \cdot \mathrm{K}^{-1}]$
$\underline{\underline{\tau}}$	Viscous stress tensor	[Pa]
$\underline{\underline{S}}$	Strain-rate tensor	$[\mathrm{s}^{-1}]$
μ	Dynamic viscosity	$[\mathrm{Pa} \cdot \mathrm{s}]$
μ_0	Dynamic viscosity at reference temperature	$[\mathrm{Pa} \cdot \mathrm{s}]$

ν	Kinematic viscosity	$[m^2/s]$
ρ	Density	$[kg/m^3]$
Θ	Dilatation rate	$[s^{-1}]$
$\underline{F}^c$	Vector of convective fluxes	
$\underline{F}^v$	Vector of viscous fluxes	
$\underline{U}$	Vector of conservative variables	
$\underline{V}$	Vector of primitive variables	
a	Speed of sound	$[m/s]$
e	Specific internal energy	$[m^2/s^2]$
e_t	Specific total internal energy	$[m^2/s^2]$
f_{V_i}	Specific body force in i direction	$[m/s^2]$
h	Specific enthalpy	$[m^2/s^2]$
h_t	Specific total enthalpy	$[m^2/s^2]$
p	Static pressure	$[Pa]$
Pr	Prandtl number	
q_i	Heat flux in i direction	$[W/m^2]$
R_g	Specific gas constant	$[J/(kg \cdot K)]$
Re	Reynolds number	
S^*	Characteristic wave speed of contact wave	$[m/s]$
S_L, S_R	Left and right characteristic wave speeds	$[m/s]$
S_μ	Sutherland temperature	$[K]$
T	Temperature	$[K]$
t	Time	$[s]$
T_{μ_0}	Reference temperature in Sutherland's law	$[K]$
u, v, w	Cartesian velocity components	$[m/s]$

CLSQ Reconstruction (Section 2.3)

$(\cdot)_{\boxtimes_i}$	Variable associated with the i^{th} Gauss-Legendre quadrature point
$(\cdot)_{\circ_i}$	Variable associated with the i^{th} Gaussian cubature point
α_ℓ	ℓ^{th} basis polynomial
$\bar{N}_\boxtimes$	Number of Gauss-Legendre quadrature points per edge
$\bar{N}_\circ$	Number of Gaussian cubature points per triangle element
$\langle\cdot\rangle_{E_i}$	Cell-averaging operator in cell E_i
$\mathbb{E}^d$	d-dimensional Euclidean space
$\mathbb{I}_{\ell,E_i}$	Surface integration moment of α_ℓ in cell E_i
$\mathbb{R}^d$	d-dimensional vector space of real numbers
$\mathcal{J}$	Constraint-free optimization functional
$\mathcal{L}$	Constrained optimization functional with Lagrange multipliers
$\mathcal{N}_i$	Set of cells in the stencil associated with cell E_i excluding E_i
$\mathcal{T}$	Triangle used for surface integration with Dunavant rules
$\mathcal{X}^m_{\text{nat}}$	m^{th}-order natural lattice
$\underline{\underline{\mathbb{I}}}$	N_b by N_c matrix containing the integration moments $\mathbb{I}_{\ell,E_i}$
$\underline{\underline{\mathcal{A}}}$	Karush–Kuhn–Tucker (KKT) matrix
$\underline{\underline{\mathcal{K}}}$	Boundary constraint matrix
ϕ	Arbitrary flow variable to reconstruct in the stencil

$\pi_m(\mathbb{R}^d)$	Vector space of polynomials on $\mathbb{R}^d$ of degree $\leq m$	
$\vec{\mathrm{n}}$	Unit face-normal vector	
$\underline{\mathbb{I}}_{E_i}$	Vector containing N_c surface integration moments $\mathbb{I}_{\ell,E_i}$ in cell E_i	
$\vec{x}_{E_i}$	Barycenter coordinates of the cell E_i	[m]
c_i	i^{th} polynomial coefficient of P_{S_i}	
d_{E_i,E_j}	Centroid-to-centroid distance between cells E_i and E_j	
E_i	Arbitrary polygonal cell with index i	
G_{ij}	j^{th} edge of polygonal cell E_i	
m	Highest degree of reconstructing polynomial P_{S_i}	
N_b	Cardinality of set $\mathcal{N}_i$	
N_c	Number of polynomial coefficients for P_{S_i}	
$N_{\boxtimes}$	Total number of Gauss-Legendre quadrature points	
$N_{\circ}$	Total number of Gaussian cubature points	
p	Order of reconstructing polynomial P_{S_i}	
P_{S_i}	Reconstructing polynomial in stencil S_i	
S_i	Set of cells in the stencil associated with cell E_i	
z_i	i^{th} Lagrange multiplier	
CLSQp	p^{th}-order CLSQ scheme	

Riemann Solver (Section 2.4)

$(\cdot)_L$	Left state variable	
$(\cdot)_L^*$	Left star region variable	
$(\cdot)_R$	Right state variable	
$(\cdot)_R^*$	Right star region variable	
$(\cdot)_{LR}$	Variable estimated at the edge between cells E_i anf E_j	
θ	Scaling function $\theta(M) = \min(M, 1)$	
$\widehat{(\cdot)}$	Roe averaged variable	
M	Mach number	
S^*	Contact wave speed	[m/s]
S_L	Left wave speed	[m/s]
S_R	Right wave speed	[m/s]
V_n	Normal velocity	[m/s]

Time-integration (Section 2.5, Section 2.6)

λ	Spectral radius of flux Jacobian	
${}^{k}(\cdot)$	Variable at k^{th} linear iteration	
${}^{m,n}(\cdot)$	Variable at m^{th} inner iteration of n^{th} outer iteration	
M_{it}	Total number of dual-time m-iterations at a given n-iteration	
EN_i	Set of direct edge-neighbors of the cell E_i	
HP_i	Hyperplane of index i in the context of unstructured grid reordering	
$\underline{\underline{\mathbf{J}}}$	Jacobian matrix	
$\underline{\underline{\mathbf{M}}}$	Sparse block matrix defined by implicit time-integration scheme	
ν_{eq}	Equivalent kinematic viscosity	
Ω	Set of cells in the computational domain	

$\underline{F}^{\text{APP}}$	Vector of low-order approximated numerical fluxes	
$\underline{F}^{\text{NUM}}$	Vector of high-order CLSQ reconstructed numerical fluxes	
$\underline{R}$	Vector of residuals	

Boundary Condition (Section 2.7)

$(\cdot)_\infty$	Variable imposed at domain infinity	
$(\cdot)_i$	Variable in the interior state	
$(\cdot)_j$	Variable in the exterior state	
$(\cdot)_o$	Variable imposed at channel outlet	
$(\cdot)_{\text{BC}}$	Variable in the boundary state	
$\mathcal{R}^+$	Incoming Riemann invariant	[m/s]
$\mathcal{R}^-$	Outgoing Riemann invariant	[m/s]
$\underline{F}^{\text{BC,APP}}$	Vector of low-order approximated boundary numerical fluxes	
$\underline{F}^{\text{BC,NUM}}$	Vector of high-order CLSQ reconstructed boundary numerical fluxes	
$\vec{t}$	Face-tangential unit vector	
$\vec{V}$	Velocity vector	[m/s]
V_t	Face-tangential velocity component	[m/s]

Miscellaneous

AoA	Angle of attack	
V_∞	incoming flow velocity at infinity $\sqrt{u_\infty^2 + v_\infty^2}$	[m/s]
$\overline{C}_D$	Time-averaged drag coefficient	
$\overline{C}_L$	Time-averaged lift coefficient	
AR	Aspect ratio	
C_D	Drag coefficient	
C_L	Lift coefficient	
ER	Expansion ratio	
H	Step height in backward-facing step test-case	[m]
H_i	Inlet channel height in backward-facing step test-case	[m]
H_o	Outlet channel height in backward-facing step test-case	[m]
L	Flat-plate length in flat-plate boundary layer test-case	[m]
L_i	Inlet channel length in backward-facing step test-case	[m]
L_o	Outlet channel length in backward-facing step test-case	[m]
L_{chord}	Chord length of an airfoil	[m]
u_B	Bulk velocity	[m/s]

Chapter 1

Introduction

1.1 Background

Accuracy and generality have long been the two centerpieces around which revolve virtually all research projects in the field of Computational Fluid Dynamics (CFD) until this day. An ideal CFD solver needs to be capable of solving a wide range of realistic flow problems on as many types of geometries as possible, while producing results as accurate as the computational resources allow. However, in reality, achieving high-order accuracy while guaranteeing robustness on complex general computational grids presents a huge challenge for any CFD solver, and in most occasions, satisfying one requires making compromises on the other.

During the development of CFD in the past few decades, four major frameworks of methods for approximately solving the Navier-Stokes equations have risen to prominence, and have gained the most popularity among all solver implementations; they are the Finite Difference Method (FDM), the Finite Volume Method (FVM), the Finite Element Method (FEM) (in particular the Petrov-Galerkin method), and the Spectral Method. The FDMs have the longest history of applications in CFD and they are designed based on solving the *strong* form of the Navier-Stokes equations, which consists of approximating the differential operator by differences of nodal data. The other three methods aim to solve the *weak* form of the Navier-Stokes equations, which involves approximating the solutions by trial functions with respect to a space of test functions. Both the FVM and Spectral methods can be regarded as variations of the FEM in a broader sense, and they differ mainly in the choices of test and trial functions.

According to Morton and Sonar [160] and Gerolymos and Vallet [91], the Finite Volume Methods are mathematically equivalent to the Petrov-Galerkin-type Finite Element Methods with piece-wise constant test functions, and the reconstruction of scalar fields based on cell-averaged input data is a special case of the optimal recovery theory developed by Micchelli and Rivlin [157], in a sense that the point values of the function to be approximated are *recovered* from a set of cell-averages. This viewpoint is also shared by other authors such as Shu [191], who establishes the framework of the Discontinuous Galerkin Method as a generalization of the FVM.

The Spectral Methods differ from the FEMs and FVMs in their choice of trial functions (or basis functions). The trial functions used by spectral methods are infinitely differentiable *global* functions, according to Canuto *et al.* [31], whereas those of FEMs (locally smooth) and FVMs (locally polynomial) are local.

Numerous efforts have been invested to construct both accurate and general CFD solvers using

the four classes of methods mentioned above, thus making the study of high-order numerical methods an extremely active branch in CFD.

For the FDMs, which are also the most mathematically straightforward methods, high-order approximation schemes can be intuitively devised by expanding the stencil associated with each node. However, the simplicity in constructing high-order schemes comes with the sacrifice in generality. The FDM are only compatible with structured computational grids therefore their applications are limited to regular and simple geometries, which results in the loss of geometric flexibility. The extension to complex geometries requires using multi-block structured grids with the associated difficulty of information transfer at block interfaces.

The Spectral Methods are inherently extensible to very high-order accuracy due to their usage of infinitely differentiable trial functions (*e.g.*, trigonometric polynomials, Legendre polynomials, Chebyshev polynomials, *etc.*) everywhere in the computational domain. However, also due to the globalness and smoothness of their trial functions, this family of methods have difficulties in treating geometric singularity (*e.g.*, sharp corners) and discontinuity in the solution [31]. Therefore, although the high-order extension is naturally incorporated in these methods, their application is restricted to simple geometries and mainly to smooth flow fields.

Until this day, the only viable candidates among the four types of methods that are able to achieve high-order accuracy while preserving generality are the FVM and the FEM. Comparing with the FVM, the high-order extensions of FEM are more straightforward and is achieved by simply adding degrees of freedom to each element. The so-called *hp*-adaptivity can also be realized since the order of approximation can be modified in specific elements [64]. However, the traditional FEMs have notable disadvantages in fluid simulations comparing to the FVMs, namely for solving problems with (pseudo-)time-dependence. In time-dependent FEMs, the residual of solution at each time-step is required to be orthogonal to the test functions. This requirement results in a large mass matrix $\underline{\underline{\mathbf{M}}}$ to be inverted at every time-step which adds considerably to the computational burden during time-marching. Moreover, as pointed out by many previous authors [109, 111, 228], the classic FEM proves to be a less natural choice for convection-dominated and wave-dominated flows since the trial functions are typically spatially symmetric and they are incompatible with the concept of *upwinding* which is natural to FDM and FVM. The Discontinuous Galerkin Finite Element Method (DG-FEM) has been developed to overcome the limitations of traditional FEM by adopting a few important features from the FVM. In the context of DG-FEM, the definitions of trial and test functions are local to each element, and the numerical flux is computed at elemental interfaces to account for information from both sides. Moreover, the large global mass matrix $\underline{\underline{\mathbf{M}}}$ in the FEM is reduced to a locally defined small matrices which are much less costly to invert during time-marching. Through a series of works by Cockburn, Shu, Bassi, Rebay, Hesthaven, Warburton and others [23, 25, 43, 50, 51, 52, 53, 54, 55, 109], the DG-FEM has been well-established as a viable candidate for solving the Euler and Navier-Stokes equations in all flow regimes. Nevertheless, despite all recent developments in this area, the DG-FEM still remains a more computationally expensive method compared to the FVM and one of the major reasons is that all interfaces between two neighboring elements need to be duplicated for the constructions of local test and trial functions. This directly doubles the computational costs and can become disadvantageous for large-scale implementations [109]. Furthermore, DG-FEMs show less robustness in the presence of strong shocks comparing to the high-order FVMs such as the WENO schemes [191].

All aspects considered, until this day, the FVM still remains the most balanced method in terms of accuracy, flexibility and economy. For numerical approximations of at most second order in smooth regions, the family of Monotonic Upstream-centered Scheme for Conservation Laws

(MUSCL) schemes and Total Variation Diminishing (TVD) schemes developed by van Leer [209] and Harten [107] have attained dominant popularity since the late 1970s, and have long been implemented in large-scale industrial applications with widely recognized robustness for various flow problems. The WENO approach of Shu [191] further improves capturing of discontinuities with the additional advantage of being scalable to arbitrary order-of-accuracy [88]. However, beyond second order, the order increase for the FVMs is less straightforward than that of the FEMs or Spectral Methods since their test functions are inherently piece-wise constant.

In order to benefit from the relatively simple implementation, the geometric flexibility and the low computational overhead of the FVM, a great number of studies in CFD have been dedicated to designing high-order (at least third-order) numerical schemes for the FVM. The most well-known and widely implemented high-order schemes for FVMs and FDMs are the family of Essentially Non-Oscillatory (ENO) schemes developed by Harten *et al.* [108], Shu and Osher [189, 190] where several high-order stencils are constructed around each computational cell in the domain, and the stencil with the smoothest solution is selected for the final reconstruction. In particular, the Weighted Essentially Non-Oscillatory (WENO) schemes developed by Liu *et al.* [148] and generalized by Jiang and Shu [119] in 1996 are a major improvement with respect to ENO schemes. For the WENO schemes, instead of picking the stencil with the smoothest solution for reconstruction, each cell is assigned with a set of lower order stencils and the high-order reconstruction is achieved by a convex combination of the solutions in all lower order stencils, each with its respective weight proportional to the smoothness of solution within that stencil. WENO schemes are capable of obtaining arbitrarily high-order solutions in convection-and-shock-dominated flows while maintaining sharp shock profiles with essentially no spurious oscillations. Among various implementations of WENO schemes on structured grids, Balsara and Shu [18] developed a family of Monotonicity-Preserving WENO (MPWENO) schemes based on the high-order monotonicity-preserving schemes of Suresh and Huynh [202], which is $\mathcal{O}(\Delta x^{2r-1})$ accurate for $r = 4, 5, 6$. Gerolymos *et al.* [88] extended this family of WENO schemes for $r = 7, 8, 9$ which is the implementation of the highest order to date on structured grids to the author's knowledge.

On general unstructured grids, the traditional reconstruction methods of ENO/WENO schemes i.e., reconstruction via deconvolution and reconstruction via primitive function fail [5], and the building block of the unstructured ENO/WENO schemes is the Least-Squares (LSQ) reconstruction proposed by Barth and Frederickson [20]. Unstructured implementations of ENO/WENO schemes have been carried out in the last three decades by Abgrall [5], Ollivier-Gooch [168], Hu and Shu [110] and Zhang and Shu [225] among others, and the theoretical order of accuracy on arbitrary grids are limited to third-order. Although the development of WENO schemes on structured grids reached its maturity [191], there still exist many difficulties in developing WENO schemes on unstructured grids, and particularly in finding positive linear weights even for the third-order WENO on triangular grids as shown by Hu and Shu [110]. Until the time of writing this thesis, high-order extensions of WENO schemes on unstructured grids still remain an active and challenging area of research [226, 227].

As mentioned earlier, the success of unstructured ENO/WENO schemes relies on an accurate and robust Least-Squares (LSQ) reconstruction scheme. For 2D advection equation in a periodic domain, the LSQ scheme implemented by Gerolymos and Vallet [91] managed to reach 10^{th}-order accuracy on non-stretched unstructured polygonal grids through *a posteriori* verification. However, in order to generalize the LSQ scheme to non-periodic domains with physical boundary conditions, it is important for the LSQ scheme to retain its accuracy everywhere in the domain *including* at boundaries. When the insertion of multiple layers of boundary ghost cells are not possible for many real-life geometries (*e.g.*, sharp corners, thin solid obstacles), the reconstructing polynomials

need to account for the specific boundary conditions while maintaining the desired order. This gives rise to a class of more general LSQ reconstruction schemes developed by Ollivier-Gooch *et al.* [116, 169], Bertolazzi and Manzini [27] and Charest *et al.* [38, 39] among others, called the Constrained LSQ (CLSQ) reconstruction schemes. This type of reconstruction schemes treat interior and boundary cells in a unified manner by inserting additional equality constraints in the LSQ system, and show great potential to become the cornerstone of a more general and robust class of high-order ENO/WENO schemes on arbitrary unstructured grids. A recent implementation of the CLSQ reconstruction in ENO-type schemes is the Central Essentially Non-Oscillatory (CENO) scheme introduced by Charest *et al.* [39]. However, no result of formal grid convergence study has been shown for wall-bounded viscous flow on stretched unstructured grids.

More research in the area of high-order CFD solver on general unstructured grids remains to be undertaken.

1.2 Motivation

This thesis falls within the scope of collaborative project ANR-15-CE06-0009 NumERICCs (Numerical and Experimental Research for Improved Control of Compressor Surge) funded by the *Agence Nationale de la Recherche*. The NumERICCs project aims to develop novel techniques for the active control of high pressure (HP) compressor surge. One of the major contributors of compressor surge is the generation of tip leakage vortices and their interactions with the complex secondary flow in the blade cascade [65, 86].

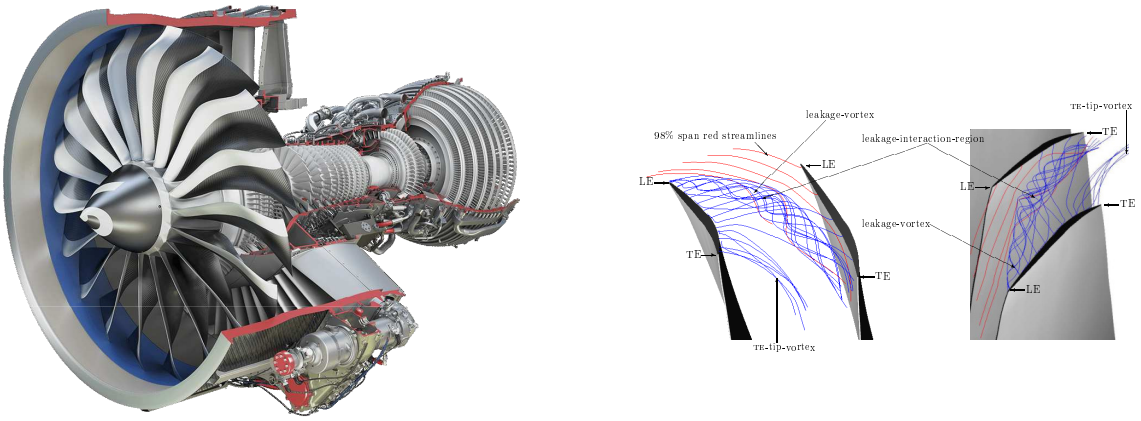

(a) (b)

Figure 1.1: (a): internal structure of an turbofan aircraft engine made by CFM; (b): tip leakage vortices in a blade cascade.

In order to gain deep insight into the compressor surge, the challenge is to simulate the generation of tip leakage vortices and their interactions with secondary flow and shock waves. To complete this challenge requires (**i**) : the CFD solver to have arbitrarily high-order resolution in smooth regions and the capability to capture shock waves; (**ii**) : an accurate turbulence model with advanced near-wall treatment; (**iii**) : the computational grid to be locally refined within the tip-clearance-gap without interfering with the coarser meshes in the blade cascade, which neces-

sitates the implementation of general unstructured grids. Extensive researches have been carried out to meet the first two requirements, a very-high-order WENO scheme has been developed by Gerolymos *et al.* [88] on structured grids, and a 7-equation (5-equation in 2D) Reynolds Stress Model capable of modeling inhomogeneity and anisotropy near and away from the wall has been proposed by Gerolymos *et al.* (GLVY-RSM) [92]. However, in order to migrate the experience acquired in the aforementioned studies to general unstructured grids (requirement (**iii**)), high-order accurate numerical methods need to be further developed for unstructured grids including the CLSQ reconstruction schemes, efficient implicit time-integration methods on unstructured grids, *etc.* This works is to be undertaken in this thesis.

1.3 Thesis Outline

This thesis begins with a detailed presentation of the governing equations for simulating compressible flows including the continuous and discretized Navier-Stokes equations and ideal gas thermodynamic relations. Next, the mathematical formulation of the novel CLSQ reconstruction scheme based on the functional with Lagrange multipliers are discussed along with an analysis on the existence and uniqueness of the solution to the system of constrained optimization problem. Other numerical methods used in the current study are also discussed, such as the approximate Riemann solver for numerical flux computation, the implicit time-integration schemes developed for general unstructured grids, and the treatments of boundary conditions encountered in compressible flow simulations. Furthermore, an detailed evaluation is dedicated to verify the robustness and accuracy of the aforementioned computational methods on 2D general polygonal grids including but not limited to a formal grid convergence study on the CLSQ scheme with wall-bounded viscous flow. Finally, all computational methods developed in this study are implemented as a 2D unstructured package within the open-source CFD code Aerodynamics [90], which is used to study the flow physics of the classic laminar backward-facing step (BFS) test-case of Armaly *et al.* [13]. Comparisons are made with the experimental data and various previous computational studies, and we demonstrate that the method gives consistent results with reported data in the literature while showing some notable advantages in the flow field prediction.

Chapter 2

Governing Equations and Computational Methods

2.1 Governing Equations

The flow is described by compressible Navier-Stokes equations are written in the indicial notation in Eqn. 2.1

$$\frac{\partial \rho}{\partial t} + \frac{\partial}{\partial x_\ell}(\rho u_\ell) = 0 \tag{2.1a}$$

$$\frac{\partial \rho u_i}{\partial t} + \frac{\partial}{\partial x_\ell}(\rho u_i u_\ell) = -\frac{\partial p}{\partial x_i} + \frac{\partial \tau_{i\ell}}{\partial x_\ell} + \rho f_{V_i} \tag{2.1b}$$

$$\frac{\partial \rho e_t}{\partial t} + \frac{\partial}{\partial x_\ell}(\rho h_t u_\ell) = \frac{\partial}{\partial x_\ell}(u_m \tau_{m\ell} - q_\ell) + \rho f_{V_m} u_m \tag{2.1c}$$

where t is the time, $x_i \in \{x, y, z\}$ represent the Cartesian space coordinates, ρ is the density, p is the static pressure, $u_i \in \{u, v, w\}$ are the velocity components in the Cartesian space coordinates, p is the static pressure, $\tau_{G_{ij}}$ is the viscous stress tensor, f_{V_i} are the body-forces in the Cartesian space coordinates which are neglected in the current study. The energy equation Eqn. 2.1c is written with respect to the specific total energy e_t with

$$\rho e_t = \rho h_t - p \tag{2.2a}$$

$$h_t = h + u_i u_i / 2 \tag{2.2b}$$

$$h = e + p/\rho \tag{2.2c}$$

where e is the specific internal energy, h is the specific enthalpy, h_t is the specific total enthalpy.

In Eqn. 2.1c, q_i are the molecular heat-fluxes in the Cartesian coordinates. In the current

thesis, the fluid is assumed to be ideal gas, which implies the following thermodynamic relations

$$p = \rho R_g T \tag{2.3a}$$
$$R_g = \text{const.} \tag{2.3b}$$
$$c_p = \frac{\gamma}{\gamma - 1} R_g = \text{const.} \tag{2.3c}$$
$$c_v = \frac{1}{\gamma - 1} R_g = \text{const.} \tag{2.3d}$$
$$a = \sqrt{\gamma \frac{p}{\rho}} = \sqrt{\gamma R_g T} \tag{2.3e}$$

where R_g is the specific gas constant ($R_g = 287.04\,\mathrm{m^2 \cdot s^{-1} \cdot K^{-1}}$ for air), γ is the heat capacity ratio ($\gamma = 1.4$ for air), $c_v = \text{const.}$ and $c_p = \text{const.}$ are respectively the specific heat capacity at constant volume and that at constant pressure, c is the speed of sound. From Eqn. 2.3, the relation between the static pressure p and the specific total energy is deduced in Eqn. 2.4

$$p = (\gamma - 1)\rho \left(e_t - u_i u_i / 2\right). \tag{2.4}$$

The viscous stress tensor τ_{ij} is linearly correlated to the strain-rate tensor S_{ij} following the Newtonian law

$$\tau_{ij} = 2\mu \left(S_{ij} - \frac{1}{3}\Theta \delta_{ij} \right) + \mu_b \Theta \delta_{ij} \tag{2.5}$$

where $S_{ij} := \frac{1}{2}\left(\frac{\partial u_i}{\partial x_j} + \frac{\partial u_j}{\partial x_i}\right)$ is the strain-rate tensor, and $\Theta := \frac{\partial u_i}{\partial x_i} = S_{ii}$ is the dilatation rate, δ_{ij} is the Kronecker symbol, $\mu := \mu(T)$ is the dynamic viscosity, μ_b is the bulk viscosity.

The heat-flux q_i is calculated with Fourier's law of thermal conduction in Eqn. 2.6

$$q_i = -\kappa \frac{\partial T}{\partial x_i} \tag{2.6}$$

where $\kappa = \kappa(T)$ is the thermal conductivity, which, along with $\mu(T)$, are determined by the Sutherland's law in Eqn. 2.7

$$\mu(T) = \mu_0 \left[\frac{T}{T_{\mu_0}}\right]^{\frac{3}{2}} \frac{S_\mu + T_{\mu_0}}{S_\mu + T} \tag{2.7a}$$
$$\kappa(T) = \kappa_0 \frac{\mu(T)}{\mu_0} [1 + A_\kappa (T - T_{\mu_0})] \tag{2.7b}$$

where, for air, the constants and coefficients in Eqn. 2.7 are due to [85, 94] : $T_{\mu_0} = 273.15\,\mathrm{K}$, $\mu_0 := \mu(T_{\mu_0}) = 17.11 \times 10^{-6}\,\mathrm{Pa \cdot s}$, $S_\mu = 110.4\,\mathrm{K}$, $\kappa_0 := \kappa(T_{\mu_0}) = 0.0242\,\mathrm{W \cdot m^{-1} \cdot K^{-1}}$, $A_\kappa = 2.3 \times 10^{-4}\,\mathrm{K^{-1}}$. Note that, since both μ and κ are functions of temperature T, the Prandtl number $Pr = c_p \mu / \kappa$ is also a function of temperature $Pr := Pr(T)$. Bulk viscosity is neglected in Eqn. 2.5 following Stokes' hypothesis

$$\mu_b = 0. \tag{2.8}$$

In order to model the system of equations Eqn. 2.1 later with a Finite Volume Method (FVM),

it is important to rewrite Eqn. 2.1 in vector form as in Eqn. 2.9

$$\frac{\partial \underline{U}}{\partial t} + \frac{\partial \underline{F}_\ell}{\partial x_\ell} = 0 \tag{2.9}$$

where $\underline{U} \in \mathbb{R}^5$ [1] is the vector of conservative variables

$$\underline{U} = [\rho, \rho u, \rho v, \rho w, \rho e_t]^\top \tag{2.10}$$

and the flux vectors $\underline{F}_\ell$ consist of the convective fluxes $\underline{F}_\ell^{\mathrm{c}}$ and the viscous fluxes $\underline{F}_\ell^{\mathrm{v}}$, which are defined as follows

$$\underline{F}_\ell(\underline{U}, \mathrm{grad}\underline{U}) = \underbrace{\begin{bmatrix} \rho u_\ell \\ \rho u u_\ell + p\delta_{x\ell} \\ \rho v u_\ell + p\delta_{y\ell} \\ \rho w u_\ell + p\delta_{z\ell} \\ \rho e_t u_\ell + p u_\ell \end{bmatrix}}_{\underline{F}_\ell^{\mathrm{c}}(\underline{U})} + \underbrace{\begin{bmatrix} 0 \\ -\tau_{x\ell} \\ -\tau_{y\ell} \\ -\tau_{z\ell} \\ -u_i\tau_{i\ell} + q_\ell \end{bmatrix}}_{\underline{F}_\ell^{\mathrm{v}}(\underline{U}, \mathrm{grad}\underline{U})}. \tag{2.11}$$

where $\mathrm{grad}\underline{U}$ is the entry-wise gradient of $\underline{U}$

$$\mathrm{grad}\underline{U} := [\mathrm{grad}\rho, \mathrm{grad}u, \mathrm{grad}v, \mathrm{grad}w, \mathrm{grad}e_t]^\top. \tag{2.12}$$

Finally we obtain the integral form of Eqn. 2.9

$$\frac{\partial}{\partial t}\int_{\mathrm{V}} \underline{U}\,\mathrm{dV} + \oint_{\partial \mathrm{V}} \vec{\underline{F}}(\underline{U}, \mathrm{grad}\underline{U}) \cdot \mathrm{d}\vec{\mathrm{S}} = 0 \tag{2.13}$$

where

$$\vec{\underline{F}} = \underline{F}_x \vec{\mathrm{e}}_x + \underline{F}_y \vec{\mathrm{e}}_y + \underline{F}_z \vec{\mathrm{e}}_z \tag{2.14}$$

and V denotes an arbitrary fixed control volume with ∂V being the collection of its bounding surfaces. Note that, in 2D, V is reduced to a planar surface with ∂V being its bounding curves.

[1] In this thesis, the symbol $\mathbb{R}^n$ is reserved for n-vectors of flow variables such as $\underline{U}$, $\underline{V}$, *etc.*, whereas symbol $\mathbb{E}^n$ is used to denote the n-dimensional Euclidean space.

2.2 Overview of Computational Methodology

The integral form of the Navier-Stokes equations Eqn. 2.13 is discretized according to the finite volume formulation

$$\frac{\partial}{\partial t}\int_{E_i}\underline{U}\mathrm{dV}+\oint_{\partial E_i}\vec{\underline{F}}(\underline{U},\mathrm{grad}\underline{U})\cdot\mathrm{d}\vec{\mathrm{S}}=0 \tag{2.15}$$

where E_i denotes a discretized control volume which is hereafter termed as a computational cell or *cell* for short, and ∂E_i denotes the bounding edges of cell E_i. In the present study, we limit ourselves to general 2D polygonal grids, therefore E_i is a general polygon with straight edges.

The semi-discrete form of Eqn. 2.15 is applied to each discrete N-gon E_i, whose N edges are denoted by G_{ij} with $j=1,\cdots,N$. Note that $\bigcup_{j=0}^{n}G_{ij}$ is the discretized form of ∂E_i

$$\frac{\mathrm{d}}{\mathrm{d}t}\langle\underline{U}\rangle_{E_i}+\frac{1}{\mathrm{A}_{E_i}}\sum_{j=0}^{N}\underline{F}_{G_{ij}}^{\mathrm{NUM}}\mathrm{L}_{G_{ij}}=\mathcal{O}(\Delta h^p) \tag{2.16}$$

where $\langle\cdot\rangle_{E_i}$ is the cell-averaging operator in cell E_i, A_{E_i} is the area of E_i, $\mathrm{L}_{G_{ij}}$ is the length of G_{ij}. The approximation error is $\mathcal{O}(\Delta h^p)$ where Δh is the characteristic grid spacing and p is the order of spatial discretization. $\underline{F}_{G_{ij}}^{\mathrm{NUM}}$ is the edge-averaged numerical flux evaluated at edge G_{ij} with Gauss-Legendre quadrature rule

$$\begin{aligned}\underline{F}_{G_{ij}}^{\mathrm{NUM}}&=\underline{F}_{G_{ij}}^{\mathrm{c,NUM}}+\underline{F}_{G_{ij}}^{\mathrm{v,NUM}}\\&=\sum_{k=1}^{\bar{N}_{\boxtimes}}w_{\boxtimes_k}\underline{F}^{\mathrm{c,NUM}}\left(\underline{U}_{L_{\boxtimes_k}},[\mathrm{grad}\underline{U}]_{L_{\boxtimes_k}},\underline{U}_{R_{\boxtimes_k}},[\mathrm{grad}\underline{U}]_{R_{\boxtimes_k}},\vec{\mathrm{n}}_{\boxtimes_k}\right)\\&+\sum_{k=1}^{\bar{N}_{\boxtimes}}w_{\boxtimes_k}\underline{F}^{\mathrm{v,NUM}}\left(\underline{U}_{L_{\boxtimes_k}},[\mathrm{grad}\underline{U}]_{L_{\boxtimes_k}},\underline{U}_{R_{\boxtimes_k}},[\mathrm{grad}\underline{U}]_{R_{\boxtimes_k}},\vec{\mathrm{n}}_{\boxtimes_k}\right)\end{aligned} \tag{2.17}$$

where $\bar{N}_{\boxtimes}$ is the number of quadrature points per edge, $\underline{F}^{\mathrm{c,NUM}}$ and $\underline{F}^{\mathrm{v,NUM}}$ are the point-wise numerical convective and viscous fluxes evaluated at each Gauss-Legendre quadrature point (denoted by $\boxtimes_k$) on the edge G_{ij}. To provide arguments for $\underline{F}^{\mathrm{c,NUM}}$ and $\underline{F}^{\mathrm{v,NUM}}$, we evaluate the left and right conservative variables $\underline{U}_{L_{\boxtimes_k}}$ and $\underline{U}_{R_{\boxtimes_k}}$, the entry-wise gradients (Eqn. 2.12) of the left and right conservative variables $[\mathrm{grad}\underline{U}]_{L_{\boxtimes_k}}$ and $[\mathrm{grad}\underline{U}]_{R_{\boxtimes_k}}$, and the unit face-normal vector $\vec{\mathrm{n}}_{\boxtimes_k}$ which points from the left state to the right state. In the context of Godunov-type FVM, the solution of $\underline{F}^{\mathrm{c,NUM}}$ is obtained with a Riemann solver (see detailed discussion in Section. 2.4), whereas $\underline{F}^{\mathrm{v,NUM}}$ is determined by simply taking the average on the high-order reconstructed viscous fluxes in the left and right states of a quadrature point $\boxtimes_k$

$$\begin{aligned}&\underline{F}^{\mathrm{v,NUM}}\left(\underline{U}_{L_{\boxtimes_k}},[\mathrm{grad}\underline{U}]_{L_{\boxtimes_k}},\underline{U}_{R_{\boxtimes_k}},[\mathrm{grad}\underline{U}]_{R_{\boxtimes_k}},\vec{\mathrm{n}}_{\boxtimes_k}\right)=\\&\frac{1}{2}\left[\underline{F}^{\mathrm{v,NUM}}\left(\underline{U}_{L_{\boxtimes_k}},[\mathrm{grad}\underline{U}]_{L_{\boxtimes_k}},\vec{\mathrm{n}}_{\boxtimes_k}\right)+\underline{F}^{\mathrm{v,NUM}}\left(\underline{U}_{R_{\boxtimes_k}},[\mathrm{grad}\underline{U}]_{R_{\boxtimes_k}},\vec{\mathrm{n}}_{\boxtimes_k}\right)\right]\end{aligned} \tag{2.18}$$

The input data on the computational grid are cell-averages, therefore, to evaluate any variable

or its derivatives at a given quadrature point (or at any point $\vec{x} \in \mathbb{E}^2$ [2] for that matter), a spatial reconstruction scheme is required. For a high-order CFD solver of order p, the point-data evaluation needs to be p^{th}-order-accurate. For this purpose, we introduce the constrained least-squares (CLSQ) reconstruction scheme later in Section. 2.3.

Expressing Eqn. 2.16 in terms of the residual vector $\underline{R}_{E_i}$ gives

$$\frac{\mathrm{d}}{\mathrm{d}t}\langle \underline{U} \rangle_{E_i} + \underline{R}_{E_i} = \mathcal{O}(\Delta h^p) \qquad \text{with} \qquad \underline{R}_{E_i} = \frac{1}{\mathrm{A}_{E_i}} \sum_{j=0}^{N} \underline{F}^{\mathrm{NUM}}_{G_{ij}} \mathrm{L}_{G_{ij}} \tag{2.19}$$

and we name $\underline{R}_{E_i}$ the "steady residual" which tends to zero when the cell-averaged solution $\langle \underline{U} \rangle_{E_i}$ reaches a steady-state $\mathrm{d}\langle \underline{U} \rangle_{E_i}/\mathrm{d}t \to 0$. For a steady-state solution of Eqn. 2.19, a first-order accurate implicit time-discretization is implemented

$$\frac{{}^{n+1}\langle \underline{U} \rangle_{E_i} - {}^{n}\langle \underline{U} \rangle_{E_i}}{\Delta t} + \left({}^{n+1}\underline{R}_{E_i} - {}^{n}\underline{R}_{E_i}\right) + {}^{n}\underline{R}_{E_i} = \mathcal{O}(\Delta t, \Delta h^p). \tag{2.20}$$

Due to the steadiness of the converged solution, the temporal order of accuracy does not interfere with the accuracy of CFD solver, and the final solution is as accurate as the p^{th}-order spatial discretization scheme. Since variables at time-step $n+1$ cannot be evaluated directly, we perform a first-order linearization on the residual increment

$${}^{n+1}\underline{R}_{E_i} - {}^{n}\underline{R}_{E_i} \approx {}^{n}\left(\frac{\partial \underline{R}_{E_i}}{\partial \langle \underline{U} \rangle_{E_i}}\right) {}^{n}\Delta\langle \underline{U} \rangle_{E_i} + \sum_{E_j \in \mathcal{N}_i} {}^{n}\left(\frac{\partial \underline{R}_{E_i}}{\partial \langle \underline{U} \rangle_{E_j}}\right) {}^{n}\Delta\langle \underline{U} \rangle_{E_j} \tag{2.21}$$

and replacing Eqn. 2.21 into Eqn. 2.20 gives

$$\frac{{}^{n}\Delta\langle \underline{U} \rangle_{E_i}}{\Delta t} + {}^{n}\left(\frac{\partial \underline{R}_{E_i}}{\partial \langle \underline{U} \rangle_{E_i}}\right) {}^{n}\Delta\langle \underline{U} \rangle_{E_i} + \sum_{E_j \in \mathcal{N}_i} {}^{n}\left(\frac{\partial \underline{R}_{E_i}}{\partial \langle \underline{U} \rangle_{E_j}}\right) {}^{n}\Delta\langle \underline{U} \rangle_{E_j} + {}^{n}\underline{R}_{E_i} = \mathcal{O}(\Delta t, \Delta h^p) \tag{2.22}$$

where ${}^{n}\Delta\langle \underline{U} \rangle_{E_i} = {}^{n+1}\langle \underline{U} \rangle_{E_i} - {}^{n}\langle \underline{U} \rangle_{E_i}$, ${}^{n}\Delta\langle \underline{U} \rangle_{E_j} = {}^{n+1}\langle \underline{U} \rangle_{E_j} - {}^{n}\langle \underline{U} \rangle_{E_j}$, $\mathcal{N}_i$ is the set of neighbor cells in the high-order reconstruction stencil S_i associated with E_i as will be illustrated later in Section. 2.3, Fig. 2.1. ${}^{n}\left(\frac{\partial \underline{R}_{E_i}}{\partial \langle \underline{U} \rangle_{E_i}}\right)$ and ${}^{n}\left(\frac{\partial \underline{R}_{E_i}}{\partial \langle \underline{U} \rangle_{E_j}}\right)$ are the residual Jacobian matrices of dimensions 4×4 for 2D Navier-Stokes equations. The steady residual $\underline{R}_{E_i}$ is computed based on cell-averaged variables in the computational stencil S_i (Fig. 2.1) through high-order reconstructing polynomials. The expressions of residual Jacobians are extremely complex for high-order reconstruction schemes, and for each cell E_i, we need to store $N_b + 1$ Jacobians where N_b is the number of neighbors in a high-order reconstruction stencil S_i. Therefore, computing directly with residual Jacobians is extremely costly both in terms of time and of memory space. To circumvent this inconvenience, we approximate the high-order numerical flux $\underline{F}^{\mathrm{NUM}}_{G_{ij}}$ in Eqn. 2.17 by a first-order-accurate Lax-Friedrichs flux $\underline{F}^{\mathrm{APP}}_{G_{ij}}$ and apply the "matrix-free" approach of Luo *et al.* [149] later in Section. 2.5.

It is important to realize that Eqn. 2.20 is a non-linear equation since $\underline{R}_{E_i}$ is a non-linear function of $\langle \underline{U} \rangle_{E_i}$. By linearizing Eqn. 2.20 into Eqn. 2.22, its non-linearity is lost. In order to recover the non-linearity, we implement the dual-time-stepping (DTS) scheme of Gerolymos and

[2] In this thesis, the symbol $\mathbb{E}^n$ is used to denote the n-dimensional Euclidean space, whereas the symbol $\mathbb{R}^n$ is reserved for n-vectors of flow variables such as $\underline{U}$, $\underline{V}$, *etc.*

Vallet [87] by introducing an additional non-linear inner m-iteration for each outer n-iteration

$$\underbrace{\frac{{}^{m+1,n+1}\langle\underline{U}\rangle_{E_i} - {}^{m,n+1}\langle\underline{U}\rangle_{E_i}}{\Delta t^*}}_{\text{non-linear iteration}} + \left[\frac{{}^{m+1,n+1}\langle\underline{U}\rangle_{E_i} - {}^{n}\langle\underline{U}\rangle_{E_i}}{\Delta t} + {}^{m+1,n+1}\underline{R}_{E_i}\right] = \mathcal{O}(\Delta t, \Delta h^p) \quad (2.23)$$

and after some algebraic manipulations we obtain

$$\begin{aligned}
&\frac{{}^{m+1,n+1}\langle\underline{U}\rangle_{E_i} - {}^{m,n+1}\langle\underline{U}\rangle_{E_i}}{\Delta t^{**}} + \left({}^{m+1,n+1}\underline{R}_{E_i} - {}^{m,n+1}\underline{R}_{E_i}\right) + {}^{m,n+1}\underline{R}^*_{E_i} = \mathcal{O}(\Delta t, \Delta h^p) \\
&\text{with} \qquad {}^{m,n+1}\underline{R}^*_{E_i} = \frac{{}^{m,n+1}\langle\underline{U}\rangle_{E_i} - {}^{n}\langle\underline{U}\rangle_{E_i}}{\Delta t} + {}^{m,n+1}\underline{R}_{E_i} \qquad (2.24) \\
&\text{and} \qquad \frac{1}{\Delta t^{**}} = \left(\frac{1}{\Delta t^*} + \frac{1}{\Delta t}\right)
\end{aligned}$$

where we call $\underline{R}^*_{E_i}$ the "unsteady residual" which tends to zero when the non-linear m-iteration (also called the "inner iteration") converges. The linear n-iteration (also called the "outer iteration") advances the series of converged non-linear solutions until $\underline{R}_{E_i} \to 0$. The unsteady residual increment ${}^{m+1,n+1}\underline{R}_{E_i} - {}^{m,n+1}\underline{R}_{E_i}$ is also linearized through Eqn. 2.21 with the superscripts ${}^{n}(\cdot)$ and ${}^{n+1}(\cdot)$ replaced by ${}^{m,n+1}(\cdot)$ and ${}^{m+1,n+1}(\cdot)$ respectively. The final linearized form of Eqn. 2.24 is the following

$$\begin{aligned}
\frac{{}^{m,n+1}\Delta\langle\underline{U}\rangle_{E_i}}{\Delta t^{**}} + {}^{m,n+1}\left(\frac{\partial \underline{R}_{E_i}}{\partial\langle\underline{U}\rangle_{E_i}}\right){}^{m,n+1}\Delta\langle\underline{U}\rangle_{E_i} + \sum_{E_j\in\mathcal{N}_i} {}^{m,n+1}\left(\frac{\partial \underline{R}_{E_i}}{\partial\langle\underline{U}\rangle_{E_j}}\right){}^{m,n+1}\Delta\langle\underline{U}\rangle_{E_j} \\
+ {}^{m,n+1}\underline{R}^*_{E_i} = \mathcal{O}(\Delta t, \Delta h^p).
\end{aligned} \quad (2.25)$$

In Section. 2.5, we will discuss in detail the solution strategy of the linear system derived from Eqn. 2.25 with the matrix-free approach.

2.3 Constrained Least-Squares (CLSQ) Reconstruction

2.3.1 Reconstructing Polynomial

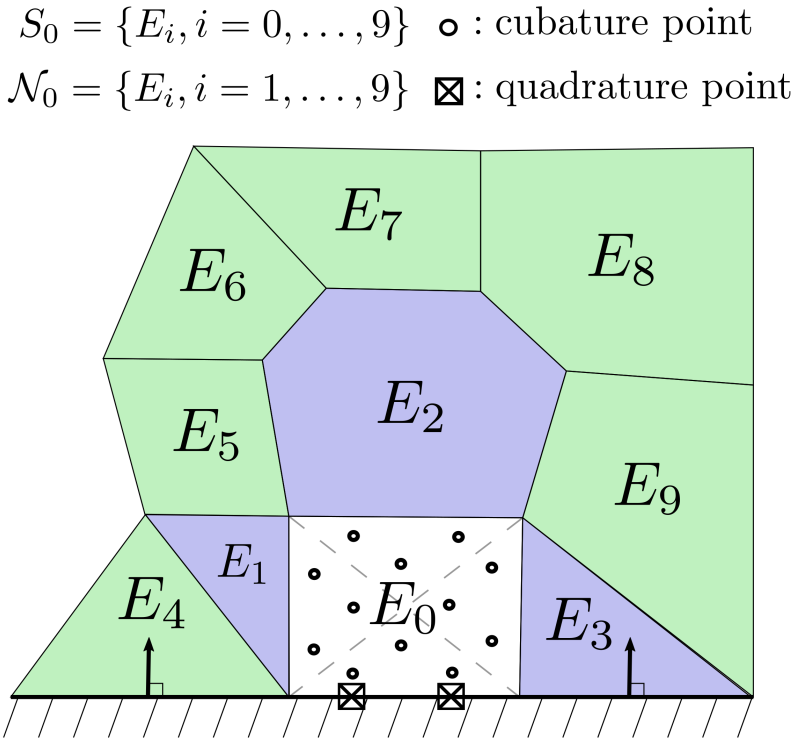

Figure 2.1: Schematic representation of a stencil associated with a boundary cell E_0.

A constrained LSQ (CLSQ) reconstruction scheme is developed to achieve arbitrarily high-order spatial discretization in the entire computational domain including near the boundaries. This CLSQ scheme is a generalization of a previous LSQ reconstruction scheme proposed by Gerolymos and Vallet [91], which has achieved a spatial order of accuracy up to $p = 10$ for solving 2D advection equation on arbitrary polygonal grids. Similar to the methods used by Ollivier-Gooch and Van Altena [169] and by Bertolazzi and Manzini [27], the current CLSQ scheme treats the interior and boundary cells in a unified manner without the need for adding ghost cells at domain boundaries to preserve order. The current CLSQ scheme aims to minimize an $\mathcal{L}$ functional with Lagrange multipliers z_i associated with both cell-average (imposed on reference cell E_0) and boundary condition (imposed on boundary quadrature points) equality constraints. The minimization problem is defined in a distance-weighted least-squares sense, whereas the unweighted LSQ formulation is adopted for the unconstrained version of the scheme in [91]. Distance weighting is indispensable in grids containing high-aspect-ratio cells. All cells considered in the current study are straight-edge polygons, and we shall extend this reconstruction scheme to curvilinear grids in future work [3].

For a general polygonal unstructured grid, consider a reference cell E_0 around which we con-

[3] The only missing building block required for the method to correctly (achieving order > 2) adapt to curvilinear grids is a module to perform numerical integration on curved edges and surfaces with high-order accuracy.

struct an associated stencil S_0 containing cells E_i, $i = 0, \cdots, N_b$ as illustrated in Fig. 2.1, where N_b is the number of cells in stencil S_0 excluding E_0 itself. The collection of cells E_i, $i = 1, \cdots, N_b$ form the neighborhood of E_0 denoted by $\mathcal{N}_0$. The stencil is constructed in a layer-by-layer manner, the algorithm searches for all immediate edge-neighbors of E_0 before moving on to the neighbors' neighbors and so forth until the number of neighbor cells N_b surpasses the number of polynomial coefficients N_c by an empirically determined safety factor. The safety factor needs to be raised whenever a unique CLSQ solution cannot be guaranteed.

The arbitrary flow variable to be reconstructed is $\phi(x, y)$. Define the reconstructing polynomial in stencil S_0 as $P_{S_0} \in \pi_m(\mathbb{R}^2)$, $\pi_m(\mathbb{R}^2)$ is the vector space of bivariate polynomials of degree $\leq m$

$$\begin{aligned} \phi(x,y) \approx P_{S_0}(x,y,\phi) &:= \sum_{\ell=1}^{N_c} c_\ell(S_0,\phi) \left(\frac{x - x_{E_0}}{\Delta x_{E_0}}\right)^{m_x(\ell)} \left(\frac{y - y_{E_0}}{\Delta y_{E_0}}\right)^{m_y(\ell)} \\ &= \sum_{\ell=1}^{N_c} c_\ell(S_0,\phi)\alpha_\ell(x,y,E_0), \quad \forall (x,y) \in S_0 \end{aligned} \tag{2.26}$$

where (x_{E_i}, y_{E_i}) are the centroid coordinates of cell E_i, Δx_{E_0} and Δy_{E_0} are the maximum distances between two vertices of cell E_0 along x and y directions, $\alpha_\ell(x, y, E_0)$ are the N_c basis polynomials of P_{S_0} with N_c being the number of polynomial coefficients of a bivariate polynomial of degree m with $m = p-1$, where p corresponds to the order-of-accuracy with which P_{S_0} approximates an arbitrary variable $\phi(x, y)$, *e.g.*, a 3^{rd}-order polynomial is of degree 2, and $\alpha_\ell(x, y, E_0) \in \{1, X, Y, X^2, XY, Y^2\}$ with $X = (x - x_{E_0})/\Delta x_{E_0}$ and $Y = (y - y_{E_0})/\Delta y_{E_0}$. Note that P_{S_0} is not only a function of (x, y) but also of $\phi(x, y)$ and S_0 since different distributions of ϕ and selections of S_0 result in different polynomial coefficients $c_\ell(S_0, \phi)$, and the basis polynomials $\alpha_\ell(x, y, E_0)$ also depend on the shape and location of cell E_0. However, when a specific reconstruction is performed, we consider the computational grid and $\phi(x, y)$ remain unchanged therefore P_{S_0}, α_ℓ only depend on (x, y) and $c_1, \cdots, c_{N_c}$ are assumed to be constant with

$$N_c = \binom{m+2}{2} = \binom{p+1}{2} = \frac{p(p+1)}{2}. \tag{2.27}$$

We compute the cell-averaged value of polynomial P_{S_0} for $E_i \in S_0$

$$\begin{aligned} \langle P_{S_0} \rangle_{E_i} &:= \frac{1}{\mathrm{A}_{E_i}} \iint_{E_i} \sum_{\ell=1}^{N_c} c_\ell \alpha_\ell(x,y) \mathrm{d}x\mathrm{d}y \\ &= \sum_{\ell=1}^{N_c} \frac{c_\ell}{\mathrm{A}_{E_i}} \iint_{E_i} \alpha_\ell(x,y) \mathrm{d}x\mathrm{d}y \\ &= \sum_{\ell=1}^{N_c} c_\ell \, \mathbb{I}_{\ell,E_i} \end{aligned} \tag{2.28}$$

where $\mathbb{I}_{\ell,E_i} = \mathrm{A}_{E_i}^{-1} \iint_{E_i} \alpha_\ell(x, y)\mathrm{d}x\mathrm{d}y$ is the $[m_x(\ell), m_y(\ell)]$-moment in cell E_i with respect to $\vec{x}_{E_0}$, $\langle\cdot\rangle_{E_i}$ is the cell-averaging operator with respect to cell E_i, $\mathbb{I}_{\ell,E_i}$ is the scalar value of the ℓ^{th} surface integration moment of cell E_i with respect to the basis polynomial $\alpha_\ell(x, y)$.

Numerically, $\mathbb{I}_{\ell,E_i}$ is computed using Gaussian cubature points (denoted by $\circ$), we define $w_{\circ_k}$ the weight associated with the k^{th} cubature point in a given cell located at $\vec{x}_{\circ_k} = (x_{\circ_k}, y_{\circ_k}) \in E_i$. The locations and weights of cubature points are readily determined by Dunavant rules [68] up to

$p = 20$ for a triangle $\mathcal{T}$ such that

$$\iint_{\mathcal{T}} \phi(x,y)\mathrm{d}x\mathrm{d}y \approx \mathrm{A}_{\mathcal{T}} \sum_{k=1}^{\bar{N}_\circ} w_{\circ_k} \phi(x_{\circ_k}, y_{\circ_k}) \tag{2.29}$$

where $\bar{N}_\circ$ is the number of cubature points per triangle and $\vec{x}_{\circ_k}$ are determined by a linear combination of coordinates of the three vertices $\vec{x}_1$, $\vec{x}_2$ and $\vec{x}_3$ and their corresponding barycentric coordinates $c_{1,k}, c_{2,k}, c_{3,k}$ tabulated in [68] for $p \leq 20$.

$$\vec{x}_{\circ_k} = c_{1,k}\vec{x}_1 + c_{2,k}\vec{x}_2 + c_{3,k}\vec{x}_3 \tag{2.30}$$

Note that for $p \in \{4, 8, 12, 16, 17, 19\}$, the orders of cubature rules are raised to the next higher orders ($p \in \{5, 9, 13, 18, 18, 20\}$) that ensure full symmetry in barycentric coordinates, and PI property (positive weights, cubature points lie within the triangle [68]). This approach was adopted by Gerolymos and Vallet in [91], and we follow it in the current study. An arbitrary N-gon is considered a union of n triangles defined by each one of its edges and its barycenter

$$E_i = \bigcup_{j=1}^{n} \mathcal{T}_{i,j} \tag{2.31}$$

and by applying the cubature rules for each triangle $\mathcal{T}_{i,j}$, the ℓ^{th}-order surface integration moment of cell E_i in Eqn. 2.28 is obtained by

$$\begin{aligned} \mathbb{I}_{\ell,E_i} &= \sum_{j=1}^{n} \frac{1}{\mathrm{A}_{\mathcal{T}_{i,j}}} \iint_{\mathcal{T}_{i,j}} \alpha_\ell(x,y)\mathrm{d}x\mathrm{d}y \\ &= \sum_{k=1}^{N_\circ} w_{\circ_k} \alpha_\ell(x_{\circ_k}, y_{\circ_k}) \end{aligned} \tag{2.32}$$

where $N_\circ = n \times \bar{N}_\circ$ is the total number of cubature points in the N-gon E_i.

The polynomial approximation $P_{S_0}(x,y)$ of the function $\phi(x,y)$ is obtained by requiring that P_{S_0} satisfies the cell-averaged values for cells $E_i \in \mathcal{N}_0$ in a distance-weighted least-squares sense, and that P_{S_0} needs to satisfy *exactly* the cell-average $\langle P_{S_0} \rangle_{E_0} = \langle \phi \rangle_{E_0}$ in the reference cell E_0.

The corresponding minimization problem is formulated as follows

$$\text{minimize} \quad \mathcal{J} := \sum_{E_i \in \mathcal{N}_0} d_{E_0,E_i}^{-2} (\langle P_{S_0} \rangle_{E_i} - \langle \phi \rangle_{E_i})^2 \tag{2.33}$$

where

$$d_{E_0,E_i} = \sqrt{(x_{E_i} - x_{E_0})^2 + (y_{E_i} - y_{E_0})^2} \tag{2.34}$$

and $\langle \phi \rangle_{E_i}$ is the cell-averaged variable in cell E_i.

Rewrite Eqn. 2.33 in matrix form

$$\text{minimize} \quad \mathcal{J} := \left[\underline{\underline{\mathbb{I}}}\, \underline{c} - \langle \underline{\phi} \rangle \right]^\top \left[\underline{\underline{\mathbb{I}}}\, \underline{c} - \langle \underline{\phi} \rangle \right] \tag{2.35}$$

with

$$\underline{c} = [c_1, \ldots, c_{N_c}]^\top \tag{2.36a}$$

$$\underline{\underline{\mathbb{I}}} = \begin{bmatrix} \frac{\mathbb{I}_{1,E_1}}{d_{E_0,E_1}} & \cdots & \frac{\mathbb{I}_{N_c,E_1}}{d_{E_0,E_1}} \\ \vdots & \ddots & \vdots \\ \frac{\mathbb{I}_{1,E_{N_b}}}{d_{E_0,E_{N_b}}} & \cdots & \frac{\mathbb{I}_{N_c,E_{N_b}}}{d_{E_0,E_{N_b}}} \end{bmatrix} \tag{2.36b}$$

$$\langle \underline{\phi} \rangle = \left[\frac{\langle \phi \rangle_{E_1}}{d_{E_0,E_1}}, \ldots, \frac{\langle \phi \rangle_{E_{N_b}}}{d_{E_0,E_{N_b}}} \right]^\top \tag{2.36c}$$

where $\underline{\underline{\mathbb{I}}}$ is an N_b by N_c matrix containing the moments of inertia of the N_c monomials in each of the N_b neighboring cells E_i with respect to $\vec{x}_{E_i}$. $\langle \underline{\phi} \rangle$ is a vector containing cell-averaged data for $E_i \in \mathcal{N}_0$. By expanding Eqn. 2.35, we obtain

$$\begin{aligned} \mathcal{J} &= \left[\underline{\underline{\mathbb{I}}}\, \underline{c} - \langle \underline{\phi} \rangle \right]^\top \left[\underline{\underline{\mathbb{I}}}\, \underline{c} - \langle \underline{\phi} \rangle \right] \\ &= \left(\underline{\underline{\mathbb{I}}}\, \underline{c} \right)^\top \left(\underline{\underline{\mathbb{I}}}\, \underline{c} \right) - \langle \underline{\phi} \rangle^\top \underline{\underline{\mathbb{I}}}\, \underline{c} - \left(\underline{\underline{\mathbb{I}}}\, \underline{c} \right)^\top \langle \underline{\phi} \rangle + \langle \underline{\phi} \rangle^\top \langle \underline{\phi} \rangle \\ &= \underline{c}^\top \left(\underline{\underline{\mathbb{I}}}^\top \underline{\underline{\mathbb{I}}} \right) \underline{c} - 2 \left(\underline{\underline{\mathbb{I}}}^\top \langle \underline{\phi} \rangle \right)^\top \underline{c} + \langle \underline{\phi} \rangle^\top \langle \underline{\phi} \rangle. \end{aligned} \tag{2.37}$$

However, solving the above-mentioned minimization problem does not satisfy **(i)** the fact that the cell-averaged value $\langle \phi \rangle_{E_0}$ needs to be satisfied *exactly*, i.e., the "cell-average constraint"; **(ii)** the boundary conditions, or the "BC constraints". In the present work, the boundary conditions are prescribed exactly at Gauss-Legendre quadrature points (denoted by the symbol $\boxtimes$) on the boundary edges of E_0. The BC is considered to be of either Dirichlet or Neumann type, and is imposed on different primitive variables, which leads to each primitive variable being associated with a degree m reconstructing polynomial.

2.3.2 Dirichlet Type

For a Dirichlet type boundary condition, at each Gauss-Legendre quadrature point on the boundary edges of E_0 we impose

$$\sum_{\ell=1}^{N_c} c_\ell \alpha_\ell(x_{\boxtimes_i}, y_{\boxtimes_i}) = \phi_{\boxtimes_i}, \quad i = 1, \ldots, N_{\boxtimes} \tag{2.38}$$

or in matrix form

$$\underline{\alpha}_{\boxtimes_i}^\top \underline{c} = \phi_{\boxtimes_i}, \quad i = 1, \ldots, N_{\boxtimes} \tag{2.39}$$

with $\underline{\alpha}_{\boxtimes_i} = [\alpha_1(x_{\boxtimes_i}, y_{\boxtimes_i}), \ldots, \alpha_{N_c}(x_{\boxtimes_i}, y_{\boxtimes_i})]^\top$. $N_{\boxtimes}$ is the total number of Gauss-Legendre quadrature points taken into account for the reconstruction, which is equal to the number of quadrature points per boundary edge $\bar{N}_{\boxtimes}$ multiplied by the number of boundary edges in cell E_0.

2.3.3 Neumann Type

At each quadrature point on the boundary edge of E_0, instead of fixing value of variable ϕ, the face-normal derivative of ϕ is imposed

$$\sum_{\ell=1}^{N_c} c_\ell \left(\frac{\partial \alpha_\ell}{\partial \mathrm{n}}\right)_{\boxtimes_i} = \left(\frac{\partial \phi}{\partial \mathrm{n}}\right)_{\boxtimes_i}, \quad i = 1, \ldots, N_{\boxtimes} \tag{2.40}$$

or in matrix form

$$\underline{\left(\frac{\partial \alpha}{\partial \mathrm{n}}\right)}_{\boxtimes_i}^{\top} \underline{c} \qquad = \left(\frac{\partial \phi}{\partial \mathrm{n}}\right)_{\boxtimes_i}, \quad i = 1, \ldots, N_{\boxtimes} \tag{2.41}$$

where $\vec{\mathrm{n}}_{\boxtimes_i}$ is the inward-pointing boundary unit face-normal at quadrature point $\boxtimes_i$ $\vec{\mathrm{n}}_{\boxtimes_i} = \mathrm{n}_x \vec{e}_x + \mathrm{n}_y \vec{e}_y$. Note that $\vec{\mathrm{n}}_{\boxtimes_i}$ is a constant vector if all quadrature points lie on a straight edge [4]. $\underline{(\partial\alpha/\partial \mathrm{n})}_{\boxtimes_i}$ is the vector containing face-normal derivatives of all α_ℓ for $\ell = 1, \cdots, N_c$ at quadrature point $\boxtimes_i$

$$\underline{\left(\frac{\partial \alpha}{\partial \mathrm{n}}\right)}_{\boxtimes_i} = \left[\frac{\partial \alpha_1}{\partial \mathrm{n}}, \cdots, \frac{\partial \alpha_{N_c}}{\partial \mathrm{n}}\right]_{\boxtimes_i}^{\top} \tag{2.42}$$

The mean constraint is imposed on the reference cell E_0

$$\langle P_{S_0} \rangle_{E_0} = \sum_{\ell=1}^{N_c} c_\ell \, \mathbb{I}_{\ell, E_0} = \langle \phi \rangle_{E_0} \tag{2.43}$$

or in matrix form

$$\langle P_{S_0} \rangle_{E_0} = \underline{\mathbb{I}}_{E_0}^{\top} \underline{c} = \langle \phi \rangle_{E_0}. \tag{2.44}$$

From equations 2.35, 2.39, 2.41, 2.44, a CLSQ minimization problem can be defined by introducing the $\mathcal{L}$ functional with Lagrange multipliers $z_1, \ldots, z_{N_{\boxtimes}+1}$.

The Lagrangian function is constructed as follows

$$\mathcal{L}(\underline{c}, \underline{z}) = \begin{cases} \mathcal{J}(\underline{c}) + \displaystyle\sum_{i=1}^{N_{\boxtimes}} z_i \left(\underline{\alpha}_{\boxtimes_i}^{\top} \underline{c} - \phi_{\boxtimes_i}\right) & \\ \qquad + z_{N_{\boxtimes}+1} \left(\underline{\mathbb{I}}_{E_0}^{\top} \underline{c} - \langle \phi \rangle_{E_0}\right) & \text{Dirichlet BC} \\ \mathcal{J}(\underline{c}) + \displaystyle\sum_{i=1}^{N_{\boxtimes}} z_i \left[\underline{(\partial\alpha/\partial \mathrm{n})}_{\boxtimes_i}^{\top} \underline{c} - (\partial\phi/\partial \mathrm{n})_{\boxtimes_i}\right] & \\ \qquad + z_{N_{\boxtimes}+1} \left(\underline{\mathbb{I}}_{E_0}^{\top} \underline{c} - \langle \phi \rangle_{E_0}\right) & \text{Neumann BC.} \end{cases} \tag{2.45}$$

The optimal state $(\hat{\underline{c}}, \hat{\underline{z}})$ is found by solving the following optimality conditions

$$\frac{\partial \mathcal{L}}{\partial c_i}(\hat{\underline{c}}, \hat{\underline{z}}) = 0, \quad i = 1 \ldots, N_c \qquad \frac{\partial \mathcal{L}}{\partial z_j}(\hat{\underline{c}}, \hat{\underline{z}}) = 0, \quad j = 1 \ldots, N_{\boxtimes} + 1 \tag{2.46}$$

[4] $\vec{\mathrm{n}}_{\boxtimes_i}$ is not a constant vector for curvilinear edges

with the first N_c conditions being determined according to the expression of $\mathcal{J}$ in Eqn. 2.37

$$\frac{\partial \mathcal{L}}{\partial \underline{c}}(\hat{\underline{c}}, \hat{\underline{z}}) = 2\left(\underline{\underline{\mathbb{I}}}^{\top}\underline{\underline{\mathbb{I}}}\right)\hat{\underline{c}} - 2\underline{\underline{\mathbb{I}}}^{\top}\langle\underline{\phi}\rangle + \left[\underline{\underline{\mathcal{K}}}^{\top},\ \underline{\mathbb{I}}_{E_0}\right]\hat{\underline{z}} = 0 \tag{2.47}$$

where $\underline{\underline{\mathcal{K}}}$ is an $N_{\boxtimes}$ by N_c BC constraint matrix

$$\underline{\underline{\mathcal{K}}} = \begin{cases} \left[\ \underline{\alpha}_{\boxtimes_1}\ ,\ldots,\ \underline{\alpha}_{\boxtimes_{N_{\boxtimes}}}\ \right]^{\top} & \text{Dirichlet BC} \\ \left[\underline{\left(\frac{\partial \alpha}{\partial \mathrm{n}}\right)}_{\boxtimes_1},\ldots,\underline{\left(\frac{\partial \alpha}{\partial \mathrm{n}}\right)}_{\boxtimes_{N_{\boxtimes}}}\right]^{\top} & \text{Neumann BC.} \end{cases} \tag{2.48}$$

By deriving $\mathcal{L}$ with respect to $\underline{z}$, the last $N_{\boxtimes}+1$ conditions correspond to the $N_{\boxtimes}+1$ constraints in matrix form

$$\frac{\partial \mathcal{L}}{\partial \underline{z}}(\hat{\underline{c}}, \hat{\underline{z}}) = \begin{bmatrix} \underline{\underline{\mathcal{K}}} \\ \underline{\mathbb{I}}_{E_0}^{\top} \end{bmatrix}\hat{\underline{c}} - \begin{bmatrix} \mathbf{\underline{k}} \\ \langle\phi\rangle_{E_0} \end{bmatrix} = 0 \tag{2.49}$$

where $\mathbf{\underline{k}}$ is an $N_{\boxtimes}$-vector

$$\mathbf{\underline{k}} = \begin{cases} \left[\ \phi_{\boxtimes_1}\ ,\ldots,\ \phi_{\boxtimes_{N_{\boxtimes}}}\ \right]^{\top} & \text{Dirichlet BC} \\ \left[\left(\frac{\partial \phi}{\partial \mathrm{n}}\right)_{\boxtimes_1},\ldots,\left(\frac{\partial \phi}{\partial \mathrm{n}}\right)_{\boxtimes_{N_{\boxtimes}}}\right]^{\top} & \text{Neumann BC.} \end{cases} \tag{2.50}$$

Finally, by regrouping equations 2.47 - 2.50, we obtain a block linear system of equations, which are named the Karush–Kuhn–Tucker (KKT) equations by Boyd and Vandenberghe [29] and can be written in compact matrix form

$$\begin{bmatrix} 2\underline{\underline{\mathbb{I}}}^{\top}\underline{\underline{\mathbb{I}}} & \underline{\underline{\mathcal{K}}}^{\top} & \underline{\mathbb{I}}_{E_0} \\ \underline{\underline{\mathcal{K}}} & \underline{\underline{\mathbf{0}}} & \underline{\underline{\mathbf{0}}} \\ \underline{\mathbb{I}}_{E_0}^{\top} & \underline{\underline{\mathbf{0}}} & 0 \end{bmatrix}\begin{bmatrix} \hat{\underline{c}} \\ \hat{\underline{z}} \end{bmatrix} = \begin{bmatrix} 2\underline{\underline{\mathbb{I}}}^{\top}\langle\underline{\phi}\rangle \\ \mathbf{\underline{k}} \\ \langle\phi\rangle_{E_0} \end{bmatrix} \tag{2.51}$$

where dividing the first row by 2 gives

$$\underbrace{\begin{bmatrix} \underline{\underline{\mathbb{I}}}^{\top}\underline{\underline{\mathbb{I}}} & \underline{\underline{\mathcal{K}}}^{\top} & \frac{1}{2}\underline{\mathbb{I}}_{E_0} \\ \underline{\underline{\mathcal{K}}} & \underline{\underline{\mathbf{0}}} & \underline{\underline{\mathbf{0}}} \\ \underline{\mathbb{I}}_{E_0}^{\top} & \underline{\underline{\mathbf{0}}} & 0 \end{bmatrix}}_{\underline{\underline{\mathcal{A}}}}\begin{bmatrix} \hat{\underline{c}} \\ \hat{\underline{z}} \end{bmatrix} = \begin{bmatrix} \underline{\underline{\mathbb{I}}}^{\top}\langle\underline{\phi}\rangle \\ \mathbf{\underline{k}} \\ \langle\phi\rangle_{E_0} \end{bmatrix} \tag{2.52}$$

with $\underline{\underline{\mathcal{A}}}$ being an $(N_c + N_{\boxtimes} + 1)$ by $(N_c + N_{\boxtimes} + 1)$ square matrix, named the KKT matrix. $\underline{\underline{\mathbf{0}}}$ is the zero matrix of flexible sizes filling the empty entries in $\underline{\underline{\mathcal{A}}}$.

Define an $(N_c + N_{\boxtimes} + 1)$ by $(N_b + N_{\boxtimes} + 1)$ matrix $\underline{\underline{\mathcal{B}}}$ as

$$\underline{\underline{\mathcal{B}}} = \begin{bmatrix} \underline{\underline{\mathbb{I}}}^{\top} & \underline{\underline{\mathbf{0}}} \\ \underline{\underline{\mathbf{0}}} & \underline{\underline{\mathbf{I}}}_{N_{\boxtimes}+1} \end{bmatrix} \tag{2.53}$$

where $\underline{\underline{\mathbf{I}}}_{N_{\boxtimes}+1}$ is the $N_{\boxtimes} + 1$ by $N_{\boxtimes} + 1$ identity matrix. Thus

$$\begin{bmatrix} \underline{\hat{c}} \\ \underline{\hat{z}} \end{bmatrix} = \underline{\underline{\mathcal{C}}} \begin{bmatrix} \underline{\langle \phi \rangle} \\ \underline{\mathbf{k}} \end{bmatrix} \tag{2.54}$$

where $\underline{\underline{\mathcal{C}}} = \underline{\underline{\mathcal{A}}}^{-1} \underline{\underline{\mathcal{B}}}$ and $\underline{\underline{\mathcal{C}}}$ is *geometry-dependent*, i.e., it does not vary with the input cell-averaged data $\langle \phi \rangle_{E_i}$.

2.3.4 Interior Cell Treatment

$$S_0 = \{E_i, i = 0, \ldots, 9\}$$
$$\mathcal{N}_0 = \{E_i, i = 1, \ldots, 9\} \quad \circ : \text{cubature point}$$

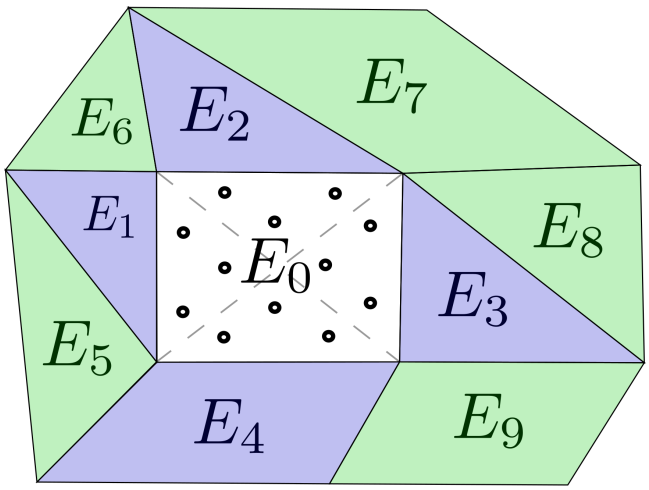

Figure 2.2: Schematic representation of a stencil associated with an interior cell E_0.

As mentioned earlier, interior and boundary cells are treated in a unified manner. For an interior cell E_0, since no boundary condition is imposed, as shown in Fig. 2.2, the BC constraint matrix $\underline{\underline{\mathcal{K}}}$ is removed from the KKT matrix $\underline{\underline{\mathcal{A}}}$, and the vector $\underline{\hat{z}}$ is reduced to a single scalar value $\hat{z}$. Both $\underline{\underline{\mathbb{I}}}_{E_0}^{\top}$ and $\hat{z}$ are associated to the cell-average constraint. The matrix form of KKT equations

can be rewritten for an interior cell as

$$\underbrace{\begin{bmatrix} \underline{\underline{\mathbb{I}}}^{\top}\underline{\underline{\mathbb{I}}} & \frac{1}{2}\mathbb{I}_{E_0} \\ \underline{\mathbb{I}}_{E_0}^{\top} & 0 \end{bmatrix}}_{\underline{\underline{\mathcal{A}}}} \begin{bmatrix} \hat{\underline{c}} \\ \hat{z} \end{bmatrix} = \begin{bmatrix} \underline{\underline{\mathbb{I}}}^{\top}\langle \underline{\phi} \rangle \\ \langle \phi \rangle_{E_0} \end{bmatrix}. \tag{2.55}$$

The $\underline{\underline{\mathcal{B}}}$ matrix for an interior cell shrinks to an $(N_c + 1)$ by $(N_b + 1)$ matrix

$$\underline{\underline{\mathcal{B}}} = \begin{bmatrix} \underline{\underline{\mathbb{I}}}^{\top} & 0 \\ 0 & 1 \end{bmatrix} \tag{2.56}$$

and the polynomial coefficients $\hat{\underline{c}}$ and the Lagrange multiplier $\hat{z}$ satisfying the optimality conditions are calculated by

$$\begin{bmatrix} \hat{\underline{c}} \\ \hat{z} \end{bmatrix} = \underline{\underline{\mathcal{C}}} \begin{bmatrix} \langle \underline{\phi} \rangle \\ \langle \phi \rangle_{E_0} \end{bmatrix} \tag{2.57}$$

with $\underline{\underline{\mathcal{C}}} = \underline{\underline{\mathcal{A}}}^{-1}\,\underline{\underline{\mathcal{B}}}$.

2.3.5 Existence and Uniqueness Analysis

The CLSQ solution exists if and only if the KKT matrix $\underline{\underline{\mathcal{A}}}$ is invertible. In Appendix. A, a detailed analysis on the invertibility of $\underline{\underline{\mathcal{A}}}$ matrix is given based on the results in [29, 49, 80, 89, 215]. Here, we briefly summarize the conclusions of the analysis by listing several *sufficient* conditions for the CLSQ reconstruction problem to admit a unique solution :

1. Stencil S_0 is adequately selected such that N_b is sufficiently greater than N_c, and the *unconstrained* LSQ reconstruction problem admits a unique solution;
2. Cell-average constraint is not a linear combination of BC constraints;
3. For Dirichlet type BC constraints: $\bar{N}_{\boxtimes}$ determined by Eqn. A.2b with $p \geq 2$ and number of boundary edges ≤ 2;
4. For Neumann type BC constraints: $\bar{N}_{\boxtimes}$ determined by Eqn. A.2b with $p \geq 3$ and number of boundary edges ≤ 1.

The LSQ reconstruction is a polynomial reconstruction problem and the satisfaction of BC constraints is a polynomial interpolation problem. In Appendix. A, the analysis is mainly focused on the BC constraints part of the problem, and the unique solution to the unconstrained LSQ reconstruction is achieved in the current study by simply adding layers of edge-neighbors to the associated stencil. However, Gerolymos [89] proved that, for 1D uniform grids, the interpolating polynomial and the reconstructing polynomial of a given data set are always related by a bijective mapping. If this proof can be generalized to general 2D polygonal grids in the future, the underlying notions of unisolvent points (Definition. A.1) and natural lattices (Definition. A.2) can be applied to the LSQ reconstruction problem for more efficient and robust construction of stencils S_i.

2.4 Low-Mach Corrected HLLC Riemann Solver

It is well-known that approximate Riemann solvers perform best for problems where the flow velocity is not excessively small compared to the local speed of sound. However, as a general Navier-Stokes solver, the current compressible code needs to be capable of correctly solving low-speed flow cases where the maximum Mach number $M \ll 1$. Numerically, due to the stiffness caused by large speed difference between the acoustic wave and local transport, it has been well established that the convergence at very low Mach number (typically lower than $M \approx 0.1$ equivalent to local flow speed $u \approx 3.4$m/s) becomes slow [48, 150, 210, 213]. Moreover, by performing asymptotic analyses on the continuous and semi-discretized Euler equations, Guillard *et al.* [102, 103] found that Roe and Godunov-type Riemann solvers give inaccurate pressure solution when the Mach number approaches zero. Guillard *et al.* [102] proved that the pressure fluctuation is of order M^2 in the continuous Euler equations while being of order M in the semi-discretized form, which results in the inaccurate solution of pressure field. Dellacherie *et al.* [63] proposed a general framework for constructing all-Mach (AM) Godunov-type schemes by modifying the interfacial numerical flux $\underline{F}^{\mathrm{X}}$ where the superscript "X" can be replaced by the name of any Riemann solver such as "HLL", "HLLC", *etc.* Based on the work of Dellacherie *et al.* [63], Xie *et al.* [218] proposed an all-Mach version of the widely used HLLC Riemann solver developed by Toro *et al.* [206]. In the present study, we focus on the low-Mach regime ($M \ll 1$) of the all-Mach correction therefore the qualifiers "all-Mach" and "low-Mach" are used interchangeably in this section.

We begin by briefly reminding the conventional HLLC approximate Riemann solver (without low-Mach correction). The HLLC solution is characterized by four distinct states, left $(\cdot)_L$, star left $(\cdot)^*_L$, star right $(\cdot)^*_R$ and right $(\cdot)_R$ states, which are delimited by the left, right and contact waves as shown in Fig. 2.3.

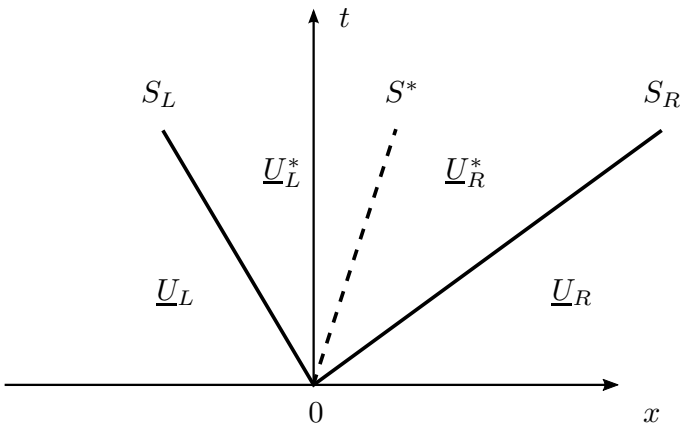

Figure 2.3: HLLC approximate Riemann solver. Four distinct constant regions are delimited by the left, right and contact waves.

The interfacial vector of conservative variables in each state is expressed as follows

$$\underline{U}^{\mathrm{HLLC}} = \begin{cases} \underline{U}_L & \text{if} \quad 0 \leq S_L \\ \underline{U}_L^* & \text{if} \quad S_L \leq 0 \leq S^* \\ \underline{U}_R^* & \text{if} \quad S^* \leq 0 \leq S_R \\ \underline{U}_R & \text{if} \quad 0 \geq S_R \end{cases} \tag{2.58}$$

with

$$\underline{U}_K^* = [\rho_K^*, (\rho u)_K^*, (\rho v)_K^*, (\rho e_t)_K^*]^\top \quad K = \{L, R\}. \tag{2.59}$$

The point-wise interfacial numerical flux $\underline{F}^{\mathrm{HLLC}}$ has the following expression

$$\underline{F}^{\mathrm{HLLC}} = \begin{cases} \underline{F}_L & \text{if} \quad 0 \leq S_L \\ \underline{F}_L^* & \text{if} \quad S_L \leq 0 \leq S^* \\ \underline{F}_R^* & \text{if} \quad S^* \leq 0 \leq S_R \\ \underline{F}_R & \text{if} \quad 0 \geq S_R \end{cases} \tag{2.60}$$

where S_L and S_R are the estimated left and right wave speeds, S^* is the speed of the contact wave. Note that for high-order flux reconstruction, $\underline{F}^{\mathrm{HLLC}}$ takes different value at each Gauss-Legendre quadrature point on the edge, while for low-order flux approximation, $\underline{F}^{\mathrm{HLLC}}$ is edge-averaged. $\underline{F}_L^*$ and $\underline{F}_R^*$ are determined by Rankine-Hugoniot jump conditions

$$\underline{F}_K^* = \underline{F}_K + S_K(\underline{U}_K^* - \underline{U}_K) \quad K = \{L, R\} \tag{2.61}$$

from which the expressions for pressure in left and right star regions are obtained after some algebraic manipulations

$$p_K^* = p_K + \alpha_K(S^* - V_{n_K}) \quad K = \{L, R\} \tag{2.62}$$

where we define $\alpha_K = \rho_K(S_K - V_{n_K})$. Since the pressure remains constant across the contact wave, by equating p_L^* with p_R^* in Eqn. 2.62 the expression of contact wave speed is obtained as

$$S^* = \frac{p_R - p_L + \alpha_L V_{n_L} - \alpha_R V_{n_R}}{\alpha_L - \alpha_R} \tag{2.63}$$

By replacing S^* in either $K = L$ or $K = R$ of Eqn. 2.62 with Eqn. 2.63, the pressure in the star region can be expressed in terms of the left and right state variables as

$$p_L^* := p_R^* = p^* = \frac{\alpha_L p_R - \alpha_R p_L - \alpha_L \alpha_R (V_{n_L} - V_{n_R})}{\alpha_L - \alpha_R}. \tag{2.64}$$

Toro [207] pointed out an important relation between the conservative variables $\underline{U}$ and the flux $\underline{F}$, which can be rewritten in the face-normal direction as

$$\underline{F}_K = V_{n_K}\underline{U}_K + p_K\underline{D}_K \qquad K = \{L, R\} \tag{2.65a}$$

$$\underline{F}_K^* = S^* \ \underline{U}_K^* + p_K^*\underline{D}^* \qquad K = \{L, R\} \tag{2.65b}$$

where

$$\underline{D}_K = (0, \mathrm{n}_x, \mathrm{n}_y, V_{n_K})^\top \qquad K = \{L, R\} \tag{2.66a}$$

$$\underline{D}^* = (0, \mathrm{n}_x, \mathrm{n}_y, S^*)^\top \qquad K = \{L, R\} \tag{2.66b}$$

V_{n_K} are the face-normal velocities in the left and right states. The contact wave speed is equal to the face-normal flow speed in the left and right star regions $S^* = V^*_{n_L} = V^*_{n_R}$.

Therefore $\underline{U}^*_K$ is derived from the jump conditions Eqn. 2.61 by substituting $\underline{F}_K$ and $\underline{F}^*_K$ with Eqn. 2.65

$$\underline{U}^*_K = \frac{(S_K - V_{n_K})\underline{U}_K + p^*_K \underline{D}^* - p_K \underline{D}_K}{S_K - S^*} \tag{2.67}$$

where p^*_K and S^* are determined in Eqn. 2.62 and Eqn. 2.63 respectively. $\underline{U}^*_K$ is subsequently inserted back into Eqn. 2.65b to obtain the final expression of $\underline{F}^*_K$. For the 2D Euler system, $\underline{F}^*_K$ can be written in vector form as

$$\underline{F}^*_K = S^* \underbrace{\begin{bmatrix} \rho^*_K \\ (\rho u)^*_K \\ (\rho v)^*_K \\ (\rho e_t)^*_K \end{bmatrix}}_{\underline{U}^*_K} + p^*_K \underbrace{\begin{bmatrix} 0 \\ \mathrm{n}_x \\ \mathrm{n}_y \\ S^* \end{bmatrix}}_{\underline{D}^*}. \tag{2.68}$$

We refer to Eqn. 2.60 for selecting the appropriate HLLC numerical flux $\underline{F}^{\mathrm{HLLC}}$ based on local wave speeds, and the final expression for the choice of HLLC numerical flux is obtained as

$$\underline{F}^{\mathrm{HLLC}} = \begin{cases} V_{n_L}\underline{U}_L + p_L \underline{D}_L & \text{if} \quad 0 \le S_L \\ S^* \ \underline{U}^*_L + p^*_L \underline{D}^* & \text{if} \quad S_L \le 0 \le S^* \\ S^* \ \underline{U}^*_R + p^*_R \underline{D}^* & \text{if} \quad S^* \le 0 \le S_R \\ V_{n_R}\underline{U}_R + p_R \underline{D}_R & \text{if} \quad 0 \ge S_R. \end{cases} \tag{2.69}$$

Remark that, in the literature, there exists different notations where p^* or $p_{LR} = \frac{1}{2}(p^*_L + p^*_R)$ is used instead of p^*_K. Since, as mentioned previously, the contact wave speed S^* is obtained by imposing $p^*_L = p^*_R$ (which is conforming to the exact solution), all notations above are mathematically equivalent.

The only unknowns in the calculation of HLLC flux remain the left and right wave speeds S_L and S_R which can be estimated based on various algorithms. In present study, the algorithm proposed by Einfeldt *et al.* [77] is adopted

$$S_L = \min(V_{n_L} - a_L, \widehat{V_n} - \widehat{a}), \quad S_R = \max(V_{n_R} + a_R, \widehat{V_n} + \widehat{a}) \tag{2.70}$$

where V_n denotes the normal velocity component $V_n := u\mathrm{n}_x + v\mathrm{n}_y$ and $\widehat{(.)}$ denotes the Roe averaged

variables

$$\begin{aligned}
&\widehat{\rho} = \sqrt{\rho_L \rho_R} \\
&\widehat{u} = \frac{\sqrt{\rho_L}u_L + \sqrt{\rho_R}u_R}{\sqrt{\rho_L} + \sqrt{\rho_R}} \qquad \widehat{v} = \frac{\sqrt{\rho_L}v_L + \sqrt{\rho_R}v_R}{\sqrt{\rho_L} + \sqrt{\rho_R}} \qquad \widehat{V_n} = \widehat{u}\mathrm{n}_x + \widehat{v}\mathrm{n}_y \\
&\widehat{h_t} = \frac{\sqrt{\rho_L}h_{tL} + \sqrt{\rho_R}h_{tR}}{\sqrt{\rho_L} + \sqrt{\rho_R}} \qquad \widehat{h} = \widehat{h_t} - \frac{1}{2}(\widehat{u}^2 + \widehat{v}^2) \qquad \widehat{a} = \sqrt{(\gamma - 1)\widehat{h}}.
\end{aligned} \tag{2.71}$$

Dellacherie *et al.* [63] developed an all-Mach Godunov scheme for both the linear wave equation and the non-linear fully compressible Euler equations. Two expressions for the all-Mach scheme are possible. In the first expression, the all-Mach corrected numerical flux $\underline{F}^{\text{AM-X}}$ is the sum of the unmodified interfacial numerical flux $\underline{F}^{\text{X}}$ computed by Riemann solver X (X can be Roe, HLLC, *etc.*), and a low-Mach correction term.

$$\underline{F}^{\text{AM-X}} = \underline{F}^{\text{X}} + (\theta_{LR} - 1)\frac{\widehat{\rho}\,\widehat{a}}{2}\begin{bmatrix} 0 \\ (V_{n_L} - V_{n_R})\mathrm{n}_x \\ (V_{n_L} - V_{n_R})\mathrm{n}_y \\ 0 \end{bmatrix} \tag{2.72}$$

where θ_{LR} is a scaling function evaluated at the same location as $\underline{F}^{\text{AM-X}}$ based on the estimated local Mach number M_{LR} (*not* computed by a Riemann solver)

$$\theta_{LR} = \theta(M_{LR}) \quad \text{with} \quad \theta(M) = \min(M, 1). \tag{2.73}$$

There exists multiple methods to evaluate M_{LR}. Dellacherie *et al.* [63] suggested two possible algorithms

$$M_{LR} = \left|\sqrt{\widehat{u}^2 + \widehat{v}^2}\right| / \widehat{a} \quad \text{or} \quad M_{LR} = \left|\widehat{V_n}\right| / \widehat{a} \tag{2.74}$$

and the latter is less dissipative than the former. Xie *et al.* [218] proposed to computed M as

$$M_{LR} = \max\left(\sqrt{u_L^2 + v_L^2}/a_L, \sqrt{u_R^2 + v_R^2}/a_R\right). \tag{2.75}$$

The second expression of Dellacherie *et al.* consists of introducing the all-Mach corrected pressure solution p^{**}

$$\underline{F}^{\text{AM-X}} = \begin{bmatrix} \rho^* V_n^* \\ (\rho u)^* V_n^* + p^{**}\mathrm{n}_x \\ (\rho v)^* V_n^* + p^{**}\mathrm{n}_y \\ (\rho e_t + p)^* V_n^* \end{bmatrix} \quad \text{with} \quad p^{**} = \theta_{LR}p^* + (1 - \theta_{LR})\frac{p_L + p_R}{2} \tag{2.76}$$

where $[\rho^*, (\rho u)^*, (\rho v)^*, (\rho e_t + p)^*]$ are solutions of the local Riemann problem at edge interface between cells E_i and E_j, and p^* is determined in Eqn. 2.64.

As pointed out by Dellacherie *et al.* [63], these two expressions 2.72, 2.76 are equivalent in the linear case but *not* for the non-linear Euler equations. Dellacherie *et al.* performed 1D and 2D numerical tests using the second expression Eqn. 2.76 which showed the all-Mach scheme is stable and robust on both triangular and Cartesian grids. Xie *et al.* [218] proposed an all-Mach corrected HLLC Riemann solver based on the second expression of Dellacherie *et al.* Eqn. 2.76 denoted by

AM-HLLC-P. "P" stands for "pressure-control", a technique developed to tackle the problem of shock instability for the HLLC solver when facing strong shocks. The pressure-control technique will be discussed in future works on computations in the hypersonic regime, and omitted in the present study. Various numerical tests with Mach number ranging from 10^{-3} to 20 were performed, the AM-HLLC-P scheme gives accurate pressure field down to $M = 10^{-3}$. The AM-HLLC-P is adopted in the present study without pressure-control technique for strong shocks. Finally, based on the solution of unmodified HLLC numerical flux, the all-Mach HLLC flux is derived using the second expression in Eqn. 2.76

$$\underline{F}^{\text{AM-HLLC}} = \begin{cases} V_{n_L}\underline{U}_L + p_L\underline{D}_L & \text{if} \quad 0 \leq S_L \\ S^* \ \underline{U}_L^* + p_L^{**}\underline{D}^* & \text{if} \quad S_L \leq 0 \leq S^* \\ S^* \ \underline{U}_R^* + p_R^{**}\underline{D}^* & \text{if} \quad S^* \leq 0 \leq S_R \\ V_{n_R}\underline{U}_R + p_R\underline{D}_R & \text{if} \quad 0 \geq S_R \end{cases} \tag{2.77}$$

$$\text{with} \begin{cases} p_K^{**} & = \theta_{LR} p_K^* + (1-\theta_{LR})\frac{p_L+p_R}{2} \\ \theta_{LR} & = \min(M_{LR}, 1) \\ M_{LR} & = \max\left(\sqrt{u_L^2+v_L^2}/a_L, \sqrt{u_R^2+v_R^2}/a_R\right). \end{cases}$$

In the current study, all test-cases are performed at $M \geq 0.2$ for higher convergence rate, therefore the benefits of the AM-HLLC-P Riemann solver are not expected to be obvious. The influence of low-Mach correction on the pressure field is demonstrated in Appendix. B. Computations are performed for Mach numbers $M = \{0.01, 0.05, 0.2\}$ and the AM-HLLC-P Riemann solver generates consistent pressure fields for all three Mach numbers, whereas considerable discrepancy is observed between different Mach numbers using the conventional HLLC Riemann solver.

2.5 Implicit Time-integration

Following Eqn. 2.25, we rewrite the implicit dual-time-stepping (DTS) scheme into a compact form in which the high-order term $\mathcal{O}(\Delta t, \Delta h^p)$ is left out, and the residual increment is expressed in terms of the sum of high-order numerical flux increments

$$\frac{{}^{m,n+1}\Delta\langle\underline{U}\rangle_{E_i}}{\Delta t_i^{**}} + \frac{\sum_{E_j\in\mathsf{EN}_i} {}^{m,n+1}\Delta\underline{F}^{\mathrm{NUM}}_{G_{ij}}\mathrm{L}_{G_{ij}}}{\mathrm{A}_{E_i}} = -{}^{m,n+1}\underline{R}^{*}_{E_i} \tag{2.78}$$

where EN_i is the set of direct *edge* neighbors of cell E_i which shall not be confused with the neighbors in a reconstruction stencil $\mathcal{N}_i$, E_j is the cell that shares the edge G_{ij} with cell E_i, ${}^{m,n+1}\underline{R}^{*}_{E_i}$ is determined in Eqn. 2.24. Note that Δt_i^{**} is local to cell E_i

$$\begin{aligned}
&\frac{1}{\Delta t_i^{**}} = \left(\frac{1}{\Delta t_i^{*}} + \frac{1}{\Delta t_i}\right)\\
&\text{with}\qquad \Delta t_i^{(*)} = \min_{E_i}\left[\mathrm{CFL}^{(*)}\frac{\Delta h_{E_i}}{S_{\max}}, \mathrm{VNN}^{(*)}\frac{\Delta h_{E_i}^2}{2\nu_{\mathrm{eq}}}\right]\\
&\qquad\quad \nu_{\mathrm{eq}} = \max_{E_i}\left\{\frac{4}{3}\nu, \frac{\gamma-1}{\rho R_g}\kappa\right\}, \qquad S_{\max} = \max_{E_i}(S_L, S^*, S_R)
\end{aligned} \tag{2.79}$$

where Δh_{E_i} is defined as twice the minimum normal distance between the cell centroid and cell edges of E_i, $S_{\max}$ is local maximum wave speed, S_L, S^* and S_R are the estimated left, contact and right wave speeds for the AM-HLLC Riemann solver discussed in Section. 2.4, equations 2.63 and 2.70, ν_{eq} is the local equivalent kinematic viscosity, κ is the thermal conductivity in $\mathrm{W.m^{-1}.K^{-1}}$. CFL denotes the convective Courant–Friedrichs–Lewy condition and VNN denotes the viscous von Neumann condition. In this study, we assume CFL = VNN and $\mathrm{CFL}^* = \mathrm{VNN}^*$.

The high-order flux increment is linearized with respect to $\langle\underline{U}\rangle_{E_i}$ and $\langle\underline{U}\rangle_{E_j}$ in the same way as with the high-order residual increment in Eqn. 2.21

$${}^{m,n+1}\Delta\underline{F}^{\mathrm{NUM}}_{G_{ij}} \approx {}^{m,n+1}\frac{\partial\underline{F}^{\mathrm{NUM}}_{G_{ij}}}{\partial\langle\underline{U}\rangle_{E_i}}{}^{m,n+1}\Delta\langle\underline{U}\rangle_{E_i} + \sum_{E_j\in\mathcal{N}_i} {}^{m,n+1}\frac{\partial\underline{F}^{\mathrm{NUM}}_{G_{ij}}}{\partial\langle\underline{U}\rangle_{E_j}}{}^{m,n+1}\Delta\langle\underline{U}\rangle_{E_j} \tag{2.80}$$

where $\mathcal{N}_i$ is the set of neighbor cells in the high-order computational stencil S_i associated with E_i, which is different from the set of direct edge neighbors $\mathsf{EN}_i \subseteq \mathcal{N}_i$.

We approximate the high-order flux $\underline{F}^{\mathrm{NUM}}_{G_{ij}}$ by a first-order Lax-Friedrichs flux $\underline{F}^{\mathrm{APP}}_{G_{ij}}$

$$\begin{aligned}
\underline{F}^{\mathrm{NUM}}_{G_{ij}} &= \underline{F}^{\mathrm{APP}}_{G_{ij}} + \mathcal{O}(\Delta h)\\
&= \frac{1}{2}\left[\underline{F}^{\mathrm{c}}(\langle\underline{U}\rangle_{E_i}, \vec{\mathrm{n}}_{G_{ij}}) + \underline{F}^{\mathrm{c}}(\langle\underline{U}\rangle_{E_j}, \vec{\mathrm{n}}_{G_{ij}}) + \lambda_{G_{ij}}(\langle\underline{U}\rangle_{E_i} - \langle\underline{U}\rangle_{E_j})\right] + \mathcal{O}(\Delta h)
\end{aligned} \tag{2.81}$$

where the first-order Lax-Friedrichs flux is computed based on cell-averaged conservative variables in E_i and E_j. Since the approximation is only first-order accurate in space, $\underline{F}^{\mathrm{APP}}_{G_{ij}}$ is evaluated on the entire edge G_{ij} rather than on each individual quadrature point $\boxtimes_k$ and no numerical integration is required. $\lambda_{G_{ij}}$ is the spectral radius of the flux Jacobian matrix evaluated on G_{ij}

$$\lambda_{G_{ij}} = |V_{n_{G_{ij}}}| + a_{G_{ij}} + \frac{2\nu_{\mathrm{eq}_{G_{ij}}}}{|\vec{\mathrm{n}}_{G_{ij}}\cdot(\vec{x}_{E_j} - \vec{x}_{E_i})|} \tag{2.82}$$

where $\vec{x}_{E_i}$ is the centroid coordinates of cell E_i, $V_{n_{G_{ij}}}$, $a_{G_{ij}}$ and $\nu_{\mathrm{eq}_{G_{ij}}}$ are respectively the normal velocity component, the local speed of sound and the local equivalent kinematic viscosity evaluated on G_{ij}. Since in the present study we are interested only in steady-state solutions, the implementation of first-order numerical flux for time-discretization does not affect the order of accuracy when convergence is reached.

The above first-order approximation of the linearized high-order Jacobian product in Eqn. 2.80 gives

$$\begin{aligned} {}^{m,n+1}\Delta\underline{F}^{\mathrm{NUM}}_{G_{ij}} &= {}^{m,n+1}\Delta\underline{F}^{\mathrm{APP}}_{G_{ij}} + \mathcal{O}(\Delta h) \\ &\approx {}^{m,n+1}\frac{\partial \underline{F}^{\mathrm{APP}}_{G_{ij}}}{\partial \langle \underline{U} \rangle_{E_i}} {}^{m,n+1}\Delta\langle \underline{U} \rangle_{E_i} + {}^{m,n+1}\frac{\partial \underline{F}^{\mathrm{APP}}_{G_{ij}}}{\partial \langle \underline{U} \rangle_{E_j}} {}^{m,n+1}\Delta\langle \underline{U} \rangle_{E_j} \end{aligned} \tag{2.83}$$

where the key difference between Eqn. 2.80 and Eqn. 2.83 is that the Jacobian product with respect to $\langle \underline{U} \rangle_{E_j}$ in Eqn. 2.83 requires no summation over $\mathcal{N}_i$ since it only concerns the edge neighbor E_j. Finally, Eqn. 2.78 can also be rewritten in terms of the low-order flux

$$\frac{{}^{m,n+1}\Delta\langle \underline{U} \rangle_{E_i}}{\Delta t_i^{**}} + \frac{\sum_{E_j \in \mathsf{EN}_i} {}^{m,n+1}\Delta\underline{F}^{\mathrm{APP}}_{G_{ij}} \mathrm{L}_{G_{ij}}}{\mathrm{A}_{E_i}} = -{}^{m,n+1}\underline{R}^{*}_{E_i}. \tag{2.84}$$

If the outer time-step Δt_i tends to infinity, then the time-integration tends to a single-time-stepping scheme with $\Delta t_i^{**} \to \Delta t_i^{*}$ and ${}^{m,n+1}\underline{R}^{*}_{E_i} \to {}^{n}\underline{R}_{E_i}$ hence the scheme is completely linearized. As will be shown in subsequent chapters, for largely separated flows (*e.g.* laminar backward-facing step at high Reynolds number), the inner time-stepping improves or makes possible the convergence.

A linear solver is required at each m-iteration to solve for ${}^{m,n+1}\Delta\langle \underline{U} \rangle_{E_i}$. When discussing linear solvers, for the sake of simplicity, the superscript ${}^{m,n+1}(\cdot)$ is hereafter dropped since it is understood that the linear system to solve is encountered only during m-iteration, and Δt_i^{**} is simply written as Δt_i.

Next, we derive the linear system of the implicit scheme for a general polygonal cell E_i admitting both interior and boundary edges. If edge G_{ij} is a boundary edge, then we consider that cell E_i admits a fictitious exterior neighbor E_j in which $\langle \underline{U} \rangle_{E_j}$ is a function of $\langle \underline{U} \rangle_{E_i}$, the boundary state variables $\underline{U}_{\mathrm{BC}}$ and $\vec{\mathrm{n}}_{G_{ij}}$. The detailed discussion on boundary conditions is found in Section 2.7. Since $\underline{U}_{\mathrm{BC}}$ and $\vec{\mathrm{n}}_{G_{ij}}$ are constant, Eqn. 2.83 can be rewritten for a boundary edge G_{ij} without superscript ${}^{m,n+1}(\cdot)$

$$\Delta\underline{F}^{\mathrm{BC,APP}}_{G_{ij}} = \frac{\partial \underline{F}^{\mathrm{BC,APP}}_{G_{ij}}}{\partial \langle \underline{U} \rangle_{E_i}} \Delta\langle \underline{U} \rangle_{E_i} + \frac{\partial \underline{F}^{\mathrm{BC,APP}}_{G_{ij}}}{\partial \langle \underline{U} \rangle_{E_j}} \frac{\partial \langle \underline{U} \rangle_{E_j}}{\partial \langle \underline{U} \rangle_{E_i}} \Delta\langle \underline{U} \rangle_{E_i}. \tag{2.85}$$

The first-order-accurate Lax-Friedrichs flux defined in Eqn. 2.81 is also reformulated for a boundary edge G_{ij} as follows

$$\begin{aligned} &\underline{F}^{\mathrm{BC,APP}}_{G_{ij}}\left(\langle \underline{U} \rangle_{E_i}, \underline{U}_{\mathrm{BC}}, \vec{\mathrm{n}}_{G_{ij}}\right) = \\ &\frac{1}{2}\left\{\underline{F}^{\mathrm{c}}\left(\langle \underline{U} \rangle_{E_i}, \vec{\mathrm{n}}_{G_{ij}}\right) + \underline{F}^{\mathrm{c}}\left(\langle \underline{U} \rangle_{E_j}, \vec{\mathrm{n}}_{G_{ij}}\right) + \lambda_{G_{ij}}\left[\langle \underline{U} \rangle_{E_i} - \langle \underline{U} \rangle_{E_j}\right]\right\} \\ &\text{with} \qquad \langle \underline{U} \rangle_{E_j} := \langle \underline{U} \rangle_{E_j}\left(\langle \underline{U} \rangle_{E_i}, \underline{U}_{\mathrm{BC}}, \vec{\mathrm{n}}_{G_{ij}}\right) \end{aligned} \tag{2.86}$$

therefore Eqn. 2.84 can be elaborated for a general cell E_i, by separating fictitious exterior neighbors ($E_j \in \mathsf{EN}_i \cap \bar{\Omega}$) from real neighbors ($E_j \in \mathsf{EN}_i \cap \Omega$), where Ω is the set of real cells in the computational domain

$$\begin{aligned}\Delta\langle\underline{U}\rangle_{E_i} + \frac{\Delta t_i}{\mathrm{A}_{E_i}}\Bigg[\sum_{E_j\in\mathsf{EN}_i\cap\Omega}\left(\frac{\partial \underline{F}^{\mathrm{APP}}_{G_{ij}}}{\partial\langle\underline{U}\rangle_{E_i}}\quad\Delta\langle\underline{U}\rangle_{E_i} + \frac{\partial \underline{F}^{\mathrm{APP}}_{G_{ij}}}{\partial\langle\underline{U}\rangle_{E_j}}\quad\Delta\langle\underline{U}\rangle_{E_j}\right)\mathrm{L}_{G_{ij}}\\ + \sum_{E_j\in\mathsf{EN}_i\cap\bar{\Omega}}\left(\frac{\partial \underline{F}^{\mathrm{BC,APP}}_{G_{ij}}}{\partial\langle\underline{U}\rangle_{E_i}}\Delta\langle\underline{U}\rangle_{E_i} + \frac{\partial \underline{F}^{\mathrm{BC,APP}}_{G_{ij}}}{\partial\langle\underline{U}\rangle_{E_j}}\frac{\partial\langle\underline{U}\rangle_{E_j}}{\partial\langle\underline{U}\rangle_{E_i}}\Delta\langle\underline{U}\rangle_{E_i}\right)\mathrm{L}_{G_{ij}}\Bigg]\\ = -\Delta t_i \underline{R}_{E_i}\end{aligned} \tag{2.87}$$

factorize $\Delta\langle\underline{U}\rangle_{E_i}$ and $\Delta\langle\underline{U}\rangle_{E_j}$ and we obtain

$$\begin{aligned}\underbrace{\left[\underline{\underline{\mathbf{I}}} + \frac{\Delta t_i}{\mathrm{A}_{E_i}}\left(\sum_{E_j\in\mathsf{EN}_i}\frac{\partial \underline{F}^{\mathrm{APP}}_{G_{ij}}}{\partial\langle\underline{U}\rangle_{E_i}}\mathrm{L}_{G_{ij}} + \sum_{E_j\in\mathsf{EN}_i\cap\bar{\Omega}}\frac{\partial \underline{F}^{\mathrm{BC,APP}}_{G_{ij}}}{\partial\langle\underline{U}\rangle_{E_j}}\frac{\partial\langle\underline{U}\rangle_{E_j}}{\partial\langle\underline{U}\rangle_{E_i}}\mathrm{L}_{G_{ij}}\right)\right]}_{\underline{\underline{\mathbf{D}}}_i}\Delta\langle\underline{U}\rangle_{E_i}\\ + \sum_{E_j\in\mathsf{EN}_i\cap\Omega}\underbrace{\frac{\Delta t_i}{\mathrm{A}_{E_i}}\frac{\partial \underline{F}^{\mathrm{APP}}_{G_{ij}}}{\partial\langle\underline{U}\rangle_{E_j}}\quad\mathrm{L}_{G_{ij}}}_{\underline{\underline{\mathbf{N}}}_{ij}}\quad\Delta\langle\underline{U}\rangle_{E_j} = -\Delta t_i\underline{R}_{E_i}.\end{aligned} \tag{2.88}$$

Knowing that for each closed cell E_i we have

$$\begin{aligned}\sum_{E_j\in\mathsf{EN}_i}\frac{\partial \underline{F}^{\mathrm{c}}(\langle\underline{U}\rangle_{E_i},\vec{\mathrm{n}}_{G_{ij}})}{\partial\langle\underline{U}\rangle_{E_i}}\mathrm{L}_{G_{ij}} &= \sum_{E_j\in\mathsf{EN}_i}\frac{\partial \vec{\underline{F}}^{\mathrm{c}}(\langle\underline{U}\rangle_{E_i})}{\partial\langle\underline{U}\rangle_{E_i}}\cdot\vec{\mathrm{n}}_{G_{ij}}\mathrm{L}_{G_{ij}}\\ &= \frac{\partial \vec{\underline{F}}^{\mathrm{c}}(\langle\underline{U}\rangle_{E_i})}{\partial\langle\underline{U}\rangle_{E_i}}\cdot\underbrace{\sum_{E_j\in\mathsf{EN}_i}\vec{\mathrm{n}}_{G_{ij}}\mathrm{L}_{G_{ij}}}_{\oint_{\partial E_i}\mathrm{grad}(1)\mathrm{dS}=0} = 0\end{aligned} \tag{2.89}$$

therefore by replacing Eqn. 2.86 into Eqn. 2.88 with some algebraic manipulations, we have

$$\begin{aligned}\underline{\underline{\mathbf{D}}}_i = \left(1 + \frac{\Delta t_i}{2\mathrm{A}_{E_i}}\sum_{E_j\in\mathsf{EN}_i}\lambda_{G_{ij}}\mathrm{L}_{G_{ij}}\right)\underline{\underline{\mathbf{I}}} + \frac{\Delta t_i}{2\mathrm{A}_{E_i}}\sum_{E_j\in\mathsf{EN}_i\cap\bar{\Omega}}\Bigg[\left(\frac{\partial \underline{F}^{\mathrm{c}}(\langle\underline{U}\rangle_{E_i},\vec{\mathrm{n}}_{G_{ij}})}{\partial\langle\underline{U}\rangle_{E_i}} + \lambda_{G_{ij}}\underline{\underline{\mathbf{I}}}\right)\\ + 2\left(\frac{\partial \underline{F}^{\mathrm{c}}(\langle\underline{U}\rangle_{E_j},\vec{\mathrm{n}}_{G_{ij}})}{\partial\langle\underline{U}\rangle_{E_j}} - \lambda_{G_{ij}}\underline{\underline{\mathbf{I}}}\right)\frac{\partial\langle\underline{U}\rangle_{E_j}}{\partial\langle\underline{U}\rangle_{E_i}}\Bigg]\mathrm{L}_{G_{ij}}\end{aligned} \tag{2.90a}$$

$$\underline{\underline{\mathbf{N}}}_{ij} = \frac{\Delta t_i}{2\mathrm{A}_{E_i}}\left(\frac{\partial \underline{F}^{\mathrm{c}}(\langle\underline{U}\rangle_{E_j},\vec{\mathrm{n}}_{G_{ij}})}{\partial\langle\underline{U}\rangle_{E_j}} - \lambda_{G_{ij}}\underline{\underline{\mathbf{I}}}\right)\mathrm{L}_{G_{ij}},\qquad E_j\in\mathsf{EN}_i\cap\Omega. \tag{2.90b}$$

For the sake of compactness, all Jacobians in Eqn. 2.90 are replaced by $\underline{\underline{\mathbf{J}}}$

$$\begin{aligned}\underline{\underline{\mathbf{D}}}_i = &\left(1+\frac{\Delta t_i}{2\mathrm{A}_{E_i}}\sum_{E_j\in\mathsf{EN}_i}\lambda_{G_{ij}}\mathrm{L}_{G_{ij}}\right)\underline{\underline{\mathbf{I}}}\\ &+\frac{\Delta t_i}{2\mathrm{A}_{E_i}}\sum_{E_j\in\mathsf{EN}_i\cap\bar{\Omega}}\left[\left(\underline{\underline{\mathbf{J}}}_i+\lambda_{G_{ij}}\underline{\underline{\mathbf{I}}}\right)+2\left(\underline{\underline{\mathbf{J}}}_j-\lambda_{G_{ij}}\underline{\underline{\mathbf{I}}}\right)\underline{\underline{\mathbf{J}}}_{ij}\right]\mathrm{L}_{G_{ij}}\end{aligned} \tag{2.91a}$$

$$\underline{\underline{\mathbf{N}}}_{ij}=\frac{\Delta t_i}{2\mathrm{A}_{E_i}}\left(\underline{\underline{\mathbf{J}}}_j-\lambda_{G_{ij}}\underline{\underline{\mathbf{I}}}\right)\mathrm{L}_{G_{ij}},\qquad E_j\in\mathsf{EN}_i\cap\Omega \tag{2.91b}$$

$$\underline{\underline{\mathbf{J}}}_i=\frac{\partial\underline{F}^{\mathrm{c}}(\langle\underline{U}\rangle_{E_i},\vec{\mathrm{n}}_{G_{ij}})}{\partial\langle\underline{U}\rangle_{E_i}}\qquad\underline{\underline{\mathbf{J}}}_j=\frac{\partial\underline{F}^{\mathrm{c}}(\langle\underline{U}\rangle_{E_j},\vec{\mathrm{n}}_{G_{ij}})}{\partial\langle\underline{U}\rangle_{E_j}}\qquad\underline{\underline{\mathbf{J}}}_{ij}=\frac{\partial\langle\underline{U}\rangle_{E_j}}{\partial\langle\underline{U}\rangle_{E_i}}. \tag{2.91c}$$

The Jacobian $\underline{\underline{\mathbf{J}}}_{ij}$ is computed based on conservative variables $\frac{\partial\langle\underline{U}\rangle_{E_j}}{\partial\langle\underline{U}\rangle_{E_i}}$, whereas, in practice, the matrix $\underline{\underline{\mathbf{J}}}'_{ij}$ is used which is computed from primitive variables $\frac{\partial\langle\underline{V}\rangle_j}{\partial\langle\underline{V}\rangle_i}$. Therefore a transformation matrix $\underline{\underline{\mathbf{T}}}$ is needed, where

$$\underline{\underline{\mathbf{T}}}=\frac{\partial\underline{U}}{\partial\underline{V}}=\begin{bmatrix}1&0&0&0\\u&\rho&0&0\\v&0&\rho&0\\\frac{u^2+v^2}{2}&\rho u&\rho v&\frac{1}{\gamma-1}\end{bmatrix} \tag{2.92a}$$

$$\underline{\underline{\mathbf{T}}}^{-1}=\frac{\partial\underline{V}}{\partial\underline{U}}=\begin{bmatrix}1&0&0&0\\\frac{-u}{\rho}&\frac{1}{\rho}&0&0\\\frac{-v}{\rho}&0&\frac{1}{\rho}&0\\\frac{(\gamma-1)(u^2+v^2)}{2}&(1-\gamma)u&(1-\gamma)v&(\gamma-1)\end{bmatrix} \tag{2.92b}$$

and we obtain the final expression for $\underline{\underline{\mathbf{D}}}_i$

$$\begin{aligned}\underline{\underline{\mathbf{D}}}_i = &\left(1+\frac{\Delta t_i}{2\mathrm{A}_{E_i}}\sum_{E_j\in\mathsf{EN}_i}\lambda_{G_{ij}}\mathrm{L}_{G_{ij}}\right)\underline{\underline{\mathbf{I}}}\\ &+\frac{\Delta t_i}{2\mathrm{A}_{E_i}}\sum_{E_j\in\mathsf{EN}_i\cap\bar{\Omega}}\left[\left(\underline{\underline{\mathbf{J}}}_i+\lambda_{G_{ij}}\underline{\underline{\mathbf{I}}}\right)+2\left(\underline{\underline{\mathbf{J}}}_j-\lambda_{G_{ij}}\underline{\underline{\mathbf{I}}}\right)\underbrace{\underline{\underline{\mathbf{T}}}_j\underline{\underline{\mathbf{J}}}'_{ij}\underline{\underline{\mathbf{T}}}_i^{-1}}_{\underline{\underline{\mathbf{J}}}_{ij}}\right]\mathrm{L}_{G_{ij}}.\end{aligned} \tag{2.93}$$

In Eqn. 2.93, the cell E_i is considered a general cell with both interior and boundary edges. If E_i is an interior cells where $\langle\underline{U}\rangle_{E_j}$ does not depend on $\langle\underline{U}\rangle_{E_i}$, Eqn. 2.93 simplifies to

$$\underline{\underline{\mathbf{D}}}_i=\left(1+\frac{\Delta t_i}{2\mathrm{A}_{E_i}}\sum_{E_j\in\mathsf{EN}_i}\lambda_{G_{ij}}\mathrm{L}_{G_{ij}}\right)\underline{\underline{\mathbf{I}}} \tag{2.94}$$

and $\underline{\underline{\mathbf{D}}}_i$ becomes an identity matrix with a scaling factor.

The face-normal flux Jacobian $\underline{\underline{\mathbf{J}}}_i$ (same for $\underline{\underline{\mathbf{J}}}_j$) is derived analytically term-by-term knowing

that

$$\underline{F}^{\mathrm{c}}(\langle \underline{U} \rangle_{E_i}, \vec{\mathrm{n}}_{G_{ij}}) = \begin{bmatrix} \mathtt{u}_\rho V_n \\ \mathtt{u}_x V_n + p\mathrm{n}_x \\ \mathtt{u}_y V_n + p\mathrm{n}_y \\ (\mathtt{u}_e + p) V_n \end{bmatrix} \tag{2.95}$$

where, for the sake of conciseness, vector $(\mathtt{u}_\rho, \mathtt{u}_x, \mathtt{u}_y, \mathtt{u}_e)^\top$ denote the cell-averaged conservative variables $\langle \underline{U} \rangle_{E_i} = (\rho, \rho u, \rho v, \rho e_t)^\top$. Note that $\mathtt{u}$ is a shorthand notation for a given component in $\langle \underline{U} \rangle_{E_i}$, which should be distinguished from the streamwise velocity component u. Therefore, the normal velocity V_n and pressure p can also be expressed in terms of $\mathtt{u}_{(\cdot)}$

$$\begin{aligned} V_n &= u\mathrm{n}_x + v\mathrm{n}_y = \frac{\mathtt{u}_x}{\mathtt{u}_\rho}\mathrm{n}_x + \frac{\mathtt{u}_y}{\mathtt{u}_\rho}\mathrm{n}_y \\ p &= (\gamma - 1)\left[\mathtt{u}_e - \frac{1}{2}\left(\frac{\mathtt{u}_x^2}{\mathtt{u}_\rho} + \frac{\mathtt{u}_y^2}{\mathtt{u}_\rho}\right)\right]. \end{aligned} \tag{2.96}$$

By deriving $\underline{F}^{\mathrm{c}}(\underline{U}) = (\mathtt{f}_\rho, \mathtt{f}_x, \mathtt{f}_y, \mathtt{f}_e)^\top$ in terms of $(\mathtt{u}_\rho, \mathtt{u}_x, \mathtt{u}_y, \mathtt{u}_e)^\top$, we obtain each term of the face-normal Jacobian matrix

$$\begin{aligned}
&\frac{\partial \mathtt{f}_\rho}{\partial \mathtt{u}_x} = \mathrm{n}_x && \frac{\partial \mathtt{f}_\rho}{\partial \mathtt{u}_y} = \mathrm{n}_y \\
&\frac{\partial \mathtt{f}_x}{\partial \mathtt{u}_\rho} = \frac{\mathtt{u}_x^2(\gamma-3)\mathrm{n}_x - 2\mathtt{u}_x\mathtt{u}_y\mathrm{n}_y + \mathtt{u}_y^2(\gamma-1)\mathrm{n}_x}{2\mathtt{u}_\rho^2} && \frac{\partial \mathtt{f}_x}{\partial \mathtt{u}_x} = \frac{\mathtt{u}_y\mathrm{n}_y - \mathtt{u}_x(\gamma-3)\mathrm{n}_x}{\mathtt{u}_\rho} \\
&\frac{\partial \mathtt{f}_x}{\partial \mathtt{u}_y} = \frac{\mathtt{u}_x\mathrm{n}_y - \mathtt{u}_y(\gamma-1)\mathrm{n}_x}{\mathtt{u}_\rho} && \frac{\partial \mathtt{f}_x}{\partial \mathtt{u}_e} = (\gamma-1)\mathrm{n}_x \\
&\frac{\partial \mathtt{f}_y}{\partial \mathtt{u}_\rho} = \frac{\mathtt{u}_x^2(\gamma-1)\mathrm{n}_y - 2\mathtt{u}_x\mathtt{u}_y\mathrm{n}_x + \mathtt{u}_y^2(\gamma-3)\mathrm{n}_y}{2\mathtt{u}_\rho^2} && \frac{\partial \mathtt{f}_y}{\partial \mathtt{u}_x} = \frac{\mathtt{u}_y\mathrm{n}_x - \mathtt{u}_x(\gamma-1)\mathrm{n}_y}{\mathtt{u}_\rho} \\
&\frac{\partial \mathtt{f}_y}{\partial \mathtt{u}_y} = \frac{\mathtt{u}_x\mathrm{n}_x - \mathtt{u}_y(\gamma-3)\mathrm{n}_y}{\mathtt{u}_\rho} && \frac{\partial \mathtt{f}_y}{\partial \mathtt{u}_e} = (\gamma-1)\mathrm{n}_y \\
&\frac{\partial \mathtt{f}_e}{\partial \mathtt{u}_\rho} = -\frac{(\mathtt{u}_x\mathrm{n}_x + \mathtt{u}_y\mathrm{n}_y)[\mathtt{u}_\rho\mathtt{u}_e\gamma - (\gamma-1)(\mathtt{u}_x^2 + \mathtt{u}_y^2)]}{\mathtt{u}_\rho^3} && \frac{\partial \mathtt{f}_e}{\partial \mathtt{u}_x} = \frac{2\gamma\mathtt{u}_\rho\mathtt{u}_e\mathrm{n}_x - (\gamma-1)(3\mathtt{u}_x^2\mathrm{n}_x + 2\mathtt{u}_x\mathtt{u}_y\mathrm{n}_y + \mathtt{u}_y^2\mathrm{n}_x)}{2\mathtt{u}_\rho^2} \\
&\frac{\partial \mathtt{f}_e}{\partial \mathtt{u}_y} = \frac{2\gamma\mathtt{u}_\rho\mathtt{u}_e\mathrm{n}_y - (\gamma-1)(\mathtt{u}_x^2\mathrm{n}_y + 2\mathtt{u}_x\mathtt{u}_y\mathrm{n}_x + 3\mathtt{u}_y^2\mathrm{n}_y)}{2\mathtt{u}_\rho^2} && \frac{\partial \mathtt{f}_e}{\partial \mathtt{u}_e} = \frac{\gamma(\mathtt{u}_x\mathrm{n}_x + \mathtt{u}_y\mathrm{n}_y)}{\mathtt{u}_\rho}.
\end{aligned} \tag{2.97}$$

All omitted partial derivatives in Eqn. 2.97 are equal to zero.

Once all matrices are determined analytically, Eqn. 2.88 can be arranged into a block linear

system as follows

$$\underbrace{\begin{bmatrix} \underline{\underline{\mathbf{D}}}_1 & \underline{\underline{\mathbf{N}}}_{12} & \cdots & \underline{\underline{\mathbf{N}}}_{1N_\Omega} \\ \underline{\underline{\mathbf{N}}}_{21} & \underline{\underline{\mathbf{D}}}_2 & \cdots & \underline{\underline{\mathbf{N}}}_{2N_\Omega} \\ \vdots & \vdots & \ddots & \vdots \\ \underline{\underline{\mathbf{N}}}_{N_\Omega 1} & \underline{\underline{\mathbf{N}}}_{N_\Omega 2} & \cdots & \underline{\underline{\mathbf{D}}}_{N_\Omega} \end{bmatrix}}_{\underline{\underline{\mathbf{M}}}} \begin{bmatrix} \Delta\langle \underline{U} \rangle_{E_1} \\ \Delta\langle \underline{U} \rangle_{E_2} \\ \vdots \\ \Delta\langle \underline{U} \rangle_{E_{N_\Omega}} \end{bmatrix} = \begin{bmatrix} -\Delta t_1 \underline{R}_{E_1} \\ -\Delta t_2 \underline{R}_{E_2} \\ \vdots \\ -\Delta t_n \underline{R}_{E_{N_\Omega}} \end{bmatrix} \tag{2.98}$$

where N_Ω is the number of cells in the computational domain Ω. $\Delta\langle \underline{U} \rangle_{E_i}$ and $\underline{R}_{E_i}$ are, for 2D laminar flows, 4-entry vectors corresponding to conservative variable increments and residuals in cell E_i. $\underline{\underline{\mathbf{M}}}$ is a sparse block matrix whose elements are 4×4 square matrices. The sparsity of $\underline{\underline{\mathbf{M}}}$ depends on the grid connectivity, that is, at the i^{th} row, $\underline{\underline{\mathbf{N}}}_{ij} = 0 \; \forall E_j \notin \mathsf{EN}_i$.

To solve the above block linear system Eqn. 2.98, three different linear solvers are investigated in the scope of this thesis: the approximately factored LU Symmetric Gauss-Seidel (LU-SGS) method [117], the iterative version of LU Symmetric Gauss-Seidel (BLU-SGS) method [42], and the classical Jacobi iterative method. The first two methods both belong to the symmetric Gauss-Seidel category in the sense that increments $\Delta\langle \underline{U} \rangle_{E_j}$ of upper/lower neighbors at the current iteration are required to compute $\Delta\langle \underline{U} \rangle_{E_i}$. The Jacobi method, on the other hand, does not require neighbor information at current time-step (only at the previous iteration). This key difference results in different boundary treatments for the two families of methods. For the two iterative methods (BLU-SGS and Jacobi), the linear iteration is indexed by k, which is performed for each m-iteration while dual-time-stepping. No k-iteration is required for the approximately factored LU-SGS method therefore the updated increment ${}^{\text{new}}\Delta\langle \underline{U} \rangle_{E_i}$ is obtained after completing the forward and backward sweeps.

As shown in Eqn. 2.91, the sub-matrices of $\underline{\underline{\mathbf{M}}}$ matrix contain Jacobian matrices which are costly to compute and to store, to obviate this inconvenience, a matrix-free approach is used whenever $\langle \underline{U} \rangle$ and $\Delta\langle \underline{U} \rangle$ of the current iteration are readily available, the objective is to approximate the convective flux increment $\Delta \underline{F}$ without computing or storing any Jacobian matrices unless absolutely necessary. Such an approximation is suggested by Luo *et al.* [149]

$$\frac{\partial \underline{F}}{\partial \langle \underline{U} \rangle} \Delta\langle \underline{U} \rangle \approx \underline{F}(\langle \underline{U} \rangle + \Delta\langle \underline{U} \rangle) - \underline{F}(\langle \underline{U} \rangle) \tag{2.99}$$

where $\underline{F}$ is a generic flux function. Eqn. 2.99 can be considered as a procedure of "*de*-linearization" for Eqn. 2.83. The idea of matrix-free method is that, the flux increment $\Delta \underline{F}$ is linearized into a Jacobian-$\Delta\langle \underline{U} \rangle$ product only when $\Delta\langle \underline{U} \rangle$ is not available at the current iteration and needs to be solved for (i.e., $\langle \underline{U} \rangle$ of the next iteration remains unknown). However, whenever $\Delta\langle \underline{U} \rangle$ is known at the current iteration, the flux increment can be evaluated directly by taking the difference between the next and current fluxes $\Delta \underline{F} = \underline{F}(\langle \underline{U} \rangle + \Delta\langle \underline{U} \rangle) - \underline{F}(\langle \underline{U} \rangle)$ without any linearization, which gives no reason to compute or to store the Jacobian matrix. Therefore, the fully linearized ${}^{m,n+1}\Delta \underline{F}^{\text{APP}}_{G_{ij}}$ in Eqn. 2.83 can be *de*-linearized with Eqn. 2.99 whenever ${}^{m,n+1}\Delta \underline{U}_{E_i}$ or ${}^{m,n+1}\Delta \underline{U}_{E_j}$ becomes known. Next, we will apply the matrix-free method to three types of linear solvers.

2.5.1 Jacobi Iterative Method

For Jacobi method, the matrix-free approach Eqn. 2.99 can be implemented for both interior and boundary cells. $\Delta\langle \underline{U} \rangle_{E_j}$ and $\langle \underline{U} \rangle_{E_j}$ from the previous linear k-iteration (${}^{k-1}\Delta\langle \underline{U} \rangle_{E_j}$ and

${}^{k-1}\langle\underline{U}\rangle_{E_j}$) are used to update ${}^{k}\Delta\langle\underline{U}\rangle_{E_i}$. For a given boundary cell, ${}^{k-1}\Delta\langle\underline{U}\rangle_{E_j}$ in its corresponding fictitious exterior cell is updated according to the appropriate boundary condition relations whenever ${}^{k-1}\Delta\langle\underline{U}\rangle_{E_i}$ is recomputed. Therefore, for Jacobi method, ${}^{k-1}\Delta\langle\underline{U}\rangle_{E_j}$ and ${}^{k-1}\langle\underline{U}\rangle_{E_j}$ are always known $\forall E_j \in \mathsf{EN}_i$ resulting in diagonal $\underline{\underline{\mathbf{D}}}_i$ matrices and matrix-free approximation for all $\underline{\underline{\mathbf{N}}}_{ij}$ matrices everywhere in the computational domain. For Jacobi method, Eqn. 2.98 becomes

$$\begin{aligned} &\underline{\underline{\mathbf{D}}}_i\,{}^{k}\Delta\langle\underline{U}\rangle_{E_i} + \sum_{j\in\Omega}\frac{\Delta t_i \mathrm{L}_{G_{ij}}}{2\mathrm{A}_{E_i}}\left[{}^{k-1}\Delta\underline{F}^{\mathrm{c}}_{E_j} - \lambda_{G_{ij}}\,{}^{k-1}\Delta\langle\underline{U}\rangle_{E_j}\right] = -\Delta t_i \underline{R}_{E_i} \\ &\text{with} \qquad {}^{k-1}\Delta\underline{F}^{\mathrm{c}}_{E_j} = \underline{F}^{\mathrm{c}}\left({}^{k-1}\langle\underline{U}\rangle_{E_j} + {}^{k-1}\Delta\langle\underline{U}\rangle_{E_j}, \vec{\mathrm{n}}_{G_{ij}}\right) - \underline{F}^{\mathrm{c}}\left({}^{k-1}\langle\underline{U}\rangle_{E_j}, \vec{\mathrm{n}}_{G_{ij}}\right) \end{aligned} \tag{2.100}$$

where $\underline{\underline{\mathbf{D}}}_i$ is given by Eqn. 2.94, and the iterative solution using Jacobi method is given by

$${}^{k}\Delta\langle\underline{U}\rangle_{E_i} = \frac{-\Delta t_i \underline{R}_{E_i} - \sum_{j\in\Omega}\frac{\Delta t_i \mathrm{L}_{G_{ij}}}{2\mathrm{A}_{E_i}}\left[{}^{k-1}\Delta\underline{F}_{E_j} - \lambda_{G_{ij}}\,{}^{k-1}\Delta\langle\underline{U}\rangle_{E_j}\right]}{1 + \frac{\Delta t_i}{2\mathrm{A}_{E_i}}\sum_{E_j\in\mathsf{EN}_i}\lambda_{G_{ij}}\mathrm{L}_{G_{ij}}}. \tag{2.101}$$

Algorithm 1: Iterative Jacobi solver

input : ${}^{\text{old}}\underline{R}_{E_i}$, ${}^{\text{old}}\langle\underline{U}\rangle_{E_i}$
output: ${}^{\text{new}}\langle\underline{U}\rangle_{E_i}$
1 ${}^{0}\langle\underline{U}\rangle_{E_i} := {}^{\text{old}}\langle\underline{U}\rangle_{E_i}$, ${}^{0}\Delta\langle\underline{U}\rangle_{E_i} := 0$;
2 **while** *convergence not reached* **do**
3 | compute ${}^{k}\Delta\langle\underline{U}\rangle_{E_i}$ (Eqn. 2.101);
4 **end**
5 update ${}^{\text{new}}\langle\underline{U}\rangle_{E_i} = {}^{\text{old}}\langle\underline{U}\rangle_{E_i} + {}^{k}\Delta\langle\underline{U}\rangle_{E_i}$

2.5.2 Block LU-SGS Iterative Method

When using a Gauss-Seidel-based method, since $\Delta\langle\underline{U}\rangle$ of boundary cells are unknown at current iteration, non-diagonal $\underline{\underline{\mathbf{D}}}_i$ matrices must be computed and stored for boundary cells using Eqn. 2.93 in order to account implicitly for the contribution of boundary conditions. The full matrix form of the iterative BLU-SGS method [42] is given by

Forward sweep :

$${}^{*}\Delta\langle\underline{U}\rangle_{E_i} = \underline{\underline{\mathbf{D}}}_i^{-1}\left[-\Delta t_i \underline{R}_{E_i} - \left(\sum_{j<i}\underline{\underline{\mathbf{N}}}_{ij}\,{}^{*}\Delta\langle\underline{U}\rangle_{E_j} + \sum_{j>i}\underline{\underline{\mathbf{N}}}_{ij}\,{}^{k-1}\Delta\langle\underline{U}\rangle_{E_j}\right)\right] \tag{2.102}$$

Backward sweep :

$${}^{k}\Delta\langle\underline{U}\rangle_{E_i} = \underline{\underline{\mathbf{D}}}_i^{-1}\left[-\Delta t_i \underline{R}_{E_i} - \left(\sum_{j<i}\underline{\underline{\mathbf{N}}}_{ij}\,{}^{*}\Delta\langle\underline{U}\rangle_{E_j} + \sum_{j>i}\underline{\underline{\mathbf{N}}}_{ij}\quad{}^{k}\Delta\langle\underline{U}\rangle_{E_j}\right)\right] \tag{2.103}$$

using $\underline{\underline{\mathbf{D}}}_i$ from Eqn. 2.93 or Eqn. 2.94 depending on whether E_i is a boundary cell. It is important to realize that $j < i$ and $j > i$ implies that cell E_i is located on a higher or lower hyperplane than E_j in a *reordered* unstructured grid, and the reordering strategy will be discussed in Section 2.6. The matrix-free approximation is applied to $\underline{\underline{\mathbf{N}}}_{ij}$ matrices to replace exact Jacobian, and the resulting

matrix-free form is as follows

Forward sweep :

$$
{}^{*}\Delta\langle\underline{U}\rangle_{E_i} = \underline{\underline{\mathbf{D}}}_i^{-1}\left\{ -\Delta t_i \underline{R}_{E_i} - \left(\sum_{j<i} \frac{\Delta t_i \mathrm{L}_{G_{ij}}}{2\mathrm{A}_{E_i}} \left[\quad {}^{*}\Delta\underline{F}^{\mathrm{c}}_{E_j} - \lambda_{G_{ij}} \quad {}^{*}\Delta\langle\underline{U}\rangle_{E_j} \right] \right.\right.
$$

$$
\left.\left. + \sum_{j>i} \frac{\Delta t_i \mathrm{L}_{G_{ij}}}{2\mathrm{A}_{E_i}} \left[{}^{k-1}\Delta\underline{F}^{\mathrm{c}}_{E_j} - \lambda_{G_{ij}} \, {}^{k-1}\Delta\langle\underline{U}\rangle_{E_j} \right] \right) \right\} \tag{2.104}
$$

$$
\text{with} \qquad {}^{*}\Delta\underline{F}^{\mathrm{c}}_{E_j} = \underline{F}^{\mathrm{c}}\left(\quad {}^{*}\langle\underline{U}\rangle_{E_j} + \quad {}^{*}\Delta\langle\underline{U}\rangle_{E_j}, \vec{\mathrm{n}}_{G_{ij}} \right) - \underline{F}^{\mathrm{c}}\left(\quad {}^{*}\langle\underline{U}\rangle_{E_j}, \vec{\mathrm{n}}_{G_{ij}} \right)
$$

$$
{}^{k-1}\Delta\underline{F}^{\mathrm{c}}_{E_j} = \underline{F}^{\mathrm{c}}\left({}^{k-1}\langle\underline{U}\rangle_{E_j} + {}^{k-1}\Delta\langle\underline{U}\rangle_{E_j}, \vec{\mathrm{n}}_{G_{ij}} \right) - \underline{F}^{\mathrm{c}}\left({}^{k-1}\langle\underline{U}\rangle_{E_j}, \vec{\mathrm{n}}_{G_{ij}} \right)
$$

Backward sweep :

$$
{}^{k}\Delta\langle\underline{U}\rangle_{E_i} = \underline{\underline{\mathbf{D}}}_i^{-1}\left\{ -\Delta t_i \underline{R}_{E_i} - \left(\sum_{j<i} \frac{\Delta t_i \mathrm{L}_{G_{ij}}}{2\mathrm{A}_{E_i}} \left[{}^{*}\Delta\underline{F}^{\mathrm{c}}_{E_j} - \lambda_{G_{ij}} \, {}^{*}\Delta\langle\underline{U}\rangle_{E_j} \right] \right.\right.
$$

$$
\left.\left. + \sum_{j>i} \frac{\Delta t_i \mathrm{L}_{G_{ij}}}{2\mathrm{A}_{E_i}} \left[{}^{k}\Delta\underline{F}^{\mathrm{c}}_{E_j} - \lambda_{G_{ij}} \, {}^{k}\Delta\langle\underline{U}\rangle_{E_j} \right] \right) \right\} \tag{2.105}
$$

$$
\text{with} \quad {}^{*}\Delta\underline{F}^{\mathrm{c}}_{E_j} = \underline{F}^{\mathrm{c}}\left({}^{*}\langle\underline{U}\rangle_{E_j} + {}^{*}\Delta\langle\underline{U}\rangle_{E_j}, \vec{\mathrm{n}}_{G_{ij}} \right) - \underline{F}^{\mathrm{c}}\left({}^{*}\langle\underline{U}\rangle_{E_j}, \vec{\mathrm{n}}_{G_{ij}} \right)
$$

$$
{}^{k}\Delta\underline{F}^{\mathrm{c}}_{E_j} = \underline{F}^{\mathrm{c}}\left({}^{k}\langle\underline{U}\rangle_{E_j} + {}^{k}\Delta\langle\underline{U}\rangle_{E_j}, \vec{\mathrm{n}}_{G_{ij}} \right) - \underline{F}^{\mathrm{c}}\left({}^{k}\langle\underline{U}\rangle_{E_j}, \vec{\mathrm{n}}_{G_{ij}} \right)
$$

The BLU-SGS method is *not* an approximate factorization method, thus providing better convergence rate comparing to LU-SGS with the help of an additional inner k-iteration.

Algorithm 2: Iterative BLU-SGS solver

input : ${}^{\mathrm{old}}\underline{R}_{E_i}$, ${}^{\mathrm{old}}\langle\underline{U}\rangle_{E_i}$
output: ${}^{\mathrm{new}}\langle\underline{U}\rangle_{E_i}$
${}^{0}\langle\underline{U}\rangle_{E_i} := {}^{\mathrm{old}}\langle\underline{U}\rangle_{E_i}$, ${}^{0}\Delta\langle\underline{U}\rangle_{E_i} := 0$;
while *convergence not reached* **do**
  forward sweep: compute ${}^{*}\Delta\langle\underline{U}\rangle_{E_i}$ (Eqn. 2.104);
  backward sweep: compute ${}^{k}\Delta\langle\underline{U}\rangle_{E_i}$ (Eqn. 2.105);
end
update ${}^{\mathrm{new}}\langle\underline{U}\rangle_{E_i} = {}^{\mathrm{old}}\langle\underline{U}\rangle_{E_i} + {}^{k}\Delta\langle\underline{U}\rangle_{E_i}$

2.5.3 Approximately Factored LU-SGS Method

The original approximately factored LU-SGS scheme is developed by Jameson *et al.* [117]. In the current study, we adopt an unstructured formulation proposed by Luo *et al.* [149]. The factorization step is the following

$$
(\underline{\underline{\mathbf{D}}} + \underline{\underline{\mathbf{L}}})\underline{\underline{\mathbf{D}}}^{-1}(\underline{\underline{\mathbf{D}}} + \underline{\underline{\mathbf{U}}})\Delta\langle\underline{U}\rangle = \underline{R} + (\cancel{\underline{\underline{\mathbf{L}}}\underline{\underline{\mathbf{D}}}^{-1}\underline{\underline{\mathbf{U}}}})\Delta\langle\underline{U}\rangle \tag{2.106}
$$

where $\underline{\underline{\mathbf{U}}}$ is the upper triangular sub-matrix of $\underline{\underline{\mathbf{M}}}$, $\underline{\underline{\mathbf{L}}}$ is the lower triangular sub-matrix of $\underline{\underline{\mathbf{M}}}$ and $\underline{\underline{\mathbf{D}}}$ is the diagonal sub-matrix. Note that the term $(\underline{\underline{\mathbf{L}}}\underline{\underline{\mathbf{D}}}^{-1}\underline{\underline{\mathbf{U}}})$ is neglected, and let

$$^{*}\Delta\langle\underline{U}\rangle = \underline{\underline{\mathbf{D}}}^{-1}(\underline{\underline{\mathbf{D}}} + \underline{\underline{\mathbf{U}}})\Delta\langle\underline{U}\rangle \tag{2.107}$$

Forward sweep :

$$^{*}\Delta\langle\underline{U}\rangle_{E_i} = \underline{\underline{\mathbf{D}}}_i^{-1}\left(-\Delta t_i \underline{R}_{E_i} - \sum_{j<i}\underline{\underline{\mathbf{N}}}_{ij}\,{}^{*}\Delta\langle\underline{U}\rangle_{E_j}\right) \tag{2.108}$$

Backward sweep :

$$^{\text{new}}\Delta\langle\underline{U}\rangle_{E_i} = {}^{*}\Delta\langle\underline{U}\rangle_{E_i} - \underline{\underline{\mathbf{D}}}_i^{-1}\sum_{j>i}\underline{\underline{\mathbf{N}}}_{ij}\,{}^{\text{new}}\Delta\langle\underline{U}\rangle_{E_j}. \tag{2.109}$$

As with the BLU-SGS, matrix-free approach is applied to $\underline{\underline{\mathbf{N}}}_{ij}$, $\underline{\underline{\mathbf{D}}}_i$ is computed in the same manner as for BLU-SGS depending on whether cell E_i is a boundary cell.

Forward sweep :

$$\begin{aligned} &^{*}\Delta\langle\underline{U}\rangle_{E_i} = \underline{\underline{\mathbf{D}}}_i^{-1}\left[-\Delta t_i \underline{R}_{E_i} - \sum_{j<i}\frac{\Delta t_i \mathrm{L}_{G_{ij}}}{2\mathrm{A}_{E_i}}\left({}^{*}\Delta\underline{F}^{\mathrm{c}}_{E_j} - \lambda_{G_{ij}}\,{}^{*}\Delta\langle\underline{U}\rangle_{E_j}\right)\right] \\ &\text{with} \quad {}^{*}\Delta\underline{F}^{\mathrm{c}}_{E_j} = \underline{F}^{\mathrm{c}}\left({}^{*}\langle\underline{U}\rangle_{E_j} + {}^{*}\Delta\langle\underline{U}\rangle_{E_j}, \vec{\mathrm{n}}_{G_{ij}}\right) - \underline{F}^{\mathrm{c}}\left({}^{*}\langle\underline{U}\rangle_{E_j}, \vec{\mathrm{n}}_{G_{ij}}\right) \end{aligned} \tag{2.110}$$

Backward sweep :

$$\begin{aligned} &^{\text{new}}\Delta\langle\underline{U}\rangle_{E_i} = {}^{*}\Delta\langle\underline{U}\rangle_{E_i} - \underline{\underline{\mathbf{D}}}_i^{-1}\sum_{j>i}\frac{\Delta t_i \mathrm{L}_{G_{ij}}}{2\mathrm{A}_{E_i}}\left[{}^{\text{new}}\Delta\underline{F}^{\mathrm{c}}_{E_j} - \lambda_{G_{ij}}\,{}^{\text{new}}\Delta\langle\underline{U}\rangle_{E_j}\right] \\ &\text{with} \quad {}^{\text{new}}\Delta\underline{F}^{\mathrm{c}}_{E_j} = \underline{F}^{\mathrm{c}}\left({}^{\text{new}}\langle\underline{U}\rangle_{E_j} + {}^{\text{new}}\Delta\langle\underline{U}\rangle_{E_j}, \vec{\mathrm{n}}_{G_{ij}}\right) - \underline{F}^{\mathrm{c}}\left({}^{\text{new}}\langle\underline{U}\rangle_{E_j}, \vec{\mathrm{n}}_{G_{ij}}\right) \end{aligned} \tag{2.111}$$

Note that the superscript $^{k}(\cdot)$ is dropped for LU-SGS method since there is no linear iteration involved.

Algorithm 3: Approximately factored LU-SGS solver

input : ${}^{\text{old}}\underline{R}_{E_i}$, ${}^{\text{old}}\langle\underline{U}\rangle_{E_i}$
output: ${}^{\text{new}}\langle\underline{U}\rangle_{E_i}$
1 forward sweep: compute ${}^{*}\Delta\langle\underline{U}\rangle_{E_i}$ (Eqn. 2.110);
2 backward sweep: compute ${}^{\text{new}}\Delta\langle\underline{U}\rangle_{E_i}$ (Eqn. 2.111);
3 update ${}^{\text{new}}\langle\underline{U}\rangle_{E_i} = {}^{\text{old}}\langle\underline{U}\rangle_{E_i} + {}^{\text{new}}\Delta\langle\underline{U}\rangle_{E_i}$

2.6 Grid Reordering Strategy

As shown in 2.102 and 2.103, performing BLU-SGS on unstructured grids requires constructing multiple hyperplanes. A general guideline for such a grid reordering procedure is proposed by Sharov and Nakahashi [184]. The key is to reorder an unstructured grid into hyperplanes in such a manner that no cell on a given hyperplane has edge-neighbors on this hyperplane, and that most cells (except for those on the first and last hyperplanes) on hyperplane i have neighboring cells on hyperplanes $j > i$ and $j < i$. Although the guideline remains identical, the grid reordering procedure in [184] is based on cell-vertex scheme while the current one is based on cell-centered data structure. Meanwhile, the current procedure starts from an hyperplane 1 (denoted by HP_1) containing an arbitrary number of non-edge-neighboring cells instead of only one cell, which is a generalization of the procedure in [184]. This generalization makes the BLU-SGS solver more parallelizable in a sense that the workload is more equally distributed among processes. However, in terms of convergence rate, the computation converges faster with a more balanced reordering, which is characterized by more cells having both upper and lower neighbors.

The current grid reordering strategy is given as follows:

1. Set the mask of each cell to `TRUE`;
2. Set $i = 1$ and $k = 0$, select N_i arbitrary non-edge-neighboring cells to form HP_i, and set masks of those cells to `FALSE`;
3. Set $i = i + k + 1$, put all `TRUE` cells that are edge-neighbors to any member of $\mathsf{HP}_{(i-k-1)}$ into HP_i, and set masks of those cells to `FALSE`;
4. Separate all edge-neighbors within HP_i : assign a color number $j(0 \leq j \leq k)$ $(k + 1$ colors) to each member of HP_i, such that any pair of cells sharing the same j are *not* neighbors;
5. Repeat from step 3 until all masks in the grid turn `FALSE`;
6. Redefine hyperplane indices such that each cell originally in HP_i now belongs to $\mathsf{HP}_{(i+j)}$, where j, if defined in step 4, is the individual color number of the cell.

Since by naively including edge-neighbors to form the next hyperplanes, there is no guarantee to obtain hyperplanes not containing edge-neighbors within themselves, the success of this strategy relies on a robust graph-coloring algorithm for separating edge-neighbors within a given hyperplane, i.e., finding the correct k and j in the fourth step of the above strategy. We define $k + 1$ as the chromatic number of a hyperplane. However, no detailed description is given for the graph-coloring algorithm used in [184], and for this reason, we have adopted the well-established Welsh-Powell graph-coloring algorithm [214] and modified this algorithm for the current purpose. The current version of the Welsh-Powell algorithm consists of the following steps:

1. Store all cells in HP_i in a list named L;
2. Sort the list L in a descending order based on the number of edge-neighbors *within* HP_i (termed as the *valence*);
3. Set the global variable $k = 0$;
4. Initialize the group number j of each cell in L to -1;
5. Loop through L, for each cell in L, assign its $j = k$ if $j < 0$ and if it is *not* a neighbor of any other member in L whose $j = k$;

6. Increment k by 1;

7. Repeat from step 5 until every cell in L has a group number $j \geq 0$.

Is is shown in [214] that the upper-bound of the chromatic number $k+1$ of a given HP_i is $\deg(\mathsf{HP}_i)+1$, where $\deg(\mathsf{HP}_i)$ is defined by the maximum valence among all its member cells. The complete grid-reordering strategy is illustrated in Fig. 2.4 through an simplified example of six triangle and quadrilateral cells.

There are several points worth noting in Fig. 2.4. Firstly, in this simplified example, the Welsh-Powell algorithm is shown in detail only for the original HP_2. In reality, we perform this algorithm for every newly discovered hyperplane since it is impossible to determine whether there exit any edge-neighbors in advance. However, it is clear that if a hyperplane does not admit any edge-neighbors (*e.g.*, HP_5 in Fig. 2.4), the Welsh-Powell algorithm will assign $j = 0$ to every one of its member cells, thus allowing their indices i to remain unmodified at the end the grid reordering procedure.

Secondly, we note that the chromatic number for the original HP_2 is $k+1=3$, which is equal to the upper bound defined by $\deg(\mathsf{HP}_2)+1$ since cells 2, 3, and 4 all have a valence of 2.

Finally, this simplified example intends to demonstrate that the current grid reordering strategy is operational on any arbitrary polygonal unstructured grids with different types of N-gons.

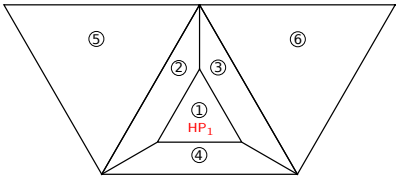

Cell ID	Mask	j	$i=1$	$k=0$
1	FALSE	–		
2	TRUE	–		
3	TRUE	–		
4	TRUE	–		
5	TRUE	–		
6	TRUE	–		

The next HP_i will have a new index $i = 1 + k + 1 = 2$

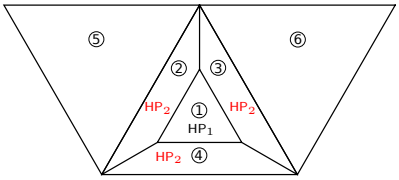

Cell ID	Mask	j	$i=2$	$k=0$
1	FALSE	–		
2	FALSE	-1		
3	FALSE	-1		
4	FALSE	-1		
5	TRUE	–		
6	TRUE	–		

Start Welsh-Powell algorithm to separate edge-neighbors in HP_2 :

Cell ID in L	Valence	j	Set $k=0$, loop through list L while any $j<0$:
2	2	0	
3	2	-1	End of loop #1, 2 cells in L with $j<0$.
4	2	-1	Restart loop with $k=0+1$

Cell ID in L	Valence	j	
2	2	0	
3	2	1	End of loop #2, 1 cell in L with $j<0$.
4	2	-1	Restart loop with $k=1+1$

Cell ID in L	Valence	j	
2	2	0	
3	2	1	End of loop #3, no cell in L with $j<0$. Algorithm termi-
4	2	2	nates with $k=\max_{2\le n\le 4}(j_n)=2$

The next HP_i will have a new index $i = 2 + k + 1 = 5$

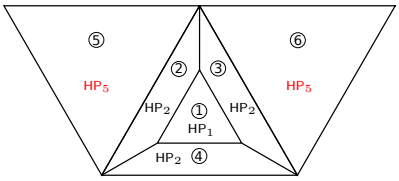

Cell ID	Mask	j	$i=5$	$k=2$
1	FALSE	–		
2	FALSE	0		
3	FALSE	1		
4	FALSE	2		
5	FALSE	-1		
6	FALSE	-1		

All cells in the grid are explored and marked as FALSE. Update hyper-plane indices $\mathsf{HP}_i = \mathsf{HP}_{i+j}$ for cells with defined color number j (*Welsh-Powell algorithm performed on* HP_5 *without being expanded here in detail to avoid repetition*)

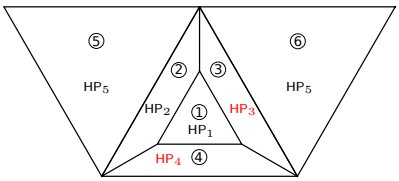

Cell ID	Mask	j	$i=5$	$k=0$
1	FALSE	–		
2	FALSE	0		
3	FALSE	1		
4	FALSE	2		
5	FALSE	0		
6	FALSE	0		

The six-cell grid is reordered into 5 hyper-planes. No edge-neighbors found in any hyper-plane. □

Figure 2.4: Illustration of the current grid reordering procedure on a simplified unstructured grid, starting from a single-cell HP_1.

2.7 Boundary Conditions

2.7.1 Boundary Numerical Flux

In this section, we discuss the computation of boundary numerical flux $\underline{F}_{G_{ij}}^{\mathrm{BC,NUM}}$ through the resolution of boundary Riemann problem [32, 67]. To begin with, we distinguish three distinct states that define a boundary Riemann problem as shown in Fig. 2.5 :

(i). Interior state, denoted by $(\cdot)_i$, is the extrapolated state from the interior computational domain, equivalent to the right state $(\cdot)_R$ in the standard Riemann problem (Section. 2.4)

(ii). Boundary state, denoted by $(\cdot)_{\mathtt{BC}}$, is associated with all boundary variables imposed regardless of the solution in the interior computational domain

(iii). Exterior state, denoted by $(\cdot)_j$, is equivalent to the left state $(\cdot)_L$ in the standard Riemann problem. For every boundary condition we have $\underline{V}_j := \underline{V}_j(\underline{V}_i, \underline{V}_{\mathtt{BC}})$ and $\underline{U}_j := \underline{U}_j(\underline{U}_i, \underline{U}_{\mathtt{BC}})$.

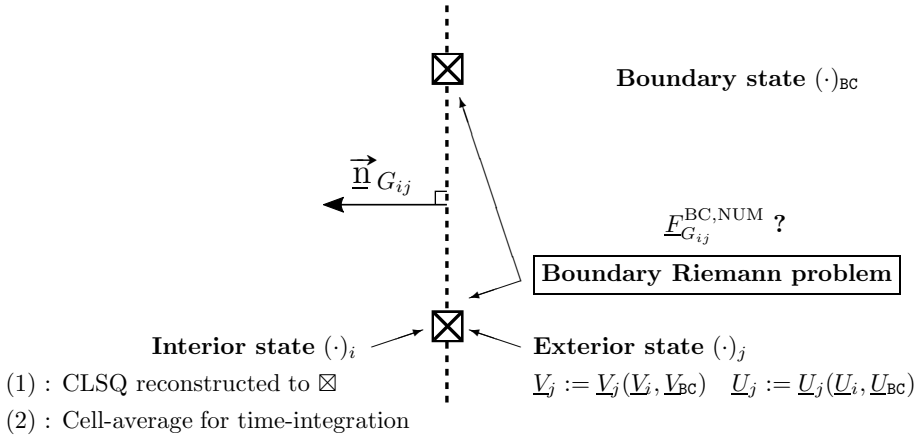

Figure 2.5: Boundary treatment in the current study, ⊠ are the Gauss-Legendre quadrature points on the boundary edge.

As illustrated in Fig. 2.5, we solve a Riemann problem at each boundary quadrature point based on the interior and exterior state variables. To clarify on the terminology, notations "interior state" and "exterior state" are used instead of "left state" and "right state" in the context of boundary Riemann problem. Left and right states are relative to the edge-normal vector $\vec{\underline{n}}_{G_{ij}}$, and since the boundary normal vectors in the current code are always inward-pointing, the terms "interior" and "exterior" states give a better representation of the flow physics.

The boundary Riemann problem is similar to the standard "interior" Riemann problem discussed in Section. 2.4 and the only difference between them lies in the computation of exterior state [5] variables. For the interior Riemann problem, both left and right state variables are reconstructed by the high-order polynomials defined within the two stencils associated with E_i and E_j (*i.e.*, S_i and S_j). However, for the boundary Riemann problem, $\underline{V}_j$ and $\underline{U}_j$ are calculated

[5] In the context of interior Riemann problem, the "exterior state" is a relative concept, it can be either the left or the right state depending on which cell is considered the reference

directly based on the specific boundary condition relations, as shown in Fig. 2.5. In both cases, the point-wise fluxes need to be numerically integrated over quadrature points on edge G_{ij}

$$\begin{aligned}\underline{F}_{G_{ij}}^{\mathrm{BC,NUM}} &= \underline{F}_{G_{ij}}^{\mathrm{c,BC,NUM}} + \underline{F}_{G_{ij}}^{\mathrm{v,BC,NUM}} \\ &= \sum_{k=1}^{\bar{N}_{\boxtimes}} w_{\boxtimes_k} \underline{F}^{\mathrm{c,BC,NUM}} \left(\underline{U}_{i_{\boxtimes_k}}, [\mathrm{grad}\underline{U}]_{i_{\boxtimes_k}}, \underline{U}_{j_{\boxtimes_k}}, [\mathrm{grad}\underline{U}]_{j_{\boxtimes_k}}, \vec{\mathrm{n}}_{\boxtimes_k} \right) \\ &+ \sum_{k=1}^{\bar{N}_{\boxtimes}} w_{\boxtimes_k} \underline{F}^{\mathrm{v,BC,NUM}} \left(\underline{U}_{i_{\boxtimes_k}}, [\mathrm{grad}\underline{U}]_{i_{\boxtimes_k}}, \underline{U}_{j_{\boxtimes_k}}, [\mathrm{grad}\underline{U}]_{j_{\boxtimes_k}}, \vec{\mathrm{n}}_{\boxtimes_k} \right)\end{aligned} \tag{2.112}$$

where the interior state variables $\underline{U}_{i_{\boxtimes_k}}$ and their gradients $[\mathrm{grad}\underline{U}]_{i_{\boxtimes_k}}$ are reconstructed to each boundary quadrature by CLSQ schemes (Section 2.3) for computations of high-order numerical fluxes $\underline{F}_{G_{ij}}^{\mathrm{BC,NUM}}$, the j index represents in this case the exterior state instead of the neighbor cell E_j. The all-Mach corrected AM-HLLC Riemann solver is used to compute the convective flux $\underline{F}_{G_{ij}}^{\mathrm{c,BC,NUM}}$ while the viscous flux $\underline{F}_{G_{ij}}^{\mathrm{v,BC,NUM}}$ is averaged between the interior and exterior states

$$\begin{aligned}&\underline{F}^{\mathrm{v,BC,NUM}} \left(\underline{U}_{i_{\boxtimes_k}}, [\mathrm{grad}\underline{U}]_{i_{\boxtimes_k}}, \underline{U}_{j_{\boxtimes_k}}, [\mathrm{grad}\underline{U}]_{j_{\boxtimes_k}}, \vec{\mathrm{n}}_{\boxtimes_k} \right) = \\ &\frac{1}{2} \left[\underline{F}^{\mathrm{v,BC,NUM}} \left(\underline{U}_{i_{\boxtimes_k}}, [\mathrm{grad}\underline{U}]_{i_{\boxtimes_k}}, \vec{\mathrm{n}}_{\boxtimes_k} \right) + \underline{F}^{\mathrm{v,BC,NUM}} \left(\underline{U}_{j_{\boxtimes_k}}, [\mathrm{grad}\underline{U}]_{j_{\boxtimes_k}}, \vec{\mathrm{n}}_{\boxtimes_k} \right) \right]\end{aligned} \tag{2.113}$$

where the exterior state gradients $[\mathrm{grad}\underline{U}]_{j_{\boxtimes_k}}$ are assumed to be identical to their interior state counterparts $[\mathrm{grad}\underline{U}]_{j_{\boxtimes_k}} = [\mathrm{grad}\underline{U}]_{i_{\boxtimes_k}}$. From Section. 2.7.2 to Section. 2.7.6, specific BC relations between $\underline{V}_i$ and $\underline{V}_j$ are given, which serve to determine $\underline{U}_{j_{\boxtimes_k}}$ and to complete the boundary numerical flux computation.

During the implicit time-integration, the interior state at each boundary quadrature point takes directly the cell-averaged variables of the parent cell, and the exterior state takes the cell-averaged variables from a fictitious cell E_j mirror-symmetrical to E_i about edge G_{ij}. The first-order-accurate boundary-reformulated Lax-Friedrichs flux $\underline{F}_{G_{ij}}^{\mathrm{BC,APP}}$ (see Eqn. 2.86) is used for the implicit time-discretization. Boundary treatment for implicit time-integration scheme is discussed in detail in Section. 2.5 and we shall not repeat in the current section. From Section. 2.7.2 to Section. 2.7.6, the Jacobian matrix $\underline{\underline{\mathbf{J}}}'_{ij}$ in Eqn. 2.93 is given for relatively simple boundary conditions which can be applied directly for implicit time-integration.

2.7.2 Adiabatic No-slip Wall

Special care needs to be taken for no-slip wall BCs, since they require different treatments for the computations of $\underline{F}_{G_{ij}}^{\mathrm{BC,NUM}}$ and $\underline{F}_{G_{ij}}^{\mathrm{BC,APP}}$. For the high-order boundary flux $\underline{F}_{G_{ij}}^{\mathrm{BC,NUM}}$

$$\underline{V}_j(\underline{V}_i, \underline{V}_{\mathrm{BC}}) = \begin{bmatrix} \rho_i \\ u_i \\ v_i \\ p_i \end{bmatrix} \tag{2.114}$$

while for the first-order $\underline{F}_{G_{ij}}^{\mathrm{BC,APP}}$, the cell-averaged velocity components in the fictitious cell E_j $\langle u \rangle_{E_j}$ and $\langle v \rangle_{E_j}$ are set opposite to those in cell E_i to ensure a zero approximation of the velocity vector on edge G_{ij}

$$\langle \underline{V} \rangle_{E_j}(\langle \underline{V} \rangle_{E_i}, \underline{V}_{\mathrm{BC}}) = \begin{bmatrix} \langle \rho \rangle_{E_i} \\ -\langle u \rangle_{E_i} \\ -\langle v \rangle_{E_i} \\ \langle p \rangle_{E_i} \end{bmatrix} \tag{2.115}$$

Based on Eqn. 2.115, we obtain $\underline{\underline{\mathbf{J}}}'_{ij}$

$$\underline{\underline{\mathbf{J}}}'_{ij} := \frac{\partial \langle \underline{V} \rangle_{E_j}}{\partial \langle \underline{V} \rangle_{E_i}} = \begin{bmatrix} 1 & 0 & 0 & 0 \\ 0 & -1 & 0 & 0 \\ 0 & 0 & -1 & 0 \\ 0 & 0 & 0 & 1 \end{bmatrix}. \tag{2.116}$$

2.7.3 Isothermal No-slip Wall

When a wall is defined as isothermal, we assign to it a constant temperature T_w. Since we always impose Neumann type boundary condition for pressure, we let $p_j = p_i$, and by following the ideal gas law, $\rho_j = p_i/(R_g T_w)$, where R_g is the specific gas constant $[\mathrm{J} \cdot \mathrm{kg}^{-1} \cdot \mathrm{K}^{-1}]$. Thus we have for the high-order flux $\underline{F}_{G_{ij}}^{\mathrm{BC,NUM}}$

$$\underline{V}_j(\underline{V}_i, \underline{V}_{\mathrm{BC}}) = \begin{bmatrix} \frac{p_i}{R_g T_w} \\ u_i \\ v_i \\ p_i \end{bmatrix} \tag{2.117}$$

while for the first-order $\underline{F}_{G_{ij}}^{\mathrm{BC,APP}}$

$$\langle \underline{V} \rangle_{E_j}(\langle \underline{V} \rangle_{E_i}, \underline{V}_{\mathrm{BC}}) = \begin{bmatrix} \frac{\langle p \rangle_{E_i}}{R_g T_w} \\ -\langle u \rangle_{E_i} \\ -\langle v \rangle_{E_i} \\ \langle p \rangle_{E_i} \end{bmatrix} \tag{2.118}$$

Based on Eqn. 2.117, we obtain $\underline{\underline{\mathbf{J}}}'_{ij}$

$$\underline{\underline{\mathbf{J}}}'_{ij} := \frac{\partial \langle \underline{V} \rangle_{E_j}}{\partial \langle \underline{V} \rangle_{E_i}} = \begin{bmatrix} 0 & 0 & 0 & \frac{1}{R_g T_w} \\ 0 & -1 & 0 & 0 \\ 0 & 0 & -1 & 0 \\ 0 & 0 & 0 & 1 \end{bmatrix}. \tag{2.119}$$

Apart from the two no-slip wall BCs (Section. 2.7.2 and Section. 2.7.3), other BCs (sections 2.7.4-2.7.6) treat the low- and high-order numerical fluxes with the same BC relations.

2.7.4 Riemann Invariant Inflow and Outflow

The Riemann invariant boundary condition is generally employed as the far-field boundary condition in the case of external aerodynamics (airfoil, *etc.*). The exterior state variables $\underline{V}_j$ are determined by combining information from interior and boundary states. Depending on the local Mach number and flow direction at inlet, the incoming ($\mathcal{R}^+$) and outgoing ($\mathcal{R}^-$) Riemann invariants are calculated based on the interior or boundary state variables, such that

$$\begin{aligned}
&\text{if} \quad M_i \leq -1 \qquad \text{(supersonic outflow)} \quad : \mathcal{R}^+ = V_{n_i} + \frac{2a_i}{\gamma - 1} \quad , \quad \mathcal{R}^- = V_{n_i} - \frac{2a_i}{\gamma - 1} \\
&\text{if} \quad M_i \geq 1 \qquad \text{(supersonic inflow)} \quad : \mathcal{R}^+ = V_{n_\infty} + \frac{2a_\infty}{\gamma - 1} \quad , \quad \mathcal{R}^- = V_{n_\infty} - \frac{2a_\infty}{\gamma - 1} \\
&\text{else} \qquad\qquad\ \text{(subsonic)} \quad\ : \mathcal{R}^+ = V_{n_\infty} + \frac{2a_\infty}{\gamma - 1} \quad , \quad \mathcal{R}^- = V_{n_i} - \frac{2a_i}{\gamma - 1}
\end{aligned} \tag{2.120}$$

where $M_i = \frac{V_{n_i}}{a_i}$, and $c = \sqrt{\frac{\gamma p}{\rho}}$. Note that the face normal unit vector $\vec{\mathrm{n}}$ always points inward (for codes having outward-pointing normal vectors, the $+/-$ signs in Eqn. 2.120 are reversed). For all three cases above

$$V_{n_j} = \frac{1}{2}(\mathcal{R}^+ + \mathcal{R}^-), \quad T_j = \frac{\left[\frac{\gamma-1}{4}(\mathcal{R}^+ - \mathcal{R}^-)\right]^2}{\gamma R} \tag{2.121}$$

where V_{n_j} and T_j are the normal velocity and temperature in the exterior state $\underline{V}_j$.

Depending on the sign of V_{n_i} (whether the local flow is entering or exiting the domain), the exterior state velocity vector $\vec{V}_j$ is computed accordingly by assuming that the tangential velocity remains constant from interior to exterior state.

$$\vec{V}_j = \begin{cases} \vec{V}_i \ + (V_{n_j} - V_{n_i}\ )\vec{\mathrm{n}} & \text{if} \quad V_{n_i} < 0 \quad \text{(outflow)} \\ \vec{V}_\infty + (V_{n_j} - V_{n_\infty})\vec{\mathrm{n}} & \text{if} \quad V_{n_i} > 0 \quad \text{(inflow)} \end{cases} \tag{2.122}$$

Exterior state density and pressure are determined by isentropic relations

$$\rho_j = \begin{cases} \rho_i \ \left(\frac{T_j}{T_i}\right)^{\frac{1}{\gamma-1}} & \text{if} \quad V_{n_i} < 0 \quad \text{(outflow)} \\ \rho_\infty \left(\frac{T_j}{T_\infty}\right)^{\frac{1}{\gamma-1}} & \text{if} \quad V_{n_i} > 0 \quad \text{(inflow)} \end{cases} \tag{2.123}$$

$$p_j = \begin{cases} p_i \left(\frac{T_j}{T_i}\right)^{\frac{\gamma}{\gamma-1}} & \text{if} \quad V_{n_i} < 0 \quad \text{(outflow)} \\ p_\infty \left(\frac{T_j}{T_\infty}\right)^{\frac{\gamma}{\gamma-1}} & \text{if} \quad V_{n_i} > 0 \quad \text{(inflow)} \end{cases} \tag{2.124}$$

The definition of primitive variables in the exterior state for Riemann invariant boundary condition depends on the local flow. We distinguish four cases: supersonic inflow (`supIn`), supersonic outflow (`supOut`), subsonic inflow (`subIn`), and subsonic outflow (`subOut`).

2.7.4.1 Supersonic Inflow

From equations 2.120 - 2.124 we obtain the expressions of exterior state primitive variables for supersonic inflows

$$\underline{V}_j^{(\texttt{supIn})}(\underline{V}_i, \underline{V}_{\text{BC}}) = \begin{bmatrix} \rho_\infty \\ u_\infty \\ v_\infty \\ p_\infty \end{bmatrix} \tag{2.125}$$

Based on Eqn. 2.125, we obtain $\underline{\underline{\mathbf{J}}}_{ij}^{\prime(\texttt{supIn})}$

$$\underline{\underline{\mathbf{J}}}_{ij}^{\prime(\texttt{supIn})} = 0. \tag{2.126}$$

It is clear that, when the local flow is entering the domain at supersonic normal velocity, the exterior state $\underline{V}_j^{(\texttt{supIn})}$ depends entirely on the infinity state, not on the interior state $\underline{V}_i$. Therefore, it is evident that the Jacobian $\underline{\underline{\mathbf{J}}}_{ij}^{\prime(\texttt{supIn})}$ is a zero matrix. The underlying physical significance is that the infinity state remains constant.

2.7.4.2 Supersonic Outflow

Similarly, from equations 2.120 - 2.124 we obtain

$$\underline{V}_j^{(\texttt{supOut})}(\underline{V}_i, \underline{V}_{\text{BC}}) = \begin{bmatrix} \rho_i \\ u_i \\ v_i \\ p_i \end{bmatrix} \tag{2.127}$$

Based on Eqn. 2.127, we obtain $\underline{\underline{\mathbf{J}}}_{ij}^{\prime(\texttt{supOut})}$

$$\underline{\underline{\mathbf{J}}}_{ij}^{\prime(\texttt{supOut})} = \underline{\underline{\mathbf{I}}}. \tag{2.128}$$

Conversely, the exterior state $\underline{V}_j^{(\texttt{supOut})}$ in the supersonic outflow case depends entirely on the interior state, not on the infinity state. Therefore, the Jacobian $\underline{\underline{\mathbf{J}}}_{ij}^{\prime(\texttt{supOut})}$ is an identity matrix.

2.7.4.3 Subsonic Inflow/Outflow

For subsonic Riemann invariant condition, the exterior state variables are computed by equations 2.120 - 2.124

$$\underline{V}_j^{(\texttt{subIn})}(\underline{V}_i, \underline{V}_{\text{BC}}) = \begin{bmatrix} \rho_\infty \left(T_j/T_\infty\right)^{\frac{1}{\gamma-1}} \\ u_\infty + (V_{n_j} - V_{n_\infty})\mathrm{n}_x \\ v_\infty + (V_{n_j} - V_{n_\infty})\mathrm{n}_y \\ p_\infty \left(T_j/T_\infty\right)^{\frac{\gamma}{\gamma-1}} \end{bmatrix} \tag{2.129}$$

$$\underline{V}_j^{(\texttt{subOut})}(\underline{V}_i, \underline{V}_{\text{BC}}) = \begin{bmatrix} \rho_i \left(T_j/T_i\right)^{\frac{1}{\gamma-1}} \\ u_i + (V_{n_j} - V_{n_i})\mathrm{n}_x \\ v_i + (V_{n_j} - V_{n_i})\mathrm{n}_y \\ p_i \left(T_j/T_i\right)^{\frac{\gamma}{\gamma-1}} \end{bmatrix}. \tag{2.130}$$

The expressions of corresponding Jacobians $\underline{\underline{\mathbf{J}}}'^{(\texttt{subIn})}_{ij}$ and $\underline{\underline{\mathbf{J}}}'^{(\texttt{subOut})}_{ij}$ become extremely cumbersome due to the involvement of incoming and outgoing Riemann invariants $\mathcal{R}^{\pm}$. Their complete expressions can be obtained by performing partial differentiation in a Computer Algebra System (CAS) such as Maxima or Mathematica.

2.7.5 Reservoir Inflow

The reservoir inflow boundary condition is characterized by constant total enthalpy H_t and outgoing Riemann invariant $\mathcal{R}^-$. The flow is adiabatic and isentropic across the boundary interface with an inward-pointing normal vector $\vec{\mathrm{n}}$.

$$H_t = \frac{a_j^2}{\gamma - 1} + \frac{1}{2}(V_{n_j}^2 + V_{t_j}^2) = \frac{a_t^2}{\gamma - 1} \tag{2.131}$$

where $V_{t_j} := \vec{V}_j \cdot \vec{\mathrm{t}}$ and $\vec{\mathrm{t}}$ is the unit face-tangential vector at inlet boundary. Note that the tangential velocity component remains constant across boundary interface, therefore exterior state V_{t_j} can be replaced by the boundary state $V_{t_{\text{BC}}} = \vec{V}_{\text{BC}} \cdot \vec{\mathrm{t}}$. a_t is the total speed of sound computed based on the total temperature and Mach number in the boundary state

$$a_t = \sqrt{\gamma R_g T_t} \tag{2.132}$$

$$T_t = T_{\text{BC}} \left[1 + \frac{M_{\text{BC}}(\gamma - 1)}{2}\right] \tag{2.133}$$

$$M_{\text{BC}} = \frac{\sqrt{u_{\text{BC}}^2 + v_{\text{BC}}^2}}{a_{\text{BC}}} = \sqrt{\frac{u_{\text{BC}}^2 + v_{\text{BC}}^2}{\gamma p_{\text{BC}}/\rho_{\text{BC}}}}. \tag{2.134}$$

The expression of outgoing Riemann invariant $\mathcal{R}^-$ is given in Eqn. 2.120, and since $\mathcal{R}^-$ is conserved along the path between interior and exterior states, it can be expressed in terms of the

exterior state variables

$$\mathcal{R}^- = V_{n_j} - \frac{2a_j}{\gamma - 1} \tag{2.135}$$

which gives

$$\frac{a_j^2}{\gamma - 1} = \frac{(\gamma - 1)(V_{n_j} - \mathcal{R}^-)^2}{4}. \tag{2.136}$$

By inserting Eqn. 2.136 back into Eqn. 2.131 we obtain a quadratic equation with respect to V_{n_j}

$$\frac{V_{n_j}^2}{2} + K_1 V_{n_j} + \frac{K_2}{2} = 0 \tag{2.137}$$

where

$$K_1 = -\frac{(\gamma - 1)\mathcal{R}^-}{\gamma + 1} \quad K_2 = \frac{(\gamma - 1)\left[\mathcal{R}^{-^2} + \frac{2t_{\text{BC}}^2}{\gamma - 1} - \left(\frac{2a_t}{\gamma - 1}\right)^2\right]}{\gamma + 1}$$

with $\mathcal{R}^-$ being rewritten by replacing exterior state variables in Eqn. 2.135 by interior state variables

$$\mathcal{R}^- = V_{n_i} - \frac{2a_i}{\gamma - 1}.$$

Coefficients K_1 and K_2 are therefore both known based on interior and boundary variables, which allows Eqn. 2.137 to be solved. For the solution to be physically consistent, we either retain the largest positive root or set V_{n_j} to zero

$$V_{n_j} = \max(0, -K_1 + \sqrt{K_1^2 - K_2}). \tag{2.138}$$

Once V_{n_j} is obtained, we can then determine the exterior state temperature T_j by inserting V_{n_j} into Eqn. 2.135

$$T_j = \frac{\left[\frac{\gamma - 1}{2}(V_{n_j} - \mathcal{R}^-)\right]^2}{\gamma R} \tag{2.139}$$

and exterior state density and pressure are deduced according to the isentropic relations

$$\begin{aligned} \rho_j &= \rho_{\text{BC}} \left(\frac{T_j}{T_{\text{BC}}}\right)^{\frac{1}{\gamma - 1}} \\ p_j &= p_{\text{BC}} \left(\frac{T_j}{T_{\text{BC}}}\right)^{\frac{\gamma}{\gamma - 1}}. \end{aligned} \tag{2.140}$$

Finally, the exterior state velocity is computed by admitting that the tangential component is kept constant between the boundary and exterior states

$$\vec{V}_j = \vec{V}_{\text{BC}} + (V_{n_j} - V_{n_{\text{BC}}})\vec{n}. \tag{2.141}$$

The exterior state variables

$$\underline{V}_j(\underline{V}_i, \underline{V}_{\text{BC}}) = \begin{bmatrix} \rho_{\text{BC}} \left(T_j/T_{\text{BC}}\right)^{\frac{1}{\gamma-1}} \\ u_{\text{BC}} + (V_{n_j} - V_{n_{\text{BC}}})\text{n}_x \\ v_{\text{BC}} + (V_{n_j} - V_{n_{\text{BC}}})\text{n}_y \\ p_{\text{BC}} \left(T_j/T_{\text{BC}}\right)^{\frac{\gamma}{\gamma-1}} \end{bmatrix}. \tag{2.142}$$

As with the subsonic Riemann invariant condition, the complete expression of Jacobian $\underline{\underline{\mathbf{J}}}'_{ij}$ for reservoir inflow also needs to be derived automatically by a Computer Algebra System (CAS).

Physically, the reservoir and the subsonic Riemann invariant inflow boundary conditions are very similar in the sense that they both assume the flow is isentropic across the boundary. However, the reservoir inl*et al*so imposes that the flow to be adiabatic (constant specific total enthalpy H_t), with the exterior state normal velocity component V_{n_j} and temperature T_j being computed based on this adiabatic assumption. The reservoir inflow condition is therefore more adapted for internal channel flows while Riemann invariant condition is more suitable for far-field of external flows.

2.7.6 Pressure Outflow

The pressure outflow boundary condition is widely implemented for internal channel flows. For a subsonic flow, the static pressure at outlet p_j is prescribed as p_o, whereas for a supersonic flow, all state variables are extrapolated from the interior state.

First, we determine the boundary pressure

$$p_j = \begin{cases} p_o & \text{if} \quad M_i < 1 \\ p_i & \text{if} \quad M_i \geq 1 \end{cases} \tag{2.143}$$

where $M_i = V_{n_i}/a_i$. The interior temperature is determined by the ideal gas law $T_i = p_i/(R_g\rho_i)$. The final expression of the exterior state is the following

$$\underline{V}_j(\underline{V}_i, \underline{V}_{\text{BC}}) = \begin{bmatrix} \frac{p_j}{R_g T_i} \\ u_i \\ v_i \\ p_j \end{bmatrix}. \tag{2.144}$$

Chapter 3

Evaluation of Computational Methods

3.1 Evaluation of Implicit Schemes

In this section, test results are compiled to compare the performances of the implicit pseudo dual-time-stepping scheme with the three implicit schemes mentioned in Section. 2.5, the iterative Jacobian scheme, BLU-SGS schemes [42], and the approximately factored LU-SGS scheme [117]. Tests are performed on a laminar backward-facing step configuration first introduced by Armaly *et al.* [13]. Again, we refer to Section. 4.2 Fig. 4.1 for a detailed description of the test-case configuration. The Reynolds number for this test-case is computed based on the bulk streamwise velocity at inlet u_B and the hydraulic diameter of the inlet channel $D_h = 2H_i$ and is denoted by the two-subscript notation $Re_{\text{vel,len}}$ where the velocities and lengths are listed in Tab. 4.1

$$Re_{u_B,D_h} = \frac{u_B D_h}{\nu} = \frac{2u_B H_i}{\nu}. \tag{3.1}$$

Experimental results [13] place the laminar flow regime at $Re_{u_B,D_h} < 1200$. For the purpose of evaluating different implicit solvers, we confine ourselves to the laminar regime by showing convergence results at three Reynolds numbers $Re_{u_B,D_h} = 100, 389, 1000$. Within the laminar regime, as the Reynolds number increases, the reattachment length x_1 becomes longer which leads to a larger recirculation zone (see Fig. 4.1). *A priori*, test cases at higher Reynolds number is more difficult to converge due to increased recirculation lengths and non-linearity, therefore the laminar BFS presents itself as a relevant test-case to evaluate the performance of the current implicit scheme, since the purpose of using pseudo dual-time-stepping is to better account for the non-linearity in the solution, which cannot be achieved by simply implementing iterative linear solvers. In the following study, we will investigate the performances of the dual-time-stepping version of Jacobi, BLU-SGS, and LU-SGS implicit schemes discussed in Section. 2.5 as well as how they interact with the flow physics and high-order spatial discretization schemes.

3.1.1 Iterative Error and Reduction

Instead of using fixed numbers of inner and linear iterations (static approach), the dynamic approach is used to terminate each iterative procedure based on fixed threshold relative error ε^* or

reduction r^*. The dynamic approach is more general and robust than the static approach, which allows automatic adjustment of the required number of iterations for different test-cases depending on parameters such as grid size, time-step size, flow complexity, *etc.* Moreover, less iterations are needed when the solution is close to convergence which reduce the total computational time. For two-dimensional laminar flows.

Here we define the function of iterative error ε estimation for an arbitrary vector of 2D flow variables $\underline{Q} \in \mathbb{R}^4$ (can be $\underline{U}$, $\Delta\underline{U}$, *etc.*) at iteration $\ell \geq 1$ on N sampling units (cells, points, *etc.*)

$$ {}^{\ell}\varepsilon\left({}^{\ell}\underline{Q}, {}^{\ell+1}\underline{Q}\right) = \log_{10}\left\{\sqrt{\frac{1}{4}\left[\frac{\sum_{i=1}^{N} {}_i^{\ell}\Delta q_{\rho}^2}{\sum_{i=1}^{N} {}_i^{\ell} q_{\rho}^2} + \frac{\sum_{i=1}^{N}\left({}_i^{\ell}\Delta q_x^2 + {}_i^{\ell}\Delta q_y^2\right)}{\sum_{i=1}^{N}\left({}_i^{\ell} q_x^2 + {}_i^{\ell} q_y^2\right)} + \frac{\sum_{i=1}^{N} {}_i^{\ell}\Delta q_e^2}{\sum_{i=1}^{N} {}_i^{\ell} q_e^2}\right]}\right\} \tag{3.2} $$

where ${}^{\ell}\Delta q = {}^{\ell+1}q - {}^{\ell}q$, q_ρ is related to the continuity equation, q_x, q_y are related to the momentum equations and q_e is related to the energy equation. The iterative reduction r at the same iteration ℓ is given by

$$ {}^{\ell}r\left({}^{\ell}\varepsilon, {}^{\ell-1}\varepsilon\right) = \log_{10}\left[\frac{\left|10^{{}^{\ell}\varepsilon} - 10^{{}^{\ell-1}\varepsilon}\right|}{10^{{}^{\ell-1}\varepsilon}}\right] = \log_{10}\left|10^{{}^{\ell}\varepsilon} - 10^{{}^{\ell-1}\varepsilon}\right| - {}^{\ell-1}\varepsilon \tag{3.3} $$

where ${}^{0}\varepsilon = 0$ and therefore ${}^{1}r = \log_{10}\left|10^{{}^{1}\varepsilon} - 1\right| - 1$. The iterative reduction can be interpreted as the convergence of the iterative increment, characterizing the acceleration of solution towards convergence. The index ℓ is generic in the sense that equations 3.2 and 3.3 remain valid for an arbitrary iterative procedure, in the context of implicit dual-time-stepping, ℓ can be replaced by k (linear solver iteration), m (inner iteration), or n (outer iteration). However, in practice, the convergence is monitored differently for each iterative procedure :

1. linear solver k-iteration : ${}^{k}\varepsilon := {}^{k}\varepsilon\left({}^{k}\Delta\underline{U}, {}^{\ell+1}\Delta\underline{U}\right)$
2. inner m-iteration : ${}^{m}r := {}^{m}r\left({}^{m}\varepsilon, {}^{m-1}\varepsilon\right)$ with ${}^{m}\varepsilon := {}^{m}\varepsilon\left({}^{m}\underline{U}, {}^{m+1}\underline{U}\right)$
3. outer n-iteration : ${}^{n}\varepsilon := {}^{n}\varepsilon\left({}^{n}\underline{U}, {}^{n+1}\underline{U}\right)$

note that for LU-SGS linear solver, calculating ${}^{k}\varepsilon$ is meaningless since no linear iteration is needed. For both BLU-SGS and Jacobi schemes, the linear solver is terminated at the k^{th} iteration if ${}^{k}\varepsilon \leq \varepsilon^*$ where ε^* is a predefined threshold error. For all three time-integration schemes above, the dual pseudo time-stepping is terminated at the m^{th} pseudo-time-step if ${}^{m}r \leq r^*$ where r^* is a predefined threshold reduction.

In general, a test-case with more complex flow features (*e.g.* large separated region) or greater number of cells tends to require more k- and m-iterations to reach ε^* and r^*. Similarly, the required iterations also increase as the Courant number CFL grows since the residual term in Eqn. 2.88 is directly multiplied by the time-step size. In loose terms, ${}^{n}\varepsilon$ decreases in three characteristic phases : (1) oscillating descent down to approximately ${}^{n}\varepsilon \approx -4 \sim -5$; (2) smooth steady descent down to ${}^{n}\varepsilon \approx -8$; (3) slow asymptotic convergence for ${}^{n}\varepsilon < -8$. Each change of phase is often marked by a change of slope in the convergence history ${}^{n}\varepsilon(t)$. However, note that the three phases are not strictly defined in a mathematical sense, but rather in an empirical sense by observation [1].

[1] it is generally accepted that the slope is related to the dominant eigenvalue of the iterative error, therefore the change of slope indicates that a different magnitude of error is dominant, *e.g.*, a steep slope indicates a large-scale error while a gentle slope implies that the error is small-scale and remains local

Once the solution enters the last phase, further variation in the flow field becomes negligible and the solution is then considered converged. The precise locations of phase changes are controlled by various factors which differ considerably from case to case, and need to be determined visually for each individual test according to its convergence history. In practice, the solution is considered converged to a steady-state if any one of the following criteria is satisfied :

- the n-iteration error ${}^{n}\varepsilon \leq -8$
- the solution reaches the third smoothly descending convergence phase.

3.1.2 Backward-Facing Step at $Re_{u_B,D_h} = 100$

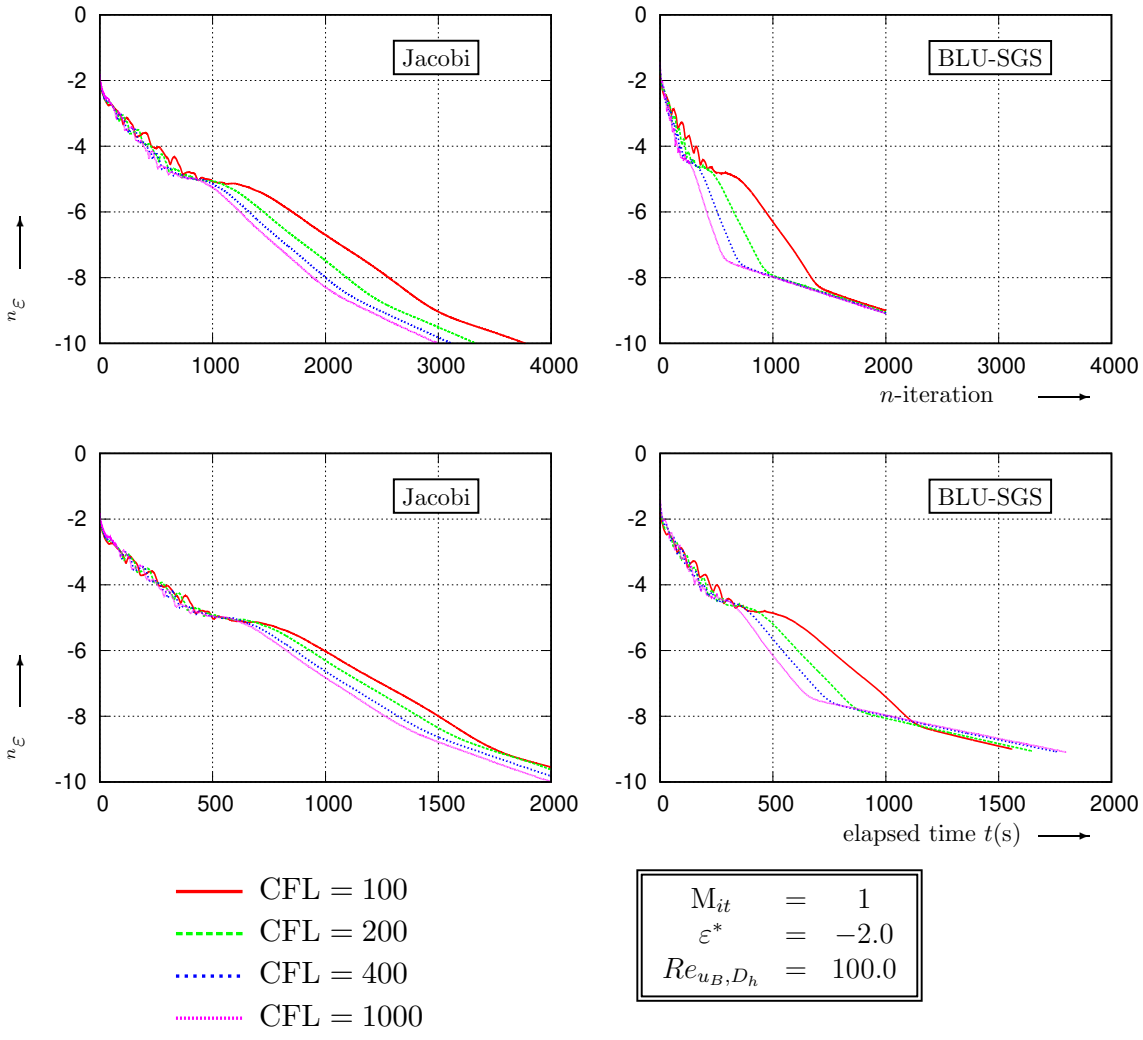

Figure 3.1: Convergence history using both Jacobi and BLU-SGS methods with different CFL at $Re_{u_B,D_h} = 100$.

At $Re_{u_B,D_h} = 100$, the reattachment length is relatively short, fast convergence can be achieved without dual time-stepping for both Jacobi and BLU-SGS methods. When increasing the Courant number CFL from 100 to 1000, as shown in Fig. 3.1, the convergence is accelerated. For a given CFL, solution reaches the last slow convergence phase faster using BLU-SGS than Jacobi method.

Different threshold linear errors ε^* are compared as shown in Fig. 3.2 using Jacobi method. With a high threshold error -1.0, the solutions diverge at the very beginning regardless of the CFL condition which indicates that the linear system is under-resolved. By decreasing ε^*, the linear system is properly resolved at $\varepsilon^* = -2.0$ and by further lowering ε^* down to -3.0, the solution enters the third phase of convergence at ${}^n\varepsilon \approx -7.5$ in less computational time. Although the convergence criterion is met slightly earlier with $\varepsilon^* = -3$, the iterative error is driven to a much lower level ${}^n\varepsilon = -10$ in less time with $\varepsilon^* = -2.0$, therefore, it is not evident to decide which one is a better choice. In practice, $\varepsilon^* = -3.0$ is retained as the optimal threshold linear error for Jacobi method, but we also admit $\varepsilon^* = -2.0$ as a valid choice. For test-cases where using $\varepsilon^* = -3.0$ tends to over-resolve the linear system, relaxing the threshold error up to $\varepsilon^* = -2.0$ can prove to be a robust solution.

Using BLU-SGS at CFL $= 400$, $\varepsilon^* = -2.0$ is clearly the optimal threshold linear error in terms of computational time as shown in Fig. 3.3. It is noteworthy that, for BLU-SGS method, the solution converges even with a high threshold linear error $\varepsilon^* = -1.0$ whereas Jacobi method fails under this condition. This is due to the fact that BLU-SGS implicitly takes into account the boundary conditions (Eqn. 2.93), knowing that ${}^n\varepsilon$ is computed based on the sum of conservative variable increments in the entire computational domain (Eqn. 3.2), it is clear that when Jacobi and BLU-SGS methods return identical ${}^n\varepsilon$, linear solution obtained by BLU-SGS at each time-step tends to respect more scrupulously the boundary conditions, which leads to better convergence with a relatively high ε^*.

Another observation is that BLU-SGS method over-resolves the linear system for a low threshold linear error $\varepsilon^* = -3.0$ and leads the solution to diverge at a high Courant number CFL $= 1000$ (curve *not* shown in Fig. 3.3).

To illustrate the performances of different linear solvers at $Re_{u_B,D_h} = 100$, the fastest converged test-case using each linear solver is shown in Fig. 3.4. The optimal threshold error has been found to be $\varepsilon^* = -2.0$ for BLU-SGS solver and $\varepsilon^* = -3.0$ for Jacobi solver. According to Fig. 3.4, BLU-SGS shows slightly faster convergence than Jacobi and both BLU-SGS and Jacobi methods demonstrate substantially enhanced convergence property comparing to the approximately factored LU-SGS method.

3.1.3 Backward-Facing Step at $Re_{u_B,D_h} = 389$

At $Re_{u_B,D_h} = 389$, the flow is approaching the upper limit of two-dimensionality dominance [13], the recirculation zone is enlarged and convergence is expected to be more difficult than the flow at $Re_{u_B,D_h} = 100$. BLU-SGS solver, from this Reynolds number onwards, starts to show higher sensitivity to the Courant number than Jacobi method and converged solution can only be obtained at Courant number less or equal to 200, whereas Jacobi method is always scalable up to CFL $= 1000$.

Cases with different threshold linear errors ε^* are compared at this Reynolds number in Fig. 3.6. As ε^* increases, Jacobi method shows the same trend as $Re_{u_B,D_h} = 100$: high $\varepsilon^* = -1.0$ causes the solution to diverge as expected and the optimal ε^* is found to be -3.0 as with $Re_{u_B,D_h} = 100$. Recall that for BLU-SGS method, $\varepsilon^* = -1.0$ is sufficient to ensure convergence at $Re_{u_B,D_h} = 100$ which still remains valid at this increased Reynolds number as shown in Fig. 3.6. Moreover, -2.0

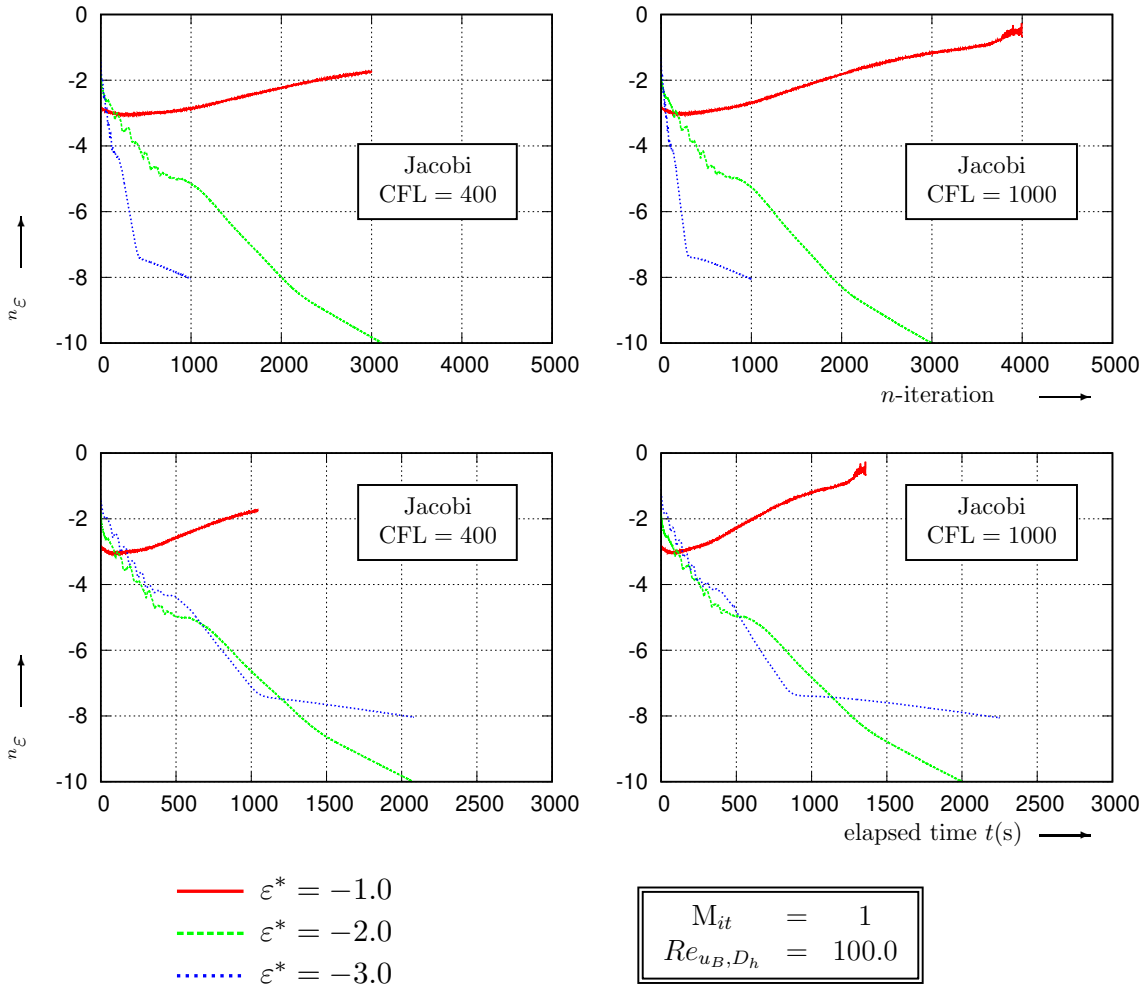

Figure 3.2: Convergence history using Jacobi method with different ε^* at $Re_{u_B,D_h} = 100$.

remains the optimal ε^* for BLU-SGS.

Fig. 3.7 shows the best performance comparison of BLU-SGS, Jacobi, and LU-SGS at $Re_{u_B,D_h} = 389$. With reduced Courant number, BLU-SGS solver with $\varepsilon^* = -2.0$ maintains only a marginal advantage over Jacobi method with $\varepsilon^* = -3.0$. LU-SGS results are given at two Courant numbers 1000 and 10000, since the two curves almost overlap, it is clear that the LU-SGS method is no longer scalable beyond CFL = 1000, and remains disadvantageous in computational time.

Compared with $Re_{u_B,D_h} = 100$, flow over the backward-facing step at $Re_{u_B,D_h} = 389$ takes slightly more computational time to reach convergence due to increased non-linearity and recirculation downstream of the step.

3.1.4 Backward-Facing Step at $Re_{u_B,D_h} = 1000$

At $Re_{u_B,D_h} = 1000$, flow approaches the upper limit of the laminar regime for the given configuration [13]. The reattachment length is almost at its peak value. Tests at this Reynolds number are

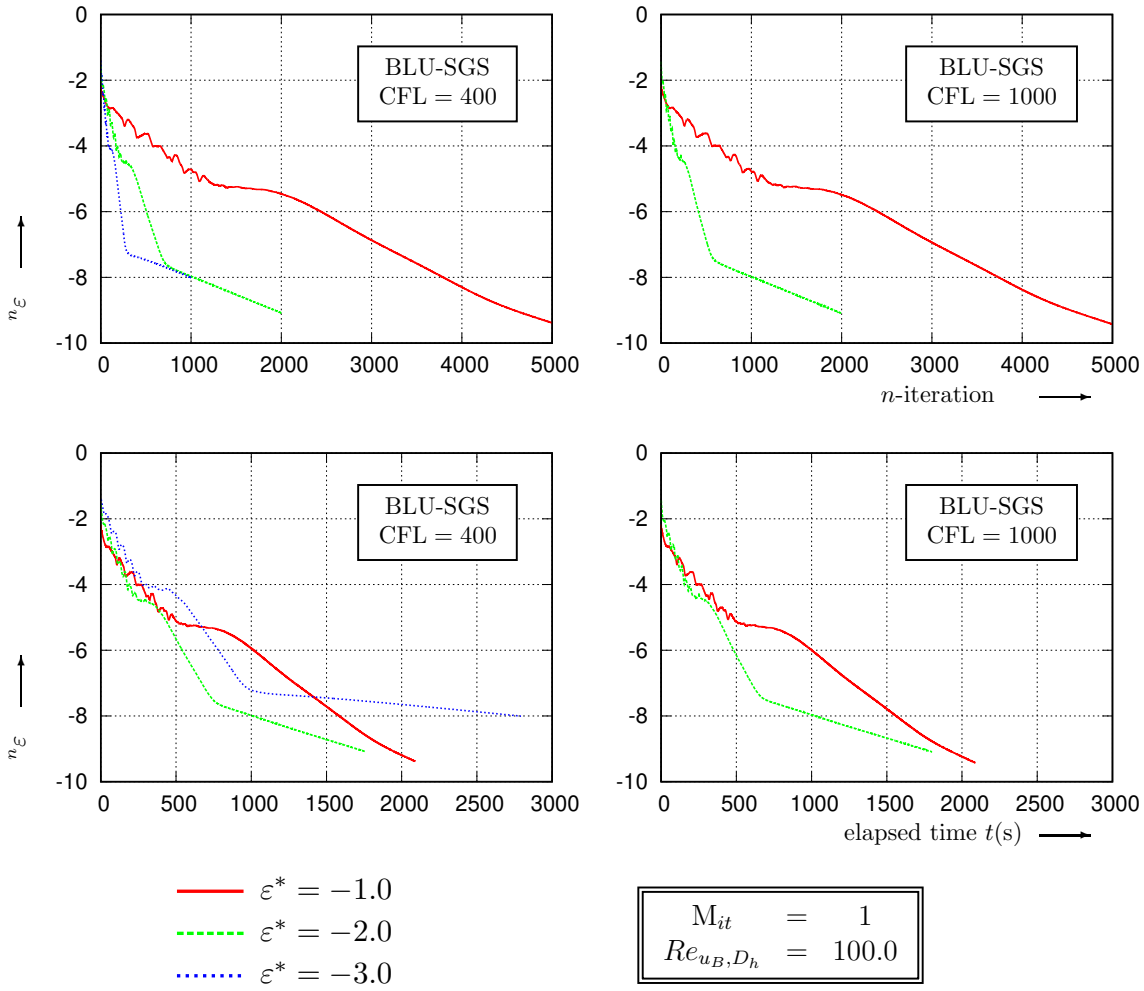

Figure 3.3: Convergence history using BLU-SGS method with different ε^* at $Re_{u_B,D_h} = 100$.

used to demonstrate the importance of dual time-stepping (m-iteration) when largely separated flow is encountered.

We first investigate the role played by the threshold non-linear reduction for the dual pseudo-time-stepping r^* on the convergence. For this purpose, we show the results obtained with Jacobi and BLU-SGS methods. As plotted in Fig. 3.8 and 3.9, when no pseudo-time-stepping (number of pseudo-time-step $M_{it} = 1$) is used, both Jacobi and BLU-SGS methods show no sigh of convergence within a reasonable amount of time.

By implementing DTS with Jacobi solver (Fig. 3.8), convergence is obtained with a threshold reduction $r^* = -0.5$ within 1000 n-iterations. As the reduction criterion becomes more stringent, the number of iterations needed to reach convergence remain almost unchanged while the computational time increases gradually with decreasing r^* from -0.5 to -1.5. However, despite longer computational time is required for $r^* = -1.5$, it can be preferred to $r^* = -0.5$ for general applications since the convergence is more likely to be guaranteed with a more stringent r^* condition.

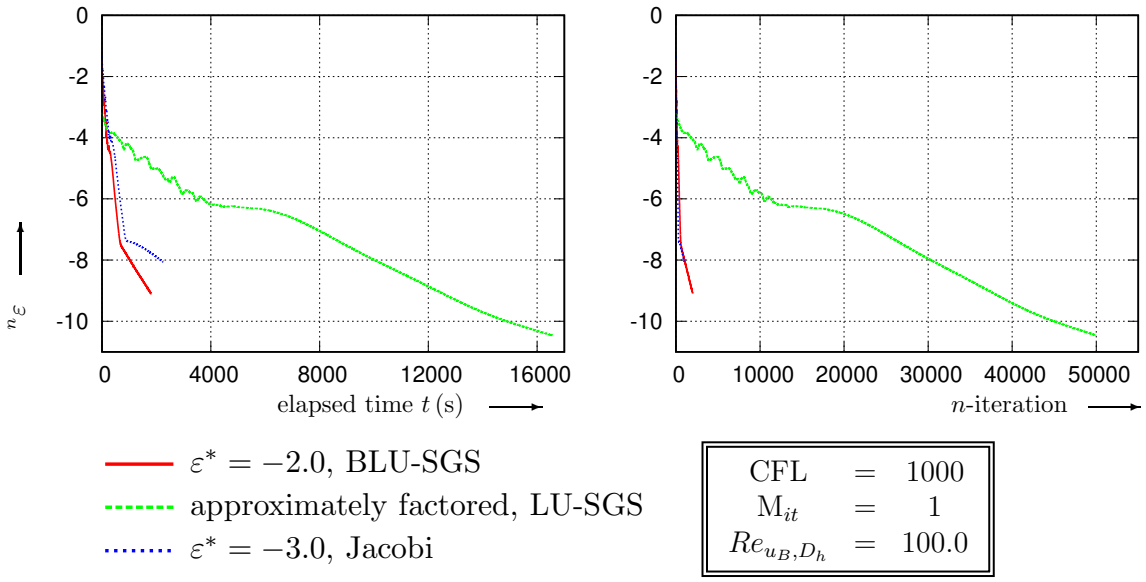

Figure 3.4: Convergence history comparison among Jacobi, BLU-SGS and LU-SGS methods at $Re_{u_B,D_h} = 100$.

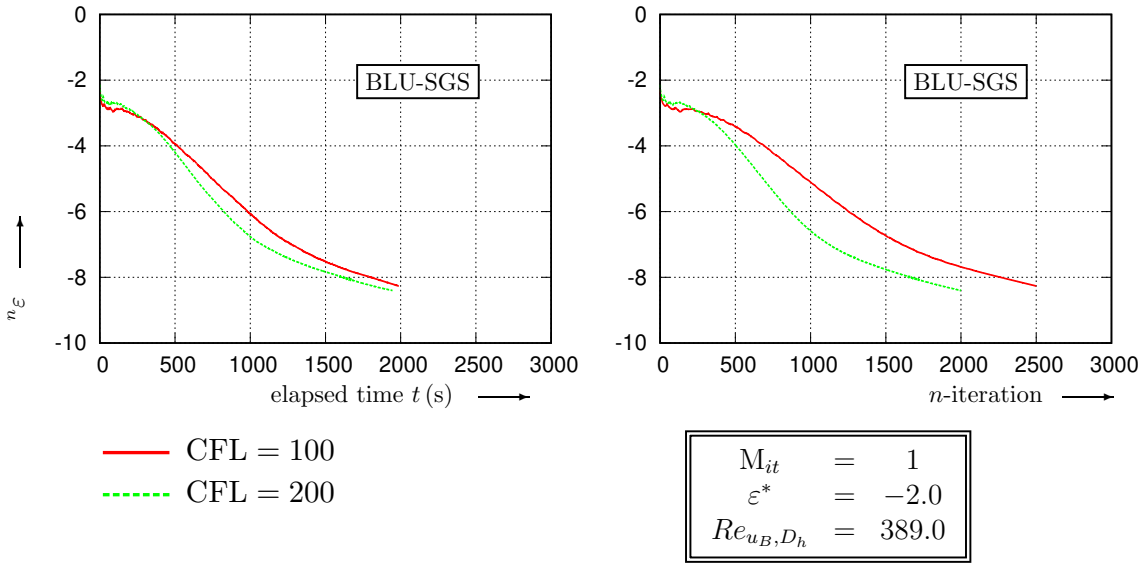

Figure 3.5: Comparison history using BLU-SGS method with different CFL at $Re_{u_B,D_h} = 389$.

With the BLU-SGS method, the convergence behavior is different from the Jacobi method with regard to r^*. When r^* is set to -0.5, the convergence history oscillates but fails to converge with a very high $\text{CFL}^* = 10^{13}$ and a low $\text{CFL}^* = 100$ is required to obtain convergence as shown in

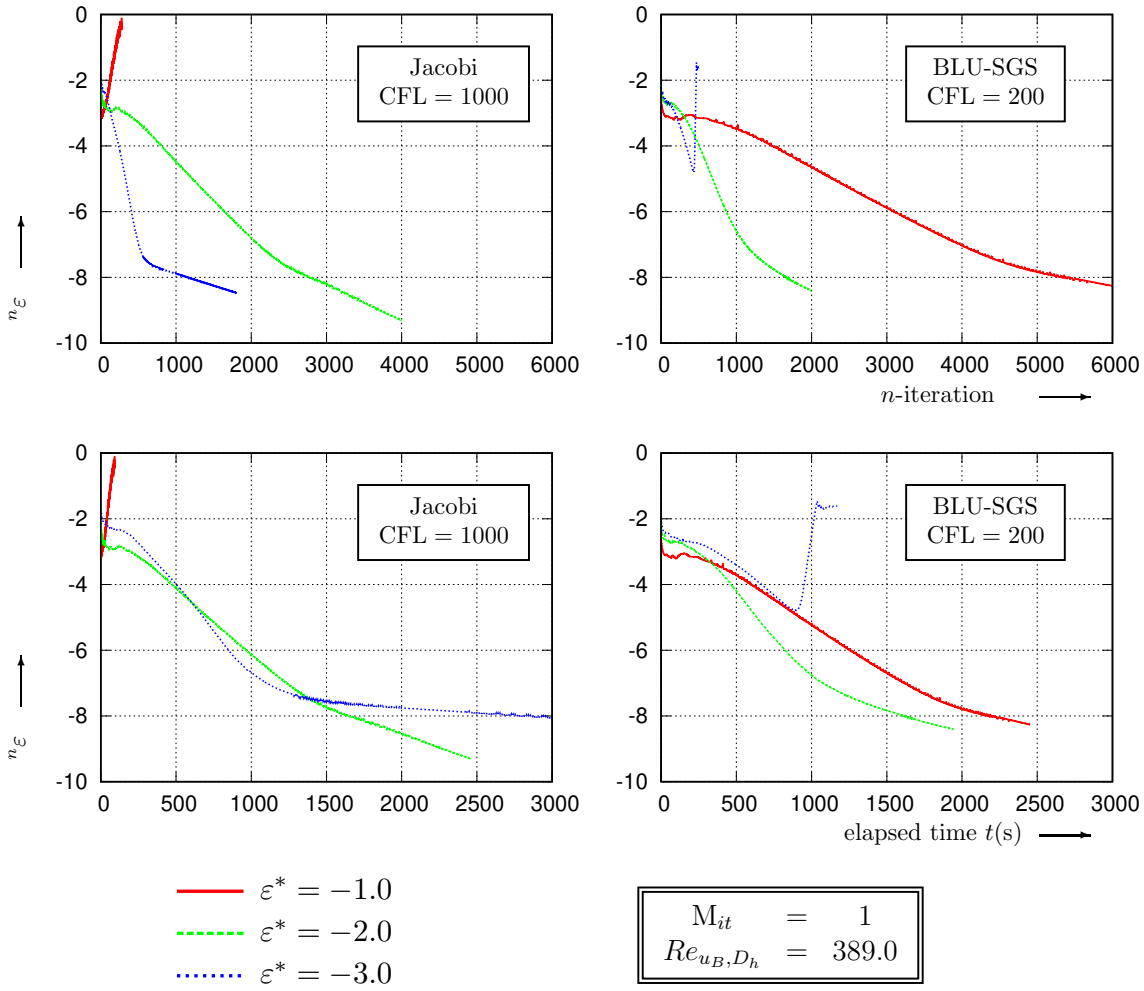

Figure 3.6: Convergence history using both Jacobi and BLU-SGS methods with different ε^* at $Re_{u_B,D_h} = 389$.

Fig. 3.10. However, by decreasing the threshold r^* to -1.0, the BLU-SGS solution manages to converge to $^n\varepsilon = -8.0$ within 15000s wall-time using the same processing power which is a tenfold increase in convergence time required comparing to the low-Reynolds case at $Re_{u_B,D_h} = 100$ (Fig. 3.4). By further bringing down the threshold reduction to $r^* = -1.5$, although convergence can eventually be achieved, the system is visibly over-resolved and the iterative error descends with an extremely low rate and it requires approximately 8 times as much computational time and 6 times as many n-iterations as using $r^* = -1.0$. Therefore, it is evident that $r^* = -1.0$ is the optimal threshold reduction for DTS with BLU-SGS method at $Re_{u_B,D_h} = 1000$ and using linear iterations alone is insufficient for BFS flows at high Reynolds number with strong recirculation. Note that at this high Reynolds number, the maximum possible Courant number for BLU-SGS is further reduced to 100 while that of Jacobi method is maintained at 1000.

Since the necessity of dual pseudo-time-steps is established, the scalability with respect to the dual Courant number CFL* needs to be viewed. As shown in Fig. 3.11, faster convergence is

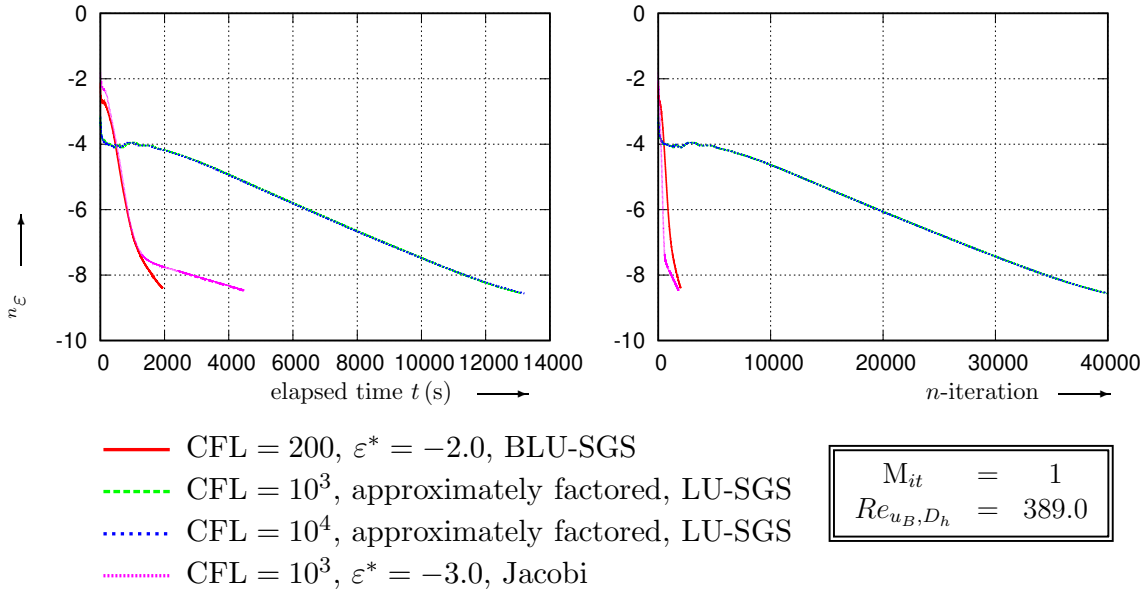

Figure 3.7: Convergence history comparison among Jacobi, BLU-SGS and LU-SGS methods at $Re_{u_B,D_h} = 389$.

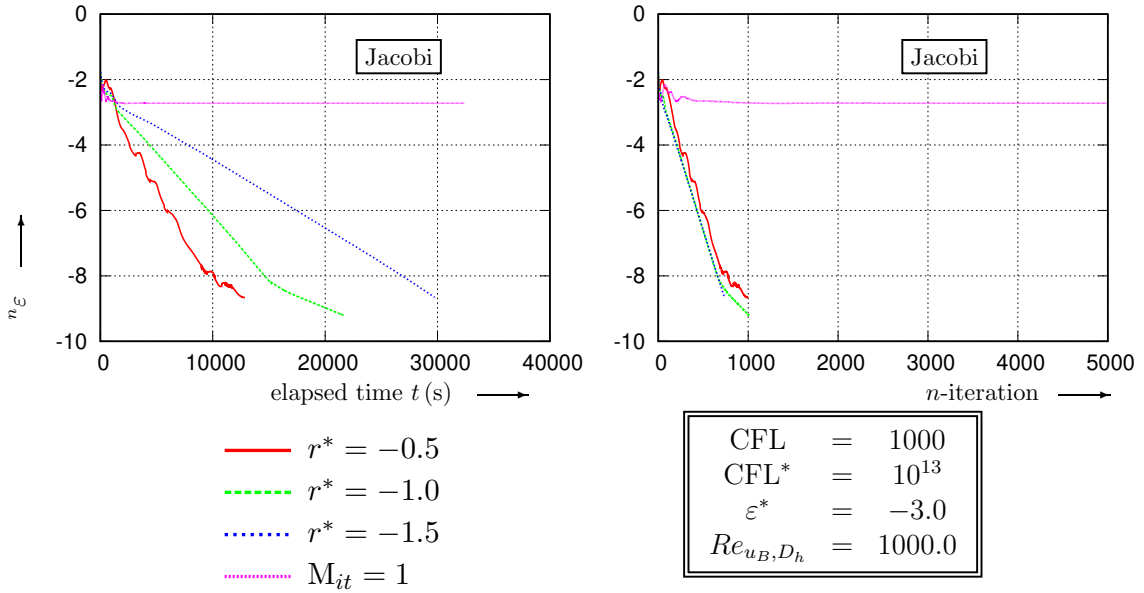

Figure 3.8: Convergence history using Jacobi method with different r^* at $Re_{u_B,D_h} = 1000$.

obtained when higher CFL* is used for the m-iteration since fewer dual-time-steps are needed (Fig. 3.11) knowing that before each m-iteration, the high-order approximation residual ${}^{m,n+1}\underline{R}^*_{E_i}$ need to be reconstructed with the CLSQ scheme, which induces a considerable computational

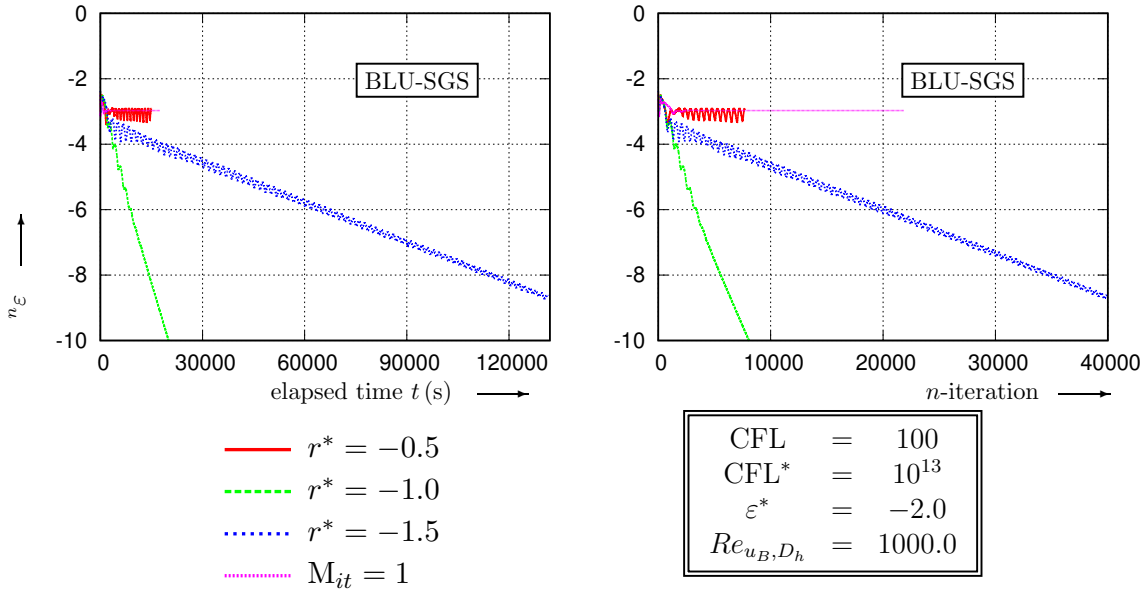

Figure 3.9: Convergence history using BLU-SGS method with different r^* at $Re_{u_B,D_h} = 1000$.

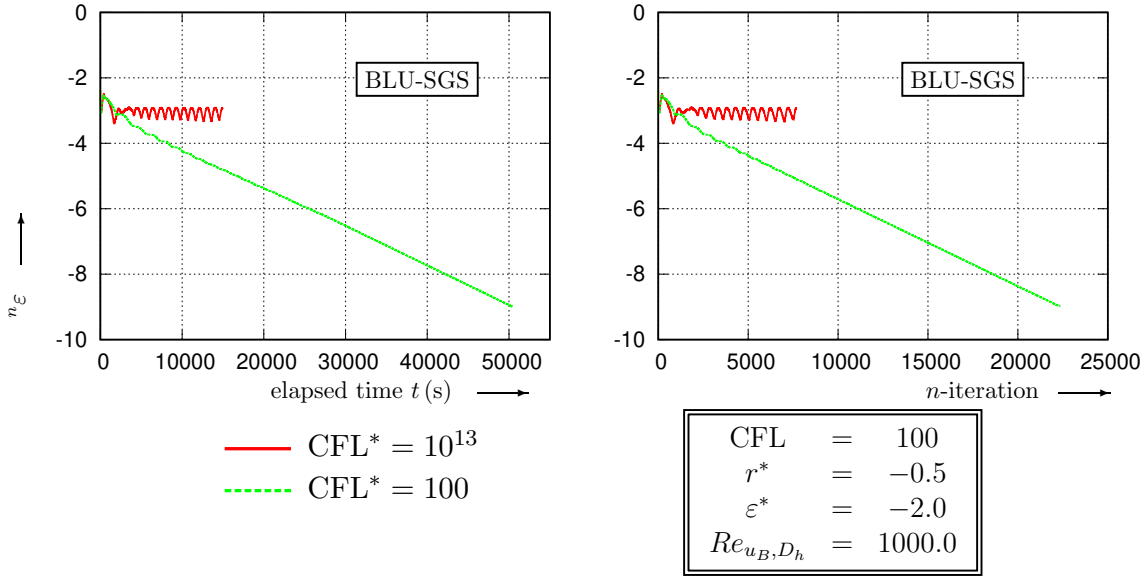

Figure 3.10: Convergence history using BLU-SGS method with different CFL* with $r^* = -0.5$ at $Re_{u_B,D_h} = 1000$. High CFL$^* = 10^{13}$ does not ensure convergence.

overhead. However, improvement brought by higher CFL* is not limitless, note that for CFL$^* \in [10^4, 10^{13}]$, a rise in CFL* even slows down the convergence slightly, this can be explained by the fact that, beyond CFL$^* = 10^3$, the number of dual-time-steps M_{it} at each n-iteration stays almost

unchanged. Meanwhile, larger dual-time-step size Δt^* takes more linear k-iterations to resolve, therefore the slower convergence rate is attributed to the increased number of linear iterations.

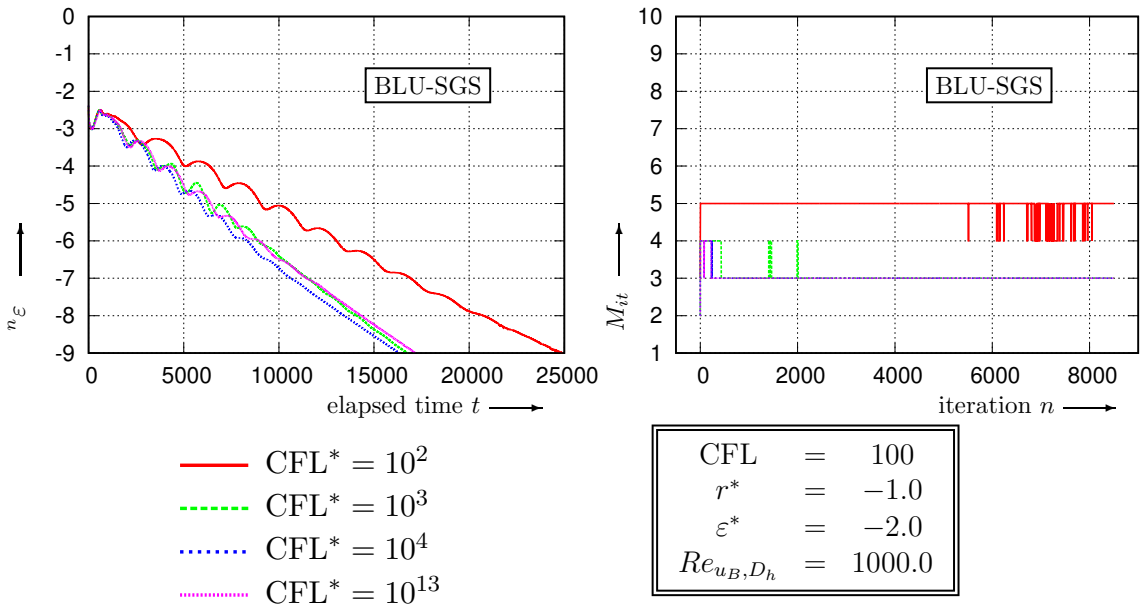

Figure 3.11: Comparison history using BLU-SGS method with different CFL* for $r^* = -1.0$ at $Re_{u_B,D_h} = 1000$.

The best performance of each linear solver is plotted for $Re_{u_B,D_h} = 1000$ in Fig. 3.12. For this critical case, Jacobi method fails to converge with threshold linear error $\varepsilon^* = -2.0$, which works perfectly at $Re_{u_B,D_h} = 100$ and 389, and only $\varepsilon^* = -3.0$ makes the convergence possible. On the other hand, BLU-SGS method is more restricted in terms of choice of CFL number and r^* and it is in turn the Jacobi method which gives the fastest convergence with CFL = 1000 and $r^* = -0.5$. The approximately factored LU-SGS method fails to give converged solution within a realistic amount of time with $r^* = -1.0$ as shown in Fig. 3.12.

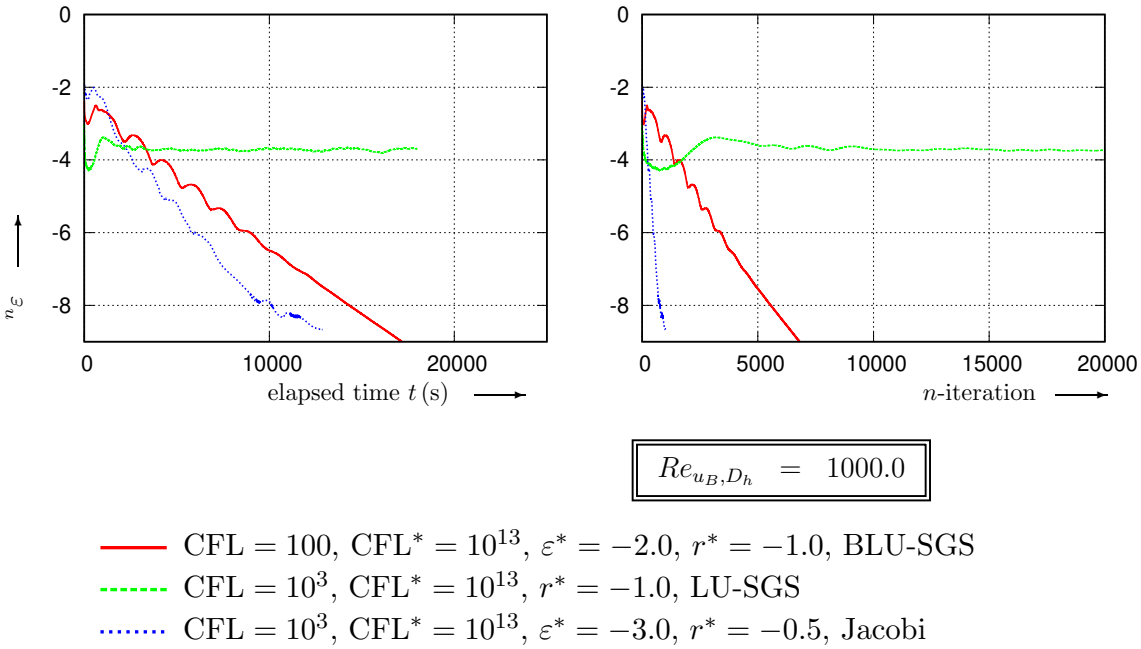

Figure 3.12: Convergence history comparison among Jacobi, BLU-SGS and LU-SGS methods at $Re_{u_B,D_h} = 1000$.

3.1.5 Implicit Scheme for High-order Spatial Discretization

It is observed that the order of accuracy of the CLSQ reconstruction also influence the convergence of implicit time-integration. As the order of accuracy is raised, the difference in approximation order between the high- and low-order numerical fluxes $\underline{F}^{\mathrm{NUM}}$ and $\underline{F}^{\mathrm{APP}}$ increases, since $\underline{F}^{\mathrm{NUM}}$ is computed using HLLC Riemann solver based on CLSQ reconstructed flow variables at interfacial quadrature points, while $\underline{F}^{\mathrm{APP}}$ is computed on the cell interface based on the cell-averages of both sides. An increase in the order of reconstruction will also elevate the order of $\underline{F}^{\mathrm{NUM}}$ whereas that of $\underline{F}^{\mathrm{APP}}$ remains unchanged. Therefore more iterations are required to eliminate this increased gap. For test-cases with relatively high Reynolds number, it might be necessary to use additional m-iterations in order to reach convergence. This is demonstrated by several examples using the Jacobi method with CLSQ3, CLSQ4, CLSQ5 and CLSQ6 reconstruction schemes as shown in Fig. 3.13.

In Fig. 3.13, for $Re_{u_B,D_h} = 200$, the difference in convergence rate is negligible among all four CLSQ schemes, and converged steady-state solutions are obtained with single-time-stepping up to CLSQ6. When the Reynolds number increases to $Re_{u_B,D_h} = 389$, although the solutions can still be driven to convergence without dual-time-stepping, CLSQ4-6 schemes clearly require more n-iterations to converge to steady-state. At $Re_{u_B,D_h} = 800$, although the convergence of Jacobi implicit scheme is considerably slower than $Re_{u_B,D_h} = 200$, $Re_{u_B,D_h} = 389$ due to stronger non-linearity as discussed previously, it still requires no dual-time-stepping for the lowest order CLSQ3 scheme. However, for higher order reconstructions CLSQ4, CLSQ5 and CLSQ6, the error level $^n\varepsilon$ shows no sign of descending with single-time-stepping. To obtain converged steady-state solution with CLSQ4, CLSQ5 and CLSQ6, it is indispensable to use additional m-iterations with

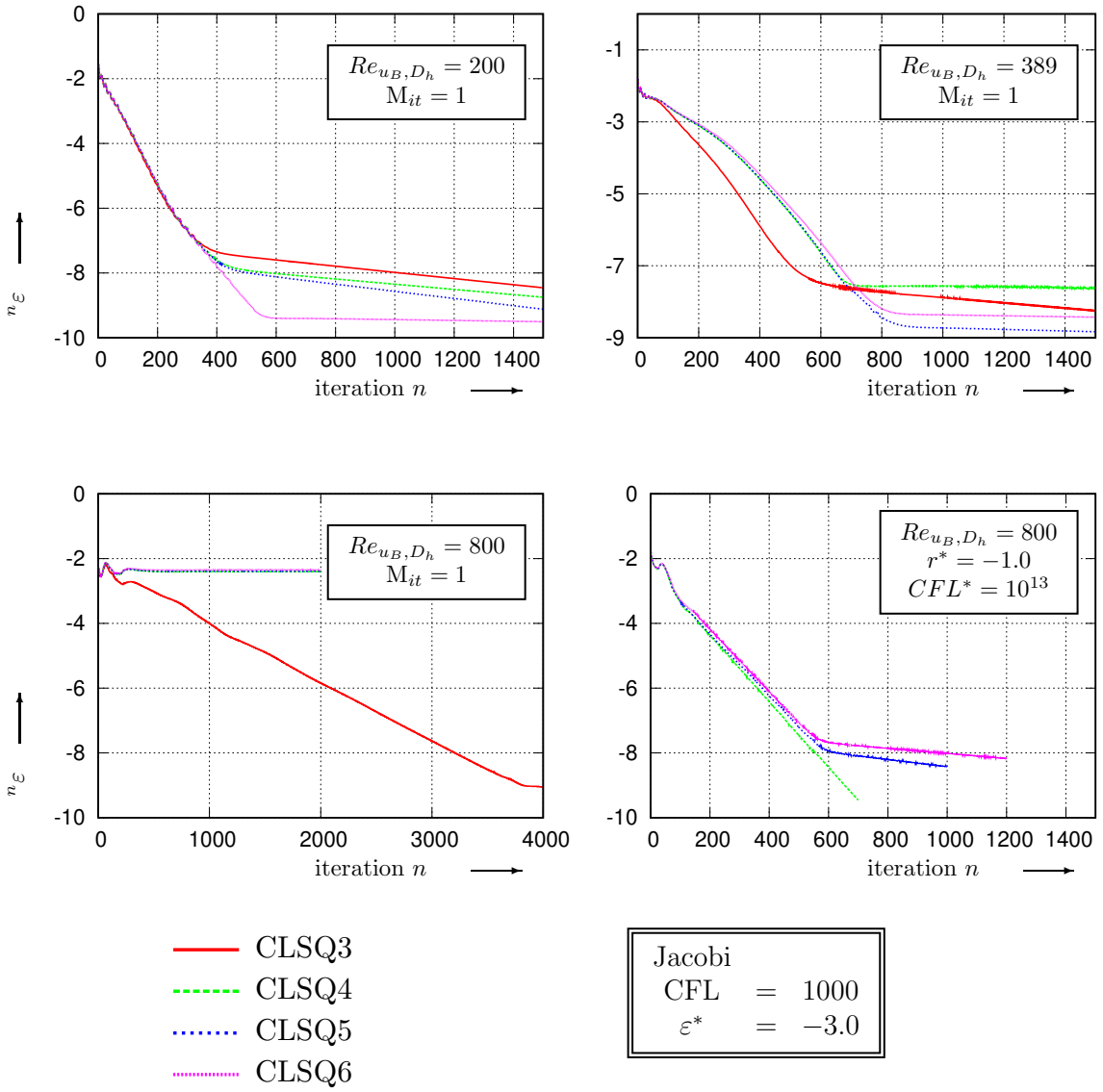

Figure 3.13: Study on the effects of high-order CLSQ reconstruction on the convergence of implicit scheme using Jacobi method. Reynolds numbers $Re_{u_B,D_h} = 200, 389, 800$ are investigated with CLSQ3, CLSQ4, CLSQ5 and CLSQ6.

a threshold reduction $r^* = -1.0$, which is not necessary for CLSQ3 reconstruction. Finally, the convergence history is given at $Re_{u_B,D_h} = 800$ using dual-time-stepping for CLSQ4, CLSQ5 and CLSQ6 in Fig. 3.13. The three high-order reconstruction schemes take comparable amount of time to converge although it is observed that the rate of convergence is progressively reduced as the order of discretization increases from 4 to 6. This is due to the fact that a greater number of m-iterations M_{it} is required to eliminate the increasing gap between low- and high-order flux approximations (Fig. 3.14) as mentioned before, and since the CLSQ reconstruction is needed for each new m-iteration, a visible computational overhead is caused.

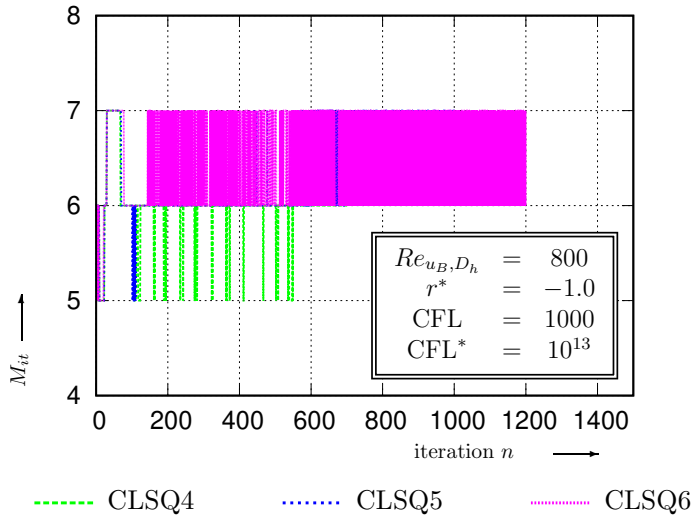

Figure 3.14: Number of m-iterations M_{it} for each n-iteration with Jacobi method using CLSQ4, CLSQ5, CLSQ6 at $Re_{u_B,D_h} = 800$.

3.1.6 Summary on Implicit Scheme Evaluation

In this section, the performance of the implicit scheme with dual-time-stepping has been evaluated using the laminar BFS configuration of Armaly *et al.* [13]. Three linear solvers have been tested and it has been demonstrated that the iterative linear solvers such as Jacobi solver and BLU-SGS solver provide substantially faster convergence than the approximately factored LU-SGS solver within a wide range of Reynolds number.

As mentioned earlier, the solution is considered converged once the third characteristic phase of slow descent of error ${}^n\varepsilon$ is reached. The entrance of the third phase is presignaled by a change-of-slope point which is located at approximately ${}^n\varepsilon = -8.0$. As the results indicated previously, by lowering the threshold linear error ε^*, the change of slope is encountered at higher value of ${}^n\varepsilon$ and the subsequent slope of error $\left|\frac{\partial {}^n\varepsilon}{\partial n}\right|$ in the third phase decreases (figures 3.2, 3.3, 3.6). For all Reynolds numbers studied, Jacobi solver requires more stringent ε^* condition than BLU-SGS solver to obtain optimal convergence rate, and tends to diverge when ε^* is relatively high (figures 3.2, 3.6). However, BLU-SGS solver is more sensitive to the increasing Courant number and to the r^* criterion at high Reynolds numbers. At $Re_{u_B,D_h} = 1000$, the maximum CFL reachable using BLU-SGS is limited to 100, and a high value of $r^* = -0.5$ does not ensure convergence either. In terms of convergence rate to a steady-state solution, BLU-SGS solver maintains a marginal advantage over Jacobi solver in this BFS configuration at $Re_{u_B,D_h} = 100,389$. This is largely due to the fact that, for OpenMP parallelized code, Jacobi method is parallelized on the entire unstructured grid while BLU-SGS method is parallelized in every reordered hyperplane, which leads to a considerable performance penalty. Furthermore, since the specific boundary conditions need to be implicitly accounted for in the $\underline{\underline{\mathbf{D}}}$ matrix for the BLU-SGS method therefore a completely matrix-free scheme cannot be achieved. As discussed in Section. 2.7, the construction of $\underline{\underline{\mathbf{D}}}$ is BC-dependent and needs

to be modified from one test-case to another. This reduces the attractiveness of the BLU-SGS method comparing to the Jacobi method especially when the improvement in convergence rate is far from impressive in a parallelized CFD solver.

The performance of implicit scheme is highly dependent on the flow conditions and the spatial order of discretization schemes. In the BFS test-case, we have demonstrated that as the Reynolds number increases, the flow tends to become increasingly non-linear with expanding recirculation zones, and that the pseudo dual-time-stepping becomes necessary to ensure the convergence at high Reynolds numbers. Moreover, high-order spatial discretization leads to larger difference in the approximation order between the high-order numerical fluxes $\underline{F}^{\mathrm{NUM}}$ used in the reconstruction phase and the low-order averaged fluxes $\underline{F}^{\mathrm{APP}}$ used in the time-integration phase. This increasing difference can only be eliminated by additional iterations during time-integration, and by the implementation of dual-time-stepping. However, considering the computational costs saved by using low-order flux approximation instead of performing CLSQ reconstruction at each linear iteration, this still proves to be a small price to pay. These two performance issues are not independent from each other, rather, they are coupled to a certain extent as shown in Fig. 3.13. The decrease in convergence rate due to order increase is not noticeable for low Reynolds number BFS flows $Re_{u_B,D_h} < 400$ while becoming increasingly important as the Reynolds number rises. Conversely, the single-time-stepping convergence is possible for CLSQ3 but not for CLSQ5-6 schemes *only* when the Reynolds number is high.

As a general rule, if a set of DTS parameters $\{\mathrm{CFL}, \mathrm{CFL}^*, \varepsilon^*, r^*\}$ ensure a converged solution for a BFS test-case at relatively high Reynolds number Re_{u_B,D_h} and/or with a relatively high order of CLSQ reconstruction, then the convergence would also be ensured with the same set of parameters for a test-case at a lower Reynolds number and/or with a lower order of CLSQ scheme. For this specific Armaly *et al.* [13] test-case, the set of parameters $\{\mathrm{CFL} = 100, \mathrm{CFL}^* = 100, \varepsilon^* = -2, r^* = -1.5\}$, which are also named the "safe parameters", can be used to achieve convergence at *any* Re_{u_B,D_h} between 100 and 1000 using BLU-SGS linear solver, although it does not guarantee the fastest convergence rate at that specific Reynolds number. For the Jacobi solver, the safe parameters are $\{\mathrm{CFL} = 1000, \mathrm{CFL}^* = 100, \varepsilon^* = -3, r^* = -1.5\}$ since, in the case of BFS, Jacobi solver does not show sensitivity to the CFL number which can be maintained at $\mathrm{CFL} = 1000$ for any Re_{u_B,D_h}, and the more stringent $\varepsilon^* = -3$ does not over-resolve the linear system. In theory, using more stringent r^* criteria further increase the stability, therefore can be preferential for general applications (not limited to BFS flows). However, for the current Armaly *et al.* [13] BFS test-case, a decrease in r^* from -1.0 to -1.5 drastically increases the computational time as shown in Fig. 3.9, therefore a judicious choice of parameters always depends on the specific test-case to solve.

3.2 Evaluation of Constrained Least-Squares (CLSQ) Reconstruction

In this section, we aim to evaluate the performance of CLSQ reconstruction scheme by carrying out a grid convergence study on the BFS test-cases of Armaly *et al.* The uniform grid refinement is implemented with a refinement ratio of two in each dimension, and solutions of primitive variables are reconstructed to the same set of sampling points for all grid levels, which are all of the barycenters of the first (coarsest) grid cells. Among the three types of polygonal grids in Fig. 3.36, the Cartesian grid is chosen for this study since the division of rectangles is angle-preserving and its convergence property is superior to the triangular grid.

Consider a grid convergence study with N successively refined grids. Converged solution of a certain primitive variable on the finest grid $\mathtt{v}_N$ is regarded as the reference solution, and the relative error on the ℓ^{th} grid is computed by the second Euclidean L_2 norm

$$\varepsilon_{\mathtt{v}_\ell} = \|\mathtt{v}_\ell - \mathtt{v}_N\|_2 \,, \quad \forall \mathtt{v} \in \{\rho, u, v, p\} \tag{3.4}$$

where $\mathtt{v}$ is the symbol for a generic primitive variable, not to be confused with the vertical velocity component v.

Meanwhile, $\varepsilon_{\mathtt{v}_\ell}$ can be expressed as a function of the characteristic grid length h_ℓ and the order of accuracy p

$$\varepsilon_{\mathtt{v}_\ell} = C h_\ell^p + \mathcal{O}(h_\ell^{p+1}) \tag{3.5}$$

with C being a constant specific to the scheme. In order to determine p, we ignore the high-order term $\mathcal{O}(h_\ell^{p+1})$ in Eqn. 3.5. Thus

$$\log_{10}(\varepsilon_{\mathtt{v}_\ell}) = \log_{10}(C) + p \log_{10}(h_\ell) \tag{3.6a}$$

$$\log_{10}(\varepsilon_{\mathtt{v}_{\ell-1}}) = \log_{10}(C) + p \log_{10}(h_{\ell-1}) \tag{3.6b}$$

and p is obtained by subtracting Eqn. 3.6a from Eqn. 3.6b

$$p = \frac{\log_{10}(\varepsilon_{\mathtt{v}_{\ell-1}}) - \log_{10}(\varepsilon_{\mathtt{v}_\ell})}{\log_{10}(h_{\ell-1}/h_\ell)} \tag{3.7}$$

where we have $h_{\ell-1}/h_\ell = 2$ for a uniform refinement ratio of 2. Note that the order of convergence p measures how fast the computational error ε_ℓ vanishes as the grid is systematically refined by a given ratio. This order also characterizes the accuracy of a reconstruction scheme such as the CLSQ. Therefore, the terms "order of convergence", "convergence rate", "order of accuracy" and "order of discretization" can be employed interchangeably.

The evaluation of observed convergence rate is performed for the backward-facing step test-case at $Re_{u_B, D_h} = 100$ on four uniformly refined Cartesian grids tabulated in Tab. 3.1. All geometric parameters of the grids are illustrated in Fig. 3.15, where N denotes the number of grid points on a given line segment, r denotes the geometric progression rate of grid spacing in the indicated direction ($r \geq 1.0$). For the grid generation procedure, the entire domain is divided into three rectangular blocks and the blue-colored lines in Fig. 3.15 represent the bounding grid lines of all three blocks. The red-colored parameters in Fig. 3.15 are prescribed as input, and other parameters are calculated based on the input such that (i): the computational grid fills exactly the physical domain and (ii): there is no discontinuity of grid spacing between two blocks of grids. A buffer

zone with a length of L_{buffer} is used to relax the vertical grid spacing so that the meshes are not unnecessarily clustered downstream of the step. The objective of this analysis is to determine the observed order of accuracy p of the third-order CLSQ reconstruction (CLSQ3) scheme, and to verify if it matches the theoretical value 3.

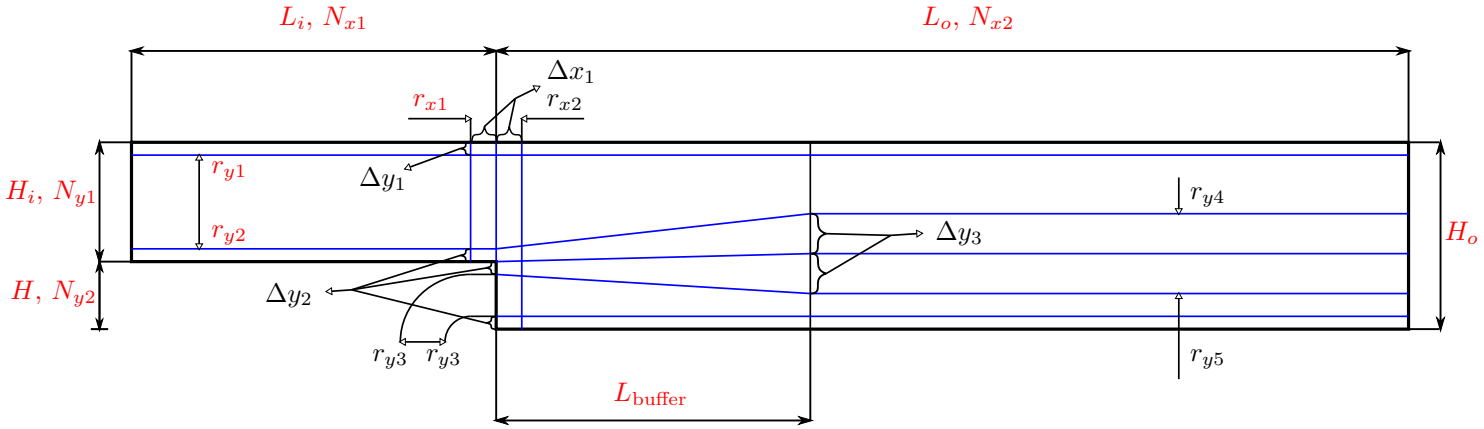

Figure 3.15: BFS Cartesian grid parameters : blue lines correspond to the bounding grid lines, parameters colored in red are independent parameters and the other parameters in black are generated automatically based on them. Parameter values for the current BFS test-case are given in Tab. 3.1.

Fig. 3.16 and Fig. 3.17 show the distributions of pressure and skin-friction coefficients on the channel floor downstream of the step (Fig. 3.16) and near the step (Fig. 3.17). Results are given from Grid 0 to Grid 3 in Tab. 3.1, and a clear tendency of grid convergence is observed as the grid is refined. The solutions of both wall coefficients are visibly improved when refining from Grid 0 to Grid 1, but start converging from Grid 1 to Grid 3. No significant difference can be discerned between solutions on Grid 2 and Grid 3 except in the close vicinity of the singularity point $x = 0$ as shown in Fig. 3.17. Since we have repeatedly shown that the wall coefficients always tend to diverge at singularity point, the results in figures 3.16 and 3.17 imply that a grid converged solution is obtained starting from Grid 2.

To quantitatively examine the order of accuracy of the CLSQ3 scheme, ε_ℓ and p are calculated using equations 3.4 and 3.7. The results are shown in log-scale for four different primitive variables ρ, p, u, and v respectively in Fig. 3.18. The normalized grid spacing for the ℓ^{th} Grid is defined as

$$\Delta h^*_\ell = \frac{\Delta h_\ell}{\Delta h_0} \tag{3.8}$$

where Δh_0 denotes the characteristic grid spacing of Grid 0.

This quantitative analysis shows that, for variables ρ, p, and u, the order of convergence p approaches or slightly overpasses the theoretical order of accuracy of the CLSQ3 scheme at Grid 3. For the vertical velocity component v, although its convergence rate fails to reach 3 at Grid 3, it follows the general increasing trend of the three other primitive variables. The very low values $|v| \ll u_B$ are probably the cause of this delay in terms of grid refinement in reaching the theoretical order of convergence.

With the results shown in figures 3.16 and 3.18, we have verified both qualitatively and quan-

Table 3.1: Uniformly refined grids used for grid convergence study for the laminar BFS test-case. * denotes the independent parameter given as input, all parameters are shown in Fig. 3.15. Grid 1-3 are generated by successive subdivisions of Grid 0, hence the geometric progression rates are not applicable.

	Grid 0	Grid 1	Grid 2	Grid 3
N_{cells}	2704	10804	43204	172804
$*N_{x1}$	31	61	121	241
$*N_{x2}$	76	151	301	601
$*N_{y1}$	16	31	61	121
$*N_{y2}$	16	31	61	121
$*r_{x1}$	1.0733	-	-	-
r_{x2}	1.0494	-	-	-
$*r_{y1}$	1.1	-	-	-
$*r_{y2}$	1.1	-	-	-
r_{y3}	1.0719	-	-	-
r_{y4}	1.0123	-	-	-
r_{y5}	1.0045	-	-	-
$*H_i/H$	52/49	52/49	52/49	52/49
$*H_o/H$	101/49	101/49	101/49	101/49
$*L_i/H$	10	10	10	10
$*L_o/H$	50	50	50	50
$*L_{\text{buffer}}/H$	10	10	10	10
$\Delta x_1/H$	15.82%	7.909%	3.955%	1.977%
$\Delta y_1/H$	5.705%	2.853%	1.426%	0.713%
$\Delta y_2/H$	5.705%	2.853%	1.426%	0.713%
$\Delta y_3/H$	6.720%	3.360%	1.680%	0.840%

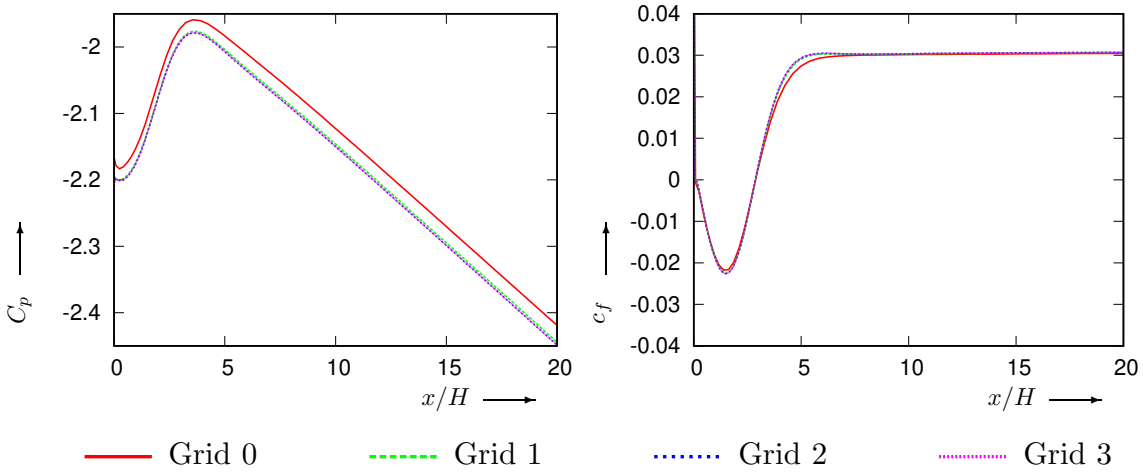

Figure 3.16: Grid convergence result of the pressure coefficient C_p and the skin-friction coefficient c_f on the bottom wall plotted against x-coordinate normalized by the step height H.

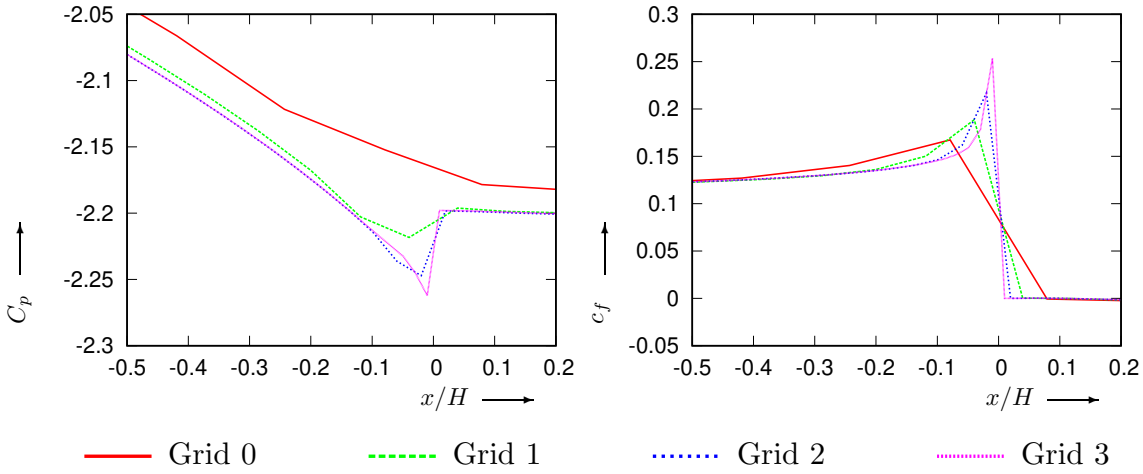

Figure 3.17: Grid convergence result of the pressure coefficient C_p and the skin-friction coefficient c_f on the bottom wall plotted against x-coordinate normalized by the step height H.

titatively that the CLSQ3 scheme is grid-converged and therefore consistent. The observed order of accuracy p proves to be close to the theoretical value of 3 for the CLSQ3 scheme as illustrated by Fig. 3.18. It is important to realize that the grid convergence study in this section verifies the order of convergence of the CLSQ3 scheme in a strict sense by using the reconstructed variables to *all* cell barycenters rather than an arbitrarily selected sub-set. This study shows that the current CLSQ3 scheme yields a discretization error of order $\mathcal{O}(\Delta h^3)$ for the laminar BFS test-case with the presence of non-periodic inlet, outlet, and adiabatic wall boundaries. The imposition of wall boundary conditions shows no effect on the spatial discretization error due to the application of constrained reconstruction mentioned in Section 2.3.

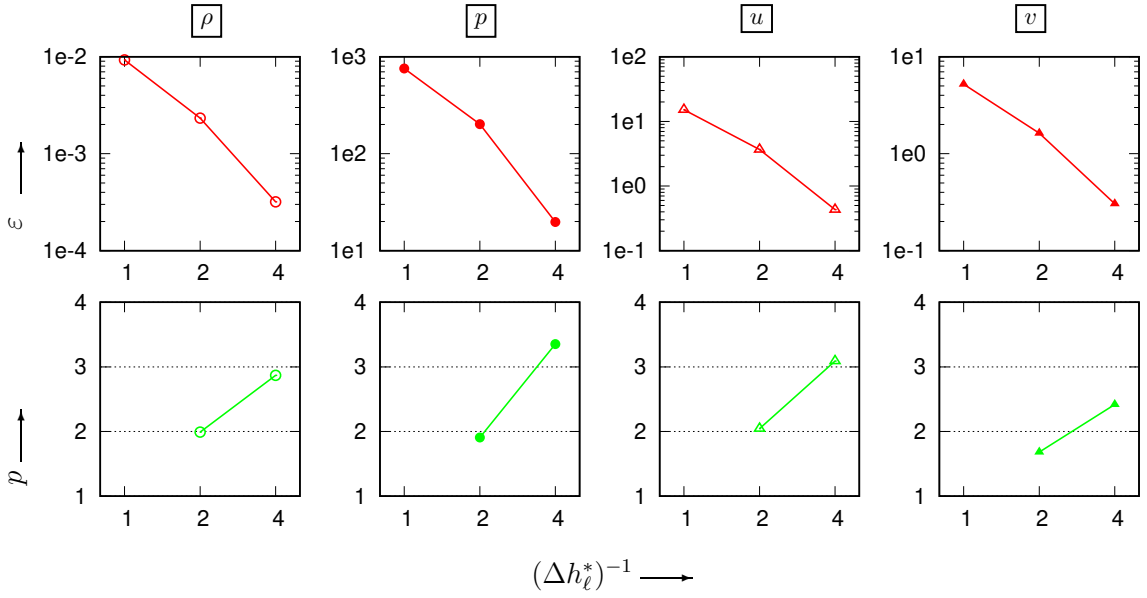

Figure 3.18: Evaluation of the observed order of accuracy p for the CLSQ3 scheme on the Backward-Facing Step. The relative error ε and observed order p are plotted against the inverse normalized grid spacing. Results are shown for four primitive variables.

The possibility to extend the CLSQ scheme to higher orders is further investigated up to CLSQ6. Four computations are performed with CLSQ schemes from the third- to sixth-order on Grid 2. In Fig. 3.19, distributions of pressure and skin-friction coefficients are plotted downstream of the step. In this region where no singularity point is present, the curves of C_p and c_f distributions remain smooth, and solutions obtained by different orders of CLSQ schemes are almost indistinguishable from one another. This shows that the current CLSQ reconstruction produces consistent results as the order is scaled up to $p = 6$.

By focusing particularly on the region in the vicinity of the discontinuous step corner, as shown in Fig. 3.20, where large gradients in the streamwise direction are expected for all flow variables due to the sudden expansion. In this region, the smoothness of C_p and c_f is conserved for all scheme orders up to $p = 6$ before and after the step. The solutions are well bounded as the order of CLSQ scheme increases, no spurious oscillation is witnessed in the immediate neighborhood of the singularity point. A good agreement is observed among solutions of all orders in the near-step region, with only a minor inconsistency for the pressure coefficient within 10% step height upstream of the step, where the even orders (CLSQ4 and CLSQ6) reach the local minimum slightly earlier than the odd orders (CLSQ3 and CLSQ5).

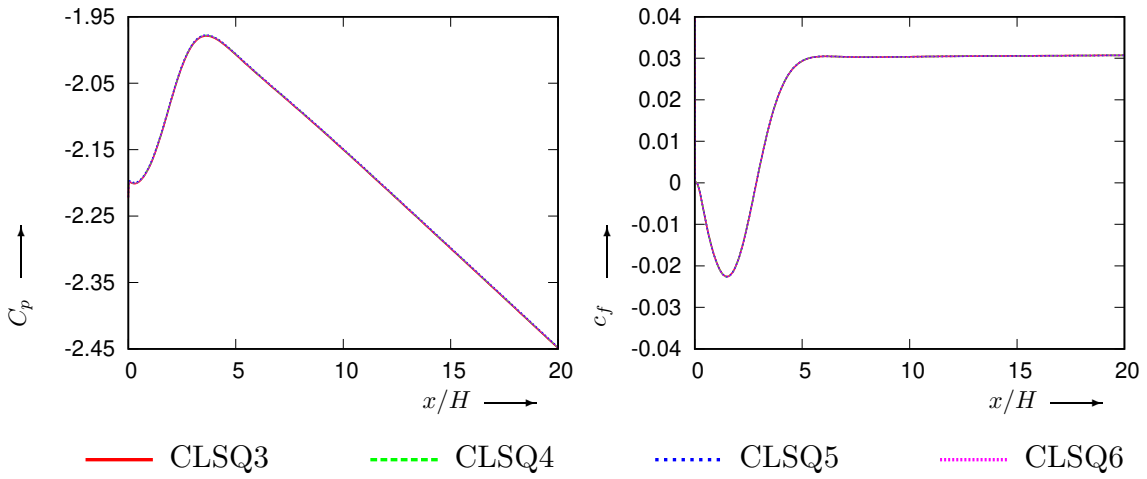

Figure 3.19: Results of the pressure coefficient C_p and the skin-friction coefficient c_f on the bottom wall plotted against x-coordinate normalized by the step height H. Spatial discretization performed with CLSQ3-CLSQ6.

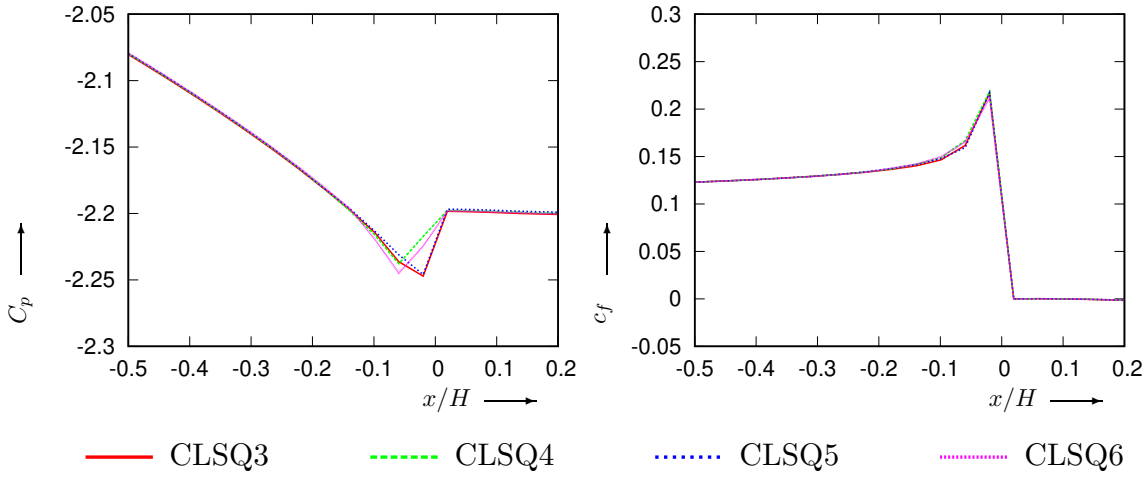

Figure 3.20: Results of the pressure coefficient C_p and the skin-friction coefficient c_f on the bottom wall plotted against x-coordinate normalized by the step height H. Results zoomed to the near-step region. Spatial discretization performed with CLSQ3-CLSQ6.

3.3 Evaluation of Arbitrary Polygonal Grids

In this section, we test the computational methods presented in the previous Chapter. 2 on general unstructured grids. The objective is to demonstrate their robustness on unstructured grids with an arbitrary combination of polygonal cells in different regions. We will also show that satisfactory results can be obtained even with the presence of stretched and skewed polygons in the domain. Three test-cases are investigated: the zero-thickness flat-plate boundary layer (FPBL) case, the

low-Reynolds NACA 0012 airfoil test-case and the backward-facing step (BFS) case. Both test-cases involve wall-bounded viscous flow therefore it is important to apply high-aspect-ratio cells in the near-wall regions for accurate results within boundary layers.

3.3.1 Zero-thickness FPBL

The computational domain is rectangular with a length of $3L$ in the x-direction and a height of $6L$ in the y-direction. The flat-plate lies on the domain centerline along the x-direction with a length of L. The domain is artificially divided into a farfield and a near-wall region as shown in Fig. 3.21, the near-wall region is defined by a bounding box with a distance of $0.05L$ to the plate in each direction. The incoming flow is parallel to the flat plate with a free-stream Mach number $M_\infty = 0.4$. The Reynolds number is defined by the free-stream velocity and the plate length $Re_{u_B,L} = \rho_\infty u_\infty L/\mu_\infty = 5 \times 10^5$. The plate is considered as a no-slip adiabatic wall, Riemann invariant boundary condition is applied to the front, upper and lower boundaries while the downstream boundary is treated as a pressure outlet.

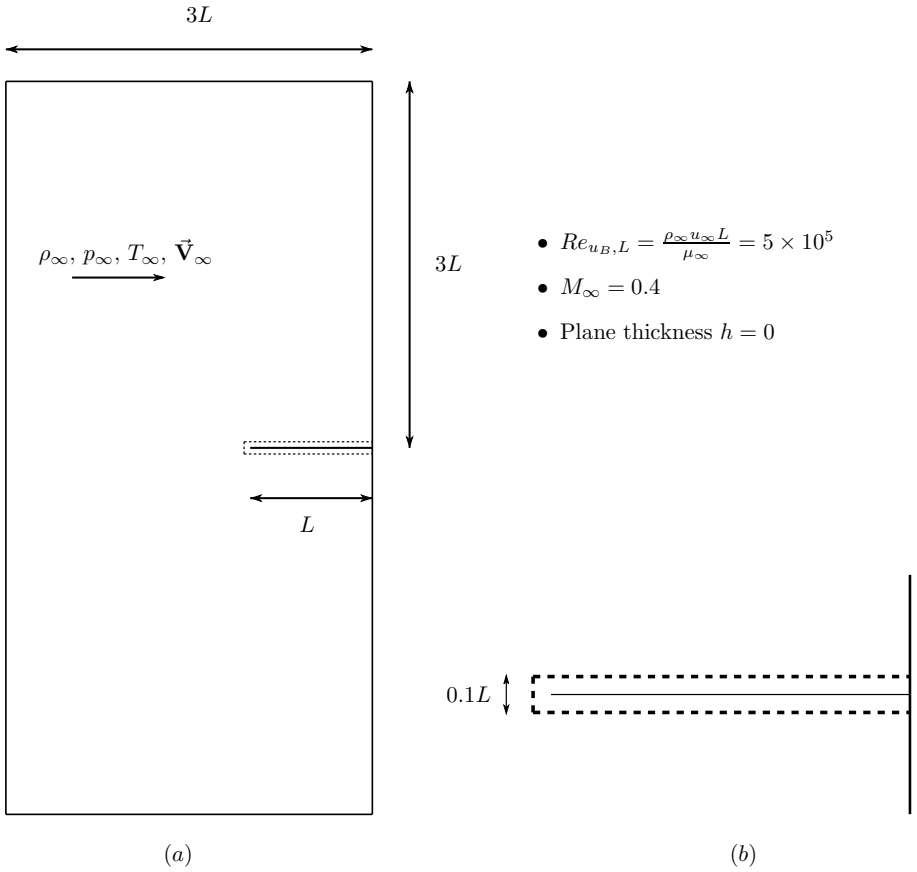

Figure 3.21: Geometric set-up of the flat-plate boundary layer test-case. (a): global computational domain; (b): near-wall region.

A series of unstructured polygonal grids are tested in this case to demonstrate flexibility in choice of grids. As shown in Fig. 3.22, the farfield and near-wall regions are meshed separately.

In the farfield region (Fig. 3.22.a), the mesh is quad-dominant with a small amount of scattered triangular cells. By splitting any number of quadrilateral cells in different ways, a tri-dominant or completely triangulated farfield mesh can also be obtained. When approaching the domain infinity, since a low level of disturbance is expected, several cells can be merged into a large polygon in order to reduce the total number of cells. Conversely, the cells close to the near-wall region can be further divided in various suitable manners, as shown in Fig. 3.22.b, to ensure a smooth transition between the farfield and near-wall meshes.

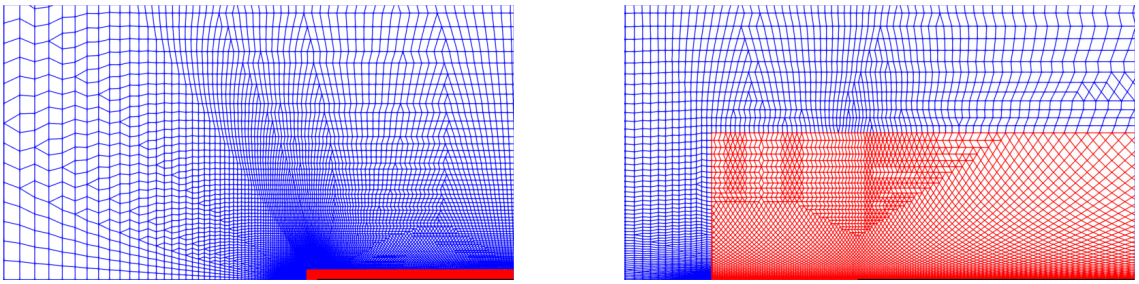

(a) (b)

Figure 3.22: Quad-dominant unstructured grid for zero-thickness flat-plate boundary layer. (a): farfield mesh; (b): interface between farfield and near-wall regions.

Different polygonal meshes are generated within the near-wall region as shown in Fig. 3.23. Meshes (a)-(d) are pseudo-structured, constructed based on their Cartesian counterpart (e) by connecting the vertices, edge-centers and cell-centers in four different manners. According to Gerolymos and Vallet [91], by examining the performance of different tessellations of the same grid, the relative advantages and disadvantages of cell-centered and center-vertex FVMs can be understood.

Five computations are performed using different combinations of farfield and near-wall meshes mentioned above with third-order CLSQ reconstruction (CLSQ3). Fig. 3.24 shows the pressure contours in the vicinity of the plate leading edge computed on all five near-wall meshes in Fig. 3.23. Close to the leading edge, high pressure gradient is expected due to the presence of singularity point at $x = 0$. According to Fig. 3.24, all five types of near-wall meshes give comparable results of pressure contours near the leading edge. Judging from the density of isobaric lines, the quad-dominant mesh (a) predicts the rapidest pressure change, while the Cartesian mesh (e) predicts the smoothest. The differences in the density and shape of isobaric lines become more pronounced in regions closer to $x = 0$, where the local meshes need to be further refined in order to accommodate the sharply increasing pressure gradient when approaching the singularity point.

The normalized static pressure p/p_∞ is reconstructed on the plate wall, as well as along the streamline on the centerline upstream of the leading edge $x < 0$, while the skin-friction coefficient c_f is reconstructed on the plate wall. Here c_f is calculated by

$$c_f = \frac{\mu \left.\frac{\partial u}{\partial y}\right|_{y=0}}{0.5\rho_\infty u_\infty^2}. \tag{3.9}$$

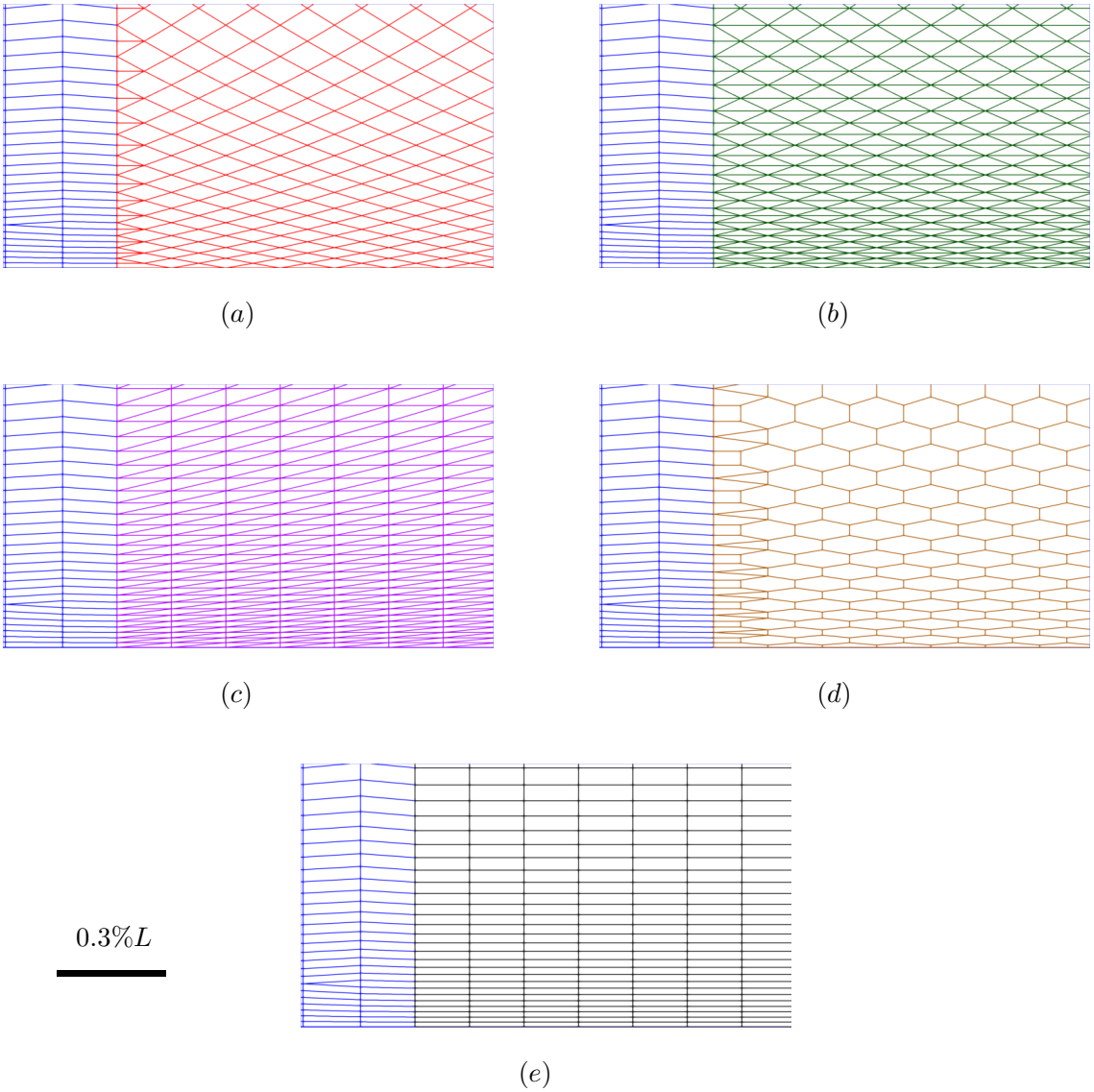

Figure 3.23: Four types of stretched polygonal meshes in the near-wall region. (a): quad-dominant; (b): isosceles triangles; (c): right-angled triangles; (d): hexagons; (e): Cartesian.

According to Fig. 3.25, identical results of both p/p_∞ and c_f are obtained on all five grids far from the leading edge at $x = 0$. Visible differences are observed only within close vicinity of the plate leading edge $-1\% < x/L < 2\%$. As shown previously in Fig. 3.24, this discrepancy is caused by the large gradients of pressure and velocity near the singularity point at $x = 0$, and by the relatively wide horizontal grid spacing in this region. We can expect that computations on the five different grids give similar results as the grid spacing in x-direction is reduced. However, as the $x = 0$ point is singular, for a zero-thickness plate, this grid-convergence is not reported here.

An important advantage of operating on arbitrary unstructured grids is the possibility for local adaptive refinement. To accurately capture the flow behavior near the leading edge singularity, the

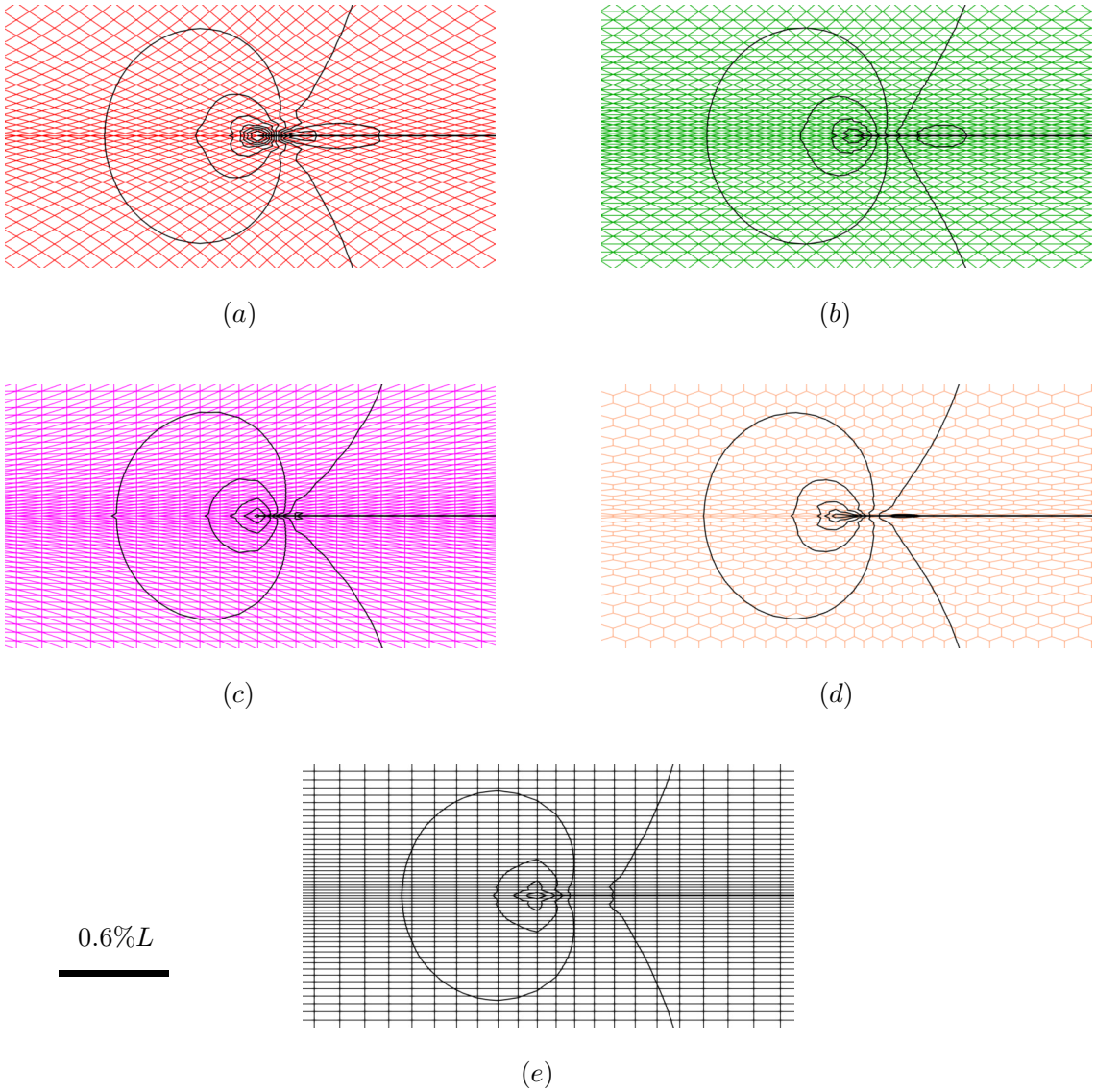

Figure 3.24: Static pressure contour plots obtained on four types of stretched polygonal meshes in the near-wall region. (*a*): quad-dominant; (*b*): isosceles triangles; (*c*): right-angled triangles; (*d*): hexagons; (*e*): Cartesian. The flat-plate is represented by the black solid line. Minor unsmoothness issue due to ParaView rendering.

grid with triangulated farfield and isosceles triangular near-wall region (TriFar-IsoTriNW) is locally refined within a rectangular bounding box centered on $x = 0$. Four levels of adaptive refinement are illustrated in Fig. 3.26 with (*a*) being the first level and (*d*) being the last. Each level of refinement takes place in a smaller bounding box contained in the one of the previous level, and is colored differently, the color blue corresponds to the unrefined original grid. Each triangular cell in the targeted region is subdivided into four smaller congruent triangles by connecting its three edge-centers (see Fig. 3.35). The local grid refinement allows us to reduce the grid spacing in the

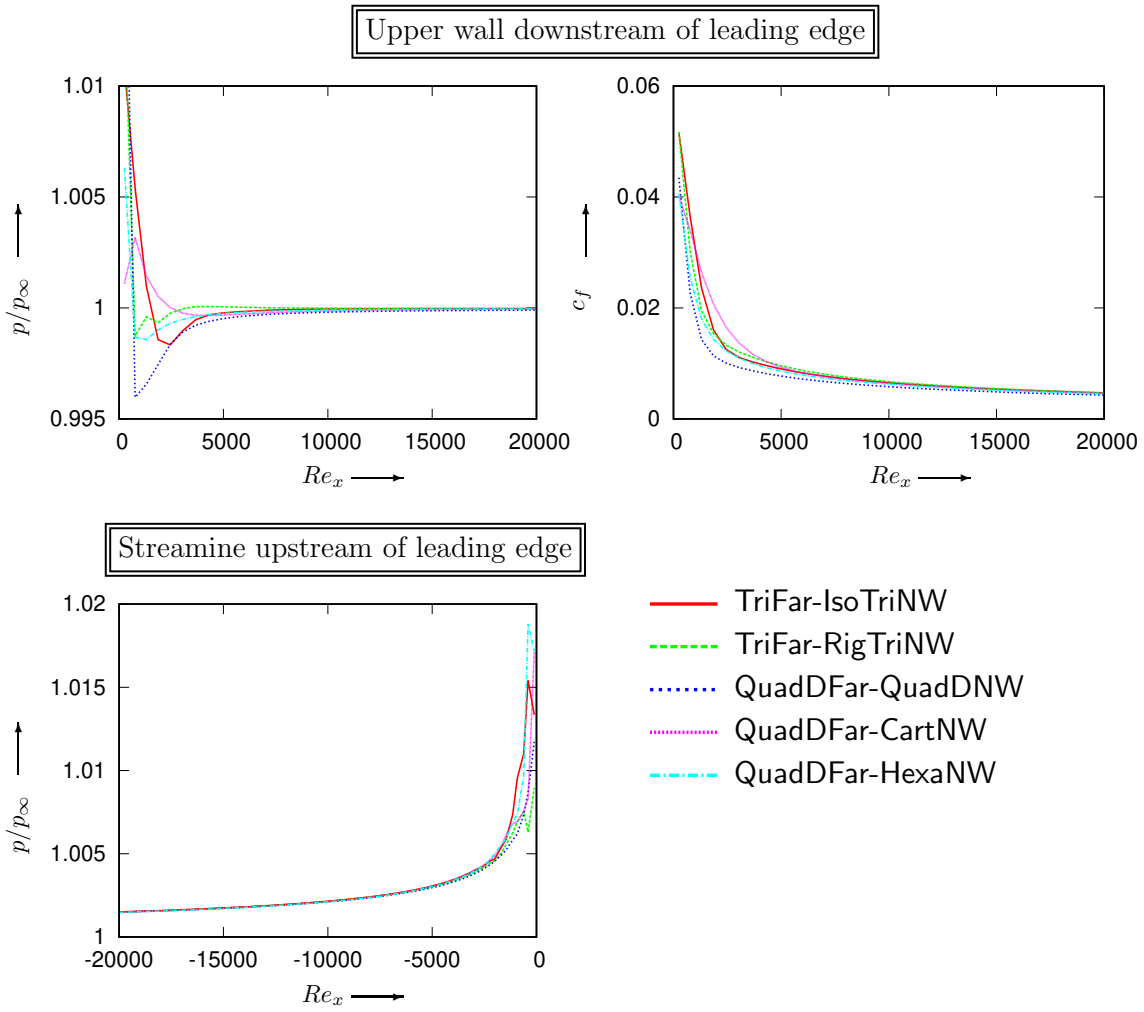

Figure 3.25: Pressure and skin-friction coefficient distributions (Eqn. 3.9) computed with different stretched near-wall meshes. TriFar-IsoTriNW: triangulated farfield, isosceles triangular near-wall; TriFar-RigTriNW: triangulated farfield, right-angled triangular near-wall; QuadDFar-QuadDNW: quad-dominant farfield, quad-dominant near-wall; QuadDFar-CartNW: quad-dominant farfield, Cartesian near-wall; QuadDFar-HexaNW: quad-dominant farfield, hexagonal near-wall.

region where large gradient is present without drastically increasing the total number of cells in the computational domain.

Results of p/p_∞ and c_f distributions are shown in Fig. 3.27 for each level of adaptive refinement. From the original grid to the 4^{th} refinement level, the curves of both p/p_∞ and c_f admit a sharper slope as the grid spacing $\Delta h \to 0$. Compared to Fig. 3.25, the maximum values of p/p_∞ and c_f located at the first sampling point next to the singularity point $x = 0$ increase substantially on the adaptively refined grids and there is no indication of converging to any upper bound. We can deduce that, by further refining the local mesh around the leading edge, the computed values of p/p_∞ and c_f will blow up and reach infinity. Note that the singularity point is a purely numerical phenomenon and does not exist in reality, any realistic flat-plate would have a nonzero thickness

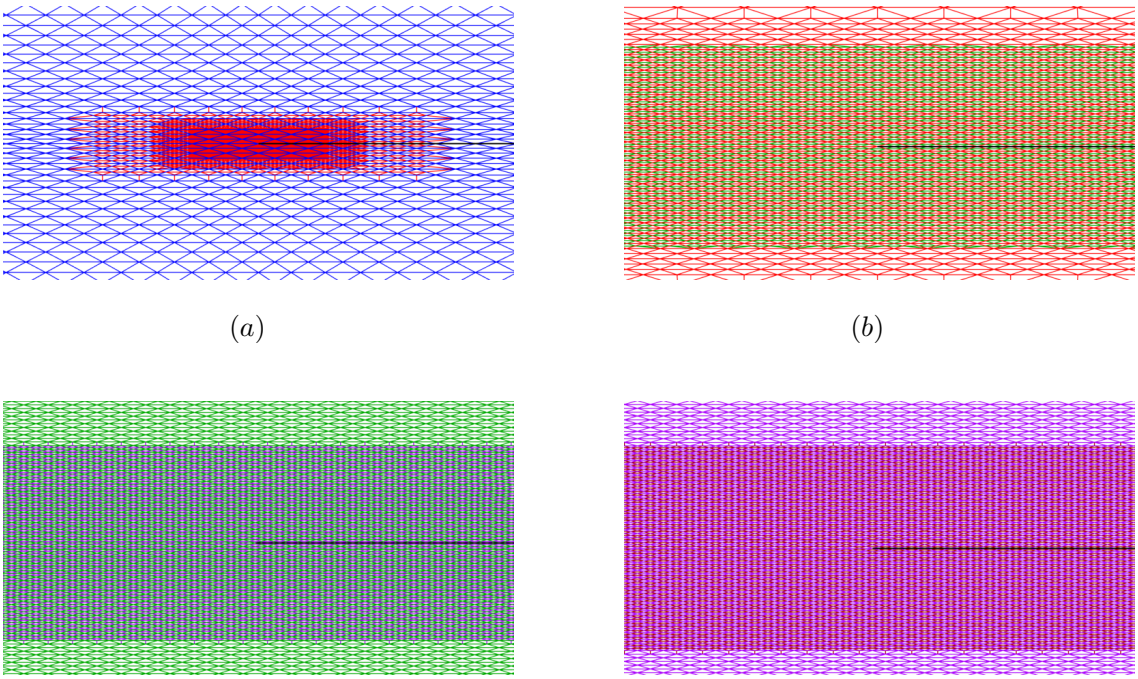

Figure 3.26: Four levels of adaptively refined grids targeting on the leading edge of a zero-thickness flat plate. (a) is the coarsest, (d) is the finest. The flat-plate is represented by the black solid line.

as well as a finite curvature at the corners. However, according to this result, it is reasonable to assume that p/p_∞ and c_f would sharply increase as the leading edge becomes thinner. Although the maximum values of p/p_∞ and c_f do not show any boundedness as the local grid spacing $\Delta h \to 0$, the p/p_∞ and c_f plots are clearly converging towards the last refinement level away from the leading edge as indicated by Fig. 3.27.

This test-case intends to demonstrate that the method performs satisfactorily with different types of grids and gives consistent and accurate results on any arbitrary polygonal grid including cases with high-aspect-ratio and/or highly skewed cells. Improved resolution can be obtained by local adaptive mesh-refinement without unnecessarily increasing the mesh density beyond the regions of interest.

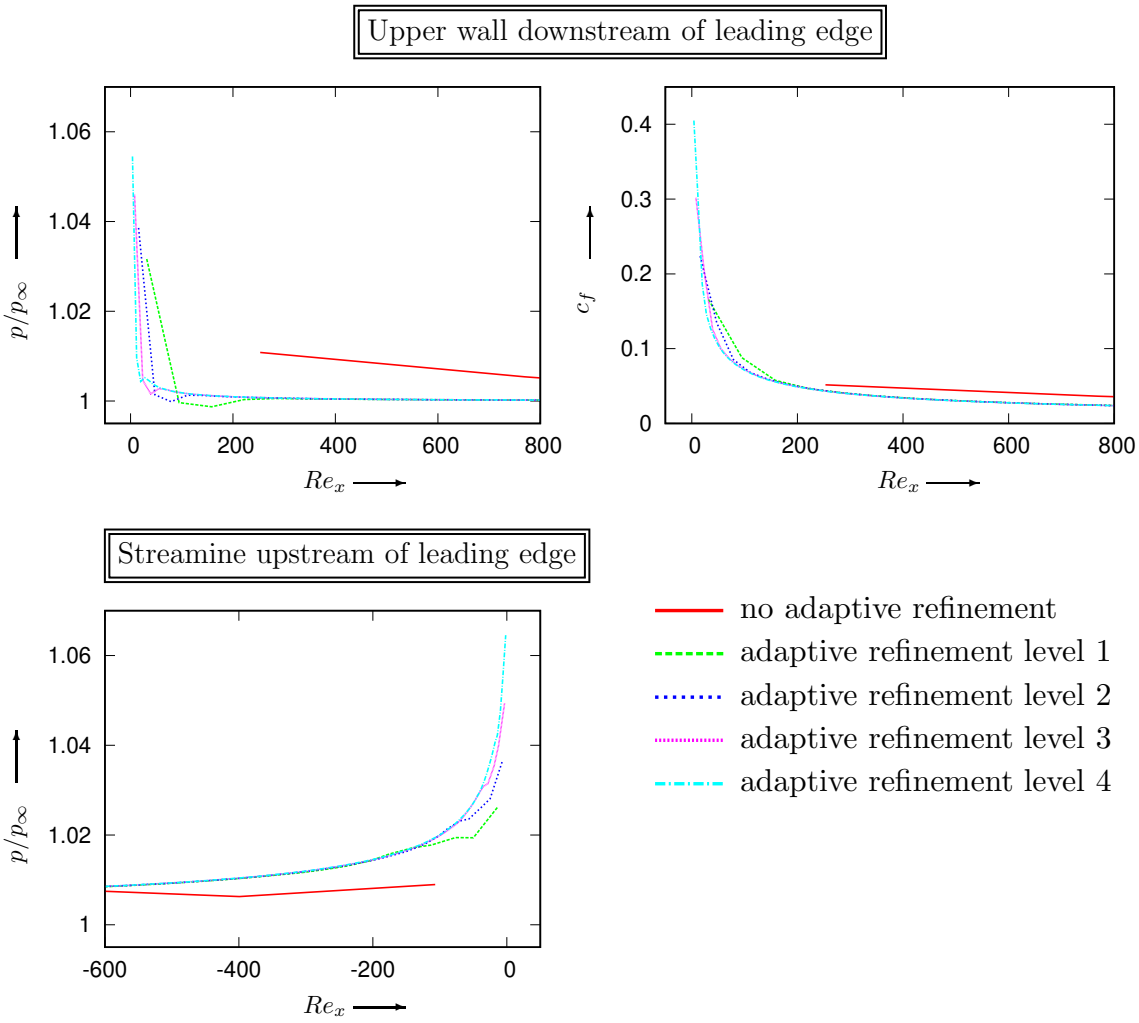

Figure 3.27: Pressure and skin-friction coefficient distributions in the close vicinity of leading edge, computed using TriFar-IsoTriNW grid with 4 levels of adaptive refinement.

3.3.2 Low-Reynolds NACA 0012 Airfoil

A low-Reynolds laminar test-case is performed on the NACA 0012 airfoil at $Re_{\mathrm{V}_\infty, L_{\mathrm{chord}}} = 1000$ where $\mathrm{V}_\infty = \sqrt{u_\infty^2 + v_\infty^2}$ is the incoming streamwise flow velocity at infinity which correspond to a Mach number $M_\infty = 0.2$ and L_{chord} is the chord length of the airfoil. The test-case geometry is shown in Fig. 3.28 with the angle of attack AoA ranging from 0° to 20°. The airfoil is placed at the center of the square computational domain with its leading edge placed at $(0, 0)$. Four boundary edges of the domain are sufficiently far from the airfoil and the Riemann invariant BC is imposed on all of them. The airfoil is considered as adiabatic no-slip wall with its trailing edge rounded to avoid singularity point. The third-order CLSQ3 reconstruction scheme is used for all computations in this section.

$Re_{\mathrm{V}_\infty, L_{\mathrm{chord}}} = 1000$ is an extremely low Reynolds number for an airfoil, which corresponds approximately to the Reynolds regime where typically fly the small insects such as dragonflies

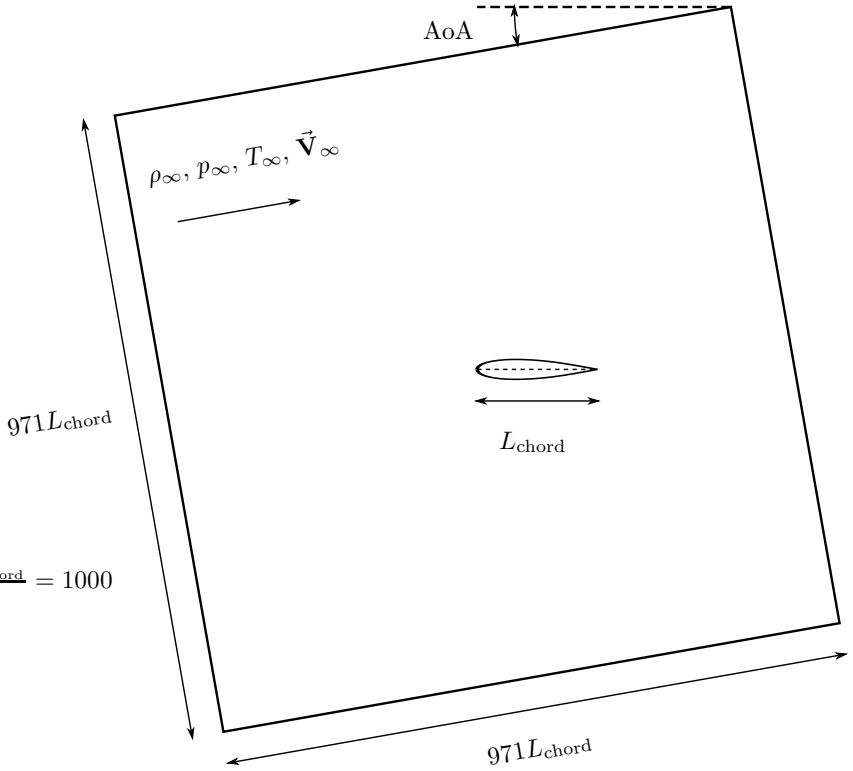

- $Re_{\mathrm{V}_\infty, L_{\text{chord}}} = \frac{\rho_\infty \mathrm{V}_\infty L_{\text{chord}}}{\mu_\infty} = 1000$
- $M_\infty = 0.2$
- $0° \leq \text{AoA} \leq 20°$

Figure 3.28: Geometric set-up of the low-Reynolds NACA 0012 test-case at $Re_{\mathrm{V}_\infty, L_{\text{chord}}} = 1000$. The dashed circle corresponds to near-wall region.

and honeybees [161, 193]. This low Reynolds number is chosen for the current study since the flow remains laminar even for high angle of attack AoA and the transition to turbulence is very unlikely to occur [161]. Following the DNS studies [98], also discussed below, the flow is laminar and steady for AoA $\leq 8°$, with laminar instability (vortex shedding) appearing at higher AoA. As will be shown later, using large Δt and non-time-consistent local time-stepping yields converged computations even at higher AoA, but they should only be considered as computational tests. With this test-case, we intend to demonstrate the robustness of the current numerical methods on different types of polygonal grids and the effectiveness of using local adaptive refinement to improve the accuracy of solutions.

Three types of unstructured grids are generated for this test-case : (i) the purely quadrilateral grid denoted by Quad, (ii) the baseline quad-dominant grid mixed with triangular cells denoted by QuadD-0 and (iii) the QuadD-0 grid refined within the separated region over the upper wall of the airfoil denoted by QuadD-1. Note that Quad and QuadD-0 are dual grids in the sense that they have the same number of grid points but with different connectivity among them. Two views of each grid are shown in Fig. 3.29 around the airfoil and near the trailing edge.

In Fig. 3.30, we compare the pressure contours and surface pressure coefficient C_p distributions obtained on grids Quad, QuadD-0 and QuadD-1 at a high angle of attack AoA = 17°. The wall

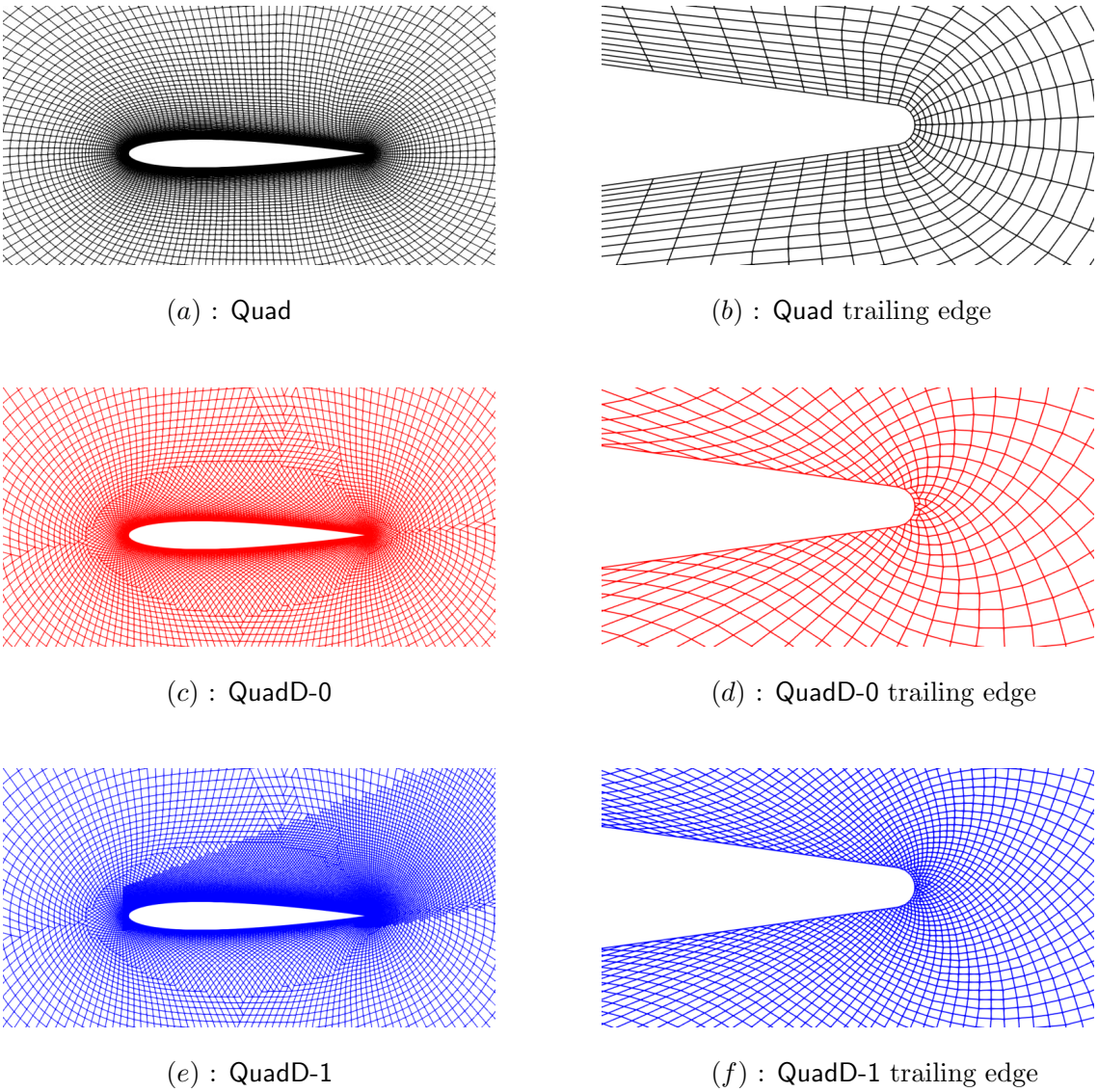

(a) : Quad

(b) : Quad trailing edge

(c) : QuadD-0

(d) : QuadD-0 trailing edge

(e) : QuadD-1

(f) : QuadD-1 trailing edge

Figure 3.29: Three types of unstructured grids used for the low-Reynolds NACA 0012 airfoil test-case : Quad is the purely quadrilateral grid, QuadD-0 is the baseline quad-dominant grid and QuadD-1 is the quad-dominant grid refined within the separation bubble. All grids are shown for AoA = 17°.

pressure coefficient is calculated as

$$C_p = \frac{p - p_\infty}{0.5\rho_\infty \mathrm{V}_\infty^2} \tag{3.10}$$

whose distribution is plotted for each grid against the normalized chord length x/L_{chord} in Fig. 3.30.d. As shown in Fig. 3.30, all three grids generate almost identical results of pressure contour lines on the lower side of the domain, and, on the lower surface, the C_p distributions show no difference up

till $x \approx 0.5L_{\text{chord}}$. On the lower surface near the trailing edge, QuadD-0 gives slightly lower C_p than the two other grids. On the upper surface, however, visible difference in pressure contour lines can be observed between the grid Quad and QuadD-0 although the two grids have the same number of vertices. C_p is slightly lower on the entire upper surface for QuadD-0 than for Quad as shown in Fig. 3.30.d. However, by refining the mesh QuadD-0 exclusively in the separation bubble, grid QuadD-1 is generated and excellent agreement is observed between QuadD-1 and Quad in terms of pressure contour lines and C_p distributions on both upper and lower surfaces.

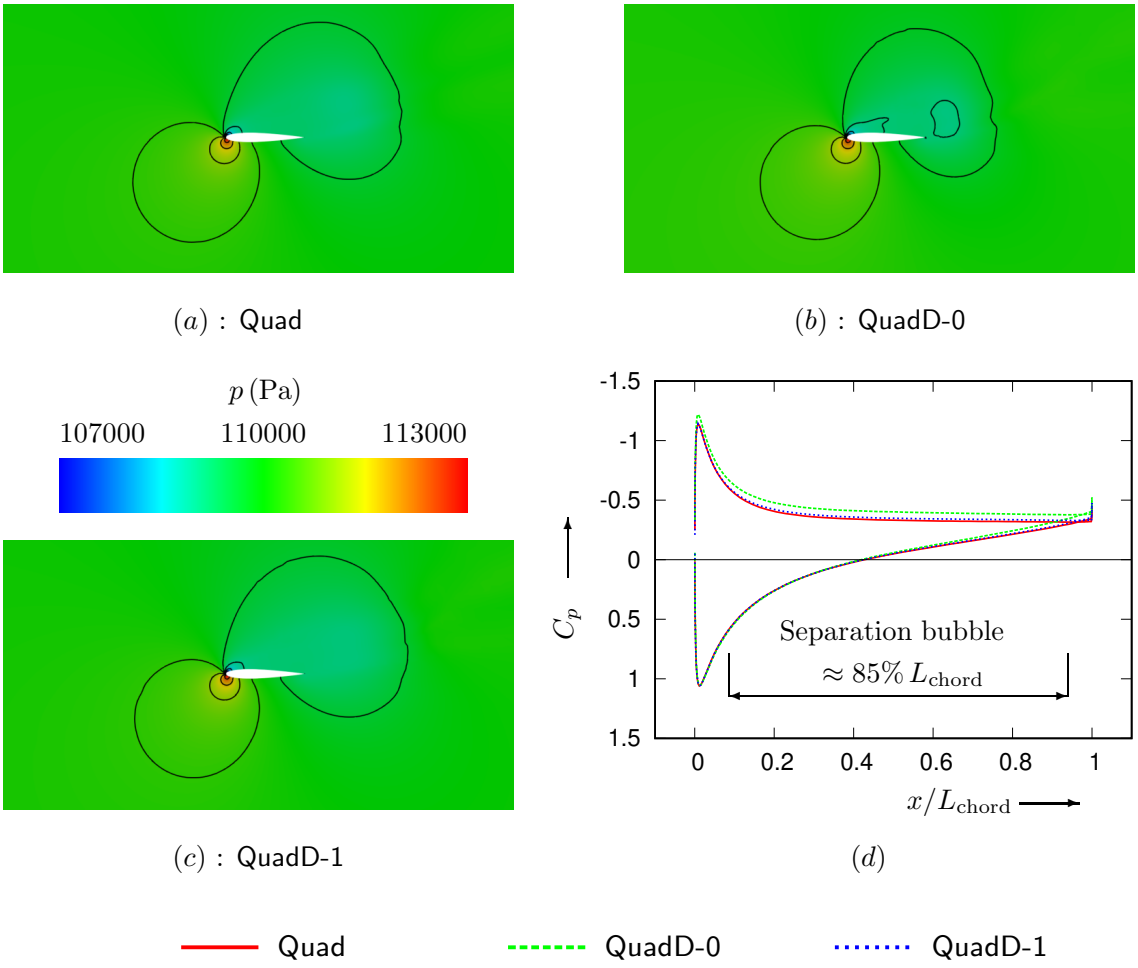

Figure 3.30: Pressure contours (a, b, c) and pressure coefficient distribution on the upper and lower surfaces of the airfoil (d). AoA = 17°. Minor unsmoothness issue due to ParaView rendering.

It is important to note that, at $Re_{V_\infty, L_{\text{chord}}} = 1000$, the C_p distribution around an airfoil is fundamentally different from high-Reynolds test-cases ($Re_{V_\infty, L_{\text{chord}}} = \mathcal{O}(10^6)$) due to the presence of the large laminar separation bubble. According to the experimental data at AoA = 15° given by Ladson *et al.* [138], for $3 \times 10^6 \leq Re_{V_\infty, L_{\text{chord}}} \leq 9 \times 10^6$, the upper surface C_p drops to around -6 and rises back to 0 at the trailing edge as shown in Fig. 3.31. This implies that the lift of the airfoil is considerably reduced at low Reynolds regime. In fact, Mueller [161] pointed out that the airfoil performance decreases sharply as $Re_{V_\infty, L_{\text{chord}}}$ drops below 10^5.

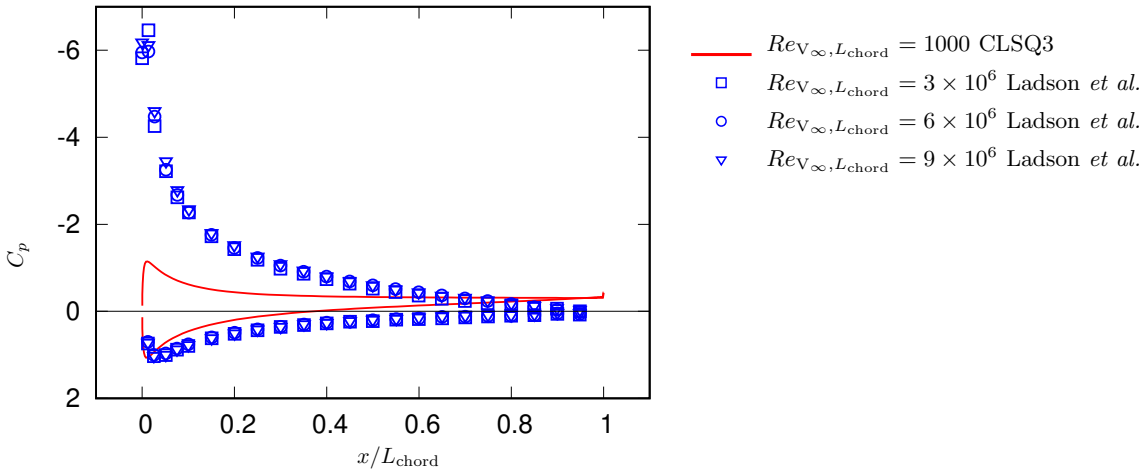

Figure 3.31: Chord-wise pressure coefficient distributions at low and high Reynolds numbers for AoA = 15°. Data source : Ladson *et al.* [138].

In Fig. 3.32, we visualize the upper wall separation bubble at AoA = 17° by coloring the region with negative cell-averaged x-velocity in black, and the skin-friction coefficient c_f on the upper surface is plotted in Fig. 3.32.d. The skin-friction coefficient is defined with respect to the wall-normal direction as follows

$$c_f = \frac{\mu \left.\frac{\partial u}{\partial n}\right|_{\text{wall}}}{0.5\rho_\infty V_\infty^2}. \tag{3.11}$$

Unlike the pressure coefficient, c_f distributions are in excellent agreement for all three grids, and the separation and reattachment locations are almost identically predicted on the three grids which gives a separated bubble of about $85\%L_{\text{chord}}$ in length as indicated by Fig. 3.32.d. Although there is no significant difference in the c_f distribution, we can observe that the unrefined QuadD-0 grid predicts a slightly shorter separation bubble comparing to Quad and QuadD-1, whereas Quad and QuadD-1 give very close predictions on the bubble size (Fig. 3.32.a and .c).

Results given in Fig. 3.30 and Fig. 3.32 show that Quad grid gives more accurate results than QuadD-0 for both pressure contour and separation bubble, since by exclusively refining the mesh within the bubble, results obtained on QuadD-1 reaches an excellent agreement with those obtained on Quad.

In Fig. 3.33, separation bubbles are visualized for four different angles of attack AoA = $\{0°, 5°, 10°, 20°\}$. At AoA = 0°, the laminar boundary layer is attached to the airfoil and no flow separation is observed. As the angle of attack progressively increases, the separation bubble begins to appear and grows larger with increasing AoA. However, even though the separated region occupies almost the entire chord length, the bubble always remains closed up till AoA = 20° and reattaches near the trailing edge.

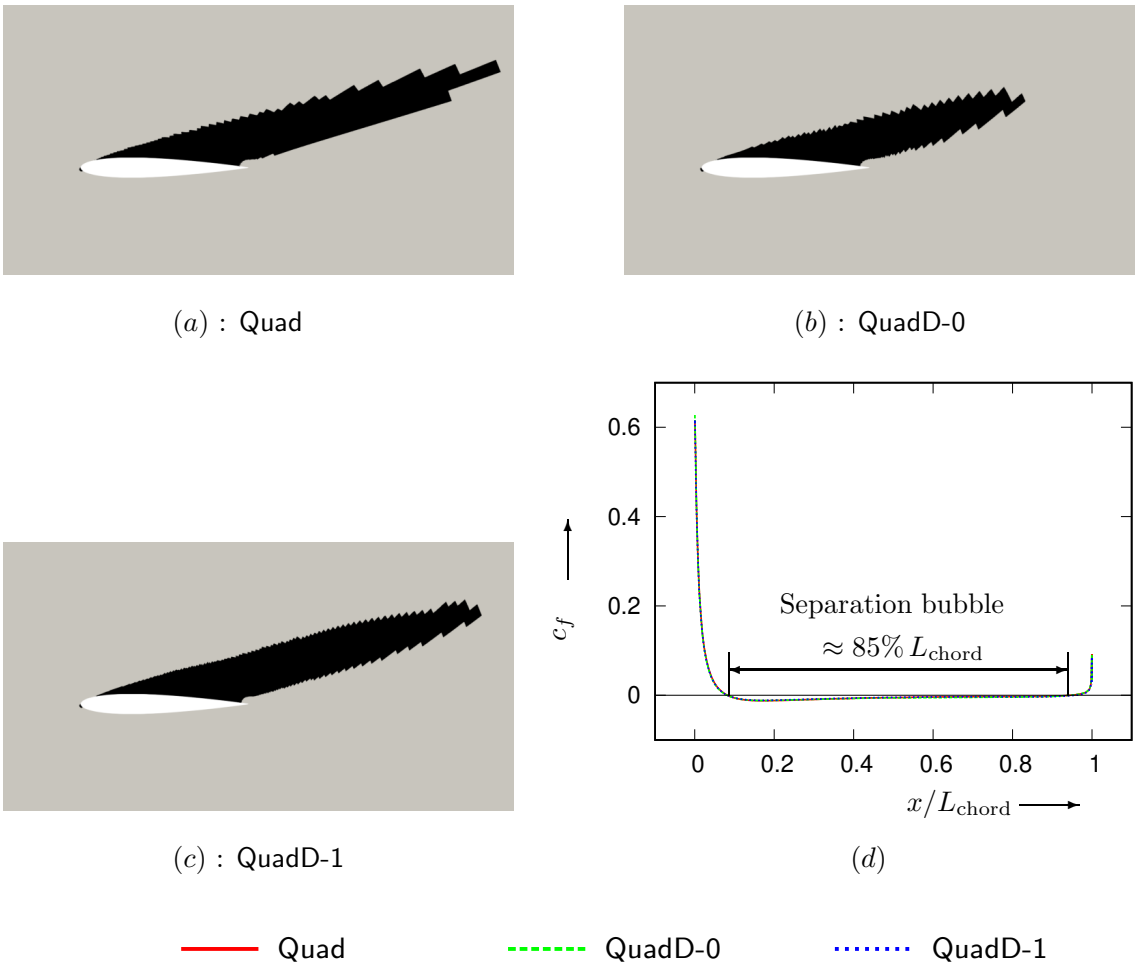

Figure 3.32: Separation bubbles colored in black containing cells with negative u (a, b, c) and distribution of the skin-friction coefficient on the upper surface of the airfoil (d). AoA = 17°.

The lift and drag coefficients are defined as

$$C_L = \frac{\vec{F} \cdot \vec{e}_{\parallel}}{0.5\rho_\infty \mathrm{V}_\infty^2} \tag{3.12a}$$

$$C_D = \frac{\vec{F} \cdot \vec{e}_{\perp}}{0.5\rho_\infty \mathrm{V}_\infty^2} \tag{3.12b}$$

where $\vec{F}$ is the vector of total force exerted on the airfoil by the surrounding flow which is computed by numerically integrating the reconstructed pressure value on all Gauss-Legendre quadrature points of each wall boundary edge and finding the sum over all those wall edges. $\vec{e}_{\parallel}$ is the unit vector parallel to the incident flow with an angle of attack AoA, $\vec{e}_{\perp}$ is the unit vector perpendicular to $\vec{e}_{\parallel}$.

C_L and C_D data are presented in Fig. 3.34 and we remark that the slope of C_L curve becomes

(a) : AoA $= 0°$

(b) : AoA $= 5°$

(c) : AoA $= 10°$

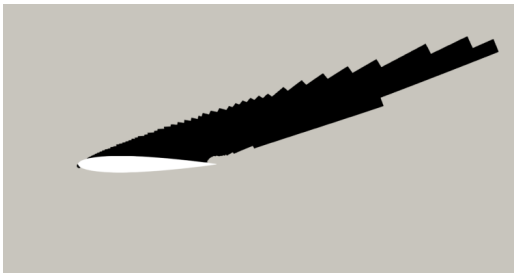

(d) : AoA $= 20°$

Figure 3.33: Cells with negative u constituting the separation bubble at four different angles of attack AoA $= 0°, 5°, 10°, 20°$. Computations performed on Quad grids.

less steep from AoA $\approx 8°$ but remains nevertheless increasing, which indicates that the airfoil does not stall at least for AoA $= 20°$. However, the lift-drag ratio C_L/C_D begins to decline from AoA $\approx 8°$ which indicates that any further increase in AoA from this point will compromise the performance of the NACA 0012 airfoil.

Previous numerical studies by Kurtulus [137] and by Gopalakrishnan Meena *et al.* [98] showed that the flow over NACA 0012 airfoil becomes unsteady for an angle of attack AoA $\geq 8°$, and different modes of periodic von Kármán vortex shedding are observed in the wake region. In Fig. 3.34.a, the time-averaged lift and drag coefficients $\overline{C}_L$ and $\overline{C}_D$ obtained from the unsteady DNS by Gopalakrishnan Meena *et al.* [98] are compared with the current steady-state solutions of C_L and C_D. A good agreement between $\overline{C}_L$ and C_L is observed for $0° \leq$ AoA $\leq 7°$ and the current C_D result is almost identical to the DNS data for $0° \leq$ AoA $\leq 9°$. However, as the unsteadiness of the flow grows stronger at higher angles of attack up till AoA $= 20°$, the current steady-state computations underestimate both C_L and C_D approximately by 50% comparing to the DNS data.

The objective of this study on very low-Reynolds NACA 0012 airfoil has managed to demonstrate that the current numerical methods are robust on arbitrary polygonal grids with the ability to handle arbitrary local grid refinement. However, by comparing to the previous DNS data [98], we realize that the flow field is predominantly unsteady for moderate and high angles of attack and therefore the current steady-state simulations tend to give inaccurate results as AoA increases beyond $8°$. It is an interesting perspective in the future to further investigate the unsteadiness of the flow field with time-consistent computations using arbitrarily high-order CLSQ schemes and

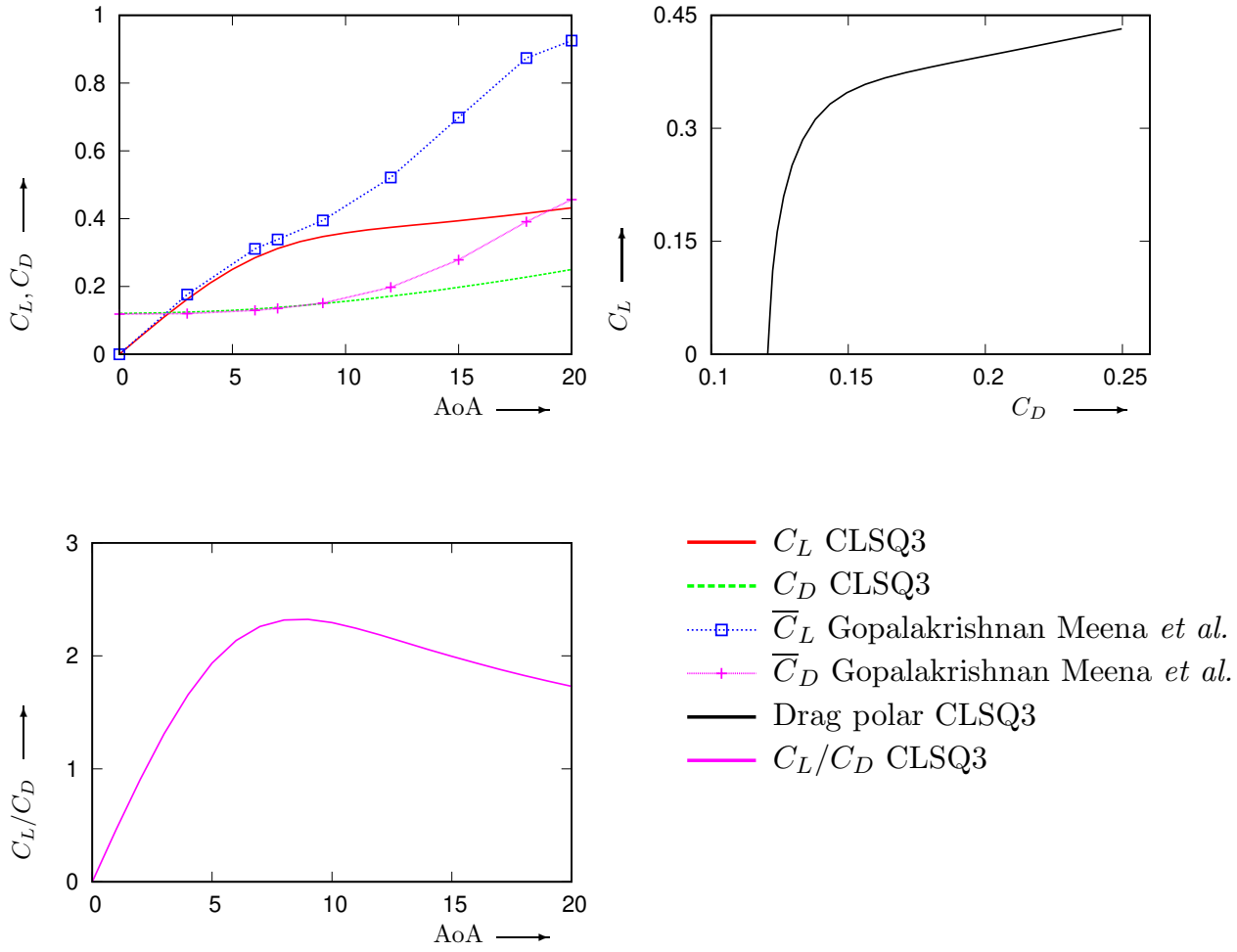

Figure 3.34: Curves of lift and drag coefficients for $0° \leq \text{AoA} \leq 20°$ compared to the time-averaged lift and drag coefficients from the unsteady DNS simulations of Gopalakrishnan Meena *et al.* [98]

adaptive local refinements within the wake region.

3.3.3 Backward-Facing Step (BFS)

The detailed description of the BFS test-case by Armaly *et al.* [13] is given in Section. 4.2 with a sketch of the computational domain shown in Fig. 4.1. In this section, we focus on discussing the possibility of meshing the domain with three different types of unstructured polygonal grids without elaborating on the flow physics.

The three types of baseline (coarse) polygonal grids are (*a*): Cartesian grid (*i.e.,* Grid 0 in Tab. 3.1), (*b*): triangular grid and (*c*): pentagonal-hexagonal grid as illustrated in Fig. 3.36. Note that the pentagonal-hexagonal grid also contains a very small number of rectangles and triangles at the vertical wall, the pentagons are used at the horizontal walls and along the dividing line between the upper and lower subdomains, and the interior domain is meshed by hexagons. Tests are performed for Reynolds number $Re_{u_B,D_h} = 100$ which admits a relatively small primary recirculation zone and no roof vortex. In order to enhance the resolution of the separated flow downstream of the step, adaptive mesh refinement is performed which created at most 3 layers of locally refined meshes enveloping the primary recirculation zone. Each cell in the refined region is divided by rules illustrated in Fig. 3.35 according to its shape. Note that the divisions of pentagons and hexagons do not preserve the angle, therefore an excessive number of divisions tends to create smaller pentagons and hexagons with angles close to 0° or 180°. For this reason, the number of refinement levels is limited to 1 for the pentagonal-hexagonal grid [2].

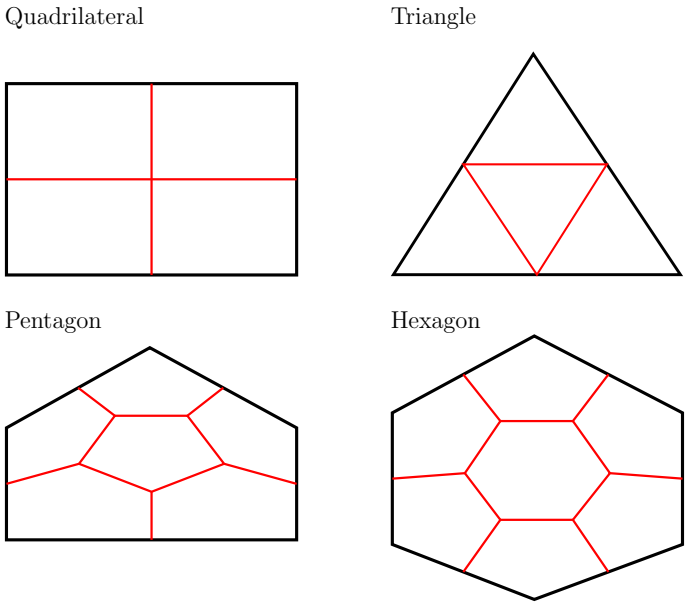

Figure 3.35: Subdivision rules for quadrilateral, triangular, pentagonal and hexagonal cells. Red line segments represent the dividing lines.

As shown in Fig. 3.37, three levels of adaptively refined layers are constructed around the primary recirculation zone colored in blue where the streamwise velocity $u < 0$. Although the

[2] this problem can be easily handled by subdividing N-gons with $N > 4$ into N quadrilaterals. It is an issue related to the adaptive subdivision methodology, not to the solver itself. The subdivision method of Fig. 3.35 for pentagon and hexagons is not appropriate for stretched grids, and is only used here for illustration purposes in order to maintain pentagons and hexagons in the level 1 refinement

(a): Cartesian

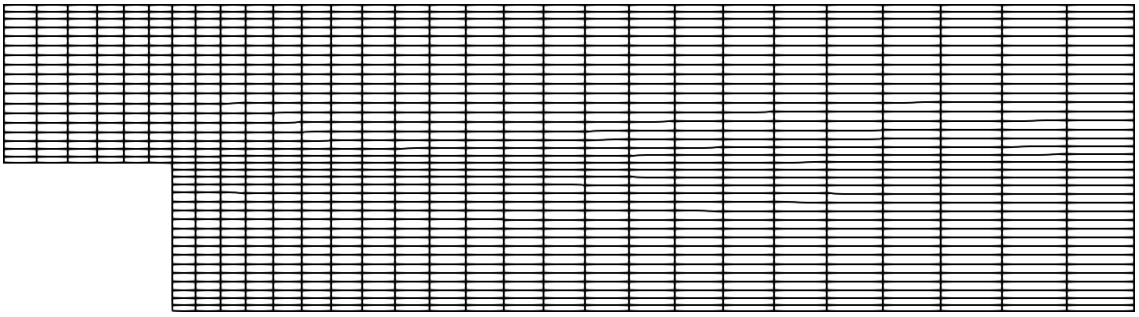

(b): Triangular

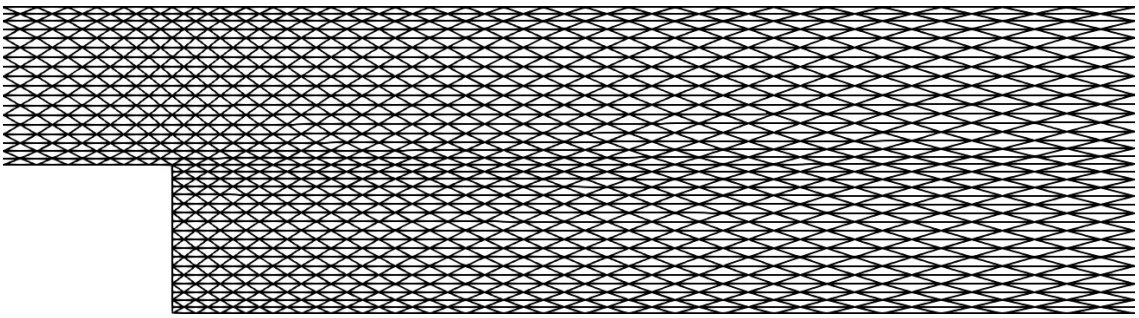

(c): Pentagonal-hexagonal

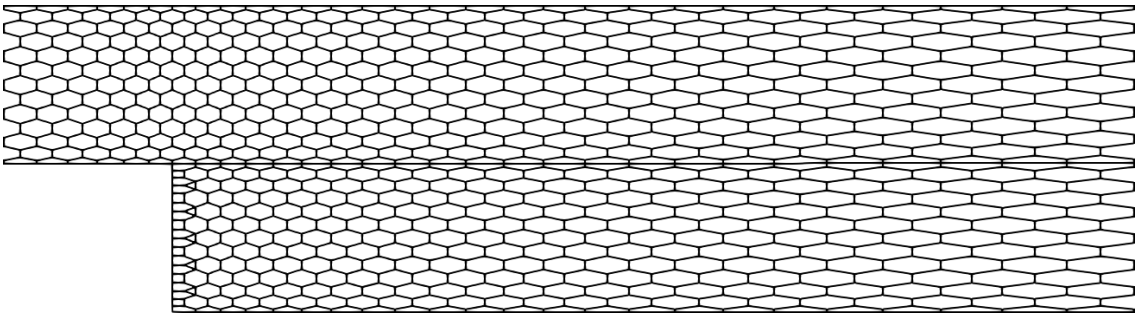

Figure 3.36: Three types of baseline unstructured meshes for the BFS test-case of Armaly *et al.* [13].

majority of cells are divided according to rules in Fig. 3.35, the interfaces between two levels of layers are meshed in different ways in order to avoid hanging nodes on edges with a jump in mesh size between both sides. By breaking the division rules in Fig. 3.35 at layer interfaces, irregular triangles and quadrilaterals are created in the process therefore the Cartesian grid in Fig. 3.36

becomes rectangle-dominant grid in Fig. 3.37, and the pentagonal-hexagonal grid in Fig. 3.36 becomes pentagon-hexagon-dominant grid in Fig. 3.37 as a matter of terminology. All three levels of refinements (level 1-3) are applied to the rectangle-dominant grid, the level 1-2 are applied to the triangular grid. Only the level 1 is applied to the pentagon-hexagon-dominant grid since any further division of the stretched near-wall pentagons and hexagons will result in increasingly skewed cells (this can be remedied using a different subdivision technique as mentioned before).

The mesh quality optimization for unstructured grids is not within the scope of the current study, rather, we intend to demonstrate that the numerical schemes remain robust and accurate for arbitrary polygonal grids even the ones with low-quality cells. As shown in Fig. 3.38, the time-integration error ${}^{n}\varepsilon$ for each type of polygonal grid is driven down to the machine epsilon $\varepsilon \approx -14$ with its respective finest level of adaptive refinement (level 3 for the rectangle-dominant grid, level 2 for the triangular grid and level 1 for the pentagon-hexagon-dominant grid). This demonstrates that the method is reasonably insensitive to mesh quality and remains robust for arbitrary polygonal grids.

The normalized streamwise velocity profiles are plotted in Fig. 3.39 at sampling stations within the level-1 refined region for the three baseline grids in Fig. 3.36 with no refinement. Excellent agreement is observed among the three polygonal grids which again confirms the insensitivity to mesh type.

Velocity profiles at the same sampling stations are shown in Fig. 3.40 for all adaptive refinement levels of each of the three types of polygonal grids. Excellent agreement is again observed across all refinement levels. Although a closer view is needed to determine if the solutions are grid-converged, it is confirmed that the profiles remain smooth and physically consistent after adaptive mesh refinements even though the mesh quality is not ideal and the mesh size is discontinuous at interfaces between two layers of refinements.

Next, we investigate the effects of adaptive mesh refinement by showing the reconstructed pressure and skin-friction coefficients on the bottom wall. Fig. 3.41 and Fig. 3.42 respectively show the wall coefficients downstream of step ($0 \leq x \leq 20$) and near the step ($-0.5 \leq x \leq 0.2$) on adaptively refined rectangle-dominant grids. Both wall coefficients show a clear converging trend towards the curves of Level 3 downstream of the step. The same converging trend is observed in the near-wall region in Fig. 3.42 except for the values of local extrema extremely close to the singularity point $x = 0$. The local extrema of C_p and c_f show no sign of converging as the mesh is progressively refined. This phenomenon is also observed in the previous Section. 3.3.1 for the zero-thickness flat-plate boundary layer test-case and we have suggested that the reason for non-converging locally extrema is caused by the geometric singularity rather than the inconsistency of spatial discretization, since the wall coefficient curves converges well towards the finest level of refinement everywhere away from $x = 0$.

Reconstructed wall coefficients on the bottom wall are also plotted for the 2-level refined triangular grid and are shown in Fig. 3.43 and Fig. 3.44. Compared to the rectangle-dominant grid, the convergence property is less ideal for the triangular grids. In Fig. 3.43, the improvement of solution is less pronounced than that in Fig. 3.41 for the rectangle-dominant grids and all three levels of grids give almost identical wall coefficient distributions downstream of the step as well as in the near-step region. This observation shows that the adaptive refinement procedure brings less improvement in solutions for the triangular grids comparing to the rectangular grids. Although the current CLSQ reconstruction schemes remain robust on arbitrary polygonal grids, the mesh quality is still an important factor for good grid convergence property. Therefore, in the next Section. 3.2, we will adopt the Cartesian grid for the formal convergence rate evaluation of the third-order CLSQ scheme.

(a): Rectangle-dominant

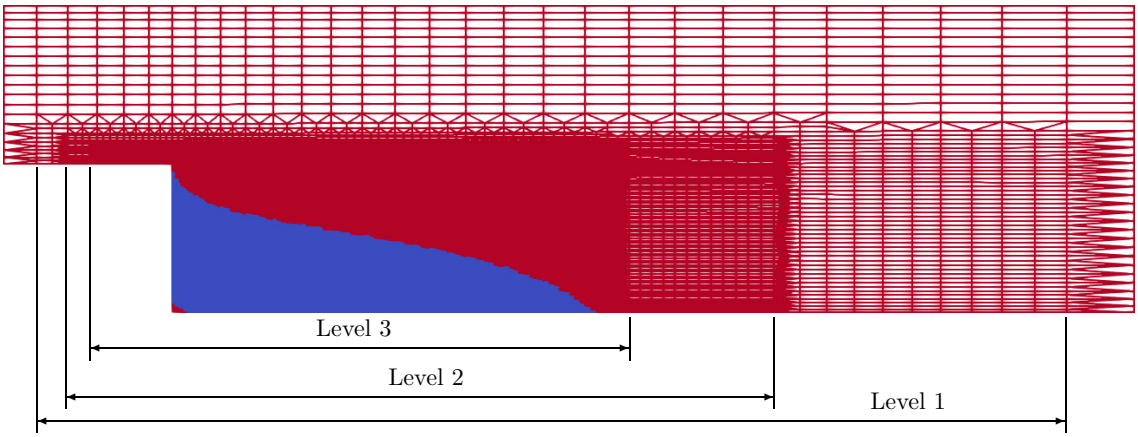

(b): Triangular

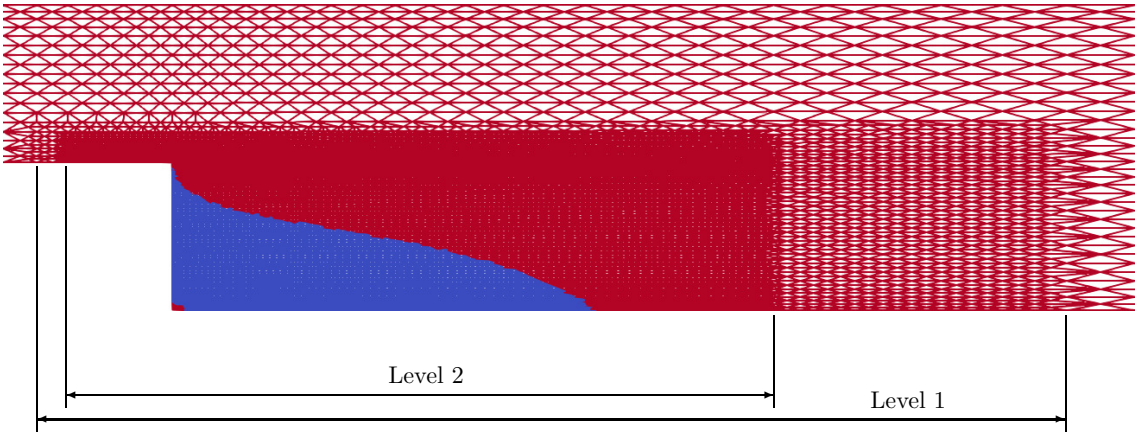

(c): Pentagon-hexagon-dominant

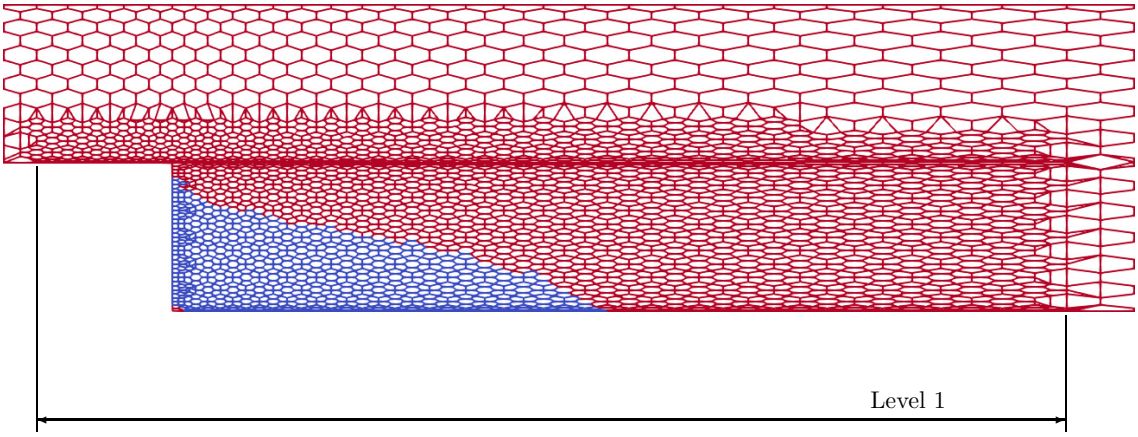

Figure 3.37: Three levels of adaptive refinement enveloping the primary recirculation zone at $Re_{u_B,D_h} = 100$. The zone colored in red has x-velocity $u > 0$ while the blue region has $u < 0$.

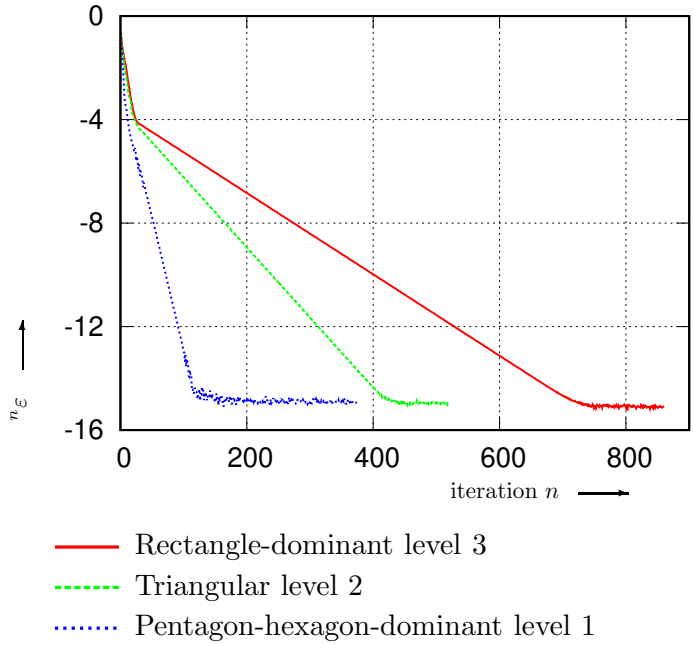

Figure 3.38: Convergence history comparison among the three types of adaptively refined polygonal grids.

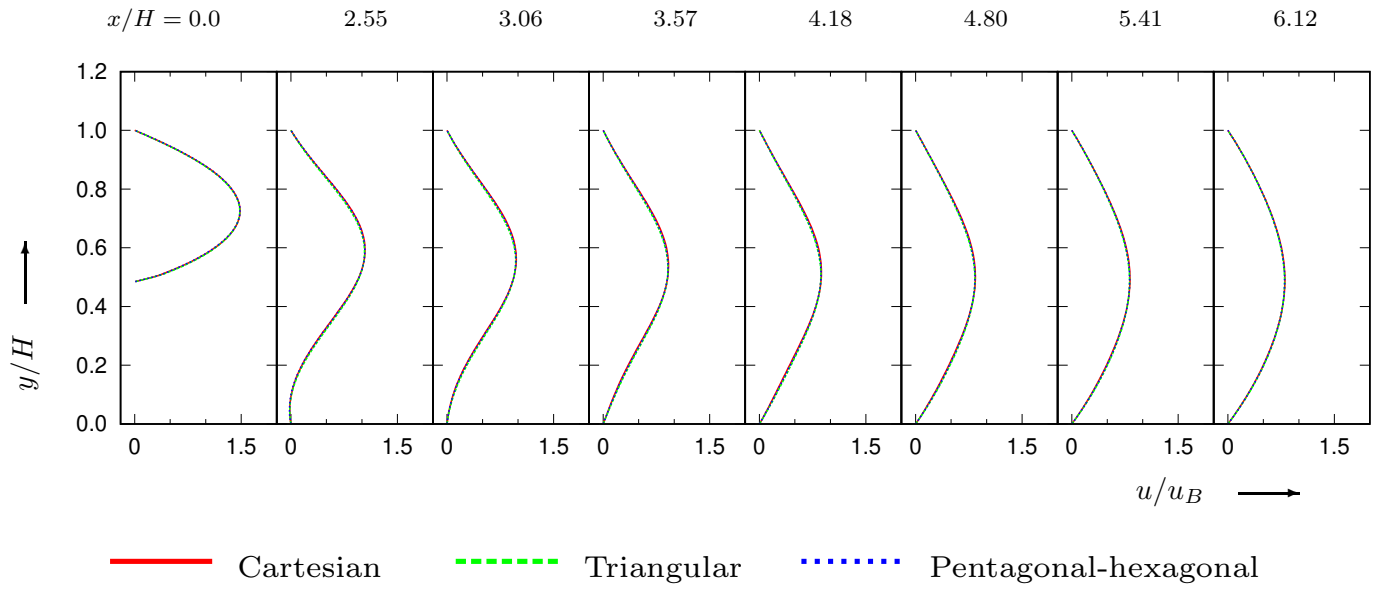

Figure 3.39: Normalized streamwise velocity profiles. Comparison made among the three baseline unstructured grids without adaptive refinement.

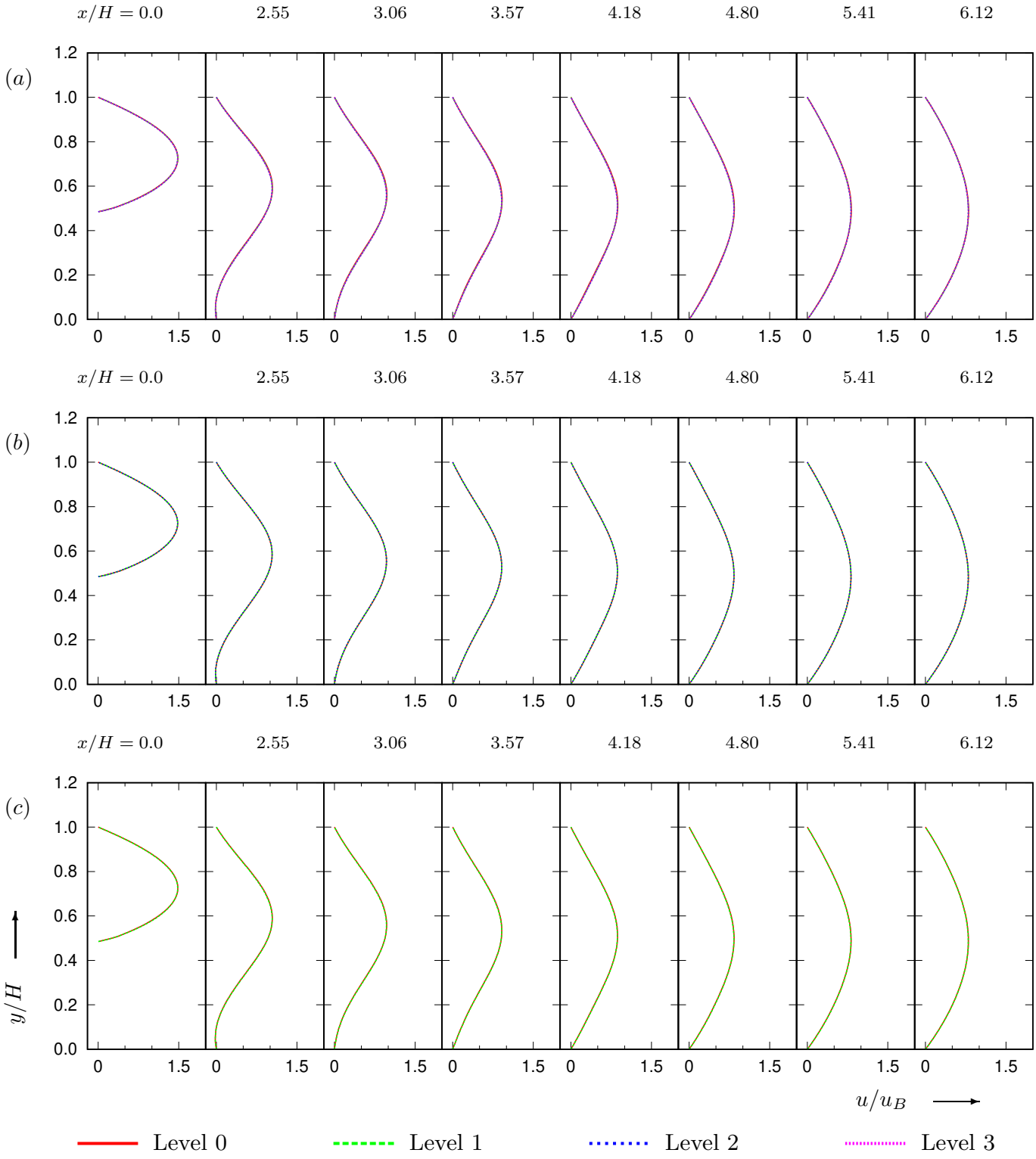

Figure 3.40: Streamwise velocity profiles on the three adaptively refined unstructured grids. Comparison made among all levels of refinement. (a) : rectangle-dominant, (b) : triangular, (c) : pentagon-hexagon-dominant.

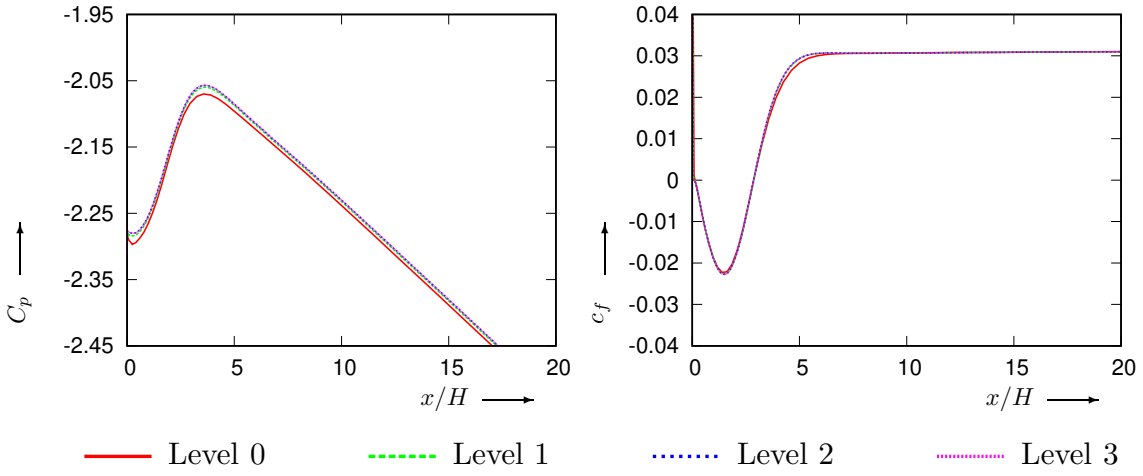

Figure 3.41: Pressure coefficient C_p and the skin-friction coefficient c_f on the bottom wall plotted against x-coordinate normalized by the step height H. Computed with 4 levels of adaptively refined Cartesian grids.

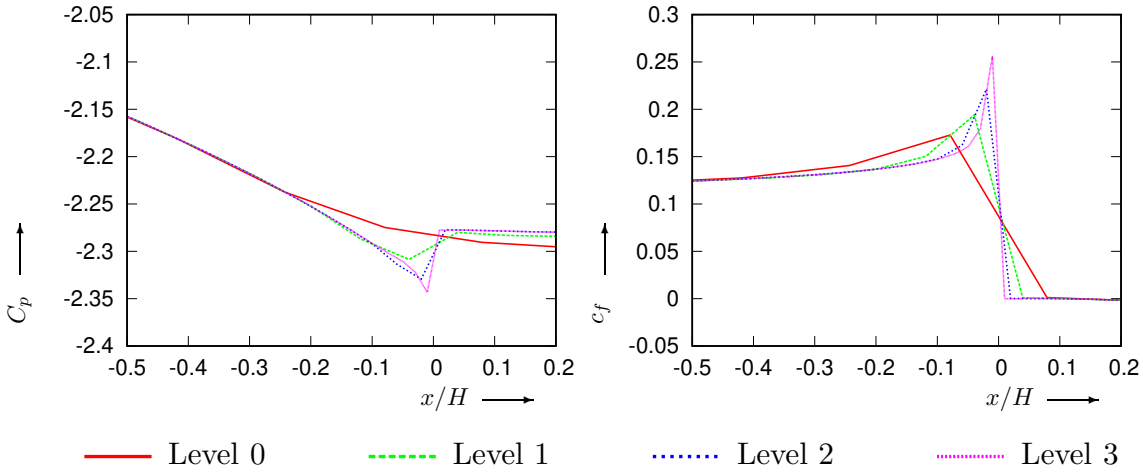

Figure 3.42: Pressure coefficient C_p and the skin-friction coefficient c_f on the bottom wall plotted against x-coordinate normalized by the step height H. Computed with 4 levels of adaptively refined Cartesian grids. Results near the step $x = 0$ are shown.

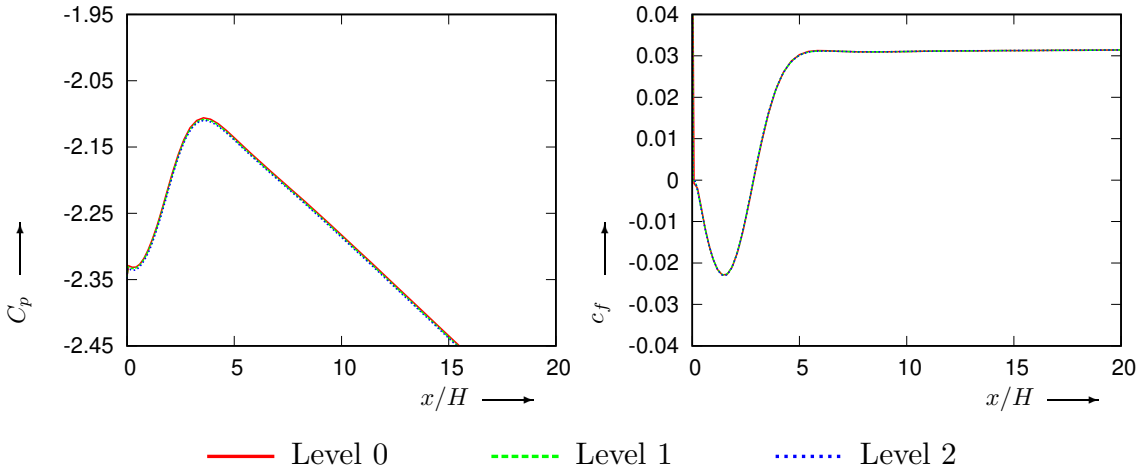

Figure 3.43: Pressure coefficient C_p and the skin-friction coefficient c_f on the bottom wall plotted against x-coordinate normalized by the step height H. Computed with 3 levels of adaptively refined triangular grids.

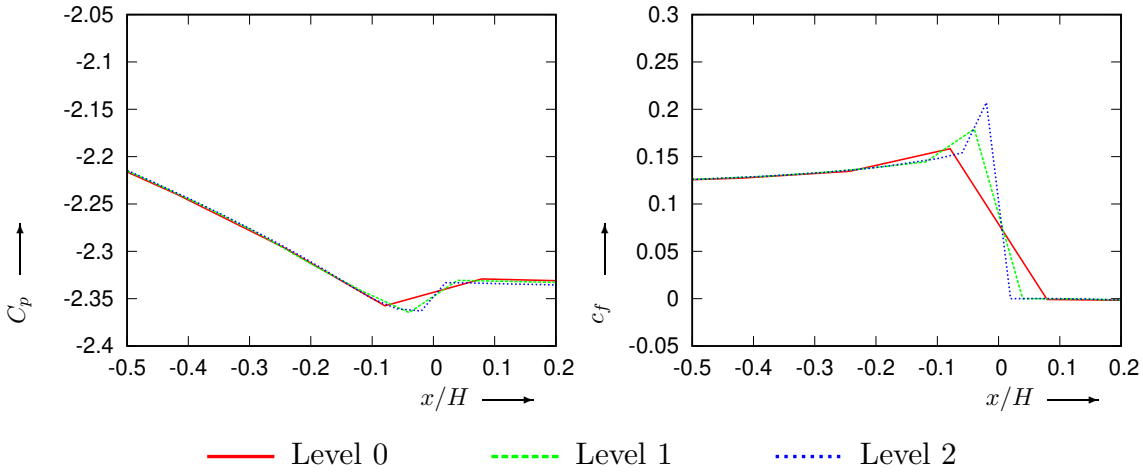

Figure 3.44: Pressure coefficient C_p and the skin-friction coefficient c_f on the bottom wall plotted against x-coordinate normalized by the step height H. Computed with 3 levels of adaptively refined triangular grids. Results near the step $x = 0$ are shown.

Chapter 4

Flow Physics Analyses

4.1 Literature Review on Laminar BFS Flows

Widely considered as one of the most studied test-cases in CFD for solver validation, the backward-facing step (BFS) flow has attracted an enormous amount of research throughout the last decades due to its relative geometrical simplicity and complex flow features such as boundary-layer separation and reattachment, adverse pressure gradient, flow instabilities, *etc.* Studies on the BFS can be categorized based on different criteria. In terms of flow regimes, one can focus on the laminar, transitional, or fully turbulent BFS flows. Based on the methodology, researches are divided into experimental and numerical investigations or a combination of these two. Given the abundance of literature, the terminology adopted by different authors varies significantly and particularly in definitions of geometrical parameters and Reynolds number. Therefore it is important to establish a standardized BFS nomenclature at the beginning of this literature review.

In the present study, unless clearly specified otherwise, the height of inlet channel upstream of the step is denoted by H_i while that of the outlet channel downstream of the step is denoted by H_o, and the step height is denoted by H, knowing that $H_o = H_i + H$ (Fig. 4.1). The Reynolds number is a pivotal parameter in the BFS configuration, and a large number of definitions are encountered in the literature. We adopt a two-subscript notation $Re_{\text{vel,len}}$ to denote different Reynolds numbers having appeared in the literature. Subscript "vel" denotes the velocity and subscript "len" denotes the length as shown in Tab. 4.1 where u_B is the bulk velocity, u_∞ is the free-stream or maximum

Table 4.1: Velocities and lengths used for Reynolds number definitions in the literature of laminar BFS.

i	velocity	j	length
1	u_B	1	H
2	u_∞	2	H_i
		3	D_h

velocity, which, for laminar channel flows, is the streamwise velocity on the centerline. Ideally, all above quantities are evaluated at the step before the separation occurs, however, many authors have computed their Reynolds numbers based on the inlet flow conditions assuming a negligible

difference between the two states. For instance, Re_{u_∞,D_h} denotes the Reynolds number based on the free-stream velocity and hydraulic diameter at step.

In 1960, Moore [159] experimentally investigated the reattachment of a laminar boundary layer over BFS and concluded that, after reattachment, the incipient laminar boundary layer often turned turbulent. Goldstein *et al.* [97] reported the possibility for a laminar BFS flow to remain laminar after reattachment as long as the displacement thickness $\delta_1 > 0.4H$ and $Re_{u_\infty,H} < 520$, empirical formulas to predict reattachment length were given. De Brederode *et al.* [62] investigated the two-dimensionality in three-dimensional BFS flow and showed that the laminar or turbulent flow was essentially 2D (negligible corner flow effects) in a channel with an aspect ratio $AR > 10$. This criterion later became a standard practice for three-dimensional experimental and computational studies to produce nominally two-dimensional flows.

Thanks to the development in flow measurement techniques such as the Laser-Doppler Velocimetry (LDV), in 1983, Armaly *et al.* [13] carefully studied the separation and reattachment locations in a range of $70 < Re_{u_B,D_h} < 8000$ with a fixed expansion ratio of 1.94 and a aspect ratio of 36. Armaly *et al.* identified the Re_{u_B,D_h} ranges for the laminar ($Re_{u_B,D_h} < 1200$), transitional ($1200 < Re_{u_B,D_h} < 6600$), and turbulent ($Re_{u_B,D_h} > 6600$) flow regimes and showed that two-dimensional flow behavior was only witnessed at $Re_{u_B,D_h} < 400$ and $Re_{u_B,D_h} > 6000$. Multiple separated regions appeared and vanished as Reynolds number increased. Following the authors' notation, in the present study, the principal reattachment length is denoted by x_1. A secondary recirculating region was found downstream of x_1 [13] which stretched over around $2H$ at the onset of flow transition ($Re_{u_B,D_h} \approx 1200$) and disappeared at $Re \approx 2300$. We denote its head and tail by x_2 and x_3 respectively. A roof vortex was also found by Armaly *et al.* at the wall opposite to step which appeared from the beginning of laminar regime to the end of transitional regime due to adverse pressure gradient. We denote the head of the roof vortex by x_4 and its tail by x_5. Second-order accurate 2D computations were performed by Kim and Moin [130] using a fractional-step incompressible code. Good agreement was obtained with [13] in terms of the prediction on principal reattachment length for $Re_{u_B,D_h} \leq 500$. Deviation from the experimental data was observed for higher Reynolds number due to three-dimensionality. Caruso *et al.* [82] obtained almost identical computational result to [130] at $Re_{u_B,D_h} \leq 600$ with an overlapping grid technique. Thangam and Knight [204] investigated the combined effects of Reynolds number and expansion ratio on the principal reattachment length and concluded that increasing ER led to delayed reattachment at a given Reynolds number Re_{u_∞,D_h} due to increased adverse pressure gradient and wall friction. Moreover, the authors reported that, with high ER at high Re_{u_∞,D_h}, the pressure rise downstream of the step caused the streamlines to deflect towards the bottom which further accelerated reattachment resulted in a non-linear reattachment-length-Re curve.

In [84], Gartling provided 2D numerical solutions of laminar BFS flows up to $Re_{u_B,D_h} = 800$ with an expansion ratio of 2.0. Computations were performed using a Galerkin-based finite element code with up to second-order accuracy for the momentum equations and first-order for pressure. At $Re_{u_B,D_h} = 800$, Gartling reported an expected discrepancy with [13] due to three-dimensional effects for $Re_{u_B,D_h} > 400$, however, the results confirmed the presence of roof vortex at $Re_{u_B,D_h} = 800$ and predictions on the separation and reattachment locations showed reasonable agreement with that of previous computations [82, 130]. Kaiktsis *et al.* [124] performed DNS computations based on a high-order spectral element method and suggested that the BFS flow experienced quasi-periodic unsteadiness at $Re_{u_B,D_h} = 800$ which contradicted most of previous experimental and numerical results. However their finding was consistent with Sethian and Ghoniem [183] who performed computations solving the two-dimensional vortex transport equation from Reynolds numbers $Re_{u_B,H} = 50$ to $Re_{u_B,H} = 5000$ and found unsteady vortex pattern at $Re_{u_B,H} = 500$

(corresponding to $Re_{u_B,D_h} \approx 1000$). Sethian and Ghoniem attributed their discrepancy with the experimental result in [13] to the lack of vortex-stretching term in their 2D simulation. Gresho *et al.* [99] later demonstrated that the flow was indeed steady and stable at $Re_{u_B,D_h} = 800$ to both large or small perturbations using four independent time-marching and steady-state methods. The authors also suggested that the unsteadiness reported by [124] was numerically induced due to under-resolution. The error committed in [124] was also recognized (according to Gresho *et al.* [99]) by one of its co-authors Karniadakis. In a later revisit on this problem, Kaiktsis *et al.* [125] argued that the fundamental frequency of perturbation close to the shear layer frequency could induce flow unsteadiness at $Re_{u_B,D_h} \leq 1200$.

Barton [21] investigated the influence of upper wall on flow reattachment and suggested that the upper recirculation region caused downward deflection of streamlines which resulted in reduced reattachment distances. Later, the author further studied the entrance effects on laminar BFS flows [22] and concluded that the use of entrance channel had the effect of reducing the principal reattachment length x_1 and the upper separation length x_3. Calculations with entrance channels gave better agreement with available experimental data than those without. By imposing a uniform velocity profile at the beginning of entrance channel, the author observed a thicker boundary layer at the upper wall than at the lower wall at the step.

Due to improvement on computational resources in the late 90's, an increasing amount of three-dimensional computations on BFS flows became available. Steady three-dimensional computations were performed by Jiang *et al.* as well as by Williams and Baker [118, 217] on the experimental configuration of Armaly *et al.* [13] to account for 3D effects at $Re_{u_B,D_h} > 400$, and the computational results of x_1 up to $Re_{u_B,D_h} = 800$ showed good agreement with [13]. A series of three-dimensional computations were published by the research group of Chiang and Sheu [44, 45, 46, 185] focusing on the vortical structure of 3D laminar BFS flows. The range of Reynolds number was limited to $100 \leq Re_{u_B,D_h} \leq 1000$ in this series. Streamline patterns were draw so that the separation/reattachment line, critical points, and vortical cores could be identified. The end-wall effects were carefully studied and more two-dimensional-like flow pattern as the channel width increased from $2H$ to $100H$ ($35H$ in [13]). For a fixed channel width, the authors noted that the end-wall effect increased with the Reynolds number which agreed with the finding of Armaly *et al.* that for a laminar BFS flow, three-dimensionality is important beyond $Re_{u_B,D_h} = 400$. However, discrepancy was shown between experimental and 3D numerical results in terms of stream-wise velocity profiles at $Re_{u_B,D_h} = 1000$ [46]. Guerrero and Cotta [101] showed computational results using a stream-function-based semi-analytical method up to $Re_{u_B,D_h} = 1942$ which corresponds to $Re_{u_B,D_h} = 1000$ in [13]. The 2D computations showed good agreement with experimental data by Armaly *et al.* at low Reynolds number but failed, as expected, at $Re_{u_B,D_h} = 1000$ although excellent similarity to 2D result in [46] at the same Reynolds number was shown. The above numerical tests showed that computations had difficulty predicting the flow approaching transitional regime, this may be attributed to the controversial unsteadiness problem at $Re_{u_B,D_h} > 800$ [99, 124, 125].

Iwai *et al.* [114] performed 3D computations based on [13] resolving also the energy equation at small Reynolds numbers $Re_{u_B,D_h} < 400$. Adiabatic condition was imposed on side walls while bottom and upper walls were considered isothermal, the study provided data for heat transfer properties namely the distribution of Nusselt number Nu at the bottom wall defined as $Nu = q_w H/[k(T_w - T_i)]$, where q_w is the wall heat flux, k is the thermal conductivity, T_w and T_i are wall and inlet temperature respectively and both are constant. Maximum Nusselt number was found to rise as the channel aspect ratio and Reynolds number increased which implied a higher heat transfer rate. Based on the experiment in [14], 3D numerical solutions were obtained by Nie and Armaly [164] in a relatively low-aspect-ratio channel (width $W = 8$cm, $H = 1$cm, $ER = 2$) at

fixed Reynolds number $Re_{u_B,D_h} = 343$ with varying step height H and the distributions of Nusselt number and its gradient were found to be highly related to the step height, authors showed that the gradient of Nusselt number increased with step height in the principal recirculating flow region. The same configuration in [14] was repeatedly adopted in numerical and experimental studies by Armaly *et al.* [15, 165, 166] to investigate flow patterns within the principal recirculation region ([166] also studied transitional and turbulent cases). This series of works demonstrated the development of multiple so-called "jet-like" flows from sidewalls which traveled in the span-wise direction and finally impinged on the bottom wall. These jet-like flows were reported to be responsible for increased Nusselt number and reduced reattachment length in the recirculating region and make it difficult to define the reattachment line other than using the two-dimensional definition $\partial u/\partial y|_w = 0$ [165]. Similar to the principal recirculation region, the size of lateral recirculation regions (jet-like flows) increased with Reynolds number [15].

In the work of Biswas *et al.* [28], computations were performed at very low Reynolds number $10^{-4} \leq Re_{u_B,D_h} \leq 1$ to capture Moffatt eddies [158] when Reynolds number approaching zero. Pressure loss was investigated in the work and was found to be positively related to the step height and negatively related to the Reynolds number except for flows with high expansion ratio $ER \geq 2.5$ at $Re_{u_B,D_h} > 200$. Three-dimensional computation confirmed the onset of transitional regime at $Re_{u_B,D_h} = 1200$ instead of 800 predicted by Kaiktsis *et al.* [124]. Reattachment locations determined by streamline pattern and by zero-gradient method were not identical which confirmed the claim in [165].

Further attention to the nonlinear dynamics approaching the transitional point was paid by Rani and Sheu [173] by employing the bifurcation theory. A more recent study by Malamataris [151] with 3D steady-state Galerkin finite element code on a configuration of $ER = 2$, $AR = 40$ (experiment set-up of Lee and Mateescu and Tylli *et al.* [145, 208]) placed the steadiness upper bound at $Re_{u_B,D_h} = 950$ while the experimental data on the same configuration showed $Re_{u_B,D_h} = 1150$ [145] and $Re_{u_B,D_h} = 800$ [208] respectively.

The latest publication on laminar BFS flow by Juste *et al.* [123] focused on the development of the roof separation region in low-aspect-ration channels with $AR = 4$ and $AR = 8$ for an expansion ratio of 2 and at Reynolds numbers from 50 to 1000. Both experiments and computations were performed, results showed a downstream movement of roof vortex as well as an increase in length with increasing Reynolds number. In the case where $AR = 8$, the roof vortex was reported to grow faster in width and height than in the $AR = 4$ case which could even cause merging with the principal recirculation zone near sidewalls at high Reynolds number. The blockage effect at upper wall increased at sidewalls as Reynolds number increased causing larger difference in reattachment length near sidewalls and at centerline.

A detailed literature review on the experimental and numerical turbulent BFS flows is given in Appendix. C.

4.2 Results of Laminar BFS Flows with CLSQ3

In this section, we study the numerical solutions to the BFS flow cases computed by the current two-dimensional compressible code, and we compare the results with experimental data documented by Armaly *et al.* [13]. In this section, we carry out the flow field study using the third-order CLSQ reconstruction scheme (CLSQ3). The grid is Cartesian generated according to the sketch in Fig. 3.15 and meshing parameters can be found in Tab. 3.1, we used the Grid 2 in this table for the rest of flow physics analysis since the grid convergence study suggests that the relative difference in second Euclidean norm between Grid 2 and Grid 3

$$\sqrt{\frac{\sum_{i=1}^{N} |^{\text{Grid3}}\mathtt{v}_i - {}^{\text{Grid2}}\mathtt{v}_i|^2}{\sum_{i=1}^{N} |^{\text{Grid3}}\mathtt{v}_i|^2}} < 1\%$$

for $\mathtt{v} := \{u, v\}$ and

$$\sqrt{\frac{\sum_{i=1}^{N} |^{\text{Grid3}}\mathtt{v}_i - {}^{\text{Grid2}}\mathtt{v}_i|^2}{\sum_{i=1}^{N} |^{\text{Grid3}}\mathtt{v}_i|^2}} = \mathcal{O}(10^{-6})$$

for $\mathtt{v} := \{\rho, p, T\}$, where N is the number of cells on the coarsest Grid 0. Therefore we consider the test results obtained on Grid 2 is effectively grid-converged.

Two vortices are observed during the experiment with increasing Reynolds number from $100 \leq Re_{u_B,D_h} \leq 1000$, namely the primary recirculation zone immediately downstream of the step, and the secondary roof vortex appearing at around $Re_{u_B,D_h} = 400$. As the flow departs from the laminar regime to transitional regime ($1200 < Re_{u_B,D_h} < 6600$), a short tertiary vortex is produced downstream of the primary vortex at the bottom wall. A schematic representation of the Armaly test-case is given in Fig. 4.1, in which the various separation and reattachment lengths are denoted by from x_1 to x_5 conforming to the notation used by Armaly *et al.* [13], x_1 denotes the primary separation length, $[x_2, x_3]$ denotes the interval of tertiary vortex in the turbulent regime and is not observed in the current numerical study, $[x_4, x_5]$ denotes the interval of roof vortex. In addition, we introduced the length of corner vortex x_c in the current data. The corner vortex is two orders of magnitude shorter than the primary recirculation zone, and is not documented in previous experimental and numerical studies. The step height is denoted by H, the inlet channel height as H_i and outlet channel height as H_o. The inlet is placed at a length of $L_i = 10H$ upstream of the step, and the outlet at $L_o = 50H$ downstream.

The reservoir inlet boundary condition, as described in Section 2.7.5, is prescribed to the inflow while the pressure outlet (Section 2.7.6) is used for the outflow boundary condition. All channel walls are considered as adiabatic no-slip (Section 2.7.2). The inflow Mach number is fixed systematically at $M = 0.2$ in order to generate as little numerical stiffness as possible while staying within the incompressible flow regime ($M < 0.3$). The step height H varies from case to case to produce the desired Reynolds number Re_{u_B,D_h} while maintaining the correct expansion ratio $ER = 101/52$. The prescribed outlet static pressure is adjusted in order to obtain a streamwise velocity of $M = 0.2$ at the midpoint of inlet plane $x = -10H$. To predict the outlet pressure *prior to* the simulation, we need to take into account of the pressure loss Δp_f related to friction and the pressure rise Δp_{exp} related to sudden expansion at the step. Due to the presence of primary recirculation zone and roof vortex, it is clear that the total friction loss Δp_f *cannot* be estimated directly by the analytical Darcy-Weisbach equation without knowing the exact locations where the

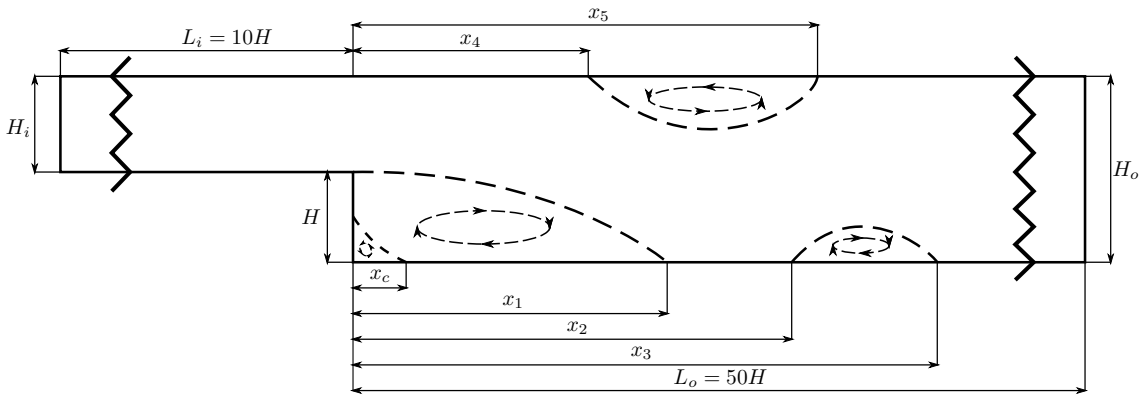

Figure 4.1: Schematic representation of Armaly *et al.* [13] test-case.

flow starts or ceases to be fully developed. In the current study, an initial estimate of Δp_{exp} is denoted by $\Delta p_{\text{exp,ini}}$ obtained from the Borda-Carnot equation [152, p. 262] for sudden expansion in a closed channel

$$\Delta E = \Delta\left(p + \frac{1}{2}\rho u_B^2\right) = \frac{1}{2}\rho(u_{B_2} - u_{B_1})^2 \tag{4.1}$$

where the change in ρ is assumed negligible, u_{B_1} and u_{B_2} are respectively the bulk velocities before and after the expansion, $\Delta E = E_1 - E_2$ is the loss of mechanical energy after the expansion, and since $u_{B_2} = (H_i/H_o)u_{B_1}$, we obtain

$$\Delta p_{\text{exp,ini}} = p_2 - p_1 = \rho u_{B_1}^2 \frac{H_i}{H_o}\left(1 - \frac{H_i}{H_o}\right), \quad H_i < H_o \tag{4.2}$$

and since the outlet pressure is given by

$$p_o = p_i + \Delta p_{f,\text{ini}} + \Delta p_{\text{exp,ini}} \tag{4.3}$$

where $\Delta p_{f,\text{ini}}$ is an initial estimate of Δp_f, we adjust $\Delta p_{f,\text{ini}}$ by "trial and error" to obtain the correct outlet pressure p_o which guarantees an inlet centerline velocity u_{∞_i} corresponding to $M = 0.2$.

It is important to note that, although values of $p_i - p_o$ for the BFS test-cases are adjusted to recover $M = 0.2$ at inlet and are therefore accurate, both $\Delta p_{f,\text{ini}}$ and $\Delta p_{\text{exp,ini}}$ are *inaccurate* initial estimates and the correct values of Δp_f and Δp_{exp} need to be reevaluated according to the converged computational results.

Flow field visualizations are presented in Fig. 4.2, Fig. 4.3 and Fig. 4.4 for a global understanding of the flow physics involved in this test-case. Fig. 4.2 shows the field of x-velocity u for three Reynolds numbers $Re_{u_B,D_h} = \{100, 389, 1000\}$. It is observed that, as the Reynolds number increases, the primary recirculation zone grows larger resulting in a longer reattachment length x_1. The secondary roof vortex is not present at low Reynolds number, however, from $Re_{u_B,D_h} = 389$, the top-wall boundary layer starts to show sign of separation and a mean-flow curvature can be observed approximately above the primary reattachment. At $Re_{u_B,D_h} = 1000$, the roof vortex is fully developed and forces the mean-flow to bend downwards which curbs the further development of the primary recirculation zone. The vortical structure of the flow is better illustrated by streamlines

Table 4.2: Table of pressure data for Armaly *et al.* [13] test-cases at different Reynolds numbers Re_{u_B,D_h} ranging from 100 to 1000.

Re_{u_B,D_h}	$Re_{u_\infty,H}$	$\Delta p_{f,\text{ini}}$ (Pa)	p_o/p_i	$\xi = \frac{p_o - p_i}{0.5 * \rho_i u_{B_i}^2}$
100	70.67	-10261.2	0.9046	-7.6900
125	88.34	-8020.0	0.9268	-5.9028
150	106.01	-6571.7	0.9412	-4.7455
200	141.35	-4784.0	0.9588	-3.3194
291	205.66	-3145.5	0.9751	-2.0115
389	274.92	-2251.9	0.9839	-1.2984
399	282.69	-2178.5	0.9846	-1.2453
437	308.66	-1960.0	0.9868	-1.0671
493	348.67	-1692.0	0.9894	-0.8536
500	353.37	-1664.9	0.9897	-0.8320
586	414.41	-1371.0	0.9926	-0.5961
643	454.41	-1220.0	0.9941	-0.4763
687	485.85	-1121.0	0.9951	-0.3972
712	503.00	-1073.0	0.9956	-0.3587
789	557.30	-941.0	0.9969	-0.2535
800	565.38	-923.6	0.9970	-0.2394
898	634.47	-796.0	0.9983	-0.1377
946	668.76	-745.0	0.9988	-0.0966
971	685.91	-722.0	0.9990	-0.0781
1000	706.73	-697.0	0.9993	-0.0571

in Fig.4.4.

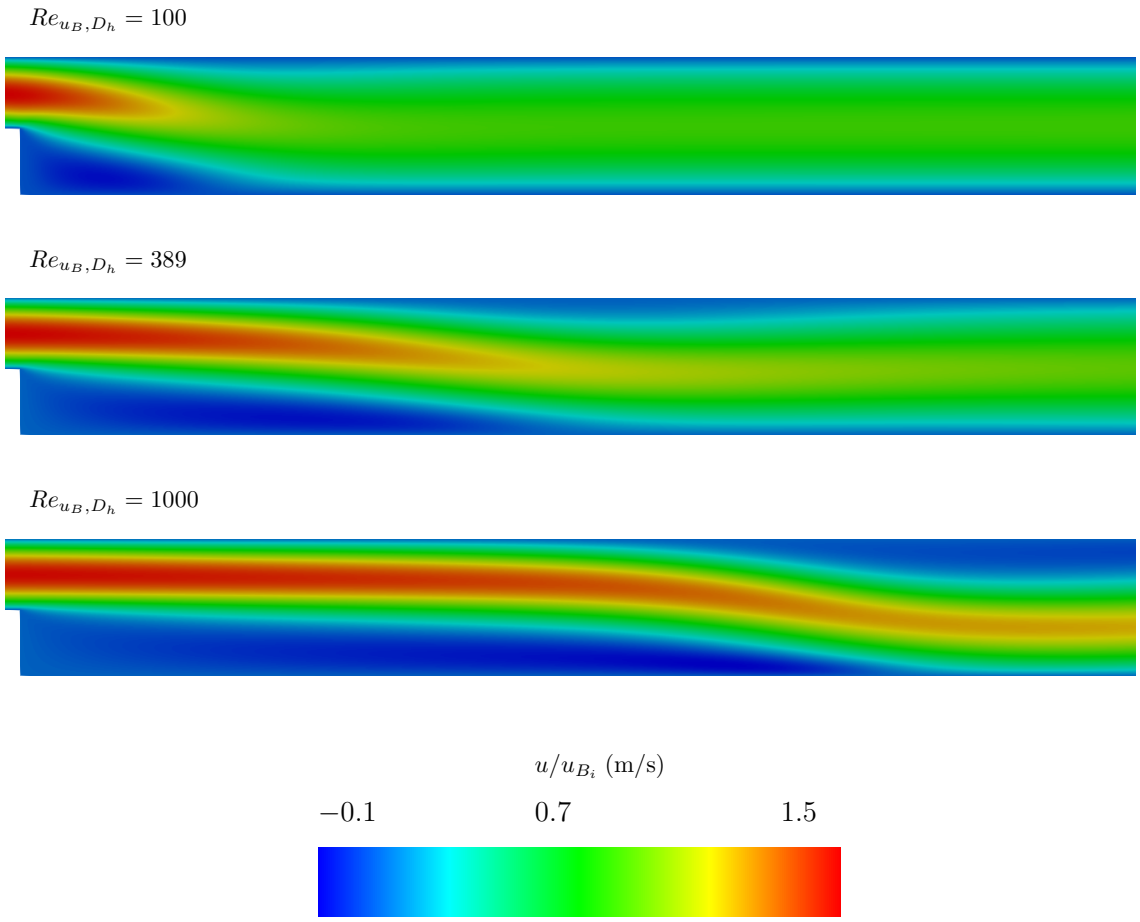

Figure 4.2: fields of x-velocity u scaled by the inlet bulk velocity $u_{B_i} = 45.37$m/s for $Re_{u_B,D_h} = \{100, 389, 1000\}$ of Armaly *et al.* [13] test-case.

The vorticity field is given in Fig. 4.3 which depicts the evolution of bottom-wall boundary layers into a separated shear layer behind the step and its subsequent restitution back to a boundary layer after the reattachment. Due to the height difference in the inlet and outlet channels, the wall-normal velocity gradient $\partial u/\partial y$ within boundary layers before the step is greater than that in the redeveloped boundary layers downstream of the step, which results in a higher level of vorticity in the former. For low and intermediate Reynolds numbers, the roof boundary layer remains attached to the wall and undergoes a smooth transition from a thinner to a thicker boundary layer. However, at $Re_{u_B,D_h} = 1000$, a boundary layer separation is observed on the roof at about a step height before the reattachment of the lower-wall boundary layer.

The streamlines are shown in Fig. 4.4 for $Re_{u_B,D_h} = \{100, 389, 1000\}$ and are colored based on local velocity magnitude. Precise locations of flow separation and reattachment can be identified by saddle points between two adjacent streamlines. An important observation in Fig. 4.4 is the presence of corner vortex extremely close to the intersection between bottom-wall and step. For $Re_{u_B,D_h} = 389, 1000$ this corner vortex is clearly visible although very small compared to the

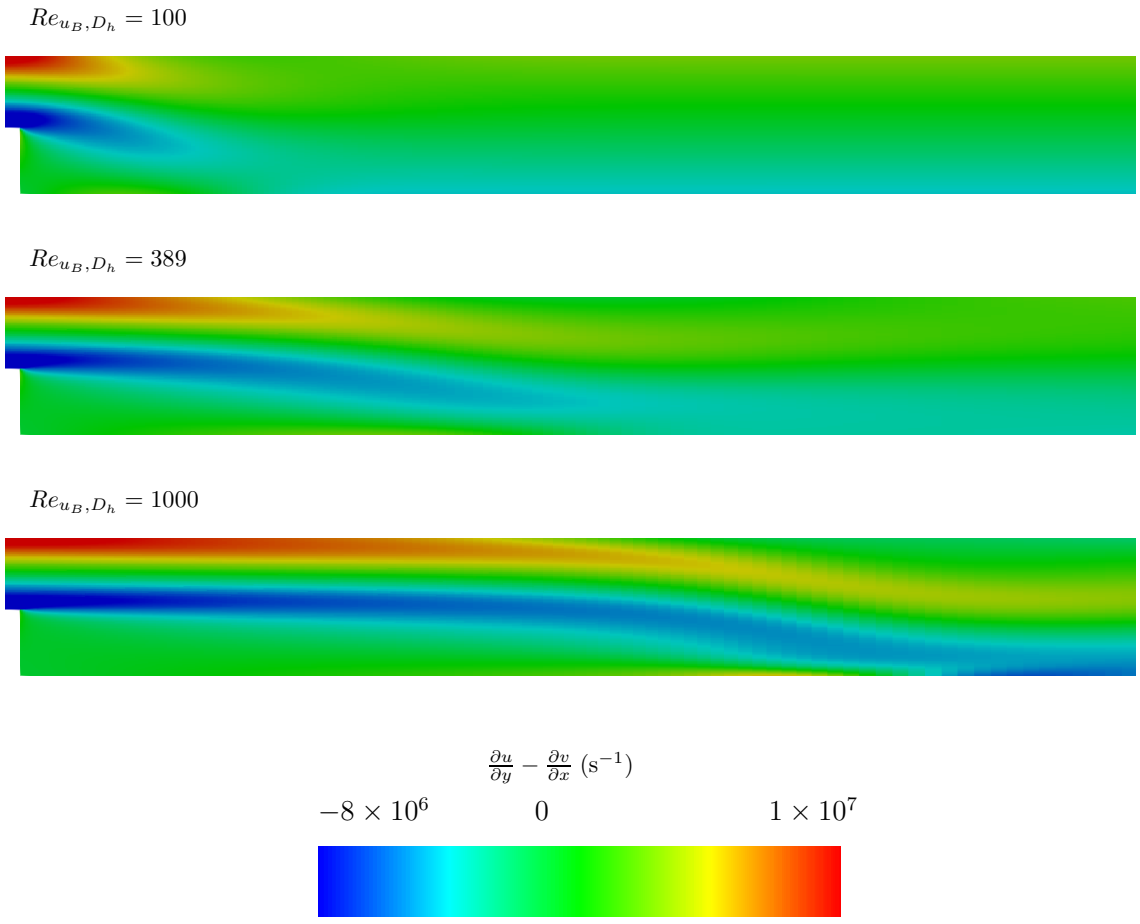

Figure 4.3: Vorticity fields for $Re_{u_B,D_h} = 100, 389, 1000$ of Armaly *et al.* [13] test-case. Minor unsmoothness issue due to ParaView rendering.

primary recirculation. For low Reynolds number, the visibility is reduced and a magnified view is required for its observation.

A close view a the corner vortex is given in Fig. 4.5 for the three Reynolds numbers mentioned before. Similar to the primary and roof vortices, the size of the corner vortex also grows with increasing Reynolds numbers from 100 to 1000. In the study of Biswas *et al.* [28], the authors suggested that the corner vortex and the primary recirculation zone are two successive levels of Moffatt eddies [158] and the latter shrinks to the former when the Reynolds number tends to zero. Biswas *et al.* provided data showing that the length of corner vortex remains constant at $x_c \approx 0.39H$ for $Re_{u_B,D_h} < 10$, however, the x_c data for $Re_{u_B,D_h} \geq 100$ is absent from their study [28]. The x_c data will be provided for several Reynolds numbers between Reynolds numbers 100 and 1000 later in this section in Fig. 4.9.

Separation and reattachment locations x_1, x_4, x_5 are compared between the current 2D numerical study and the experimental data measured at the center plane of the test section. The result shown in Fig. 4.6 covers the laminar regime from $Re_{u_B,D_h} = 100$ to 1000.

As observed by multiple previous studies [13, 28, 44, 46, 130], in terms of the primary reattach-

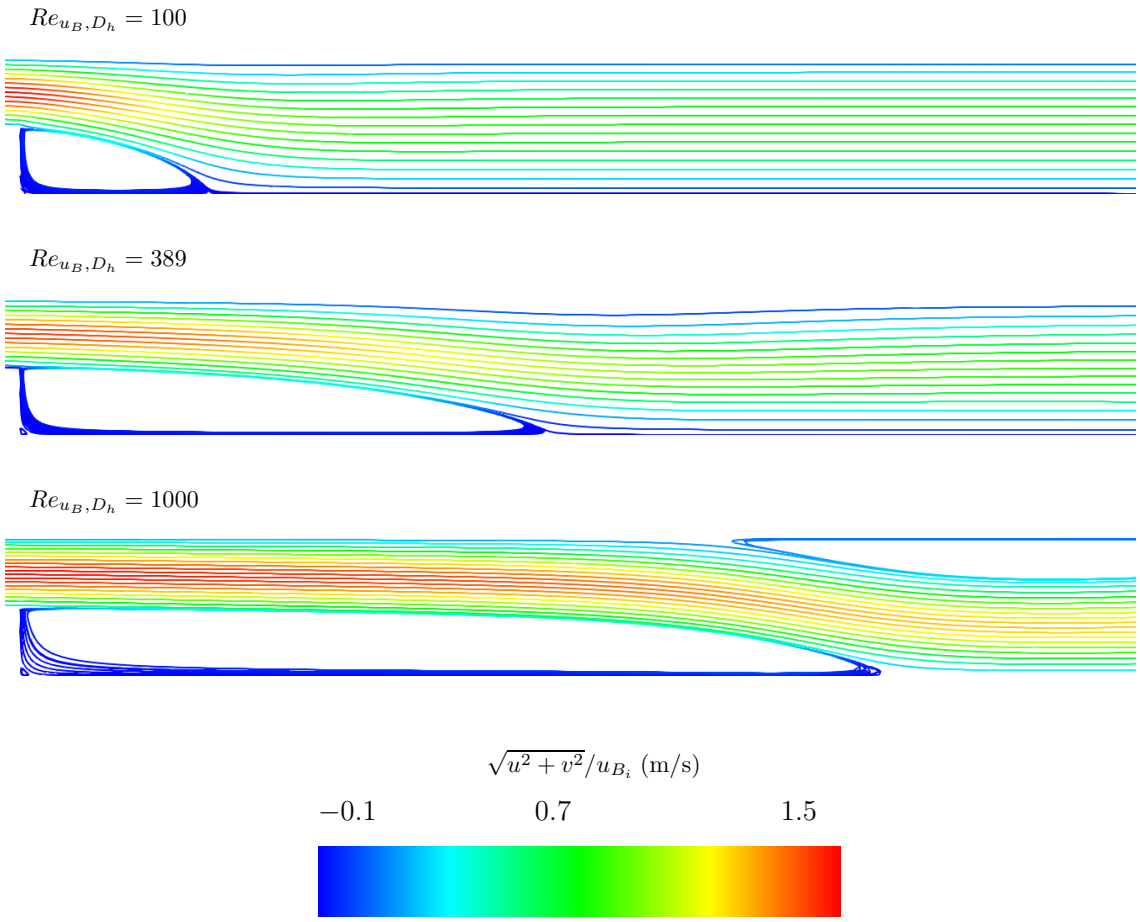

Figure 4.4: Streamlines colored by velocity magnitude scaled by the inlet bulk velocity $u_{B_i} = 45.37$m/s for $Re_{u_B,D_h} = \{100, 389, 1000\}$ of Armaly *et al.* [13] test-case.

ment length x_1, excellent agreement with the experimental data is obtained by 2D computations up to $Re_{u_B,D_h} \approx 400$ beyond which the effects of three-dimensionality become dominant as a secondary separated region starts to appear. The first appearance of the secondary roof vortex is reported by Armaly *et al.* at $Re_{u_B,D_h} \approx 430$ in their experiment, where it occupies a length $(x_5 - x_4)$ of $3.65H$. However the Reynolds number at which the onset of this vortex occurs remains unclear in [13].

In the current study, the onset of roof vortex is detected at $Re_{u_B,D_h} = 399$, where its length is as short as $x_5 - x_4 = 0.1708H$. It is noteworthy that, at $Re_{u_B,D_h} = 399$, the height of the roof vortex is smaller than the minimum cell height $\Delta y_{min} = 0.0093H$. In the numerical study of Biswas *et al.* [28], the finest grid has $\Delta y_{min} = 0.01H$ which is close to the current study. We compare the current 2D grid and the finest grid adopted by Biswas *et al.* in Tab.4.3. However, Biswas *et al.* failed to detect the presence of roof vortex up till $Re_{u_B,D_h} = 500$. Earlier 2D computation performed by Chiang and Sheu [44, 46] managed to detect the appearance roof vortex at $Re_{u_B,D_h} = 450$. In terms of discretization scheme, Chiang and Sheu [46] implemented the second-order Quadratic Upstream Interpolation for Convective Kinematics (QUICK) scheme while

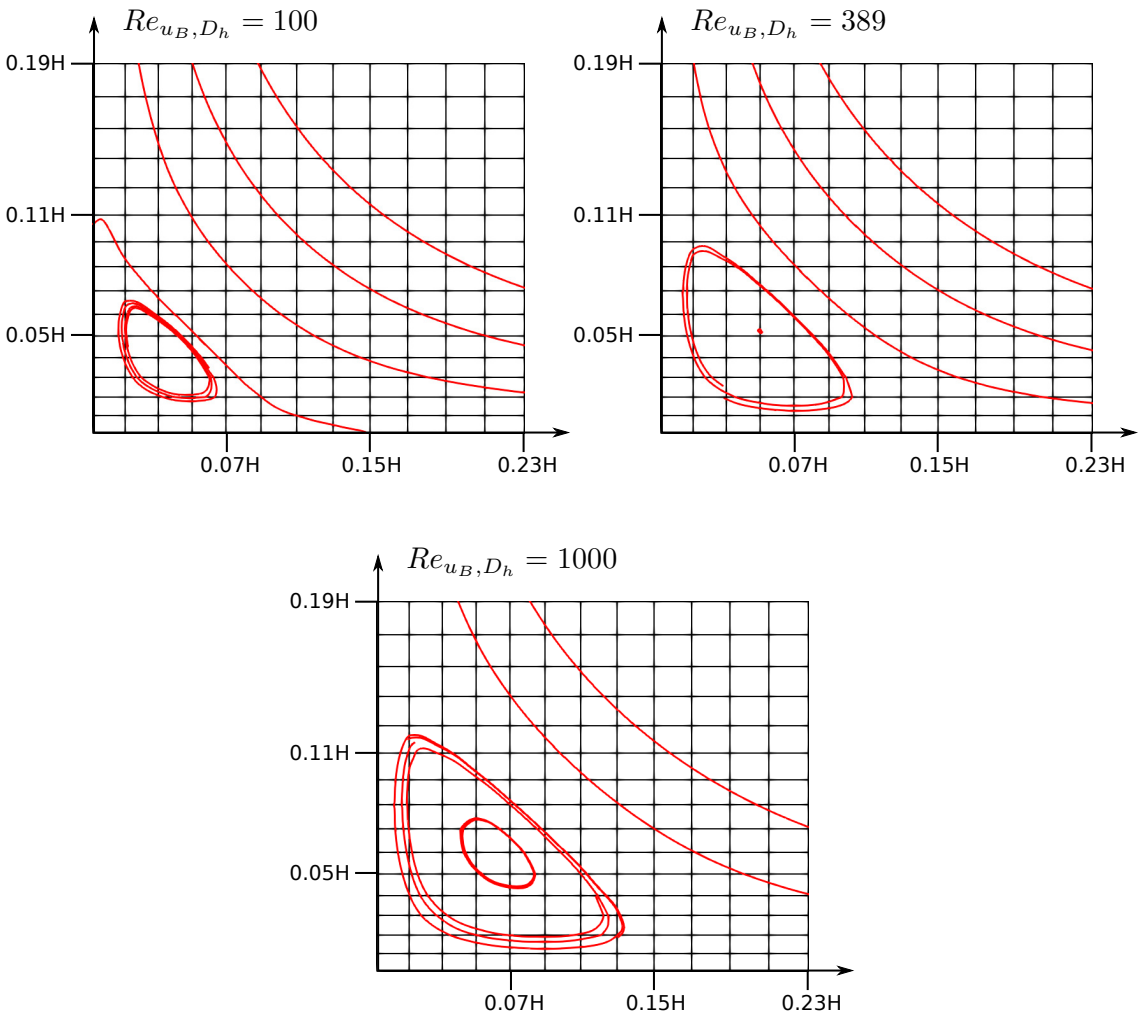

Figure 4.5: Magnified view of corner vortex for $Re_{u_B,D_h} = \{100, 389, 1000\}$ of Armaly *et al.* [13] test-case.

Biswas *et al.* [28] adopted a second-order central differencing scheme. The methods used to evaluate velocity gradient at wall edges remain unclear for both of the two previous studies. However, since neither author implemented a constrained polynomial-based reconstruction, it is reasonable to assume that "mirror state" ghost cells are involved for near-wall cells, and, for the velocity gradient $\nabla \underline{V}$, the wall ghost cell takes the value of associated interior cell while taking the opposite value for $\underline{V}$. Generally, a Green-Gauss-type gradient evaluation method is used along side with QUICK and central-differencing schemes. To detect a separation bubble in which the streamwise velocity gradient turns negative, at least one cell needs to be placed inside the bubble. Since the separation bubble remains extremely small at its onset, Green-Gauss gradient evaluation requires a very fine mesh near wall to detect this separation. We assume that it is due to this reason that the roof vortex is already relatively large when first detected in the previous studies [28, 44, 46].

This limitation is avoided by using the current CLSQ reconstruction since the velocity gradient is directly constructed to Gauss-Legendre quadrature points of wall edges. Specifically, a separa-

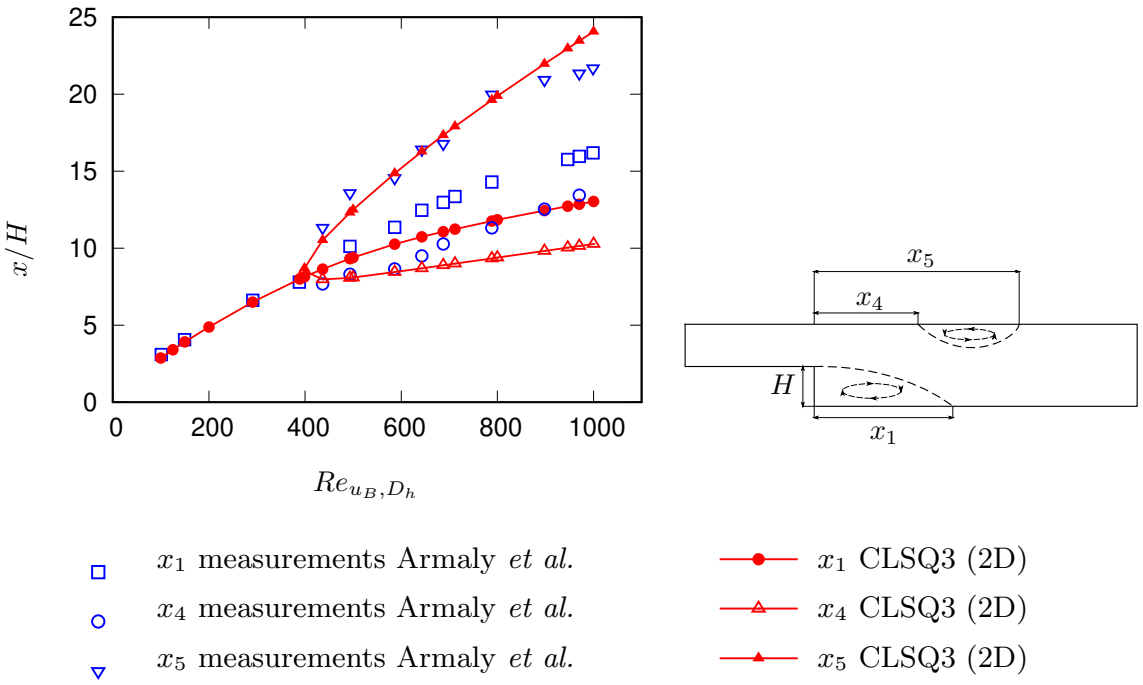

Figure 4.6: Flow separation and reattachment locations of Armaly *et al.* [13] test-case, comparison with experimental data.

Table 4.3: 2D grid comparison between present study and Biswas *et al.* [28]

Grid	$\Delta y_{min}/H$	N_{elm}	L_i/H	L_o/H
Biswas *et al.*	0.01	44000	5	25
Present Gird 2 (Tab. 3.1)	0.0093	43204	10	50

tion/reattachment point is predicted by linear interpolation between a pair of adjacent quadrature points with positive and negative values of wall-normal velocity gradient $\partial u/\partial y$, as illustrated in Fig. 4.7.

Even if the first grid point is place beyond the separation bubble, the scheme can still detect a separation if wall-normal velocity gradient turns out to be negative at quadrature points. This detection has the same accuracy as the order of CLSQ scheme, and a separation bubble can be detection if its length is larger than the interval between two neighboring quadrature points, with no requirement on its height (coverage in wall-normal direction).

The predicted separation location of the roof recirculation zone coincides with the experimental data up to $Re_{u_B,D_h} \approx 600$, whereas predicted computed reattachment location agrees with the measurements up to $Re_{u_B,D_h} \approx 800$. As Re_{u_B,D_h} increases from 100 to 1000, the 2D code yields a shorter primary recirculation zone starting from $Re_{u_B,D_h} \approx 400$, and an earlier separation on the roof from $Re_{u_B,D_h} \approx 600$ resulting in a larger roof vortex comparing to the Armaly experiment. Our current predictions on the separation and reattachment locations are compared with 2D computational results in [28, 44, 130] as shown in Fig. 4.8. Although data are not found for

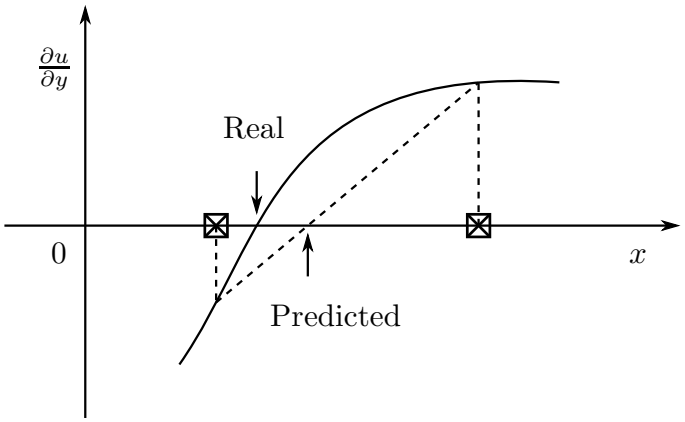

Figure 4.7: Prediction of flow separation and reattachment locations by linear interpolation between two Gaussian quadrature points denoted by ⊠.

$Re_{u_B,D_h} > 800$ or $400 < Re_{u_B,D_h} < 450$, excellent agreement with current results is observed for Reynolds range reported by previous authors. However, computational results of Kim and Moin [130] and Chiang *et al.* [44] give slightly higher values for all separation and reattachment lengths. Results given by Biswas *et al* [28] are almost identical to the current data.

This good agreement among four sets of independent 2D predictions shows that the discrepancy between numerical and experimental results is caused by the 3D effects when Re_{u_B,D_h} exceeds 400 rather than inaccurate numerical resolutions.

In addition, prediction of the corner vortex length x_c is obtained in the current study as shown in Fig. 4.9. The growth of corner vortex follows a similar trend as that of the primary recirculation zone in Fig. 4.6 but the curve x_c has a less sharp slope everywhere than the curve x_1.

Normalized pressure drop distributions are extracted at the inlet channel centerline $y = H + H_i/2$ extending to the outlet for different Re_{u_B,D_h} and compared with those presented in the Biswas study [28], the results are plotted in Fig. 4.10. According to [28], the Reynolds-scaled pressure drop $Re_{u_B,D_h}(p-p_{\text{ref}})/(0.5\rho_{\text{ref}}u^2_{B,\text{ref}})$ is computed with respect to the reference streamwise station $x_{\text{ref}} = -5H$. Note that, by scaling with Re_{u_B,D_h}, all curves are superposed on one another upstream of the step, and share the same downward slope downstream of the step after reaching the peak pressure caused by the sudden expansion, which indicates that the two occurrences of pressure drops remain linear and therefore follow the Darcy-Weisbach equation

$$\Delta p_f = \frac{\lambda}{Re}\frac{L}{D_h}\rho\frac{u_B^2}{2} \tag{4.4}$$

where λ is the friction coefficient depending on the shape of cross section.

The pressure rise Δp_{exp} and the pressure loss related to friction Δp_f are reevaluated based on converged computational results which are different from the initial estimates $\Delta p_{\text{exp,ini}}$ and $\Delta p_{f,\text{ini}}$. Pressure data are extracted along $y = H + H_i/2$ based on which we calculate the total drop of pressure $p_o - p_i$ and the exact pressure rise due to sudden expansion Δp_{exp}. The friction-induced pressure drop Δp_f is obtained by taking the difference between the total pressure drop and the

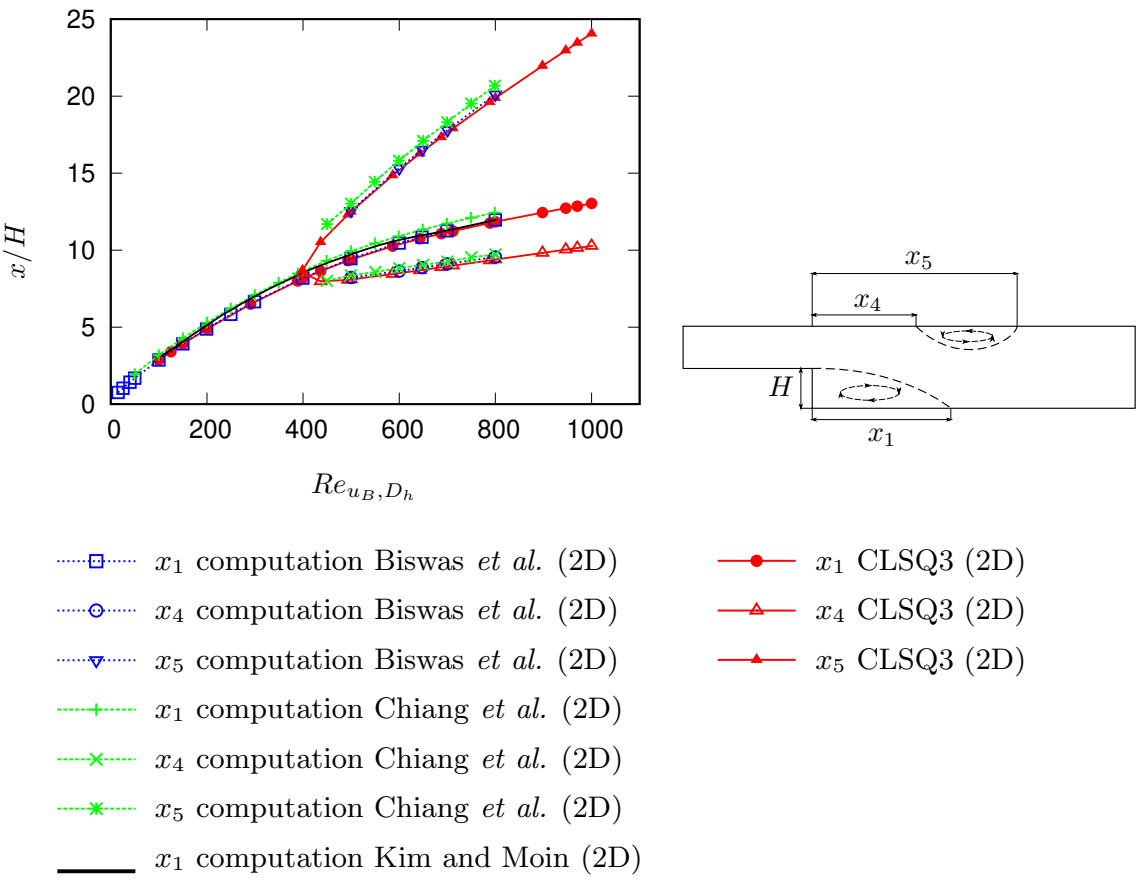

Figure 4.8: Flow separation and reattachment locations of Armaly *et al.* [13] test-case, comparison with previous 2D computational results. Data sources : Biswas *et al.* [28], Chiang *et al.* [44], Kim and Moin [130].

pressure rise

$$\Delta p_f = (p_o - p_i) - \Delta p_{\text{exp}}. \tag{4.5}$$

The values of $p_o - p_i$, Δp_{exp} and Δp_f are scaled by $0.5\rho_i u_{B_i}^2$ and are plotted against the Reynolds number Re_{u_B,D_h} in Fig. 4.11, where ρ_i, u_{B_i} are the flow density and bulk velocity evaluated at channel inlet $x = -10H$ corresponding to a centerline Mach number $M = 0.2$. It is clear that the dimensionless $(p_i - p_o)/(0.5\rho_i u_{B_i}^2)$, $\Delta p_f/(0.5\rho_i u_{B_i}^2)$ and $\Delta p_{\text{exp}}/(0.5\rho_i u_{B_i}^2)$ are all functions of Re_{u_B,D_h}, and that the pressure rise Δp_{exp} increases sharply from $Re_{u_B,D_h} = 100$ to $Re_{u_B,D_h} \approx 400$ before reaching a constant value. Note that the flattening of the Δp_{exp} curve occurs at almost the same Reynolds number where the onset of roof vortex is observed ($Re_{u_B,D_h} = 399$). This phenomenon can be explained by the fact that, starting from $Re_{u_B,D_h} = 399$, the rapidly enlarging roof vortex restricts the flow passage between the primary and roof separation zones, resulting in a decreased effective expansion ratio and curtailed pressure rise behind the step. Therefore, we observe that Δp_{exp} increases sharply from $Re_{u_B,D_h} = 100$ to $Re_{u_B,D_h} \approx 400$, and once the roof

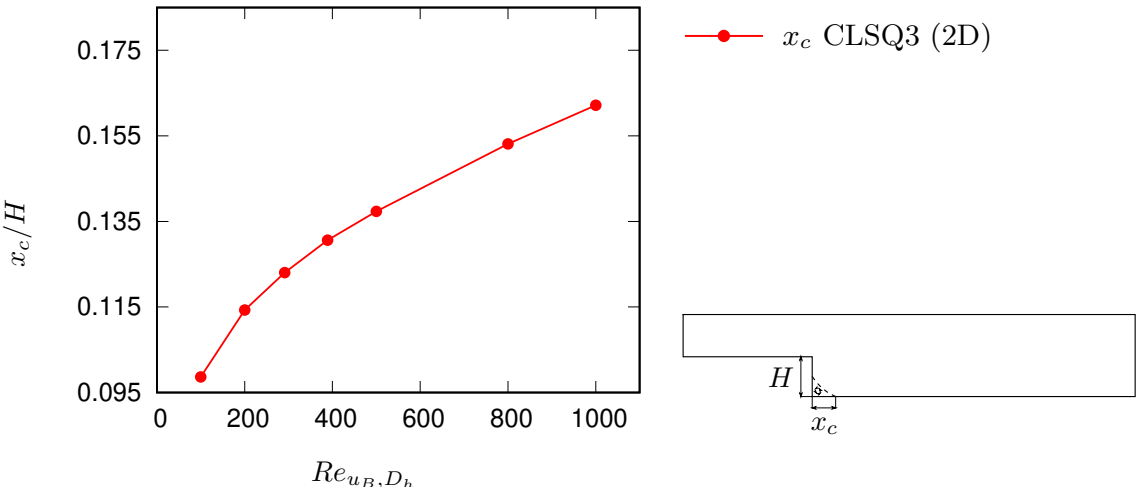

Figure 4.9: Length of corner vortex x_c normalized by step height H for Re_{u_B,D_h} = 100, 200, 291, 389, 500, 800, 1000 of Armaly *et al.* [13] test-case.

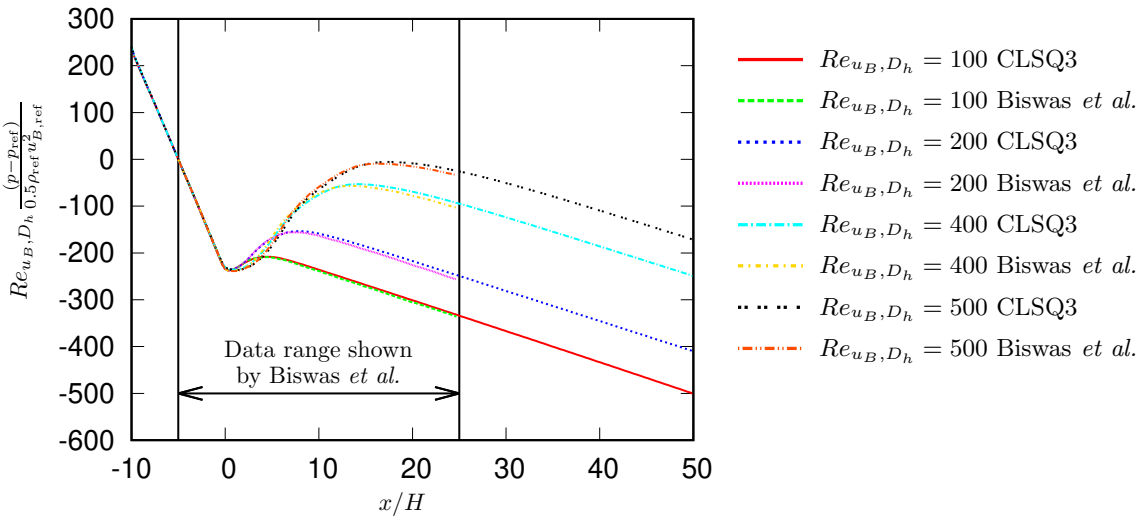

Figure 4.10: Reynolds-scaled pressure drop distribution along channel axis, comparison with Biswas *et al.* [28] results.

vortex appears, the growth slows down drastically and flattens after $Re_{u_B,D_h} \approx 500$.

The dimensionless friction-induced pressure drop $\Delta p_f/(0.5\rho_i u_{B_i}^2)$ can be computed by applying Eqn. 4.4 to 2D channel flows

$$\Delta p_f = -\frac{\lambda}{Re_{u_B,D_h}}\frac{L}{D_h}\frac{\rho}{2}u_B^2 \tag{4.6}$$

where λ is the friction coefficient, and White [216, p. 382] showed that $\lambda = 96$ for parallel plates

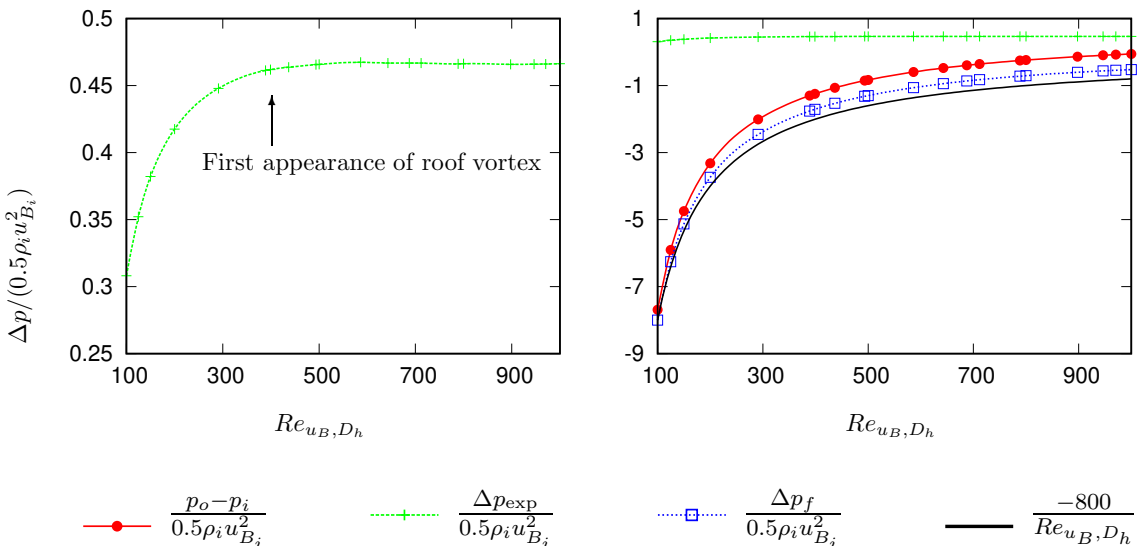

Figure 4.11: Normalized pressure drops and pressure rise in the entire channel plotted against Reynolds number.

with infinite width, which is equivalent to a 2D channel flow. The hydraulic diameter $D_h = 2H_i$ before the step and $D_h = 2H_o$ after, therefore the total friction-induced pressure drop is given by

$$\Delta p_f = -\frac{48}{Re_{u_B,2H_i}} \left(\frac{L_{i,\text{dev}}}{H_i} \frac{\rho_i}{2} u_{B_i}^2 + \frac{H_i^2}{H_o^2} \frac{L_{o,\text{dev}}}{H_i} \frac{\rho_o}{2} u_{B_o}^2 \right) \tag{4.7}$$

where $L_{i,\text{dev}}$ and $L_{o,\text{dev}}$ are the lengths in the inlet and outlet channels over which the flow is fully developed. While the flow can be considered fully developed in the entire inlet channel therefore $L_{i,\text{dev}} = L_i$, $L_{o,\text{dev}}$ decreases with increasing Reynolds number since the primary recirculation zone grows with Re_{u_B,D_h} (Fig. 4.6). Assume that the density variation is negligible at $M = 0.2$, the final expression of Δp_f is given by

$$\Delta p_f = -\frac{48}{Re_{u_B,2H_i}} \frac{\rho_i}{2} u_{B_i}^2 \left[\frac{L_{i,\text{dev}} + (H_i/H_o)^4 L_{o,\text{dev}}}{H_i} \right] \tag{4.8}$$

$$\text{with} \quad L_{o,\text{dev}} := L_{o,\text{dev}}(Re_{u_B,2H_i}).$$

As shown in Fig. 4.11, the curve of dimensionless friction-induced pressure drop $\Delta p_f/(0.5\rho_i u_{B_i}^2)$ is very close to that of $-800/Re_{u_B,D_h}$, and, according to Eqn. 4.8, the slight difference is caused by the fact that $L_{o,\text{dev}}$ is a function of Re_{u_B,D_h} rather than a constant.

By examining the flow separations and pressure distribution at different Reynolds numbers, we realize that the onset of roof vortex is a critical point within the laminar flow regime. It marks the transition from a two-dimensional flow to a three-dimensional flow, and it has significant influence on the pressure rise downstream of the step. Accurately capturing the first appearance of the roof vortex has therefore an important engineering interest for channel flows facing an sudden expansion.

Velocity profiles at multiple streamwise stations for three Reynolds numbers 100, 389 and 1000

are shown in Fig. 4.12, and the present results are compared against the experimental data by Armaly *et al.* [13], the 2D numerical results by Chiang and Sheu [46] and by Guerrero and Cotta [101].

From Fig. 4.12 we observe that, for $Re_{u_B,D_h} < 400$, all 2D numerical results including the current ones show excellent agreement with the experimental data. However, although the primary reattachment length x_1 predicted by Chiang *et al.* is almost identical to that obtained in the current study, we note that the present code gives slightly better agreement with the experimental data at the step ($x/H = 0.0$) as well as in the primary separated region as shown in Fig. 4.12.(a) and (b). At $Re_{u_B,D_h} = 1000$, all 2D computations deviate from experimental data as expected due to dominant three-dimensional effects as shown in Fig. 4.12.(c). However, the deviation from experimental data mainly takes place at stations in the vicinity (approximately $\pm 3H$) of the primary reattachment point $x_1 = 13.04H$ for $Re_{u_B,D_h} = 1000$. This implies that, far from the reattachment region, the flow remains two-dimensional. A great agreement is still observed among all three sets of 2D computational data at $Re_{u_B,D_h} = 1000$.

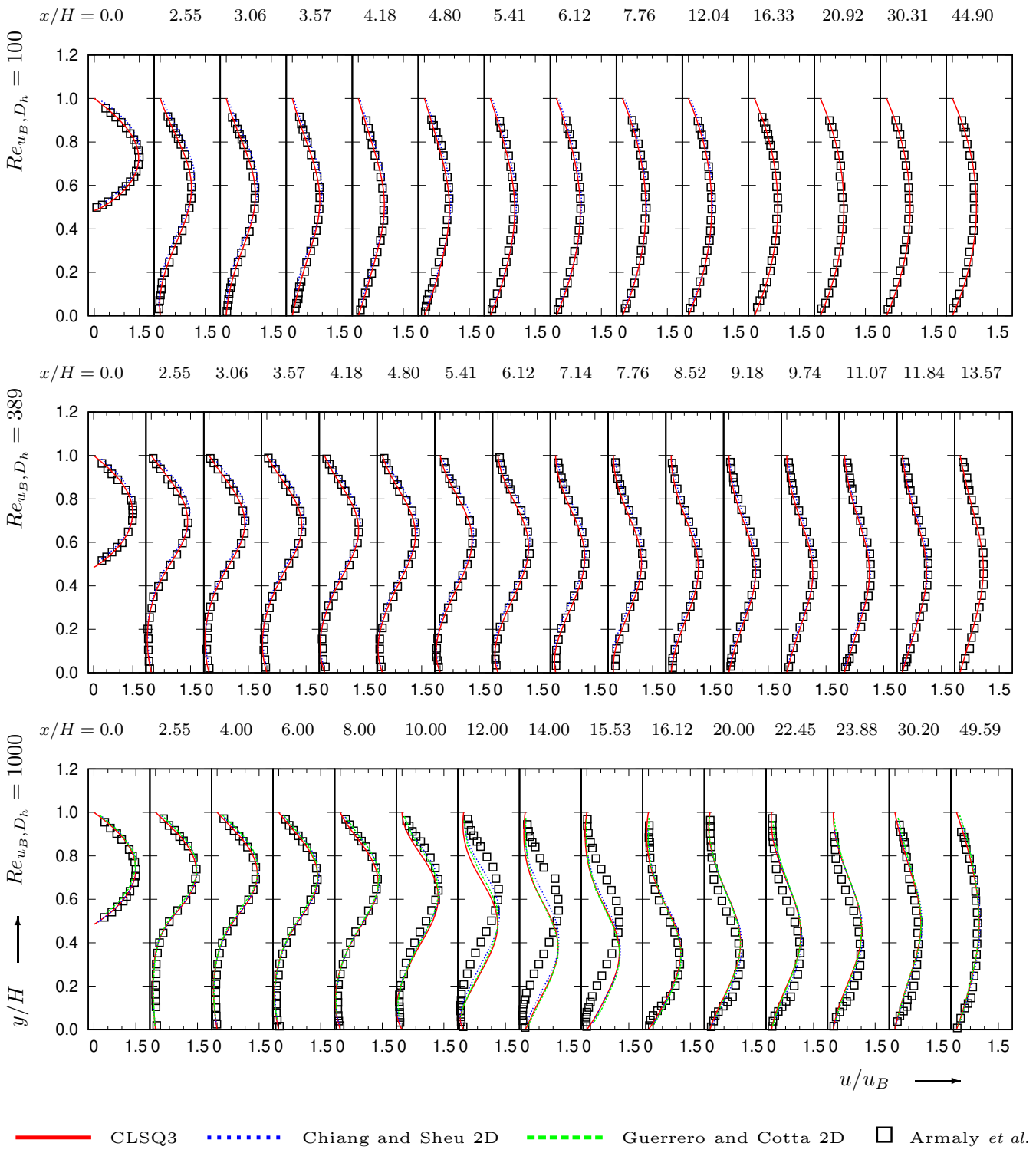

Figure 4.12: Streamwise velocity profiles compared with data from different experimental and numerical studies at $Re_{u_B,D_h} = 100$, 389, 1000. Data sources : Chiang and Sheu [46], Guerrero and Cotta [101], Armaly *et al.* [13].

4.3 Results with High-order CLSQ schemes

In Section. 3.2, we have demonstrated the consistency of the current CLSQ scheme with increasing spatial discretization order by comparing the pressure coefficient C_p and skin-friction coefficient c_f reconstructed to the lower wall (Fig. 3.19 and Fig. 3.20). Here, we further investigate the effects of high-order spatial discretization on the flow features of BFS by showing more test results from the 3^{rd} to the 6^{th}-order CLSQ reconstruction.

The separation and reattachment locations for different orders of CLSQ schemes are given in Fig. 4.13 up to 6^{th}-order. For x_1, x_4 and x_5, perfect agreement is observed among the four orders of CLSQ schemes even at high Reynolds numbers $Re_{u_B,D_h} = 800, 1000$ where the convergence to steady-state becomes difficult for CLSQ4, CLSQ5 and CLSQ6 as shown in Section. 3.1 due to the increasing gap between the high and low order numerical fluxes and non-linearity of the flow.

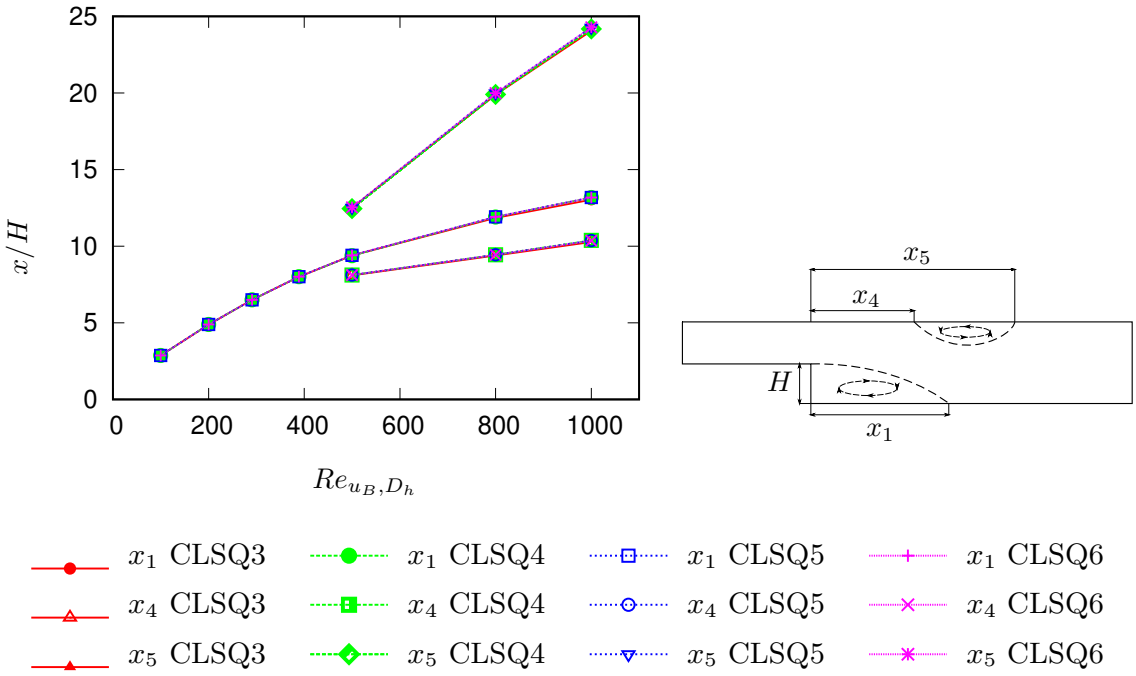

Figure 4.13: Flow separation and reattachment locations of Armaly *et al.* [13] test-case for $Re_{u_B,D_h} = 100, 200, 291, 389, 500, 800, 1000$. Comparison made among results obtained by CLSQ3, CLSQ4, CLSQ5 and CLSQ6.

The same observation is made with the normalized streamwise velocity profiles at $Re_{u_B,D_h} = 100, 389, 1000$. As shown in Fig. 4.14, velocity profiles remain almost identical for CLSQ3-6 schemes at all sampling stations for Reynolds numbers $\{100, 389, 1000\}$.

The corner vortex is also investigated using the four CLSQ schemes and the result at $Re_{u_B,D_h} = 100$ is shown in Fig. 4.15. With different orders of spatial discretization, the vortical structure remains almost identical near the corner.

Furthermore, the length of corner vortex x_c is plotted for seven different Reynolds numbers $Re_{u_B,D_h} = 100, 200, 291, 389, 500, 800, 1000$ in Fig. 4.16. As indicated by the plots, the difference progressively grows larger as the Reynolds number increases from 100 to 1000. This trend is not

observed in Fig. 4.16 for the curves of x_1, x_4, x_5 as they remain almost identical for all orders of CLSQ schemes. However, the x_c prediction at each Reynolds number is clearly converging towards the result obtained with the highest order CLSQ6 scheme. This difference between x_c prediction and those of x_1, x_4, x_5 can be explained by the ratio between the vortex size and the local grid spacing. In the case of the corner vortex, the vortex size is comparable to the local grid spacing as shown in Fig. 4.15, therefore the approximation error is mostly dictated by the order of spatial discretization. Theoretically, this phenomenon also exists for x_1, x_4, x_5, however, since their vortex-size-grid-spacing ratios are substantially higher than that of x_c, the primary and roof vortices are considerably better resolved thus leading to a negligible difference caused by the spatial discretization.

As discussed in the previous Section. 4.2, the onset of the roof vortex is an important flow feature which indicates the precise Reynolds number from which the BFS flow becomes essentially three-dimensional. This onset can be accurately captured with the current CLSQ3 reconstruction scheme without extremely fine near-wall mesh. In this section, we further investigate the location and length of the nascent roof vortex with higher order CLSQ schemes.

Computations are performed with CLSQ3, CLSQ4, CLSQ5 and CLSQ6 for Reynolds numbers around 400 and the onset of roof vortex is found at $Re_{u_B,D_h} = 399$ for all four orders of CLSQ schemes. In Fig. 4.17, separation and reattachment locations of the roof vortex x_4 and x_5 are shown for CLSQ3-6 schemes at $Re_{u_B,D_h} = 399$. The length of roof vortex $x_5 - x_4$ is comparable to the local horizontal grid spacing $\Delta x \approx 0.17H$. The vortex lengths computed with CLSQ5 and CLSQ6 are almost twice as long as those computed with CLSQ3 and CLSQ4, since according to Eqn. A.2b, the number of quadrature points per edge $\bar{N}_{\boxtimes} = 2$ for CLSQ3 and CLSQ4, $\bar{N}_{\boxtimes} = 3$ for CLSQ5 and CLSQ6. Remind that the separation and reattachment points are determined by linear interpolation between a pair of adjacent quadrature points with positive and negative velocity gradient $\partial u/\partial y$ (Fig. 4.7), a larger number of quadrature points per edge allows a more precise capture of separation locations. This difference in vortex length is clearly due to the linear interpolation procedure rather than the spatial accuracy of the CLSQ scheme, since the difference between two CLSQ schemes with the same number of $\bar{N}_{\boxtimes}$ (CLSQ3 and CLSQ4, CLSQ5 and CLSQ6) is negligible.

In this section, some important flow features of the BFS test-case are investigated by using different orders of reconstruction schemes CLSQ3, CLSQ4, CLSQ5 and CLSQ6, and the results show a great consistency among all four orders of CLSQ schemes. The predictions of the primary and roof separation and reattachment locations (Fig. 4.13) are almost identical with the four CLSQ schemes including the prediction of the onset of roof vortex (Fig. 4.17). This proves that the boundary constraints imposed at wall quadrature points are well satisfied regardless of the reconstructing polynomial order p. The streamwise velocity profiles are also compared among the four CLSQ schemes and no visible difference is observed in Fig. 4.14, which shows that the polynomial reconstruction is consistent for interior cells with increasing spatial order of accuracy.

Furthermore, as we have discussed in Section. 3.1, the increase in the spatial order of discretization leads to a slower convergence towards steady-state solution with the current implicit dual-time-stepping schemes. This is due to the increasing gap between the low- and high-order numerical fluxes which requires more iterations to eliminate, especially when the Reynolds number is high. Results in the current section have demonstrated that the implicit dual-tile-stepping can indeed successfully eliminate the difference in flux approximation and always give identical results for CLSQ3, CLSQ4, CLSQ5 and CLSQ6 reconstructions.

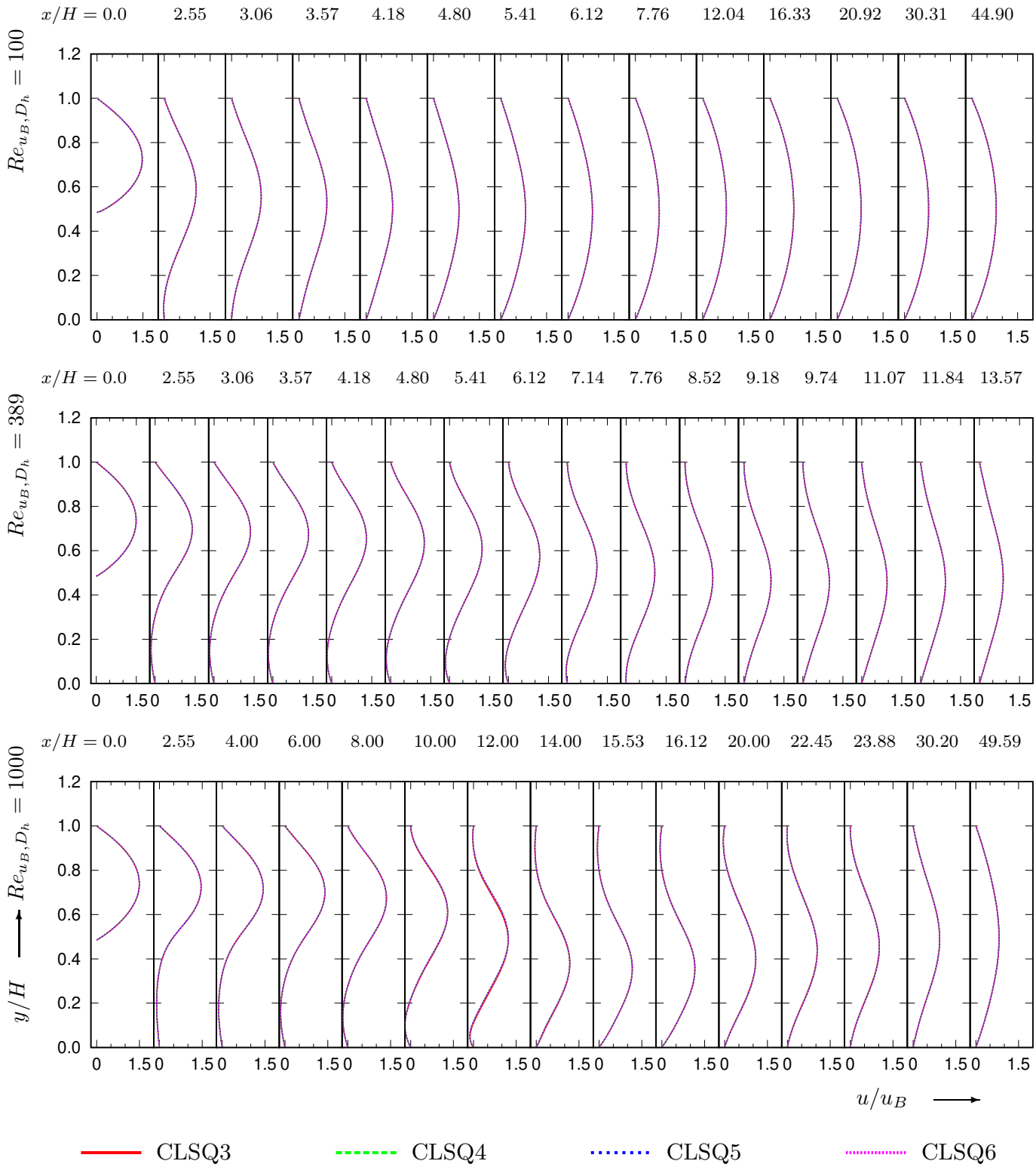

Figure 4.14: Streamwise velocity profiles of Armaly *et al.* [13] test-case for $Re_{u_B,D_h} = 100, 389, 1000$. Comparison made among results obtained by CLSQ3, CLSQ4, CLSQ5 and CLSQ6.

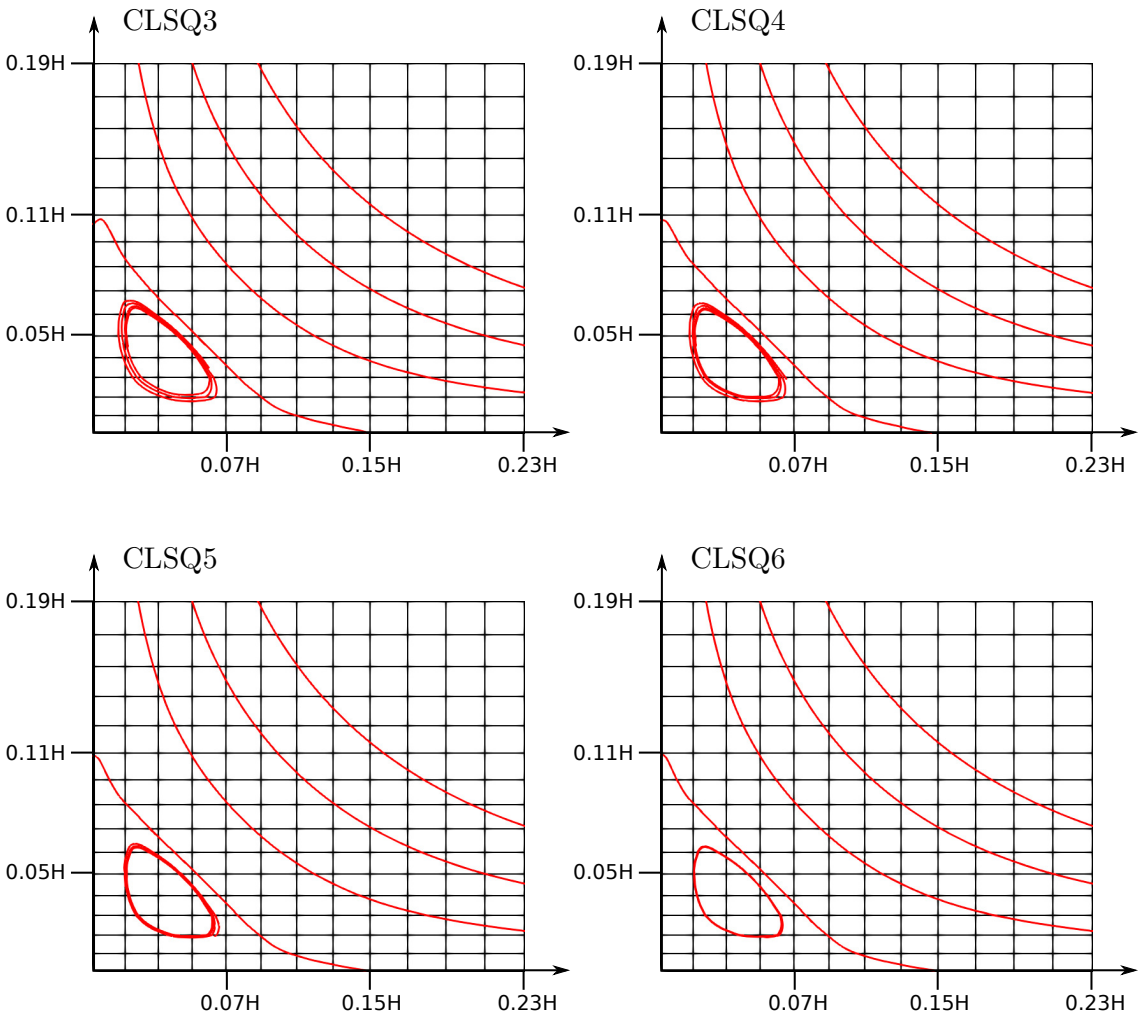

Figure 4.15: Magnified view of corner vortex at $Re_{u_B,D_h} = 100$ of Armaly *et al.* [13] test-case. Comparison made among results obtained by CLSQ3, CLSQ4, CLSQ5 and CLSQ6.

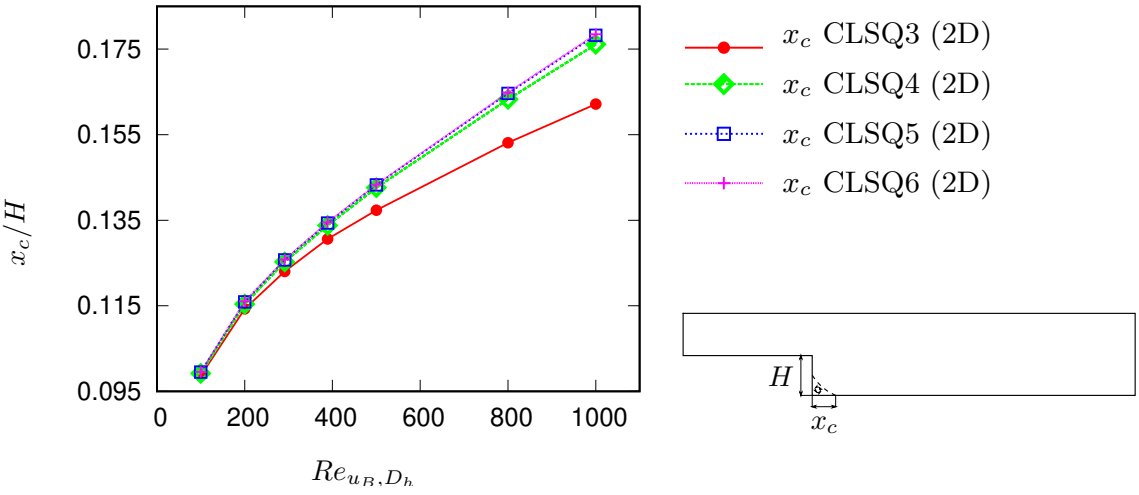

Figure 4.16: Length of corner vortex x_c normalized by step height H for Re_{u_B,D_h} = 100, 200, 291, 389, 500, 800, 1000 of Armaly *et al.* [13] test-case. Comparison made among results obtained by CLSQ3, CLSQ4, CLSQ5 and CLSQ6.

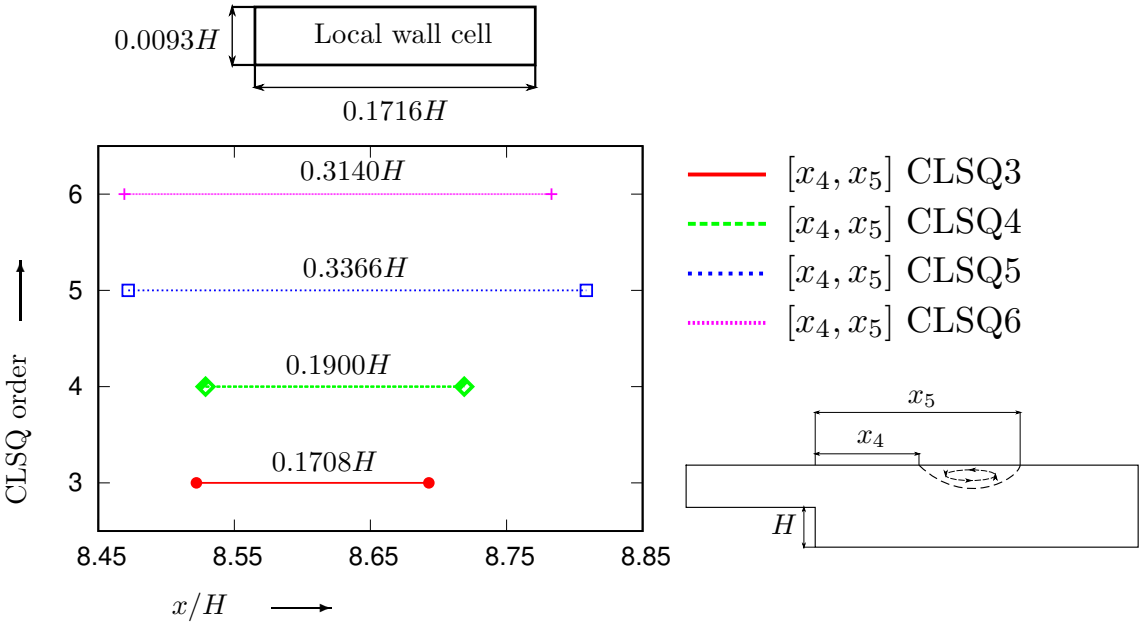

Figure 4.17: First appearance of roof vortex at Re_{u_B,D_h} = 399, the left end of each line segment represents x_4/H, the right end is x_5/H. Comparison made among results obtained by CLSQ3, CLSQ4, CLSQ5 and CLSQ6.

Chapter 5

Conclusions and Perspectives

5.1 Summary

In the present study, numerical methods have been developed in the context of a two-dimensional finite-volume CFD solver for compressible Navier-Stokes equations with arbitrarily high spatial order on arbitrary polygonal grids. The cell-averaged input data is reconstructed in a stencil associated with every cell in the computational domain by a bivariate polynomial, whose coefficients are determined by minimizing a functional with Lagrange multipliers. Each Lagrange multiplier is associated with an equality constraint including the cell-average constraint (that the cell-average in the reference must be satisfied exactly), and a number of Dirichlet or Neumann type boundary constraints on the boundary edges. This reconstruction method is termed as the Constrained Least-Squares (CLSQ) scheme, which is a generalized version of the constraint-free LSQ scheme developed by Gerolymos and Vallet [91], and an extension of the p^{th}-order ($p \leq 4$) method of Ollivier-Gooch and Van Altena [169] to arbitrary spatial order. The interfacial numerical flux is computed using the method of Godunov which involves solving the Riemann problem at every Gauss-Legendre quadrature point on the intercell edge including the boundary edges. The Riemann problem is solved by the approximate-state HLLC Riemann solver developed by Toro *et al.* [206] with the all-Mach correction proposed by Xie *et al.* [218]. For a steady-state solution, the implicit pseudo dual-time-stepping scheme is used and tested with different linear solvers such as the Jacobi iterative solver, the LU-SGS solver by Jameson and Yoon [117], and the Block LU-SGS (BLU-SGS) solver by Chen and Wang [42].

Extensive tests have been conducted in Chapter. 3 on general polygonal unstructured grids for three laminar flow test-cases : the zero-thickness flat-plate boundary layer (FPBL), the low-Reynolds NACA 0012 airfoil and the backward-facing step (BFS) of Armaly *et al.* [13]. Progressively, we have demonstrated that

- the implicit pseudo dual-time-stepping scheme is stable for a Courant number up to CFL = 1000 beyond which the improvement in convergence rate is very limited. Iterative linear solvers Jacobi and BLU-SGS give comparable convergence rate and both are superior to the approximately factored LU-SGS solver.
- the numerical methods in the current study give physically consistent results on all unstructured polygonal meshes tested in the current study with good agreement among them. The solver shows good robustness even on grid with low-quality computational cells.

- the third-order CLSQ (CLSQ3) scheme is indeed third-order accurate according to a formal grid convergence study on the BFS test-case, and the scheme is consistent up to sixth spatial order (CLSQ6).

For the NACA 0012 airfoil test-case, previous studies [98, 137] showed that the flow field becomes unsteady and periodic von Kármán vortex shedding appears in the wake region for an angle of attack AoA $\geq 8°$. The current steady-state simulations with large Δt and local time-stepping tend to underestimate the lift and drag coefficients by approximately 50% at high AoA comparing to the unsteady DNS data [98] suggesting a strongly beneficial effect of the vortex-shedding on lift. Unsteady simulations of low-Reynolds airfoils need to be performed in the future in order to thoroughly understand the dynamics of airfoils in a viscosity-dominated flow.

A detailed flow field analysis has been performed on the BFS test-case of Armaly *et al.* [13]. The current computational results are compared with the experimental data and previous 2D numerical studies. An excellent agreement with the experiment has been observed for $Re_{u_B,D_h} < 400$, which corresponds to the regime where the BFS flow remains essentially two-dimensional. For $100 \leq Re_{u_B,D_h} \leq 1000$, the current computational results are in excellent agreement with different previous 2D computations. Two new flow features are observed in the present study which have not been reported previously thanks to the implementation of high-order CLSQ reconstruction schemes :

- the onset of the secondary roof vortex is found at $Re_{u_B,D_h} = 399$ which corresponds to the beginning of three-dimensional effects
- the length of the small corner vortex x_c is determined for $100 \leq Re_{u_B,D_h} \leq 1000$.

These new observations can provide reference data for future experimental and numerical investigations on BFS flows.

5.2 Perspectives

The extensive numerical studies conducted in this thesis have shown that the implementation of current 2D unstructured CFD solver based the high-order CLSQ reconstruction is successful. However, further improvements still remain to be carried out for more complex CFD applications. Three important perspectives for future work will be briefly discussed in this section.

5.2.1 Finite-curvature Boundary Edges

The current CLSQ reconstruction schemes manage to achieve arbitrarily high-order accuracy at boundaries by imposing boundary conditions exactly at quadrature points of boundary edges. However, a limitation is encountered when the physical boundary is curved with a finite curvature while the boundary cells remain straight-edge polygons. As pointed out by Bassi and Rebay [24], the geometric approximation at boundaries needs to be of at least the same order as the spatial discretization in order to obtain true high-order accurate solutions. This means that for the CLSQ3 scheme to preserve order with curved physical boundaries, the geometric approximation of boundary edges needs to be at least quadratic.

Several possible approaches to treat curved boundaries will be considered. The most straightforward method is to use isoparametric boundary cells and to map the curved cells into straight-edge reference cells by Jacobian transformations [24]. This method is accurate and efficient for

low-order approximations, however, the systematic call for Jacobian transformations can create excessive computational overhead for high-order approximations on moving grids. For fixed grids, on the other hand, this problem is not particularly concerning since the transformed quadrature points and weights are computed only once and stored for the rest of the simulation. Moreover, the generation of curved meshes is not completely solved and remains a matter of ongoing research [57, 212].

An alternative method is the Reconstruction of Off-site Data (ROD) proposed recently by Costa *et al.* [57, 58]. In short, the ROD method performs reconstruction on the straight-edge polygonal computational domain while taking into account of data on the physical boundaries *outside* of this discretized polygonal grid. This method requires no modification to the original polygonal grids but rather modifies the boundary constraints in the least-squares reconstruction procedure, which appears to be a more natural choice to solve the curved boundary problem in the context of the current CLSQ scheme.

Both of the aforementioned approaches will be implemented and investigated in a future work.

5.2.2 Turbulence Modeling

As mentioned in Chapter. 1, this thesis is a part of a larger project intended to model the complex flow interactions within the blade cascade of an aircraft engine. For this purpose, an accurate and efficient RANS turbulence model needs to be integrate in the package of numerical methods. The 7-equation Reynolds Stress Model developed by Gerolymos-Lo-Vallet-Younis (GLVY-RSM) [92] will be integrated in the current CFD solver among other RANS models. The turbulent variables introduced by the model will be reconstructed in a unified manner using the high-order CLSQ schemes. We refer to Appendix. D for the Favre-Reynolds-averaged Navier-Stokes equations to model compressible turbulent flows and the equations of the GLVY-RSM second-moment closure. The turbulent extensions of the boundary conditions listed in Section. 2.7 are also given in this appendix.

The first step in the future is to validate the current numerical methods equipped with GLVY-RSM on the well-defined turbulent BFS test-case proposed by Driver and Seegmiller [66], whose parameters are tabulated in Appendix. C, Tab. C.2. According to the literature review on the studies of turbulent BFS flows in Appendix. C, the low-Reynolds RSMs generally give the most accurate prediction on the BFS flows among all RANS models known to date. Since GLVY-RSM is a wall-normal-free low-Reynolds RSM, we intend to perform a comprehensive study on the Driver and Seegmiller [66] test-case and to compare results with the experimental data and previous numerical studies.

Numerically, since we have shown in Section. 3.3 that the current CFD solver is robust on arbitrary polygonal grids and is able to handle multiple levels of adaptive local refinement, it is interesting to investigate the improvement brought by adaptive refinement on the prediction of turbulent BFS flows. Furthermore, the effects of high-order CLSQ reconstruction scheme on the performance of RSM will be thoroughly investigated in this test-case. As shown in Tab. C.4, most turbulent numerical studies on BFS flows in the literature to date use second-order accurate numerical schemes for mean-flow equations and first-order schemes for the turbulence model. It is reasonable to expect that a comprehensive study on turbulent BFS flows using arbitrarily high-order CLSQ schemes can throw light upon the connection between spatial reconstruction order and accurate Reynolds-Stress modeling.

5.2.3 Unstructured WENO Extension

For simulations of transonic and supersonic flows on unstructured polygonal grids, a WENO scheme needs to be developed based on the current CLSQ reconstruction. Major challenges are expected in this future development including finding positive linear weights and selecting appropriate substencils by a more sophisticated algorithm, and both of them remain very active fields of research to date.

Bibliography

[1] Abbott, D. E. and Kline, S. J. (1962). Experimental Investigation of Subsonic Turbulent Flow Over Single and Double Backward Facing Steps. *Journal of Basic Engineering*, 84(3):317–325.

[2] Abe, K., Kondoh, T., and Nagano, Y. (1994). A new turbulence model for predicting fluid flow and heat transfer in separating and reattaching flows-l. Flow field calculations. *International Journal of Heat and Mass Transfer*, 37(1):139–151.

[3] Abe, K., Kondoh, T., and Nagano, Y. (1995). A new turbulence model for predicting fluid flow and heat transfer in separating and reattaching flows II. Thermal field calculations. *International Journal of Heat and Mass Transfer*, 38(8):1467–1481.

[4] Abe, K., Kondoh, T., and Nagano, Y. (1997). On Reynolds-stress expressions and near-wall scaling parameters for predicting wall and homogeneous turbulent shear flows. *International Journal of Heat and Fluid Flow*, 18(3):266–282.

[5] Abgrall, R. (1994). On Essentially Non-oscillatory Schemes on Unstructured Meshes: Analysis and Implementation. *Journal of Computational Physics*, 114(1):45–58.

[6] Adams, E. W., Johnston, J. P., and Eaton, J. K. (1984). Experiments on the Structure of Turbulent Reattaching Flow. Technical Report MD-43, Thermoscience Division, Department of Mechanical Engineering, Stanford University, Stanford, CA.

[7] Adams, E. W. and Johnston, J. P. (1988a). Effects of the separating shear layer on the reattachment flow structure Part 1: Pressure and turbulence quantities. *Experiments in Fluids*, 6(6):400–408.

[8] Adams, E. W. and Johnston, J. P. (1988b). Effects of the separating shear layer on the reattachment flow structure part 2: Reattachment length and wall shear stress. *Experiments in Fluids*, 6(7):493–499.

[9] Akselvoll, K. and Moin, P. (1993). Large Eddy Simulation of a Backward Facing Step Flow. In *Engineering Turbulence Modelling and Experiments*, pages 303–313, Florence, Italy. Elsevier.

[10] Amano, R. S. (1984). Development of a Turbulence Near-Wall Model and its Application to Separated and Reattached Flows. *Numerical Heat Transfer*, 7(1):59–75.

[11] Amano, R. S. and Goel, P. (1985). Computations of turbulent flow beyond backward-facing steps using Reynolds-stress closure. *AIAA Journal*, 23(9):1356–1361.

[12] Amano, R. S. and Goel, P. (1986). Triple-velocity products in a channel with a backward-facing step. *AIAA Journal*, 24(6):1040–1043.

[13] Armaly, B. F., Durst, F., Pereira, J. C. F., and Schönung, B. (1983). Experimental and theoretical investigation of backward-facing step flow. *Journal of Fluid Mechanics*, 127(-1):473.

[14] Armaly, B. F., Nie, J. H., and Li, A. (2002). Three-dimensional separated flow adjacent to backward-facing step. In *Proceeding of International Heat Transfer Conference 12*, Grenoble, France. Begellhouse.

[15] Armaly, B. F., Li, A., and Nie, J. H. (2003). Measurements in three-dimensional laminar separated flow. *International Journal of Heat and Mass Transfer*, 46(19):3573–3582.

[16] Avva, R., Kline, S., and Ferziger, J. (1988). Computation of turbulent flow over a backward-facing step - Zonal approach. In *26th Aerospace Sciences Meeting*, Reno, NV, U.S.A. American Institute of Aeronautics and Astronautics.

[17] Baker, S. (1977). *Regions of Recirculating Flow Associated with Two- Dimensional Step*. PhD Thesis, University of Surrey.

[18] Balsara, D. S. and Shu, C.-W. (2000). Monotonicity Preserving Weighted Essentially Non-oscillatory Schemes with Increasingly High Order of Accuracy. *Journal of Computational Physics*, 160(2):405–452.

[19] Barri, M., Khoury, G. K. E., Andersson, H. I., and Pettersen, B. (2010). DNS of backward-facing step flow with fully turbulent inflow. *International Journal for Numerical Methods in Fluids*, 64(7):777–792.

[20] Barth, T. and Frederickson, P. (1990). Higher order solution of the Euler equations on unstructured grids using quadratic reconstruction. In *28th Aerospace Sciences Meeting*, Reno, NV, U.S.A. American Institute of Aeronautics and Astronautics.

[21] Barton, I. E. (1994). Laminar flow past an enclosed and open backward-facing step. *Physics of Fluids*, 6(12):4054–4056.

[22] Barton, I. E. (1997). The entrance effect of laminar flow over a backward-facing step geometry. *International Journal for Numerical Methods in Fluids*, 25(6):633–644.

[23] Bassi, F. and Rebay, S. (1997a). A high-order accurate discontinuous finite element method for the numerical solution of the compressible Navier-Stokes equations. *J. Comp. Phys.*, 131:267–279.

[24] Bassi, F. and Rebay, S. (1997b). High-Order Accurate Discontinuous Finite Element Solution of the 2D Euler Equations. *Journal of Computational Physics*, 138(2):251–285.

[25] Bassi, F. and Rebay, S. (2002). Numerical evaluation of two discontinuous Galerkin methods for the compressible Navier-Stokes equations. *Int. J. Numer. Meth. Fluids*, 40:197–207.

[26] Benocci, C. and Skovgaard, M. (1989). Prediction of Turbulent Flow Over a Backward-Facing Step. In Taylor, C., Gresho, P. M., Sani, R. L., and Hauser, J., editors, *Numerical Methods for Laminar and Turbulent Flows*, volume 6, pages 655–665. Pineridge, UK.

[27] Bertolazzi, E. and Manzini, G. (2005). A unified treatment of boundary conditions in least-square based finite-volume methods. *Computers & Mathematics with Applications*, 49(11):1755–1765.

[28] Biswas, G., Breuer, M., and Durst, F. (2004). Backward-Facing Step Flows for Various Expansion Ratios at Low and Moderate Reynolds Numbers. *Journal of Fluids Engineering*, 126(3):362.

[29] Boyd, S. and Vandenberghe, L. (2018). *Introduction to Applied Linear Algebra: Vectors, Matrices, and Least Squares*. Cambridge University Press, 1 edition.

[30] Bradshaw, P. and Wong, F. Y. F. (1972). The reattachment and relaxation of a turbulent shear layer. *Journal of Fluid Mechanics*, 52(1):113–135.

[31] Canuto, C., Hussaini, M. Y., Quarteroni, A., and Zang, T. A. (1988). *Spectral Methods in Fluid Dynamics*. Springer Berlin Heidelberg, Berlin, Heidelberg.

[32] Carlson, J.-R. (2011). Inflow/Outflow Boundary Conditions with Application to FUN3D. Technical Report NASA/TM-2011-217181, NASA Langley Research Center, Hampton, Virginia.

[33] Castro, I. P. and Bradshaw, P. (1976). The turbulence structure of a highly curved mixing layer. *Journal of Fluid Mechanics*, 73(02):265.

[34] Celenligil, M. C. and Mellor, G. L. (1985). Numerical Solution of Two-Dimensional Turbulent Separated Flows Using a Reynolds Stress Closure Model. *Journal of Fluids Engineering*, 107(4):467–476.

[35] Chakravarthy, S. and Osher, S. (1985). A new class of high accuracy TVD schemes for hyperbolic conservationlaws. In *23rd Aerospace Sciences Meeting*, Reno, NV, U.S.A. American Institute of Aeronautics and Astronautics.

[36] Chandrsuda, C. (1975). *A Reattaching Turbulent Shear Layer in Incompressible Flow*. PhD Thesis, Imperial College of Science and Technology, London.

[37] Chandrsuda, C. and Bradshaw, P. (1981). Turbulence structure of a reattaching mixing layer. *Journal of Fluid Mechanics*, 110:171–194.

[38] Charest, M. R. J., Groth, C. P. T., and Gauthier, P. Q. (2012). High-Order CENO Finite-Volume Scheme for Low-Speed Viscous Flows on Three-Dimensional Unstructured Mesh. In *ICCFD7 Proceedings*, Big Island, Hawaii.

[39] Charest, M. R. J., Groth, C. P. T., and Gauthier, P. Q. (2015). A High-Order Central ENO Finite-Volume Scheme for Three-Dimensional Low-Speed Viscous Flows on Unstructured Mesh. *Communications in Computational Physics*, 17(3):615–656.

[40] Chen, C. P. (1985). Multiple-Scale Turbulence Closure Modeling of Confined Recirculating Flows. NASA Contractor Report NASA CR-178536, Marshall Space Flight Center, Alabama.

[41] Chen, H. C. and Patel, V. C. (1988). Near-wall turbulence models for complex flows including separation. *AIAA Journal*, 26(6):641–648.

[42] Chen, R. F. and Wang, Z. J. (2000). Fast, Block Lower-Upper Symmetric Gauss-Seidel Scheme for Arbitrary Grids. *AIAA Journal*, 38(12):2238–2245.

[43] Chevant, G. and Cockburn, B. (1989). The local projection p^0p^1-discontinuous Galerkin finite element method for scalar conservation laws. *Model. Math. Anal. Numer.*, 23:565–592.

[44] Chiang, T. P., Sheu, T. W. H., and Tsai, S. F. (1997). Topological flow structures in backward-facing step channels. *Computers & Fluids*, 26(4):321–337.

[45] Chiang, T. P. and Sheu, T. W. H. (1997). Vortical Flow over a 3-D Backward-Facing Step. *Numerical Heat Transfer, Part A: Applications*, 31(2):167–192.

[46] Chiang, T. P. and Sheu, T. W. H. (1999). A numerical revisit of backward-facing step flow problem. *Physics of Fluids*, 11(4):862–874.

[47] Chien, K.-Y. (1982). Predictions of Channel and Boundary-Layer Flows with a Low-Reynolds-Number Turbulence Model. *AIAA Journal*, 20(1):33–38.

[48] Choi, Y. H. and Merkle, C. L. (1993). The Application of Preconditioning in Viscous Flows. *Journal of Computational Physics*, 105(2):207–223.

[49] Chung, K. C. and Yao, T. H. (1977). On Lattices Admitting Unique Lagrange Interpolations. *SIAM Journal on Numerical Analysis*, 14(4):735–743.

[50] Cockburn, B. and Shu, C. W. (1989). TVB Runge-Kutta local projection discontinuous Galerkin finite element method for conservation laws II: General framework. *Math. Comp.*, 52(186):411–435.

[51] Cockburn, B., Hou, S., and Shu, C. W. (1990). TVB Runge-Kutta local projection discontinuous Galerkin finite element method for conservation laws IV: The multidimensional case. *Math. Comp.*, 54:545–581.

[52] Cockburn, B. and Shu, C. W. (1991). The Runge-Kutta local projection p^1-discontinuous Galerkin finite element method for scalar conservation laws. *Model. Math. Anal. Numer.*, 25(3):337–361.

[53] Cockburn, B. and Shu, C. W. (1998a). The local discontinuous Galerkin method for time-dependent convection-diffusion systems. *J. Numer. Anal*, 35:2440–2463.

[54] Cockburn, B. and Shu, C. W. (1998b). The Runge-Kutta discontinuous Galerkin method for conservation laws V: Multidimensional systems. *J. Comp. Phys.*, 141:199–224.

[55] Cockburn, B. (1999). Discontinuous Galerkin method for convection-dominated problems. *Springer-Verlag, Berlin*, pages 69–224.

[56] Cormack, D. E., Leal, L. G., and Seinfeld, J. H. (1978). An Evaluation of Mean Reynolds Stress Turbulence Models: The Triple Velocity Correlation. *Journal of Fluids Engineering*, 100(1):47–54.

[57] Costa, R., Clain, S., Loubère, R., and Machado, G. J. (2018). Very high-order accurate finite volume scheme on curved boundaries for the two-dimensional steady-state convection-diffusion equation with Dirichlet condition. *Applied Mathematical Modelling*, 54:752–767.

[58] Costa, R., Nóbrega, J. M., Clain, S., Machado, G. J., and Loubère, R. (2019). Very high-order accurate finite volume scheme for the convection-diffusion equation with general boundary conditions on arbitrary curved boundaries. *International Journal for Numerical Methods in Engineering*, 117(2):188–220.

[59] Craft, T. J. and Launder, B. E. (1996). A Reynolds stress closure designed for complex geometries. *International Journal of Heat and Fluid Flow*, 17(3):245–254.

[60] Craft, T. J. (1998). Developments in a low-Reynolds-number second-moment closure and its application to separating and reattaching flows. *International Journal of Heat and Fluid Flow*, 19(5):541–548.

[61] Daly, B. J. (1970). Transport Equations in Turbulence. *Physics of Fluids*, 13(11):2634.

[62] De Brederode, V. and Bradshaw, P. (1972). *Three-Dimensional Flow in Nominally Two-Dimensional Separation Bubbles: Flow behind a rearward-facing step. I.* Number v. 1 in I.C. aero report 72-19 April 1972. Department of Aeronautics, Imperial College of Science and Technology.

[63] Dellacherie, S., Jung, J., Omnes, P., and Raviart, P.-A. (2016). Construction of modified Godunov-type schemes accurate at any Mach number for the compressible Euler system. *Mathematical Models and Methods in Applied Sciences*, 26(13):2525–2615.

[64] Demkowicz, L. (2007). *Computing with hp-adaptive finite elements.* Chapman & Hall/CRC applied mathematics and nonlinear science series. Chapman & Hall/CRC, Boca Raton.

[65] Denton, J. D. (1993). Loss Mechanisms in Turbomachines. In *Volume 2: Combustion and Fuels; Oil and Gas Applications; Cycle Innovations; Heat Transfer; Electric Power; Industrial and Cogeneration; Ceramics; Structures and Dynamics; Controls, Diagnostics and Instrumentation; IGTI Scholar Award*, page V002T14A001, Cincinnati, Ohio, USA. ASME.

[66] Driver, D. M. and Seegmiller, H. L. (1985). Features of a reattaching turbulent shear layer in divergent channelflow. *AIAA Journal*, 23(2):163–171.

[67] Dubois, F. (2001). Partial Riemann problem, boundary conditions, and gas dynamics. In et Laurence Halpern, L. T., editor, *Absorbing Boundaries and Layers, Domain Decomposition Methods: Applications to Large Scale Computations*, ISBN: 1-56072-940-6, pages pages 16–77. Nova Science Publishers, Inc, New York. 65 pages.

[68] Dunavant, D. A. (1985). High degree efficient symmetrical Gaussian quadrature rules for the triangle. *International Journal for Numerical Methods in Engineering*, 21(6):1129–1148.

[69] Durbin, P. A. (1991). Near-Wall Turbulence Closure Modeling Without "Damping Functions". *Theoretical and Computational Fluid Dynamics*, 3(1):1–13.

[70] Durbin, P. A. (1993). A Reynolds stress model for near-wall turbulence. *Journal of Fluid Mechanics*, 249:465–498.

[71] Durbin, P. A. (1995). Separated flow computations with the $k-\varepsilon-v^2$ model. *AIAA Journal*, 33(4):659–664.

[72] Durst, F. and Tropea, C. (1983). Flows over Two-Dimensional Backward-Facing Steps. In Dumas, R. and Fulachier, L., editors, *Structure of Complex Turbulent Shear Flow*, pages 41–52. Springer Berlin Heidelberg, Berlin, Heidelberg.

[73] Durst, F. and Schmitt, F. (1985). Experimental studies of high Reynolds number backward-facing step flow. In *Proc. 5th Symposium on Turbulent Shear Flows*, pages 5.19–5.24, Pennsylvania State University.

[74] Eaton, J. K., Johnston, J. P., and Jeans, A. H. (1979). Measurements in a Reattaching Turbulent Shear Layer. In *Proc. 2nd Symp. Turbulent Shear Flows*, London.

[75] Eaton, J. K. and Johnston, J. P. (1980). Turbulent flow reattachment : an experimental study of the flow and structure behind a backward-facing step. Technical Report MD-39, Thermoscience Division, Department of Mechanical Engineering, Stanford University, Stanford, CA.

[76] Eaton, J. K. and Johnston, J. P. (1981). A Review of Research on Subsonic Turbulent Flow Reattachment. *AIAA Journal*, 19(9):1093–1100.

[77] Einfeldt, B., Munz, C. D., Roe, P. L., and Sjögreen, B. (1991). On Godunov-type methods near low densities. *Journal of Computational Physics*, 92(2):273–295.

[78] Etheridge, D. W. and Kemp, P. H. (1978). Measurements of turbulent flow downstream of a rearward-facing step. *Journal of Fluid Mechanics*, 86(3):545–566.

[79] Fadai-Ghotbi, A., Manceau, R., and Borée, J. (2008). Revisiting URANS Computations of the Backward-Facing Step Flow Using Second Moment Closures. Influence of the Numerics. *Flow, Turbulence and Combustion*, 81(3):395–414.

[80] Fasshauer, G. E. (2007). *Meshfree Approximation Methods with Matlab*, volume 6 of *Interdisciplinary Mathematical Sciences*. WORLD SCIENTIFIC.

[81] Favre, A. J. A. (1992). Formulation of the Statistical Equations of Turbulent Flows with Variable Density. In Gatski, T. B., Speziale, C. G., and Sarkar, S., editors, *Studies in Turbulence*, pages 324–341. Springer New York, New York, NY.

[82] Ferziger, J. and Oliger, J. (1986). Adaptive grid techniques for elliptic fluid flow problems. In *24th Aerospace Sciences Meeting*, Reno, NV, U.S.A. American Institute of Aeronautics and Astronautics.

[83] Frendi, A., Tosh, A., and Girimaji, S. (2006). Flow Past a Backward-Facing Step: Comparison of PANS, DES and URANS Results with Experiments. *International Journal for Computational Methods in Engineering Science and Mechanics*, 8(1):23–38.

[84] Gartling, D. K. (1990). A test problem for outflow boundary conditions-flow over a backward-facing step. *International Journal for Numerical Methods in Fluids*, 11(7):953–967.

[85] Gerolymos, G. A. (1990). Implicit multiple-grid solution of the compressible Navier-Stokes equations using k-epsilon turbulence closure. *AIAA Journal*, 28(10):1707–1717.

[86] Gerolymos, G. A. and Vallet, I. (1999). Tip-Clearance and Secondary Flows in a Transonic Compressor Rotor. *Journal of Turbomachinery*, 121(4):751–762.

[87] Gerolymos, G. A. and Vallet, I. (2005). Mean-Flow-Multigrid for Implicit Reynolds-Stress-Model Computations. *AIAA Journal*, 43(9):1887–1898.

[88] Gerolymos, G. A., Sénéchal, D., and Vallet, I. (2009). Very-high-order weno schemes. *J. Comput. Phys.*, 228(23):8481–8524.

[89] Gerolymos, G. A. (2011). Approximation error of the Lagrange reconstructing polynomial. *Journal of Approximation Theory*, 163(2):267–305.

[90] Gerolymos, G. A. and Vallet, I. (2012a). Aerodynamics. sourceforge.net/projects/aerodynamics/.

[91] Gerolymos, G. A. and Vallet, I. (2012b). High-order finite-volume reconstruction on arbitrary unstructured grids. In *ICCFD7 Proceedings*, Big Island, Hawaii.

[92] Gerolymos, G. A., Lo, C., Vallet, I., and Younis, B. A. (2012). Term-by-Term Analysis of Near-Wall Second-Moment Closures. *AIAA Journal*, 50(12):2848–2864.

[93] Gerolymos, G. A., Sénéchal, D., and Vallet, I. (2013). Wall effects on pressure fluctuations in turbulent channel flow. *Journal of Fluid Mechanics*, 720:15–65.

[94] Gerolymos, G. A. and Vallet, I. (2014). Pressure, density, temperature and entropy fluctuations in compressible turbulent plane channel flow. *J. Fluid Mech.*, 757:701–746.

[95] Gibson, M. M. and Launder, B. E. (1978). Ground effects on pressure fluctuations in the atmospheric boundary layer. *Journal of Fluid Mechanics*, 86(3):491–511.

[96] Gillis, J. C. and Johnston, J. P. (1983). Turbulent boundary-layer flow and structure on a convex wall and its redevelopment on a flat wall. *Journal of Fluid Mechanics*, 135(-1):123.

[97] Goldstein, R. J., Eriksen, V. L., Olson, R. M., and Eckert, E. R. G. (1970). Laminar Separation, Reattachment, and Transition of the Flow Over a Downstream-Facing Step. *Journal of Basic Engineering*, 92(4):732–739.

[98] Gopalakrishnan Meena, M., Taira, K., and Asai, K. (2018). Airfoil-Wake Modification with Gurney Flap at Low Reynolds Number. *AIAA Journal*, 56(4):1348–1359.

[99] Gresho, P. M., Gartling, D. K., Torczynski, J. R., Cliffe, K. A., Winters, K. H., Garratt, T. J., Spence, A., and Goodrich, J. W. (1993). Is the steady viscous incompressible two-dimensional flow over a backward-facing step at Re = 800 stable? *International Journal for Numerical Methods in Fluids*, 17(6):501–541.

[100] Gritskevich, M. S., Garbaruk, A. V., Schütze, J., and Menter, F. R. (2012). Development of DDES and IDDES Formulations for the $k-\omega$ Shear Stress Transport Model. *Flow, Turbulence and Combustion*, 88(3):431–449.

[101] Guerrero, J. and Cotta, R. (1996). Benchmark integral transform results for flow over a backward-facing step. *Computers & Fluids*, 25(5):527–540.

[102] Guillard, H. and Viozat, C. (1999). On the behaviour of upwind schemes in the low Mach number limit. *Computers & Fluids*, 28(1):63–86.

[103] Guillard, H. and Murrone, A. (2004). On the behavior of upwind schemes in the low Mach number limit: II. Godunov type schemes. *Computers & Fluids*, 33(4):655–675.

[104] Hanjalić, K. and Launder, B. E. (1972). A Reynolds stress model of turbulence and its application to thin shear flows. *Journal of Fluid Mechanics*, 52(4):609–638.

[105] Hanjalić, K. and Launder, B. E. (1976). Contribution towards a Reynolds-stress closure for low-Reynolds-number turbulence. *Journal of Fluid Mechanics*, 74(4):593–610.

[106] Hanjalić, K. and Jakirlić, S. (1998). Contribution towards the second-moment closure modelling of separating turbulent flows. *Computers & Fluids*, 27(2):137–156.

[107] Harten, A. (1983). High resolution schemes for hyperbolic conservation laws. *Journal of Computational Physics*, 49(3):357–393.

[108] Harten, A., Engquist, B., Osher, S., and Chakravarthy, S. R. (1997). Uniformly High Order Accurate Essentially Non-oscillatory Schemes, III. In Hussaini, M. Y., van Leer, B., and Van Rosendale, J., editors, *Upwind and High-Resolution Schemes*, pages 218–290. Springer, Berlin, Heidelberg.

[109] Hesthaven, J. S. and Warburton, T. (2008). *Nodal Discontinuous Galerkin Methods*, volume 54 of *Texts in Applied Mathematics*. Springer New York, New York, NY.

[110] Hu, C. and Shu, C.-W. (1999). Weighted Essentially Non-oscillatory Schemes on Triangular Meshes. *Journal of Computational Physics*, 150(1):97–127.

[111] Hughes, T. (2012). *The Finite Element Method: Linear Static and Dynamic Finite Element Analysis*. Dover Civil and Mechanical Engineering. Dover Publications.

[112] Hwang, R. R. and Peng, Y. F. (1995). Computation of backward-facing step flows by a second-order Reynolds stress closure model. *International Journal for Numerical Methods in Fluids*, 21(3):223–235.

[113] Iacovides, H. and Raisee, M. (2001). Computation of flow and heat transfer in two-dimensional rib-roughened passages, using low-Reynolds-number turbulence models. *International Journal of Numerical Methods for Heat & Fluid Flow*, 11(2):138–155.

[114] Iwai, H., Nakabe, K., and Suzuki, K. (2000). Flow and heat transfer characteristics of backward-facing step laminar flow in a rectangular duct. *Int. J. Heat Mass Transfer*, page 15.

[115] Jakirlić, S. and Hanjalić, K. (2002). A new approach to modelling near-wall turbulence energy and stress dissipation. *Journal of Fluid Mechanics*, 459:139–166.

[116] Jalali, A. and Ollivier-Gooch, C. F. (2017). Higher-order unstructured finite volume RANS solution of turbulent compressible flows. *Computers & Fluids*, 143:32–47.

[117] Jameson, A. and Yoon, S. (1987). Lower-upper implicit schemes with multiple grids for the Euler equations. *AIAA Journal*, 25(7):929–935.

[118] Jiang, B.-N., Hou, L.-J., Lin, T.-L., and Povinelli, L. A. (1995). Least-Squares Finite Element Solutions for Three-Dimensional Backward-Facing Step Flow. *International Journal of Computational Fluid Dynamics*, 4(1-2):1–19.

[119] Jiang, G.-S. and Shu, C.-W. (1996). Efficient Implementation of Weighted ENO Schemes. *Journal of Computational Physics*, 126(1):202–228.

[120] Jones, W. and Launder, B. (1972). The prediction of laminarization with a two-equation model of turbulence. *International Journal of Heat and Mass Transfer*, 15(2):301–314.

[121] Jovic, S. and Driver, D. M. (1994). Backward-Facing Step Measurements at Low Reynolds Number, Re_h=5000. NASA Technical Memorandum 108807, Ames Research Center, Moffett Field, CA.

[122] Jovic, S. and Driver, D. M. (1995). Reynolds number effect on the skin friction in separated flows behind a backward-facing step. *Experiments in Fluids*, 18(6):464–467.

[123] Juste, G. L., Fajardo, P., and Guijarro, A. (2016). Assessment of secondary bubble formation on a backward-facing step geometry. *Physics of Fluids*, 28(7):074106.

[124] Kaiktsis, L., Karniadakis, G. E., and Orszag, S. A. (1991). Onset of three-dimensionality, equilibria, and early transition in flow over a backward-facing step. *Journal of Fluid Mechanics*, 231:501–528.

[125] Kaiktsis, L., Karniadakis, G. E., and Orszag, S. A. (1996). Unsteadiness and convective instabilities in two-dimensional flow over a backward-facing step. *Journal of Fluid Mechanics*, 321:157–187.

[126] Karniadakis, G. E., Yakhot, A., Rakib, S., Orszag, S. A., and Yakhot, V. (1989). Spectral Element-RNG Simulations of Turbulent Flows in Complex Geometries. In Durst, F., Launder, B. E., Schmidt, F. W., and Whitelaw, J. H., editors, *Proceedings of the Seventh Symposium on Turbulent Shear Flows*. Stanford University Press, Stanford, CA.

[127] Kasagi, N. and Matsunaga, A. (1995). Three-dimensional particle-tracking velocimetry measurement of turbulence statistics and energy budget in a backward-facing step flow. *International Journal of Heat and Fluid Flow*, 16(6):477–485.

[128] Keating, A., Piomelli, U., Bremhorst, K., and Nesic, S. (2004). Large-eddy simulation of heat transfer downstream of a backward-facing step. *Journal of Turbulence*, 5:N20.

[129] Kim, J., Kline, S. J., and Johnston, J. P. (1980). Investigation of a Reattaching Turbulent Shear Layer: Flow Over a Backward-Facing Step. *Journal of Fluids Engineering*, 102(3):302.

[130] Kim, J. and Moin, P. (1985). Application of a fractional-step method to incompressible Navier-Stokes equations. *Journal of Computational Physics*, 59(2):308–323.

[131] Kline, S. J., Cantwell, B. J., and Lilley, G. M., editors (1981). *Proceedings of the 1980-81 AFOSR-HTTM Stanford Conference on Complex Turbulent Flows*. Stanford University Press, Stanford, CA.

[132] Ko, S. H. (1993). Computation of turbulent flows over backward and forward-facing steps using a near-wall Reynolds stress model. Annual Research Briefs 1993, Center for Turbulence Research.

[133] Ko, S. H. (1999). A near-wall reynolds stress model for backward-facing step flows. *KSME International Journal*, 13(2):200–210.

[134] Kopera, M. A., Kerr, R. M., Blackburn, H. M., and Barkley, D. (2014). Direct numnerical simulation of turbulent flow over a backward-facing step. *Under consideration for publication in Journal of Fluid Mechanics*.

[135] Kostas, J., Soria, J., and Chong, M. (2002). Particle image velocimetry measurements of a backward-facing step flow. *Experiments in Fluids*, 33(6):838–853.

[136] Kuehn, D. M. (1980). Effects of Adverse Pressure Gradient on the Incompressible Reattaching Flow over a Rearward-Facing Step. *AIAA Journal*, 18(3):343–344.

[137] Kurtulus, D. F. (2015). On the Unsteady Behavior of the Flow around NACA 0012 Airfoil with Steady External Conditions at Re=1000. *International Journal of Micro Air Vehicles*, 7(3):301–326.

[138] Ladson, C. L., Hill, A. S., and Johnson, W. G. (1987). Pressure Distributions from High Reynolds Number Transonic Tests of an NACA 0012 Airfoil in the Langley 0.3-Meter Transonic Cryogenic Tunnel. NASA Technical Memorandum 100526, Langley Research Center, Hampton, Virginia.

[139] Lasher, W. C. and Taulbee, D. B. (1992). On the computation of turbulent backstep flow. *International Journal of Heat and Fluid Flow*, 13(1):30–40.

[140] Launder, B. E. and Sharma, B. I. (1974). Appication of the Energy-Dissipation Model of Turbulence to the Calculation of Flow near a Spinning Disc. *Letters in Heat and Mass Transfer*, 1(2):131–138.

[141] Launder, B. E. and Spalding, D. B. (1974). The Numerical Computation of Turbulent Flows. *Computer Methods in Applied Mechanics and Engineering*, 3:269–289.

[142] Launder, B. E., Reece, G. J., and Rodi, W. (1975). Progress in the development of a Reynolds-stress turbulence closure. *Journal of Fluid Mechanics*, 68(3):537–566.

[143] Launder, B. E., Leschziner, M., and Sinder, M. (1981). Comparison of computation with experiment: summary report. In Kline, S. J., Cantwell, B. J., and Lilley, G. M., editors, *Proceedings of the AFOSR-HTTM-Stanford Conference on Complex Turbulent Flows*, volume 3, pages 1390–1407, Stanford, CA. Stanford University Press.

[144] Le, H., Moin, P., and Kim, J. (1997). Direct numerical simulation of turbulent flow over a backward-facing step. *Journal of Fluid Mechanics*, 330:349–374.

[145] Lee, T. and Mateescu, D. (1998). Experimental and Numerical Investigation of 2-D Backward-Facing Step Flow. *Journal of Fluids and Structures*, 12(6):703–716.

[146] Lien, F. S. and Leschziner, M. A. (1993). Computational Modelling of 3d Turbulent Flow in S-Diffuser and Transition Ducts. In Rodi, W. and Martelli, F., editors, *Engineering Turbulence Modelling and Experiments*, pages 217–228. Elsevier.

[147] Lien, F. S. and Leschziner, M. A. (1994). Assessment of turbulence-transport models including non-linear rng eddy-viscosity formulation and second-moment closure for flow over a backward-facing step. *Computers & Fluids*, 23(8):983–1004.

[148] Liu, X.-D., Osher, S., and Chan, T. (1994). Weighted Essentially Non-oscillatory Schemes. *Journal of Computational Physics*, 115(1):200–212.

[149] Luo, H., Baum, J. D., and Löhner, R. (1998). A Fast, Matrix-Free Implicit Method for Compressible Flows on Unstructured Grids. *Journal of Computational Physics*, 146(2):664–690.

[150] Luo, H., Baum, J. D., and Löhner, R. (2005). Extension of Harten-Lax-van Leer Scheme for Flows at All Speeds. *AIAA Journal*, 43(6):1160–1166.

[151] Malamataris, N. A. (2013). A numerical investigation of wall effects in three-dimensional, laminar flow over a backward facing step with a constant aspect and expansion ratio. *International Journal for Numerical Methods in Fluids*, 71(9):1073–1102.

[152] Massey, B. and Ward-Smith, J. (2006). *Mechanics of Fluids*. Taylor & Francis, 8 edition.

[153] Mellor, G. L. (1973). Analytic Prediction of the Properties of Stratified Planetary Surface Layers. *Journal of Atmospheric Sciences*, 30(6):1061–1069.

[154] Mellor, G. L. and Yamada, T. (1982). Development of a turbulence closure model for geophysical fluid problems. *Reviews of Geophysics*, 20(4):851–875.

[155] Menter, F. R. (1993). Zonal Two Equation $k-\omega$ Turbulent Models for Aerodynamic Flows. page 22, Orlando, Florida. AIAA.

[156] Meri, A. and Wengle, H. (2004). DNS and LES of Turbulent Backward-Facing Step Flow Using 2nd-and 4th-Order Discretization. In Friedrich, R. and Rodi, W., editors, *Advances in LES of Complex Flows*, volume 65, pages 99–114. Kluwer Academic Publishers, Dordrecht.

[157] Micchelli, C. A. and Rivlin, T. J. (1977). A Survey of Optimal Recovery. In Micchelli, C. A. and Rivlin, T. J., editors, *Optimal Estimation in Approximation Theory*, pages 1–54. Springer US, Boston, MA.

[158] Moffatt, H. K. (1964). Viscous and resistive eddies near a sharp corner. *Journal of Fluid Mechanics*, 18(1):1–18.

[159] Moore, T. W. F. (1960). Some Experiments on the Reattachment of a Laminar Boundary Layer Separating From a Rearward Facing Step on a Flat Plate Aerofoil. *The Journal of the Royal Aeronautical Society*, 64(599):668–672.

[160] Morton, K. W. and Sonar, T. (2007). Finite volume methods for hyperbolic conservation laws. *Acta Numerica*, 16:155–238.

[161] Mueller, T. J. and DeLaurier, J. D. (1999). Aerodynamic Measurements at Low Raynolds Numbers for Fixed Wing Micro-Air Vehicles. RTO AVT/VKI Special Course on Development and Operation of UAVs for Military and Civil Applications, Von-Karman Institute, Brussels.

[162] Myong, H. K. and Kasagi, N. (1990). A new approach to the improvement of $k-\epsilon$ turbulence model for wall-bounded shear flows. *JSME International Journal Series II*, 33:63–72.

[163] Nadge, P. M. and Govardhan, R. N. (2014). High Reynolds number flow over a backward-facing step: structure of the mean separation bubble. *Experiments in Fluids*, 55(1):1657.

[164] Nie, J. H. and Armaly, B. F. (2002). Three-dimensional convective flow adjacent to backward-facing step-effects of step height. *International Journal of Heat and Mass Transfer*, 45(12):2431–2438.

[165] Nie, J. H. and Armaly, B. F. (2003). Reattachment of Three-Dimensional Flow Adjacent to Backward-Facing Step. *Journal of Heat Transfer*, 125(3):422–428.

[166] Nie, J. H. and Armaly, B. F. (2004). Reverse flow regions in three-dimensional backward-facing step flow. *International Journal of Heat and Mass Transfer*, 47(22):4713–4720.

[167] Obi, S., Peric, M., and Scheuerer, G. (1991). Second-moment calculation procedure for turbulent flows with collocated variable arrangement. *AIAA Journal*, 29(4):585–590.

[168] Ollivier-Gooch, C. F. (1997). Quasi-ENO Schemes for Unstructured Meshes Based on Unlimited Data-Dependent Least-Squares Reconstruction. *Journal of Computational Physics*, 133(1):6–17.

[169] Ollivier-Gooch, C. F. and Van Altena, M. (2002). A High-Order-Accurate Unstructured Mesh Finite-Volume Scheme for the Advection–Diffusion Equation. *Journal of Computational Physics*, 181(2):729–752.

[170] Otügen, M. V. (1991). Expansion ratio effects on the separated shear layer and reattachment downstream of a backward-facing step. *Experiments in Fluids*, 10(5):273–280.

[171] Pont-Vílchez, A., Trias, F. X., Gorobets, A., and Oliva, A. (2019). Direct numerical simulation of backward-facing step flow at and expansion ratio 2. *Journal of Fluid Mechanics*, 863:341–363.

[172] Probst, A., Radespiel, R., Wolf, C., Knopp, T., and Schwamborn, D. (2010). A Comparison of Detached-Eddy Simulation and Reynolds-Stress Modeling Applied to the Flow over a Backward-Facing Step and an Airfoil at Stall. In *48th AIAA Aerospace Sciences Meeting Including the New Horizons Forum and Aerospace Exposition*, Orlando, Florida. American Institute of Aeronautics and Astronautics.

[173] Rani, H. P. and Sheu, T. W. H. (2006). Nonlinear dynamics in a backward-facing step flow. *Physics of Fluids*, 18(8):084101.

[174] Rodi, W. (1972). *The prediction of free turbulent boundary layers by use of a two equation model of turbulence*. PhD Thesis, Faculty of Engineering, University of London.

[175] Rodi, W. (1976). A New Algebraic Relation for Calculating the Reynolds Stresses. *ZAMM - Journal of Applied Mathematics and Mechanics / Zeitschrift für Angewandte Mathematik und Mechanik*, 56(S1).

[176] Rubinstein, R. and Barton, J. M. (1990). Nonlinear Reynolds stress models and the renormalization group. *Physics of Fluids A: Fluid Dynamics*, 2(8):1472–1476.

[177] Sarkar, A. and So, R. M. C. (1997). A critical evaluation of near-wall two-equation models against direct numerical simulation data. *International Journal of Heat and Fluid Flow*, 18(2):197–208.

[178] Scarano, F. and Riethmuller, M. L. (1999). Iterative multigrid approach in PIV image processing with discrete window offset. *Experiments in Fluids*, 26(6):513–523.

[179] Scarano, F., Benocci, C., and Riethmuller, M. L. (1999). Pattern recognition analysis of the turbulent flow past a backward facing step. *Physics of Fluids*, 11(12):3808–3818.

[180] Schlichting, H. and Gersten, K. (2017). *Boundary-Layer Theory*. Springer Berlin Heidelberg, Berlin, Heidelberg.

[181] Seban, R. A. (1964). Heat Transfer to the Turbulent Separated Flow of Air Downstream of a Step in the Surface of a Plate. *Journal of Heat Transfer*, 86(2):259–264.

[182] Seegmiller, H. L. and Driver, D. M. (1984). Private communications with Amano and Goel.

[183] Sethian, J. and Ghoniem, A. F. (1988). Validation study of vortex methods. *Journal of Computational Physics*, 74(2):283–317.

[184] Sharov, D. and Nakahashi, K. (1998). Reordering of hybrid unstructured grids for lower-upper symmetric Gauss-Seidel computations. *AIAA Journal*, 36(3):484–486.

[185] Sheu, T. W. H., Chiang, T. P., and Tsai, S. F. (1996). Vortical Structures in Channel Flows with a Backward-Facing Step. *International Journal of Turbo and Jet Engines*, 13(4).

[186] Shih, T.-H. and Lumley, J. L. (1993). Kolmogorov Behavior of Near-Wall Turbulence and its Application in Turbulence Modeling. *International Journal of Computational Fluid Dynamics*, 1(1):43–56.

[187] Shima, N. (1988). A Reynolds-Stress Model for Near-Wall and Low-Reynolds-Number Regions. *Journal of Fluids Engineering*, 110(1):38–44.

[188] Shir, C. C. (1973). A Preliminary Numerical Study of Atmospheric Turbulent Flows in the Idealized Planetary Boundary Layer. *Journal of Atmospheric Sciences*, 30:1327–1339.

[189] Shu, C.-W. and Osher, S. (1988). Efficient implementation of essentially non-oscillatory shock-capturing schemes. *Journal of Computational Physics*, 77(2):439–471.

[190] Shu, C.-W. and Osher, S. (1989). Efficient implementation of essentially non-oscillatory shock-capturing schemes, II. *Journal of Computational Physics*, 83(1):32–78.

[191] Shu, C.-W. (2009). High Order Weighted Essentially Nonoscillatory Schemes for Convection Dominated Problems. *SIAM Review*, 51(1):82–126.

[192] Shur, M. L., Spalart, P. R., Strelets, M. K., and Travin, A. K. (2015). An Enhanced Version of DES with Rapid Transition from RANS to LES in Separated Flows. *Flow, Turbulence and Combustion*, 95(4):709–737.

[193] Shyy, W., Lian, Y., Tang, J., Viieru, D., and Liu, H. (2011). *Aerodynamics of Low Reynolds Number Flyers*. Cambridge University Press, Cambridge.

[194] Sindir, M. M. S. (1982). *A numerical study of turbulent flows in backward-facing step geometries: A comparison of 4 models of turbulence*. PhD Thesis, University of California, Davis, California.

[195] Smirnov, E. M., Smirnovsky, A. A., Schur, N. A., Zaitsev, D. K., and Smirnov, P. E. (2018). Comparison of RANS and IDDES solutions for turbulent flow and heat transfer past a backward-facing step. *Heat and Mass Transfer*, 54(8):2231–2241.

[196] So, R. M. C. and Yoo, G. J. (1986). On the Modeling of Low-Reynolds-Number Turbulence. NASA Contractor Report NSA CR-3994, Arizona State University, Tempe , Arizona.

[197] So, R. M. C., Aksoy, H., Sommer, T. P., and Yuan, S. (1994). Development of a near-wall Reynolds-stress closure based on the SSG model for the pressure strain. NASA Contractor Report NASA CR-4618, Langley Research Center, Hampton, Virginia.

[198] So, R. M. C., Sarkar, A., Gerodimos, G., and Zhang, J. (1997). A Dissipation Rate Equation for Low-Reynolds-Number and Near-Wall Turbulence. *Theoretical and Computational Fluid Dynamics*, 9(1):47–63.

[199] So, R. M. C. and Yuan, S. (1998). Near-wall two-equation and Reynolds-stress modeling of backstep flow. *International Journal of Engineering Science*, 36(3):283–298.

[200] Speziale, C. G. (1987). On nonlinear $k - l$ and $k - \epsilon$ models of turbulence. *Journal of Fluid Mechanics*, 178:459–475.

[201] Steffen, Jr., C. (1993). A critical comparison of several low Reynolds number $k-\epsilon$ turbulence models for flow over a backward-facing step. In *29th Joint Propulsion Conference and Exhibit*, Monterey, CA, U.S.A. American Institute of Aeronautics and Astronautics.

[202] Suresh, A. and Huynh, H. T. (1997). Accurate Monotonicity-Preserving Schemes with Runge-Kutta Time Stepping. *Journal of Computational Physics*, 136(1):83–99.

[203] Tani, I., Iuchi, M., and Komoda, H. (1961). Experimental Investigation of Flow Separation Associated with a Step or a Groove. Technical Report 364, Aeronautical Research Institute, University of Tokyo, Tokyo.

[204] Thangam, S. and Knight, D. D. (1989). Effect of stepheight on the separated flow past a backward facing step. *Physics of Fluids A: Fluid Dynamics*, 1(3):604–606.

[205] Thangam, S. and Speziale, C. G. (1992). Turbulent flow past a backward-facing step - A critical evaluation of two-equation models. *AIAA Journal*, 30(5):1314–1320.

[206] Toro, E. F., Spruce, M., and Speares, W. (1994). Restoration of the contact surface in the HLL-Riemann solver. *Shock Waves*, 4(1):25–34.

[207] Toro, E. F. (2009). *Riemann solvers and numerical methods for fluid dynamics: a practical introduction*. Springer, Berlin, 3. ed edition. OCLC: 391057413.

[208] Tylli, N., Kaiktsis, L., and Ineichen, B. (2002). Sidewall effects in flow over a backward-facing step: Experiments and numerical simulations. *Physics of Fluids*, 14(11):3835–3845.

[209] van Leer, B. (1979). Towards the ultimate conservative difference scheme. V. A second-order sequel to Godunov's method. *Journal of Computational Physics*, 32(1):101–136.

[210] Viozat, C. (1997). Implicit Upwind Schemes for Low Mach Number Compressible Flows. Technical Report inria-00073607, RR-3084, INRIA.

[211] Vogel, J. C. and Eaton, J. K. (1985). Combined Heat Transfer and Fluid Dynamic Measurements Downstream of a Backward-Facing Step. *Journal of Heat Transfer*, 107(4):922–929.

[212] Wang, Z. J. (2014). High-order computational fluid dynamics tools for aircraft design. *Philosophical Transactions of the Royal Society A: Mathematical, Physical and Engineering Sciences*, 372(2022):20130318.

[213] Weiss, J. M. and Smith, W. A. (1995). Preconditioning applied to variable and constant density flows. *AIAA Journal*, 33(11):2050–2057.

[214] Welsh, D. J. A. and Powell, M. B. (1967). An upper bound for the chromatic number of a graph and its application to timetabling problems. *The Computer Journal*, 10(1):85–86. Publisher: Oxford Academic.

[215] Wendland, H. (2004). Haar spaces and multivariate polynomials. In *Scattered Data Approximation*, Cambridge Monographs on Applied and Computational Mathematics, pages 18–23. Cambridge University Press, Cambridge.

[216] White, F. M. (2011). *Fluid Mechanics*. McGraw-Hill, New York, NY, 7 edition.

[217] Williams, P. T. and Baker, A. J. (1997). Numerical simulations of laminar flow over a 3D backward-facing step. *International Journal for Numerical Methods in Fluids*, 24(11):1159–1183.

[218] Xie, W., Zhang, R., Lai, J., and Li, H. (2019). An accurate and robust HLLC-type Riemann solver for the compressible Euler system at various Mach numbers. *International Journal for Numerical Methods in Fluids*, 89(10):430–463.

[219] Yakhot, V. and Orszag, S. A. (1986). Renormalization group analysis of turbulence. I. Basic theory. *Journal of Scientific Computing*, 1(1):3–51.

[220] Yakhot, V., Orszag, S. A., Thangam, S., Gatski, T. B., and Speziale, C. G. (1992). Development of turbulence models for shear flows by a double expansion technique. *Physics of Fluids A: Fluid Dynamics*, 4(7):1510–1520.

[221] Yang, Z. and Shih, T. H. (1993). New time scale based $k - \epsilon$ model for near-wall turbulence. *AIAA Journal*, 31(7):1191–1198.

[222] Yap, C. R. (1987). *Turbulent heat and momentum transfer in recirculating and impinging flows*. PhD Thesis, University of Manchester Institute of Science and Technology (UMIST).

[223] Yoo, J. Y., Choi, H. C., and Han, S. M. (1989). Numerical analysis of turbulent flow over a backward-facing step using reynolds stress closure model. *KSME Journal*, 3(1):31–37.

[224] Yuan, S. P. and So, R. M. C. (1997). A Near-Wall Reynolds-Stress without Wall Normals. NASA Contractor Report NASA CR-4785, Langley Research Center.

[225] Zhang, Y.-T. and Shu, C.-W. (2009). Third Order WENO Scheme on Three Dimensional Tetrahedral Meshes. *Commun. Comput. Phys.*, page 14.

[226] Zhong, D. and Sheng, C. (2020). A new method towards high-order WENO schemes on structured and unstructured grids. *Computers & Fluids*, 200:104453.

[227] Zhu, J. and Qiu, J. (2017). A new third order finite volume weighted essentially non-oscillatory scheme on tetrahedral meshes. *Journal of Computational Physics*, 349:220–232.

[228] Zienkiewicz, O. C. and Taylor, R. L. (2000). *The finite element method*. Butterworth-Heinemann, Oxford ; Boston, 5th ed edition.

Appendix A

Existence and Uniqueness of the CLSQ Solution

The CLSQ solution exists if and only if the KKT matrix $\underline{\underline{\mathcal{A}}}$ is invertible. Here we strive to examine under which circumstances does the singularity arise and how to solve it in order to make the CLSQ reconstruction more robust.

We consider Eqn. 2.51 is equivalent to Eqn. 2.52 and Eqn. 2.51 is in KKT form.

Theorem A.1. A KKT matrix of the form $\begin{bmatrix} \underline{\underline{\mathcal{M}}}^\top \underline{\underline{\mathcal{M}}} & \underline{\underline{\mathcal{Q}}}^\top \\ \underline{\underline{\mathcal{Q}}} & 0 \end{bmatrix}$ is invertible iff $\underline{\underline{\mathcal{Q}}}$ has linearly independent rows and that $\left[\underline{\underline{\mathcal{M}}}^\top, \underline{\underline{\mathcal{Q}}}^\top\right]^\top$ has linearly independent columns.

Theorem A.1 is proved by Boyd and Vandenberghe in [29, p. 345]. The column-independence needs to be respected by $\left[\underline{\underline{\mathbb{I}}}^\top, \underline{\underline{\mathcal{K}}}^\top, \underline{\mathbb{I}}_{E_0}\right]^\top$, and since the constraint sub-matrix consists of BC constraints and cell-average constraint, the row independence needs to be satisfied by $\left[\underline{\underline{\mathcal{K}}}^\top, \underline{\mathbb{I}}_{E_0}\right]^\top$. A necessary condition for $\underline{\underline{\mathcal{A}}}$ to be invertible requires that $N_{\boxtimes}+1 \leq N_c$ and that $N_c \leq N_b + N_{\boxtimes} + 1$. To summarize

$$N_c - N_b \leq N_{\boxtimes} \leq N_c - 1. \tag{A.1}$$

In practice, two necessary but not sufficient criteria are respected for determining N_b and $\bar{N}_{\boxtimes}$ in order to satisfy Eqn. A.1 :

$$N_b > N_c \tag{A.2a}$$

$$\bar{N}_{\boxtimes} = \lfloor (p-1)/2 \rfloor + 1 \tag{A.2b}$$

and since the number of boundary edges in cell E_0 is generally ≤ 2, $N_{\boxtimes} \leq N_c - 1$ is satisfied as we impose Eqn. A.2b knowing that N_c is calculated by Eqn. 2.27. Eqn. A.2 is not a sufficient condition for $\underline{\underline{\mathcal{A}}}$ to be invertible, however, it provides a starting point to gain more insights on its invertibility.

Firstly, for $\left[\underline{\underline{\mathbb{I}}}^\top, \underline{\underline{\mathcal{K}}}^\top, \underline{\mathbb{I}}_{E_0}\right]^\top$ to have linearly independent columns, it is sufficient for $\underline{\underline{\mathbb{I}}}$ to be column-independent which is equivalent to

$$\operatorname{rank}(\underline{\underline{\mathbb{I}}}) = N_c \tag{A.3}$$

Table A.1: Number of Gauss-Legendre quadrature points per boundary edge $\bar{N}_{\boxtimes}$ and number of polynomial coefficients N_c for different polynomial orders p [91].

p	$\bar{N}_{\boxtimes}$	N_c
2	1	3
3	2	6
4	2	10
5	3	15
6	3	21

and since $\text{rank}(\underline{\underline{\mathbb{I}}}) = \text{rank}(\underline{\underline{\mathbb{I}}}^{\top}\underline{\underline{\mathbb{I}}})$, Eqn. A.3 is equivalent to

$$\text{rank}(\underline{\underline{\mathbb{I}}}^{\top}\underline{\underline{\mathbb{I}}}) = N_c \tag{A.4}$$

which implies that the $\underline{\underline{\mathcal{A}}}$ matrix for the *unconstrained* LSQ system (Eqn. 2.55) is invertible, hence the unconstrained LSQ reconstruction problem admits a unique solution. Since the computational grid is an arbitrary polygonal unstructured grid, Eqn. A.3 cannot be mathematically guaranteed simply by the number of neighbors N_b in the stencil S_0. It is possible for an N_b by N_c matrix $\underline{\underline{\mathbb{I}}}$ ($N_b > N_c$) to be rank-deficient for a specific stencil configuration. Therefore, it is important to increase the stencil size so that N_b is sufficiently larger than N_c to such an extent that the full-rankedness of $\underline{\underline{\mathbb{I}}}$ is preserved. The stencil selection algorithm needs to be carefully designed to avoid any drastic local increase of stencil size. As mentioned earlier in Section. 2.3, the current stencil construction algorithm absorbs immediate edge-neighbors in a layer-by-layer fashion until the number of neighbor cells in the stencil N_b surpasses the number of polynomial coefficients N_c by an empirically determined safety factor. We need to increase the safety factor whenever the matrix $\underline{\underline{\mathbb{I}}}$ is rank-deficient and the unique solution of the *unconstrained* LSQ reconstruction problem cannot be guaranteed.

For the rest of this chapter, we will focus on examining the row-independence of $\left[\underline{\underline{\mathcal{K}}}^{\top},\ \underline{\underline{\mathbb{I}}}_{E_0}\right]^{\top}$ matrix. First, we make the assumption that $\underline{\underline{\mathbb{I}}}_{E_0}^{\top}$ is not a linearly combination of rows of matrix $\underline{\underline{\mathcal{K}}}$. In practice, this assumption is verified by *a posteriori* results in almost all cases. Therefore we study whether $\underline{\underline{\mathcal{K}}}$ is row-independent. The row-independence of the BC constraint matrix $\underline{\underline{\mathcal{K}}}$ can be interpreted as a multivariate interpolation problem in two-dimensions $\mathbb{R}^2$, which is also equivalent to studying whether the boundary Dirichlet and Neumann BCs are well-posed. It is important to realize that, for the CLSQ reconstruction problem to yield a unique solution, we need to ensure two conditions : (i). the stencil is *admissible* in the sense that the corresponding unconstrained LSQ reconstruction problem admits a unique solution; (ii). the BC constraints are well-posed. The second condition will be studied in detail next.

The $\underline{\underline{\mathcal{K}}}$ matrix is row-independent iff there exists a bivariate polynomial that interpolates arbitrary data set at all boundary quadrature points. In order to study the existence of such polynomials, it is necessary to introduce the definition of $\pi_m(\mathbb{R}^d)$-unisolvent points by Wendland [215], where $\pi_m(\mathbb{R}^d)$ is the vector space of polynomials on $\mathbb{R}^d$ of degree $\leq m$.

Definition A.1 (Unisolvency)**.** [215, Def. 2.6, p. 21] The set of points $\mathcal{X} = \{p_1, \cdots, p_N\} \subseteq \mathbb{R}^d$ with $N \geq \dim \pi_m(\mathbb{R}^d)$ are $\pi_m(\mathbb{R}^d)$-unisolvent if the zero polynomial is the only polynomial in the polynomial space $\pi_m(\mathbb{R}^d)$ that vanishes on all of them.

Note that $\dim \pi_m(\mathbb{R}^d) = \binom{m+d}{d}$, where $m = p - 1$, and for $d = 2$ we obtain Eqn. 2.27.

Theorem A.2. [215, Lemma 2.8, p. 22] A set of $\pi_m(\mathbb{R}^d)$-unisolvent points $\mathcal{X} = \{p_1, \cdots, p_N\} \subseteq \mathbb{R}^d$ guarantees a unique d-variate polynomial interpolation of order at most m if $N = \dim \pi_m(\mathbb{R}^d) = \binom{m+d}{d}$.

Theorem A.2 has been proved by many previous authors [80, 215] to whom we refer the detailed proof.

Chung and Yao [49] introduced the notion of m^{th}-order "natural lattice" of cardinality $\binom{m+d}{d}$ which is a set of $\pi_m(\mathbb{R}^d)$-unisolvent points. Thus, according to Theorem A.2, the m^{th}-order natural lattice guarantees a unique d-variate polynomial interpolation of degree at most m.

Definition A.2 (Natural lattice)**.** [49, Def. 2, p. 737] Suppose that there exist $M = m + d$ distinct hyperplanes $H_1, \cdots, H_M$ in $\mathbb{R}^d$ such that the intersection of any d distinct hyperplanes $\subseteq \{H_1, \cdots, H_M\}$ is a point in $\mathbb{R}^d$ and that different choices of hyperplanes generate different points. Then this set of points is defined as the m^{th}-order natural lattice generated by $H_1, \cdots, H_M$ denoted by $\mathcal{X}^m_{\text{nat}}$.

Chung and Yao further proved the existence of a m^{th}-order natural lattice on $\mathbb{R}^d$ for any given m and d. In particular, natural lattices on $\mathbb{R}^2$ are shown in Fig. A.1. Note that a hyperplane in $\mathbb{R}^2$ is a line.

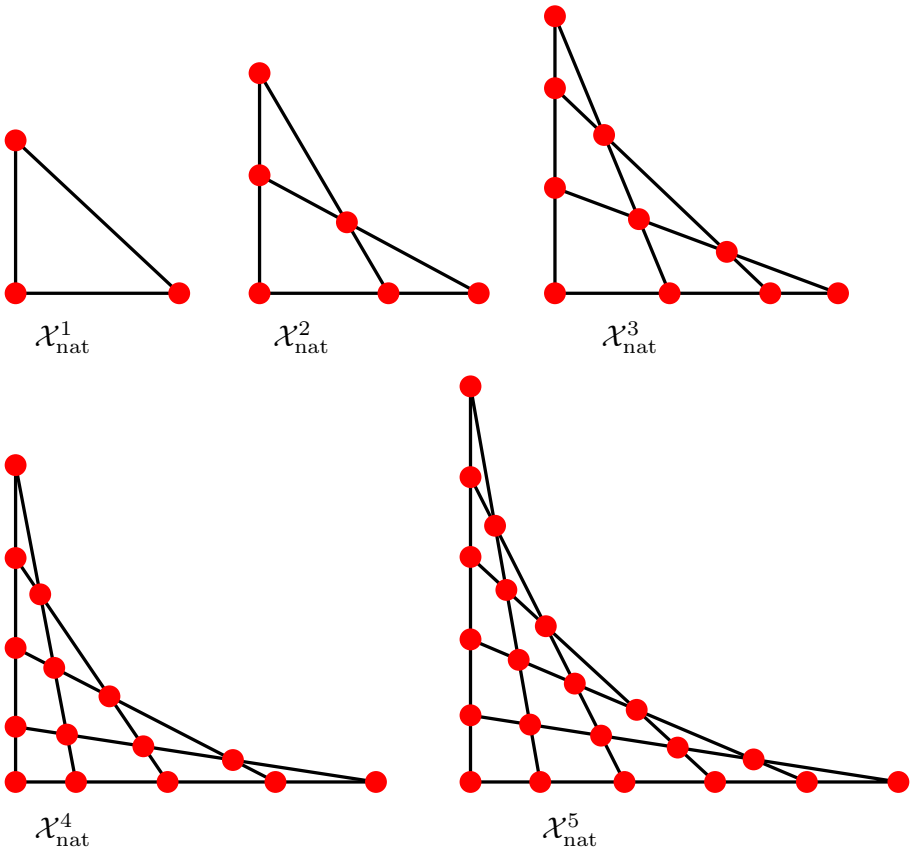

Figure A.1: Schematic representations of two-dimensional natural lattices $\mathcal{X}^m_{\text{nat}}$, where $m = p - 1$ is the highest polynomial degree [49].

A. Existence and Uniqueness of the CLSQ Solution

In the context of the current CLSQ scheme, the number of Gauss-Legendre quadrature points per boundary edge $\bar{N}_{\boxtimes}$ is determined by Eqn. A.2b, therefore, for a p^{th}-order CLSQ scheme, if a boundary cell has no more than 2 boundary edges, all of its boundary quadrature points must form a subset of a $(p-1)^{th}$-order natural lattice in two dimensions.

Corollary A.2.1. If a set points $\mathcal{X} = \{p_1, \cdots, p_N\} \subseteq \mathbb{R}^d$ is a subset of the m^{th}-order natural lattice $\mathcal{X}^m_{\text{nat}}$ as defined in Definition A.2, then the associated matrix $\underline{\underline{\mathcal{K}}} = [\underline{\alpha}_{p_1}, \ldots, \underline{\alpha}_{p_N}]^\top$ has linearly independent rows.

Proof. Matrix $\underline{\underline{\mathcal{P}}} = [\underline{\alpha}_{p_1}, \ldots, \underline{\alpha}_{p_{N_c}}]^\top$ is an N_c by N_c square matrix associated with the m^{th}-order natural lattice $\mathcal{X}^m_{\text{nat}}$, where $N_c = \binom{m+d}{d}$. Since a unique interpolation is guaranteed according Theorem A.2, $\underline{\underline{\mathcal{P}}}$ must be invertible, which implies that all rows of $\underline{\underline{\mathcal{P}}}$ are linearly independent. Therefore, any subset $\mathcal{X} \subseteq \mathcal{X}^m_{\text{nat}}$ of cardinality $N \leq N_c$ must admit an associated matrix $\underline{\underline{\mathcal{K}}} = [\underline{\alpha}_{p_1}, \ldots, \underline{\alpha}_{p_N}]^\top$ with linearly independent rows. □

In two-dimensional space, Corollary A.2.1 guarantees that the BC constraint matrix $\underline{\underline{\mathcal{K}}}$ is row-independent if boundary conditions are imposed on no more than 2 boundary edges, and if the number of quadrature points per edge $\bar{N}_{\boxtimes}$ is determined by Eqn. A.2b for $p \geq 2$ (at least for Dirichlet type constraints, next we will demonstrate that this is not sufficient for Neumann type constraints).

Next, consider the Neumann type boundary conditions where the wall-normal gradient is imposed on each quadrature point of a boundary edge. According to Eqn. 2.48, an example of $\underline{\underline{\mathcal{K}}}^4_{\text{neu}}$ is shown in Eqn. A.5 for the 4^{th}-order CLSQ scheme with Neumann type constraints.

$$\underline{\underline{\mathcal{K}}}^4_{\text{neu}} = \begin{bmatrix} 0 & \mathrm{n}_x & \mathrm{n}_y & 2X_1\mathrm{n}_x & Y_1\mathrm{n}_x + X_1\mathrm{n}_y & 2Y_1\mathrm{n}_y & 3X_1^2\mathrm{n}_x & 2X_1Y_1\mathrm{n}_x + X_1^2\mathrm{n}_y & Y_1^2\mathrm{n}_x + 2X_1Y_1\mathrm{n}_y & 3Y_1^2\mathrm{n}_y \\ 0 & \mathrm{n}_x & \mathrm{n}_y & 2X_2\mathrm{n}_x & Y_2\mathrm{n}_x + X_2\mathrm{n}_y & 2Y_2\mathrm{n}_y & 3X_2^2\mathrm{n}_x & 2X_2Y_2\mathrm{n}_x + X_2^2\mathrm{n}_y & Y_2^2\mathrm{n}_x + 2X_2Y_2\mathrm{n}_y & 3Y_2^2\mathrm{n}_y \\ 0 & \mathrm{n}_x & \mathrm{n}_y & 2X_3\mathrm{n}_x & Y_3\mathrm{n}_x + X_3\mathrm{n}_y & 2Y_3\mathrm{n}_y & 3X_3^2\mathrm{n}_x & 2X_3Y_3\mathrm{n}_x + X_3^2\mathrm{n}_y & Y_3^2\mathrm{n}_x + 2X_3Y_3\mathrm{n}_y & 3Y_3^2\mathrm{n}_y \end{bmatrix} \tag{A.5}$$

$\underline{\underline{\mathcal{K}}}^4_{\text{neu}}$ is column-equivalent to $\underline{\underline{\mathcal{K}}}^4_{\dagger}$ by elementary column operations (exchanging two columns, scaling a column by a nonzero factor, adding a multiple of one column to another) assuming that $\mathrm{n}_x = \text{const}$, $\mathrm{n}_y = \text{const}$.

$$\underline{\underline{\mathcal{K}}}^4_{\dagger} = \begin{bmatrix} 0 & 0 & 0 & 0 & 1 & X_1 & Y_1 & X_1^2 & X_1Y_1 & Y_1^2 \\ 0 & 0 & 0 & 0 & 1 & X_2 & Y_2 & X_2^2 & X_2Y_2 & Y_2^2 \\ 0 & 0 & 0 & 0 & 1 & X_3 & Y_3 & X_3^2 & X_3Y_3 & Y_3^2 \end{bmatrix} = \begin{bmatrix} \underline{\underline{\mathbf{0}}} & \underline{\underline{\mathcal{K}}}^3_{\text{dir}} \end{bmatrix} \tag{A.6}$$

where the nonzero columns of $\underline{\underline{\mathcal{K}}}^4_{\dagger}$ form a third-order Dirichlet type constraint matrix $\underline{\underline{\mathcal{K}}}^3_{\text{dir}}$. To generalize, a p^{th}-order Neumann type constraint matrix $\underline{\underline{\mathcal{K}}}^p_{\text{neu}}$ is column-equivalent to an $\bar{N}_{\boxtimes}$ by N_c matrix $\underline{\underline{\mathcal{K}}}^p_{\dagger} = \begin{bmatrix} \underline{\underline{\mathbf{0}}} & \underline{\underline{\mathcal{K}}}^{p-1}_{\text{dir}} \end{bmatrix}$. Therefore we have $\text{rank}(\underline{\underline{\mathcal{K}}}^p_{\text{neu}}) = \text{rank}(\underline{\underline{\mathcal{K}}}^{p-1}_{\text{dir}})$, which implies that a set of quadrature points generate a row-independent $\underline{\underline{\mathcal{K}}}^p_{\text{neu}}$ matrix iff they also generate a row-independent $\underline{\underline{\mathcal{K}}}^{p-1}_{\text{dir}}$ matrix.

According to Fig. A.1 and Eqn. A.2b, the set of boundary quadrature points for the p^{th}-order CLSQ scheme is also a subset of the $(p-2)^{th}$-order natural lattice for $p \geq 3$. For instance, when $p = 3$, the number of quadrature points per edge $\bar{N}_{\boxtimes} = 2$ while each hyperplane in $\mathcal{X}^2_{\text{nat}}$ also contains 2 colinear points, and since there are $m+1$ colinear points on each hyperplane of $\mathcal{X}^m_{\text{nat}}$,

the gap between $\bar{N}_{\boxtimes}$ and $m+1$ widens as the order grows. Therefore, the BC constraint matrix $\underline{\underline{\mathcal{K}}}$ of Neumann type is row-independent for the CLSQ scheme with $p \geq 3$ if only one boundary edge is associated with a given reconstruction stencil.

A further revisit to the matrix $\underline{\underline{\mathcal{K}}}^4_{\text{neu}}$ in Eqn. A.5 shows that, for quadrature points on boundary edges with different unit normal vectors $\vec{\mathrm{n}}_{\boxtimes_i}$ such as in a corner boundary cell, $\underline{\underline{\mathcal{K}}}^4_{\text{neu}}$ is no longer column-equivalent to $\underline{\underline{\mathcal{K}}}^4_{\dagger}$ therefore the row-independence of the sub-matrix $\underline{\underline{\mathcal{K}}}^3_{\text{dir}}$ does not guarantee the row-independence of $\underline{\underline{\mathcal{K}}}^4_{\dagger}$ or that of $\underline{\underline{\mathcal{K}}}^4_{\text{neu}}$. In practice, the row-independence of $\underline{\underline{\mathcal{K}}}^p_{\text{neu}}$, although not mathematically guaranteed, can still be achieved in many cases, special attention is needed to monitor the full-rankedness of $\underline{\underline{\mathcal{K}}}^p_{\text{neu}}$ matrix if the reference cell E_0 contains multiple boundary edges. Alternatively, in case that E_0 is a corner boundary cell, we can split E_0 from the corner into two boundary cells, each with one single boundary edge to enhance robustness of the scheme.

Proposition A.1. In general, if the number of quadrature per edge $\bar{N}_{\boxtimes}$ is determined by Eqn. A.2b, there exists a p^{th}-order bivariate polynomial in stencil S_0 which can either interpolate the values (Dirichlet type BC) of $\phi(x, y)$ at all boundary quadrature points on no more than 2 boundary edges for $p \geq 2$, or interpolate the gradient projected onto a fixed face-normal vector $\vec{\mathrm{n}}$ (Neumann type BC) for $p \geq 3$.

In summary, this analysis shows that the current CLSQ reconstruction scheme guarantees a unique solution in a given stencil S_0 when the following conditions are satisfied :

1. Stencil S_0 is adequately selected such that N_b is sufficiently greater than N_c, such that the *unconstrained* LSQ reconstruction problem admits unique solution;
2. Cell-average constraint is not a linear combination of BC constraints (assumed);
3. For Dirichlet type BC constraints: $\bar{N}_{\boxtimes}$ determined by Eqn. A.2b with $p \geq 2$ and number of boundary edges ≤ 2;
4. For Neumann type BC constraints: $\bar{N}_{\boxtimes}$ determined by Eqn. A.2b with $p \geq 3$ and number of boundary edges ≤ 1.

The above-mentioned conditions can be satisfied in most cases for an arbitrary polygonal grid with special care taken at domain corners. However, when they cannot be ensured occasionally, we need to pay close attention to the invertibility of matrix $\underline{\underline{\mathcal{A}}}$ and make necessary modifications to the grid or to the local order of the scheme. An approach adopted by many previous authors [38, 169] is to perform Gaussian elimination to remove all linearly dependent constraints, and the $\underline{\underline{\mathcal{K}}}$ matrix is thus reduced to row echelon form before being assembled into $\underline{\underline{\mathcal{A}}}$. This approach guarantees a full-ranked BC constraint matrix, but can also lead to an over-constrained or ill-constrained stencil being left undetected. Therefore, an analysis on the existence and uniqueness of CLSQ solutions allows us to understand under which circumstances can we expect a singular KKT matrix $\underline{\underline{\mathcal{A}}}$ and to remedy this defect *a priori*.

Finally, we remark that, although this analysis addresses mainly the well-posedness problem of BC constraints, the notions of unisolvency and natural lattices can be potentially extended for the construction of admissible LSQ stencils S_i. As shown by Gerolymos [89], polynomial interpolation and reconstruction problems are closely related. For a 1D grid with constant Δx, the interpolating polynomial and the reconstructing polynomial of a given data set are related by a bijective mapping $R : \pi_m(\mathbb{R}^d) \to \pi_m(\mathbb{R}^d)$ [89, Theorem 5.1, p. 296]. This relation will be studied in the future for general 2D polygonal grids, which can potentially contribute to a more efficient stencil construction algorithm.

Appendix B

Low-Mach Laminar BFS Flow Tests

The laminar BFS test-case of Armaly *et al.* [13] is used to evaluate the performance of the AM-HLLC-P Riemann solver proposed by Xie *et al.* [218] (see Section. 2.4 for detailed expressions). The test-case configuration is given in Fig. 4.1 and we perform all computations on the Grid 2 in Tab. 3.1 with 43204 computational cells and a minimum wall-normal grid spacing $\Delta y_1 = \Delta y_2 = 1.426\%H$ (grid parameters in Fig. 3.15).

Three computations are performed at inlet centerline Mach numbers $M = \{0.01, 0.05, 0.2\}$ with each of the HLLC and AM-HLLC-P Riemann solvers at $Re_{u_B, D_h} = 100$. We intend to investigate the difference in pressure field solutions obtained with and without the low-Mach correction technique.

The normalized pressure field $p_N(x, y)$ enables us to compare pressure field solutions among flows with different Mach numbers, and it is defined by Guillard and Viozat [102] and Xie *et al.* [218] as

$$p_N(x, y) = \frac{p(x, y) - p_{\min}}{p_{\max} - p_{\min}} \tag{B.1}$$

where $p_{\min}$ and $p_{\max}$ are respectively the minimum and maximum pressure values in the domain. Note that p_N ranges from 0 to 1 which characterizes the magnitude of pressure fluctuation. Obviously, as Mach number $M \to 0$ (quasi-incompressible flow), we expect $p_N(x, y)$ to be independent of the inflow Mach number M. In practice, this limit is achieved for $\max_{\vec{x} \in \Omega} M \leq 0.35$ [93, Appendix A].

Fig. B.1 shows the normalized pressure fields obtained using the conventional HLLC Riemann solver without any low-Mach correction. The region near the step is examined since it corresponds to the location where large pressure gradient is observed due to the sudden expansion as shown previously in Fig. 4.10. In Fig. B.1, we observe that the conventional HLLC solver does not give correct pressure fields as the Mach number decreases from 0.2 to 0.01. By reducing the Mach number, the lower bound of p_N drops rapidly from 0.28 to 0.09 and the pressure contour lines cluster heavily towards the singular step corner. This deterioration of pressure solution at decreasing Mach number was already observed previously by Guillard and Viozat [102], Guillard and Murrone [103] and Xie *et al.* [218] with inviscid airfoil test-cases.

Improved pressure solutions are obtained with the AM-HLLC-P Riemann solver on the same grid as shown in Fig. B.2. An essentially constant range of p_N is maintained with decreasing inlet Mach number, and structure of pressure contour lines remains consistent from $M = 0.01$ to

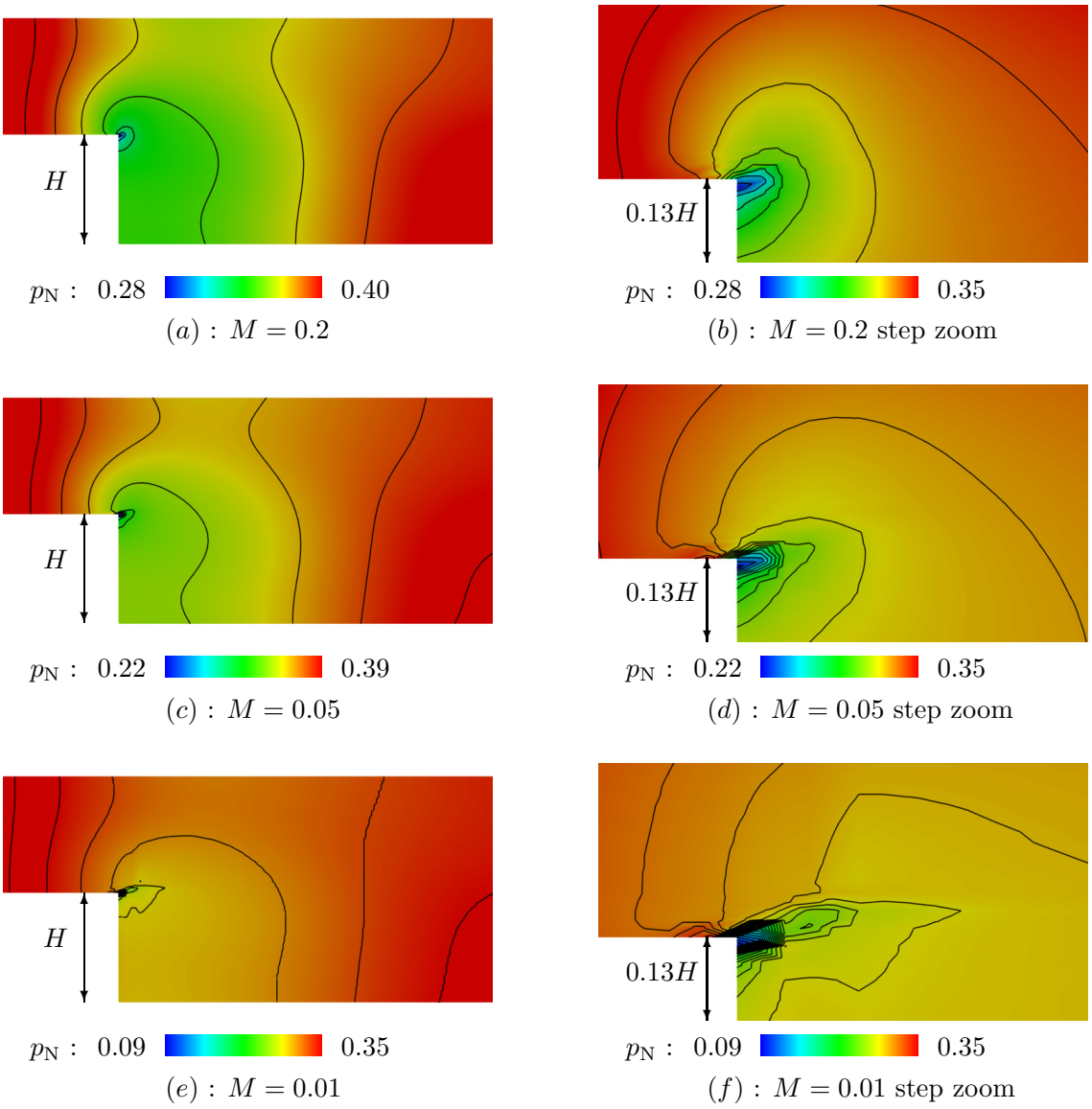

Figure B.1: Normalized pressure p_N field for the Armaly *et al.* [13] test-case at $Re_{u_B,D_h} = 100$ and $M = 0.01, 0.05, 0.2$. HLLC Riemann solver without low-Mach correction is used for numerical flux computations.

$M = 0.2$. In Fig. B.2.e and .f, oscillations of small amplitude are observed on certain pressure contour lines at $M = 0.01$. This phenomenon is also present in the original publication of Xie *et al.* at $M = 0.01$ for a channel flow with circular arc bump. These oscillations typically occur at low Mach number when the mesh is stretched and irregular. However, comparing to the uncorrected HLLC solver the accuracy of pressure field solution at low Mach number is substantially improved.

Finally, Fig. B.3 shows the streamwise velocity u profiles at multiple different stations. Com-

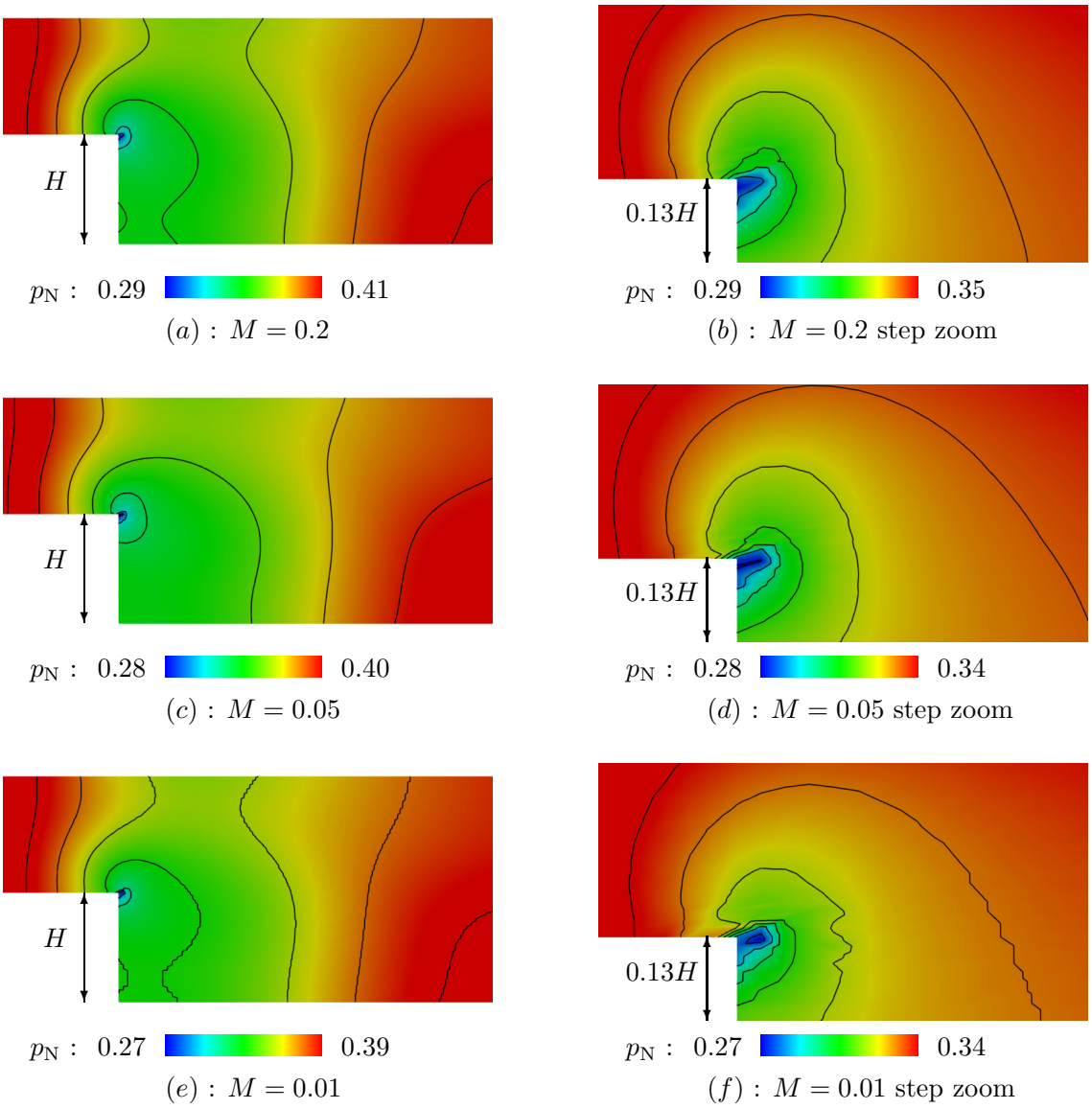

Figure B.2: Normalized pressure p_N field for the Armaly *et al.* [13] test-case at $Re_{u_B,D_h} = 100$ and $M = 0.01, 0.05, 0.2$. Low-Mach corrected HLLC Riemann solver AM-HLLC-P [218] is used for numerical flux computations.

putations are performed on the same grid (Grid 2 in Tab. 3.1) with both HLLC and AM-HLLC-P Riemann solvers. We verify that the low Mach number $M \ll 1$ only has influence on the pressure field solutions, and in particular in the immediate neighborhood of the step-corner geometric singularity, since it can be observed that u profiles at all stations are identical for $M = 0.01, 0.05, 0.2$ with and without low-Mach correction technique. In other words, although the experimental study of Armaly *et al.* [13] is conducted at extremely low Mach numbers ($\mathcal{O}(10^{-4})$), performing computations at $M = 0.2$ with the same Reynolds number does not reduce the accuracy of the results,

and the convergence rate is considerably accelerated at $M = 0.2$ due to the relatively low numerical stiffness.

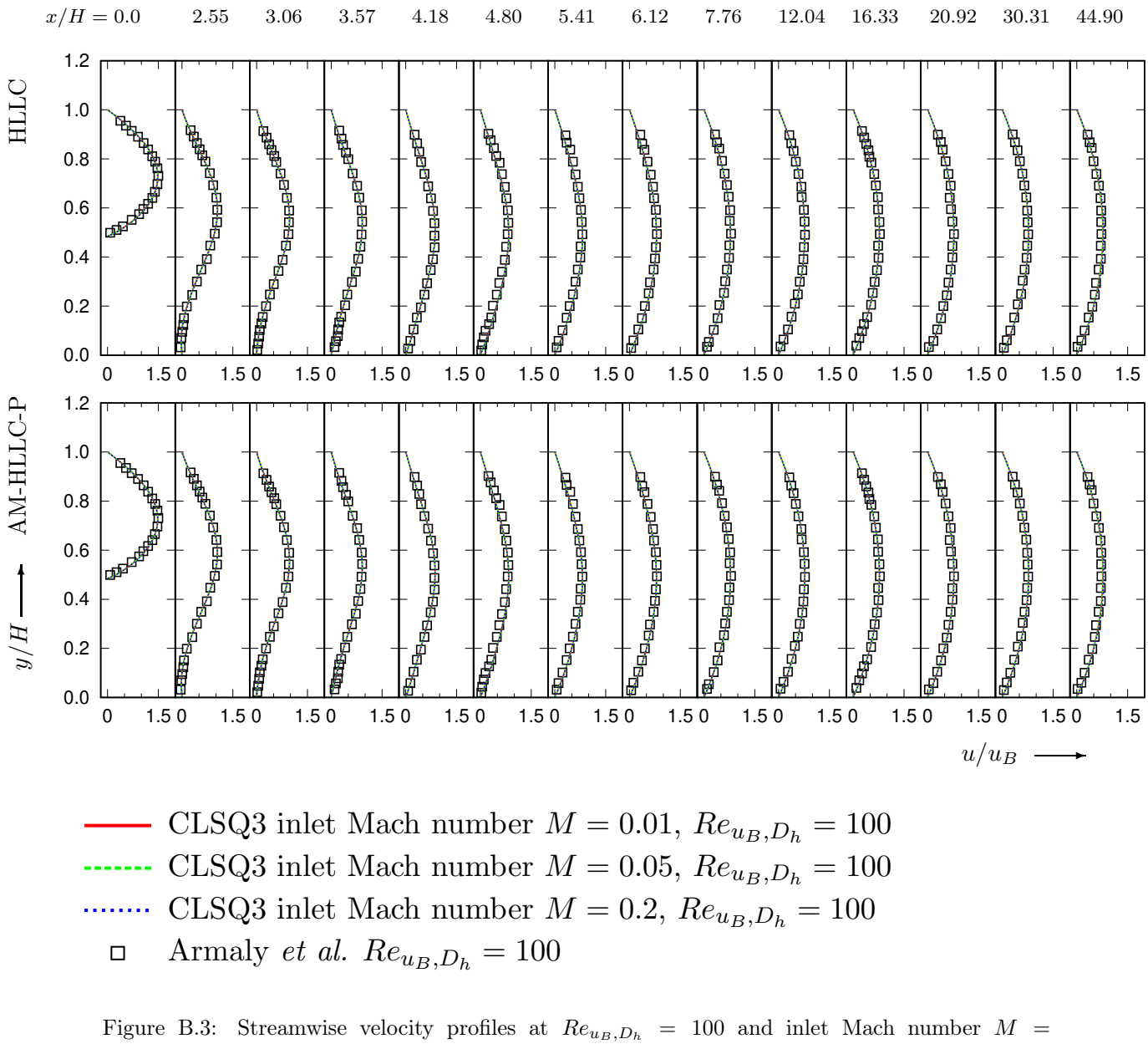

Figure B.3: Streamwise velocity profiles at $Re_{u_B,D_h} = 100$ and inlet Mach number $M = 0.01, 0.05, 0.2$ computed with HLLC and AM-HLLC-P Riemann solvers. Experimental data sources : Armaly *et al.* [13].

Appendix C

Literature Review on Turbulent BFS Flows

Many different velocities and lengths appear in the literature to define the Reynolds number $Re_{\text{vel,len}}$ and these physical quantities are listed in Tab. C.1 where u_τ is the wall-friction velocity, δ

Table C.1: Velocities and lengths used for Reynolds number definitions in the literature of turbulent BFS.

i	velocity	j	length
1	u_B	1	H
2	u_∞	2	H_i
3	u_τ	3	D_h
		4	δ
		5	δ_1
		6	δ_2

is the boundary layer thickness, δ_1 is the displacement thickness and δ_2 is the momentum thickness. The definitions of δ_1 and δ_2 are given by Schlichting and Gersten [180, p. 258] for a flow parallel to a longitudinal wall along x-axis

$$\delta_1 = \int_0^\delta \left(1 - \frac{\rho u}{\rho_\infty u_\infty}\right) \mathrm{d}y \tag{C.1a}$$

$$\delta_2 = \int_0^\delta \frac{\rho u}{\rho_\infty u_\infty} \left(1 - \frac{\rho u}{\rho_\infty u_\infty}\right) \mathrm{d}y \tag{C.1b}$$

In this appendix, the subscripts of $Re_{\text{vel,len}}$ are replaced by the quantities in Tab. C.1 to avoid any ambiguity. For instance, the Reynolds number defined by the bulk velocity and the step height is denoted by $Re_{u_B,H}$. A sketch of a generic BFS test-case is provided in Fig. C.1, where we denote the inlet channel height by H_i, the outlet channel height by H_o, the step height by H and the channel width by W. As with the laminar test-cases, the expansion ratio is defined by

$ER = H_o/H_i$, the aspect ratio is defined by $AR = W/H_o$. The length of the primary recirculation region is denoted by x_1.

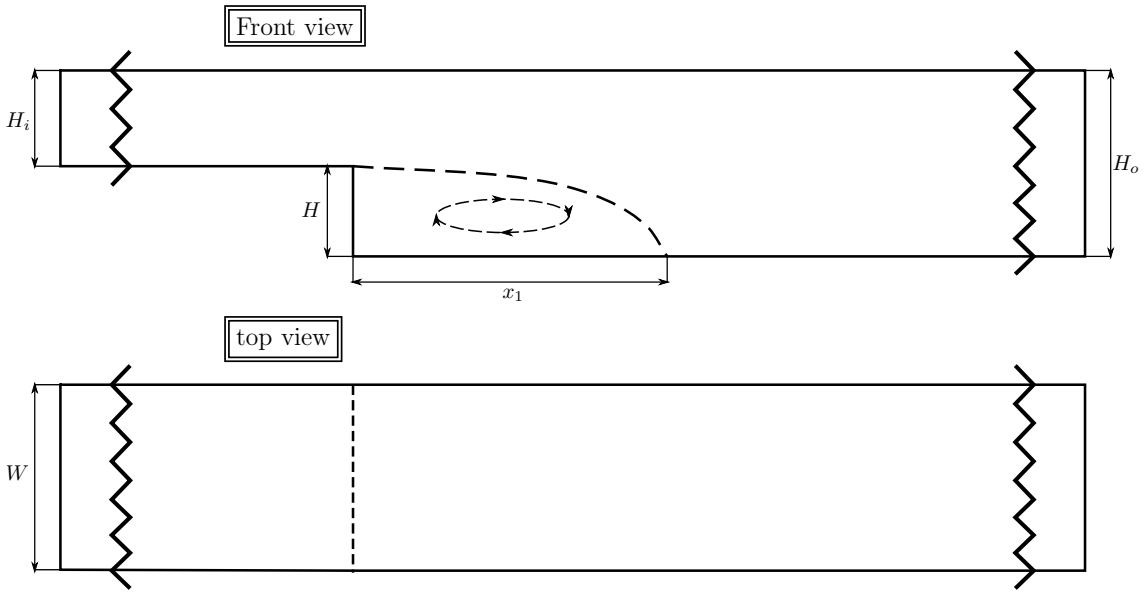

Figure C.1: Schematic representation of a generic turbulent BFS test-case with front and top views.

Due to its vast engineering applications, turbulent BFS flows have received substantial attention in the literature. Early experiments conducted by Tani *et al.* [203] at Reynolds numbers $Re_{u_\infty,H}$ up to 6×10^4 demonstrated insensitivity of bottom wall pressure distribution to the step height and incoming boundary layer thickness. Abbott and Kline [1] performed experiments on fully turbulent BFS flows from $Re_{u_\infty,H_i} = 2\times10^4$ to 5×10^4 in both single and double expansion channels and suggested that the reattachment length x_1 was independent of Reynolds number in their Re_{u_∞,H_i} range. Heat transfer and temperature distribution was measured by Seban [181]. De Brederode *et al.* gave an estimate of minimum aspect ratio of $AR = 10$ to yield a essentially two-dimensional flow [62]. Always limited to the low Reynolds number regime, Bradshaw and Wong [30] first rigorously studied the reattachment mechanism of the turbulent shear layer. They suggested that large-scale eddies in the separated turbulent shear layer were divided into upstream and downstream-propagating portions, which caused rapid reduction in turbulent length scale and shear stress downstream. A very slow recovery to the thin boundary layer was discovered by the authors which extended at least 30 times the boundary layer thickness at step. Chandrsuda and Chandrsuda and Bradshaw [36, 37] provided hot-wire anemometry measurements of fluctuating turbulent velocity statistics of separating thin laminar boundary layers ($0.04H$) reattaching to fully turbulent states over a BFS. The Reynolds numbers $Re_{u_\infty,\delta_2} = 400$ with $\delta_2 : H = 1 : 255$ which gives $Re_{u_\infty,H} \approx 10^5$, and although the boundary layer was laminar before the step, results showed sharp changes of turbulent quantities before and after the reattachment, concretely, the decreases of triple velocity correlations and turbulent shear stresses in the wall-normal direction, and increase of then pressure redistribution term due to wall effects. Their results provided valuable insights for future design of near-wall Reynolds Stress Models (RSM). Chandrsuda [36] also recommended the use of LDV for more reliable measurements of turbulent quantities. Kim *et al.* [129] performed experiments to

study BFS flows already turbulent before separation using hot-wire anemometer. Being aware of the limits of this device, measurements were not made in the recirculation zone. Reynolds numbers in this study ranged from $Re_{u_\infty,H} = 3 \times 10^4$ to 4.5×10^4 and the independence of flow structures from Reynolds number was demonstrated in this range, and a reattachment length of $x_1 \approx 7H$ was measured for all Reynolds numbers. The authors made similar observations on the decay of turbulent fluctuations after the reattachment as in [36, 37]. However, the intermittency report showed that large eddies in the turbulent mixing layer traveled alternately up and downstream instead of being split in two parts as suggested by Bradshaw and Wong [30]. In addition, Castro and Bradshaw and Gillis and Johnston [33, 96] showed that convex streamwise curvature of separated shear layer had stabilizing effects which reduced turbulent shear stresses.

Multiple experimental works using improved devices such as pulsed-wire anemometer and LDV allowing to measure back-flow regions were conducted. Baker [17] used both experimental and numerical approaches to study the fully turbulent reattaching shear layer at $Re_{u_\infty,H} = 5 \times 10^4$, since the emphasis of the study was on the recirculation zone, pulsed-wire technique was adopted and showed better results in regions where turbulent intensity was high compared to hot-wire measurements. The author [17] also performed 2D computations using the two-equation model by Launder and Spalding [141] with a wall-function, which gave good agreement with experimental data in terms of mean-flow variables but under-predicted the reattachment length. Etheridge and Kemp [78] was one of the first to use LDV measurement on BFS flows. Their results confirmed that the turbulent length scale decreased rapidly at reattachment as observed by Chandrsuda and Bradshaw [37] even though the initial boundary layer thickness in [78] was much higher ($\delta/H \approx 2.0$) than that in [37] ($\delta/H \approx 0.04$) and was in a transitional state. Eaton *et al.* [74] and Eaton and Johnston [75] experimentally studied effects of the state of the separating boundary layer (laminar, transitional, or turbulent) on the BFS flow using pulsed-wire. Boundary layer thicknesses were identical while their states were different. The authors [74, 75] found that the reattachment length x_1 increased rapidly with increasing Reynolds number when the initial boundary layer remained laminar, the maximum value of x_1 was obtained at the beginning of the transitional regime and started to decrease until the boundary layer became fully turbulent where the flow was no longer dependent of the Reynolds number. Kuehn [136] was the first to show that the reattachment length x_1 was strongly influenced by the adverse pressure gradient caused by sudden expansion. He concluded that the reattachment length increased with increasing step height and upper wall deflection at the same Reynolds number and boundary layer state. In 1981, Eaton and Johnston [76] reviewed then existing experimental data and suggested that five independent parameters could affect the reattachment length : (1) state of initial boundary layer (before the step), (2) thickness of initial boundary layer δ, (3) turbulent intensity in the free-stream, (4) adverse pressure gradient due to channel geometry, (5) channel aspect ratio which introduces end-wall effects. Durst and Tropea [72] systematically studied BFS flows ranging from $2000 < Re_{u_\infty,H} < 20000$ and $1.06 < ER < 3.0$ using LDV. Within the given Reynolds number range, the flow was identified to be in the transitional regime and showed high Reynolds number dependence. The expansion ratio ER affected the reattachment length to similar extent for all Reynolds numbers studied, but the effect saturated for high expansion ratio $2 < ER < 3$.

In 1985, Driver and Seegmiller [66] proposed a well defined turbulent BFS flow test case to validate turbulence models. The test-case consisted of a nominally two-dimensional channel with a low expansion ratio step ($ER = 1.125$). The incoming boundary layer was fully turbulent with a thickness of $\delta \approx 1.5H$ and the Reynolds number based on momentum thickness $Re_{u_\infty,\delta_2} = 5000$ which corresponded to $Re_{u_\infty,H} \approx 37500$. Inlet Mach number was $Ma = 0.128$ to ensure incompressibility. Experimental measurements gave a reattachment length $x_1 = 6.26H$. Measurements were com-

pared with numerical results obtained by Sindir [194] using $k-\varepsilon$ model and Algebraic-Stress Model (ASM) with and without modified dissipation rate of turbulent kinetic energy (production term modified). Authors showed that the modified ASM gave excellent prediction of the reattachment length x_1 while unmodified ASM and both $k-\varepsilon$ models gave almost 30% of under-prediction. However, all turbulence closures in [66, 194] failed to predict the locations and values of the maximum Reynolds-stresses in the reattachment zone due to their inherent defects. To overcome the shortcoming that ASM does not model the convection or diffusion of Reynolds-stresses, Amano and Goel [11] numerically studied the turbulent BFS flow using a hybrid eddy-viscosity Reynolds Stress model in a sense that the diffusion of turbulent kinetic energy k and its dissipation ε was approximated by the eddy-viscosity hypothesis while Reynolds stresses were modeled separately with their own transport equations. Results of $k-\varepsilon$ model, ASM, and hybrid RSM were compared against experimental data at $Re_{u_\infty,\delta_2} = 5000$ and $ER = 1.5$ and $ER = 1.33$ documented in a private communication with Seegmiller and Driver [182], RSM gave best prediction in the relaxing region while ASM performed best in the recirculation zone, and all statistical turbulence models under-predicted the reattachment length. No significant improvement of RSM was observed versus ASM. A later paper by the same authors [12] compared the abilities to correctly predict the triple velocity correlations of different RSMs [56, 61, 104, 188] under the hybrid framework in [11]. Based on comparisons with experimental data in [37], the authors concluded that all existing RSMs failed to predict the magnitudes of triple velocity correlations due to the lack of their transport equations. Celenligil and Mellor [34] numerically reproduced the test case of Kim *et al.* [129] using a RSM with wall-function introduced in [153, 154]. The authors obtained an over-predicted reattachment length $x_1 \approx 7.89H$ while the experimental data gave $x_1 \approx 7.0H$. Yoo *et al.* [223] compared numerical results using the standard $k-\varepsilon$ model, the RSM with standard ε equation, the RSM with ε modification proposed by Hanjalić and Launder [104], and the RSM with ε modification proposed by Launder *et al.* [143]. The authors showed that the best overall agreement with the experimental data provided by Kim *et al.* [129] was obtained with the RSM in [143] ($x_1 = 7.10H$ compared to $x_1 \approx 7.0H$ in the experiment [129]). All turbulence closures showed slower return to turbulent boundary layer downstream of reattachment than the experimental data. Obi *et al.* [167] also compared the performances of $k-\varepsilon$ model and a RSM with wall-function and showed that, as opposed to the finding of [223], all models under-predicted the primary reattachment length. The RSM not only gave better results than $k-\varepsilon$ model in terms of the primary reattachment length ($x_1 = 6.73H$ for RSM, $x_1 = 6.08H$ for $k-\varepsilon$, $x_1 \approx 7.0H$ for the experiment) but also predicted the length of the secondary corner vortex with much closer agreement with the experimental data by a factor of three. However, the authors [167] also noted that the *ad hoc* wall-damping created excessively high anisotropy in the recirculation zone which caused the reattaching streamline to bend unrealistically towards the bottom wall. They suggested that an improved pressure-strain ϕ_{ij} model which took into account of the flow anisotropy was needed for better predictions. Note that all RSMs discussed until this point do not account for near-wall (wall-functions are used) or low Reynolds number effects.

Various numerical simulations using modified $k-\varepsilon$ turbulence models were also carried out on turbulent BFS flows. Chen [40] suggested that the considerable discrepancies in BFS flows predictions produced by earlier two-equation models and RSMs [131] were due to the inability of the single turbulence scale to model the whole turbulent energy spectrum. By decomposing the turbulent kinetic energy dissipation rate ε into low and high-wave-number parts, the author showed a significant overall improvement over the single-scale model with respect to the experimental data provided by [129], specifically in terms of the reattachment length where the experimental study gave $x_1 \approx 7H$, the multi-scale $k-\varepsilon$ model predicted $x_1 = 6.7H$ while the single-scale counterpart

predicted $x_1 = 5.2H$. Other modifications on the two-equation $k-\varepsilon$ model were made to better predict BFS flows. Speziale [200] and Benocci and Skovgaard [26] suggested that by introducing anisotropy (or non-linearity) to the $k-\varepsilon$ equations, the prediction could be largely improved. So and Yoo [196] and Karniadakis *et al.* [126] showed that new wall-functions could significantly improve the prediction of the reattachment length. Avva *et al.* [16] attributed the inaccuracies of two-equation models to the insufficient order of numerical schemes, by using a second-order accurate scheme and by taking into account the streamline curvature effects [33], the authors were able to eliminate the error produced by the baseline $k-\varepsilon$ model of Launder and Spalding [141]. Thangam and Speziale [205] made an important review to address the inadequacies of two-equation turbulence model (namely the $k-\varepsilon$ model) to predict BFS flow due to inaccurate assumption of isotropic turbulent eddy-viscosity. Thangam and Speziale introduced an anisotropic eddy-viscosity which improved the prediction of reattachment length to $x_1 = 6.9H$ compared to $x_1 \approx 7.0H$ showed by experimental data [129]. Steffen, Jr. [201] evaluated four different low-Reynolds-number $k-\varepsilon$ models [47, 120, 140, 186] on their predictions of the Driver and Seegmiller [66] test-case, and comparison was made to a high-Reynolds-number $k-\varepsilon$ model with wall-function. The author [201] showed that, while similar mean-flow quantities were obtained, the four low-Reynolds-number models (without anisotropic eddy-viscosity of Speziale [200]) severely under-predicted the reattachment length $x_1 = 6.26H$ (from 4.9 [120] to 5.4 [47, 140]). Although the wall-function slightly improved the result ($x_1 = 5.5H$ with wall-function), the defects of $k-\varepsilon$ models in predicting the Reynolds stresses and turbulent kinetic energy reported by [205] were still present. A new low-Reynolds-number $k-\varepsilon$ model was proposed by Abe *et al.* [2, 3] which replaced the wall shear velocity u_τ by the Kolmogorov velocity $u_\varepsilon := (\nu\varepsilon)^{1/4}$ to account for the low-Reynolds-number effects near-wall. The numerical results showed good agreement with multiple BFS flow experiments in terms of reattachment length, and, by solving the temperature equation [3], the heat transfer coefficient distribution was well predicted comparing to the experimental data provided by Vogel and Eaton [211] (will be reviewed later). Abe *et al.* [4] further developed a non-linear version of [2, 3] by taking into account of features in the RSM and ASM. Excellent agreements in terms of reattachment lengths with five BFS cases [73, 75, 127, 144, 211] were shown, and the prediction on skin friction distribution was improved compared to the original linear eddy-viscosity model [2]. Durbin [71] developed a three-equation $k-\omega-\overline{v^2}$ model to account for the transport effects of turbulent fluctuation normal to streamlines $\overline{v^2}$. Tests were performed on cases of Jovic and Driver [121] (will be reviewed later) and Driver and Seegmiller [66], the reattachment lengths predicted in both cases agreed perfectly with experimental data. The low skin friction coefficient in the recirculation zone in the Jovic and Driver test-case [121] was also reproduced by the computation. The $k-\omega-\overline{v^2}$ model [71] proved able to predicted largely separated, non-equilibrium turbulent flows.

Vogel and Eaton [211] experimentally studied the heat transfer downstream of a BFS at $Re_{u_\infty,H} = 2.8\times10^4$ with an expansion ratio of $ER = 1.25$, and showed that the heat transfer coefficient rose near reattachment and reached its maximum just before the reattached point where the highest level of turbulence intensity was measured. Adams and Johnston [7, 8] systematically investigated the effects of inflow conditions on the downstream reattaching flow. Reynolds number $8000 < Re_{u_B,H_i} < 4\times10^4$ and the boundary layer thickness $0 < \delta/H < 2$. Suction tools were used so that the boundary layer thickness could be adjusted without changing the Reynolds number based on step height $Re_{u_\infty,H}$, and the expansion ratio was fixed at $ER = 1.25$. In terms of static pressure distribution, the authors [7, 8] reported that, within the given Reynolds number range, the maximum pressure recovery and the streamwise pressure gradient $\partial C_p^*/\partial X^*$ ($X^* = x/x_1$) both decreased as the boundary layer thickness δ/H increased, and did not depend

on the state of the boundary layer or the Reynolds number. The turbulent intensity and Reynolds stresses also followed this trend. In terms of the reattachment length, the authors showed that x_1/H could increase by as much as 30% when laminar boundary layer transitioned to turbulent, however, once the boundary layer became fully turbulent, any further increase in δ/H would not affect x_1/H. The authors also suggested that if boundary layer state transition occurred when $Re_{u_\infty,H}$ was increasing, x_1/H could still depend on $Re_{u_\infty,H}$ up to $Re_{u_\infty,H} = 4 \times 10^4$. Ötügen [170] studied the effect of expansion ratio on the reattachment length, contradictory result was obtained to previous works [72, 136] as the author discovered a decrease in x_1/H when ER was high and increasing. According to a more recent analysis [163], the discrepancy was most likely due to insufficient aspect ratio at high expansion ratio.

Lasher and Taulbee [139] were one of the first to use low-Reynolds-number RSM on the BFS flow. Near-wall turbulence models of Hanjalić and Launder [105] and Shima [187] were employed. Numerical results were compared with multiple experiments [66, 129, 182]. Short reattachment lengths were obtained for all cases comparing to the experimental data although improvement was showed over the hybrid model by Amano and Goel [11]. The authors [139] attributed this discrepancy to the incorrect modeling of the pressure-strain term ϕ_{ij}. The authors also suggested that the inherent unsteadiness of the flow could induce inaccuracies to the prediction of reattachment length. Lien and Leschziner [147] carefully evaluated then existing $k-\varepsilon$ and RSM turbulence models of the Launder-Reece-Rodi (LRR) type [142] on their abilities to predict BFS flows. The study showed that $k-\varepsilon$ models could not produce similarly accurate predictions as the RSMs unless a Re-Normalization Group (RNG) formulation [219, 220] was adopted within the non-linear $k-\varepsilon$ model framework proposed by Speziale [200]. A high level of anisotropy was observed as in previous studies [139, 167] which, according to the authors, implied "fundamental defects in the pressure-strain proposals" [147]. Later, Hwang and Peng [112] tested a LRR type RSM using the near-wall model proposed by Chen and Patel [41] on two BFS benchmark cases [66, 129] and very good agreement with the experimental data. In terms of reattachment lengths, the model of Hwang and Peng gave $x_1 = 6.1H$ for [129] where the experimental result was $x_1 \approx 6.2H$, and they predicted $x_1 = 7.0H$ for [66] where the experimental length was $x_1 \approx 7.0H$.

An important reference-setting work was carried out by Le *et al.* [144] in collaboration with Jovic and Driver [121]. Le *et al.* [144] performed a Direct Numerical Simulation (DNS) on the turbulent BFS flow at Reynolds number $Re_{u_\infty,H} = 5100$ with an expansion ratio of $ER = 1.20$. The experiment conducted by Jovic and Driver [121] was to validate the results obtained by the DNS simulation, all mean velocity components and velocity fluctuations were measured by LDV. At this relatively low Reynolds number, a large corner vortex extending to $x = 1.76H$ could be found, and the maximum skin friction coefficient (negative) in the recirculation zone was reported to be 2.5 times higher than that in high-Reynolds-number BFS flows. The time-averaged primary reattachment length $x_1 = 6.28H$ in the DNS study and $6.0H < x_1 < 6.1H$ in the experimental data. By plotting the budget of the turbulent kinetic energy in the recirculation zone ($x = 4.0H$), Le *et al.* [144] showed that the maximum production and dissipation occurred at the same y/H but the latter accounted for only 60% of the former which implied the break-down of equilibrium assumption in the recirculation zone. The turbulent kinetic energy budget at near the domain outlet at $x = 20H$ showed influence of the separated shear layer which implied that the flow was not recovered. A later study by Jovic and Driver [122] systematically investigated the change in the skin friction coefficient in the recirculation zone with increasing Reynolds number $Re_{u_\infty,H}$. They concluded that the minimum $C_{f,min}$ in the recirculation zone decreased with increasing $Re_{u_\infty,H}$ by following $C_{f,min} = -0.19 Re_{u_\infty,H}^{-0.5}$ indicating a "laminar-like" behavior. Kasagi and Matsunaga [127] conducted detailed measurements of the flow over a three-dimensional BFS at $Re_{u_\infty,H} = 5540$ with

$ER = 1.504$ using Particle-Tracking Velocimeter (PTV). They found a mean reattachment length of $x_1 = 6.51H$, and demonstrated the anisotropy of Reynolds stresses near the reattachment as well as the important influence of the triple velocity correlations on the Reynolds stress transport. Although the inflow conditions were different from the DNS study by Le *et al.* [144], results of multiple turbulent quantities and the turbulent kinetic energy budget showed excellent agreement with those in [144]. Later experiments using Particle Image Velocimeter (PIV) measurement at similar Reynolds numbers [135, 178, 179] all showed good qualitative and quantitative agreements with the DNS data [144].

Ever since the publication of the DNS data [144], results obtained by many numerical studies using low-Reynolds-number RSMs were compared with results in [144]. Ko [132, 133] used the RSM with elliptic relaxation proposed by Durbin [70] on multiple turbulent BFS test-cases including [66, 121, 129, 144] ($5100 \leq Re_{u_\infty,H} \leq 45000$, $1.125 \leq ER \leq 1.5$). This near-wall RSM [70] was developed from a simpler eddy-viscosity-based version of Durbin [69], the latter did not perform well for largely separated flow with strong adverse pressure gradient [70]. Slight under-prediction was observed compared to the experimental (or DNS) data in terms of the reattachment length but good agreement with differences less than 10% was obtained nevertheless ([129]: $x_1 = 6.8H$ measured $7.0H$, [66]: $x_1 = 6.1H$ measured $6.3H$, [121, 144]: $x_1 = 5.4H$ measured $6.0H - 6.28H$). Significant under-prediction on the peak negative skin friction coefficient in the recirculation zone was observed for all test-cases. At low Reynolds number $Re_{u_\infty,H} = 5100$ [121, 144], Durbin's RSM model gave accurate prediction on the recovery of turbulent boundary layer downstream of the reattachment, while for high Reynolds test-cases [66, 129], the predicted recoveries were slow indicated by low skin friction coefficient in the recovery region. So and Yuan [199] examined the performances of many non-linear $k - \varepsilon$ models and low-Reynolds RSMs including those proposed by So *et al.* [197] and by Yuan and So [224], the latter is a wall-normal-free version of the former. Comparisons were made based on the experimental data of Jovic and Driver [121]. While the two new near-wall RSMs [197, 224] more accurately predicted the skin friction distribution in the recirculation zone, that in the recovery region downstream of reattachment was severely over-predicted compared to the eddy-viscosity-based model of Durbin [69]. The implementation of wall-normal did not appear to affect the prediction of RSM. The authors reported that the non-linear $k - \varepsilon$ models predicted the reattachment length better than the RSMs as long as their wall models had "asymptotic consistency" when approaching the wall.

The low-Reynolds-number RSM proposed by Hanjalić and Jakirlić [106] gave better overall predictions on both the low- [121, 144] and high-Reynolds number [66] test-cases compared to those given by Ko [132] with the elliptic relaxation RSM, especially in terms of wall skin friction coefficient distribution. The authors compared the new low-Reynolds RSM to high-Reynolds RSMs of LRR type with wall-functions and the low-Reynolds model showed significant improvement in the near-wall regions. Compared with the DNS data [144], the low-Reynolds model accurately predicted the primary ($x_1 = 6.38H$ DNS $6.28H$), secondary, and tertiary reattachment bubbles. This low-Reynolds model was later modified and developed into the ε^h-Reynolds-Stress Model [115]. Craft [60] made modifications to the low-Reynolds-number RSM developed by Craft and Launder [59] tested it on Driver and Seegmiller [66] and Le *et al.* [144] cases. Detailed report on the reattachment lengths was *not* given in [60] but the mean velocity profiles showed reasonable agreement with the experimental and DNS data. The velocity fluctuations u' and v' agreed well with the DNS data at $Re_{u_\infty,H} = 5100$ but showed significant under-prediction in the recovery region of Driver and Seegmiller case at higher Reynolds number.

Up to this point, we have covered most of the results on turbulent BFS flows using advanced RANS models. Thanks to the increasing computational power in more recent years, LES, hybrid

RANS-DNS and RANS-LES methods were tested on turbulent BFS benchmark cases. Although Akselvoll and Moin [9] had already performed LES on BFS flow, the test-case was that of the DNS case by Le *et al.* [144] where the Reynolds number was low ($Re_{u_\infty,H} = 5100$). However, in that study [9], the authors showed that the LES gave better overall results than a DNS with coarse grid. Keating *et al.* [128] used LES to study the test-case of Vogel and Eaton [211] ($Re_{u_\infty,H} = 28000$, $ER = 1.25$). The authors [128] confirmed the observation by Vogel and Eaton [211] that the maximum heat transfer occurred slightly before the reattachment, and the computed mean reattachment length was within 3% of error comparing to the measurements. Frendi *et al.* [83] compared the predictive abilities of the Detached Eddy Simulation (DES), Unsteady RANS (URANS), and Partially Averaged Navier-Stokes (PANS) models on the Driver and Seegmiller benchmark case [66]. Better agreement with the experimental data was showed for the PANS model comparing to DES and URANS. Fadai-Ghotbi *et al.* [79] performed URANS simulations on the Driver and Seegmiller case and showed that the grid-converged URANS solution returned to a steady RANS solution which indicated that URANS models were unable to reproduce the physical unsteadiness of the BFS flow. Probst *et al.* [172] compared two variants of DES, the Delayed DES (DDES) and the Improved Delayed DES (IDDES) with the steady-state low-Reynolds ε^h-Reynolds Stress Model by Jakirlić and Hanjalić [115]. The Driver and Seegmiller benchmark case [66] was used for the comparison, and both DES-based models showed improvement over the RSM in terms of the prediction of reattachment length (the RSM tended to over-predict x_1/H). Gritskevich *et al.* [100] introduced the $k-\omega$ Shear Stress Transport (SST) based DDES and IDDES approaches. Numerical results were compared to the experimental data of Vogel and Eaton [211] and the SST-IDDES approach gave excellent prediction in terms of the skin friction distribution and the mean velocity profiles. Shur *et al.* [192] made modifications to the DES approach to accelerate the transition from RANS to DES and these modifications gave improved solution to the BFS problem. Smirnov *et al.* [195] compared the IDDES solution to RANS solution using the $k-\omega$ SST model [155]. The Vogel and Eaton [211] experiment was used as the test-case and the authors concluded that IDDES model gave better prediction on the skin friction coefficient while $k-\omega$ SST model showed advantage on the prediction of heat transfer coefficient distribution.

More DNS computations and PIV flow measurements have been performed from 2000 to recent years. Meri and Wengle [156] simulated a turbulent BFS flow at $Re_{u_\infty,H} = 3300$ with $ER = 1.5$ the incoming flow was a fully developed turbulent channel flow with $Re_{u_\tau,H_i} = 360$. The DNS data was used to validate their LES results. Barri *et al.* [19] used DNS to compute a fully turbulent BFS flow at $Re_{u_B,H} = 5600$ with an expansion ratio of $ER = 2.0$. The inflow Reynolds number based on H_i and the wall-friction velocity u_τ was the same as in [156] at $Re_{u_\tau,H_i} = 360$. Normalized turbulent flow quantities were compared to the PIV measurements by Kasagi and Matsunaga [127], although the two studies had different geometries (in [127], $ER = 1.5$), the DNS solution was almost identical to the PIV measurement everywhere in the computational domain. The latest PIV measurements on turbulent BFS flows were made by Nadge and Govardhan [163] which consisted of a complete parametric study on the effects of Reynolds number and expansion ratio. Among other important findings in this study, the authors suggested that the flow structure within the recirculation zone became independent of Reynolds number $Re_{u_\infty,H}$ and the expansion ratio ER when the $Re_{u_\infty,H} > 3.6 \times 10^4$. However, the reattachment length was already independent of $Re_{u_\infty,H}$ if $Re_{u_\infty,H} > 2 \times 10^4$ for all ERs investigated which indicated that the constant reattachment length is necessary but insufficient for the flow structure to be also constant. In terms of the expansion ratio, the authors showed that for $ER > 1.80$, the reattachment length was very weakly influenced by the expansion ratio. A recent DNS study was carried out by Kopera *et al.* [134] on a similar geometry to Le *et al.* [144] ($ER = 2.0$) with increased Reynolds

number $Re_{u_\infty,H} = 9000$. The authors computed a mean reattachment length of $x_1 = 8.62H$ and showed that the skin friction coefficient distribution agreed with that in [144] while the peak negative c_f decreased slightly due to increased Reynolds number as shown by Jovic and Driver [122].

The latest DNS data on the BFS flow to the author's knowledge was obtained by Pont-Vílchez *et al.* [171]. The inflow Reynolds number $Re_{u_\tau,H_i} = 790$ was more than twice as high as that of Barri *et al.* [19]. The Reynolds number based on the inlet bulk velocity was not directly given by the authors but since the expansion ratio is identical to that of Barri *et al.* [19] ($ER = 2.0$), $Re_{u_B,H} \approx 12289$ can be deduced. By comparing the computed mean reattachment length $x_1 = 8.8H$ with the measured data in [163], the authors deduced that the flow was closed to the Reynolds-independent range $Re_{u_\infty,H} > 2 \times 10^4$. A notable increase in the negative peak skin friction coefficient in the recirculation region compared to Barri *et al.* [19] was observed which agreed with the conclusion drawn by Jovic and Driver [122]. The DNS data in this study can be used as valuable reference for future works on turbulence modeling.

In order to summarize the progress made in the study of turbulent BFS flows, benchmark cases (experiments and Direct Numerical Simulations) are summarized in Table (C.2). Each case is codified by the initials of its authors.

Table C.2: Turbulent benchmarks cases tested for BFS flows in the literature.

Case	$Re_{u_\infty,H}$	Re_{u_∞,δ_2}	δ/H	B.L. state	ER	x_1/H	Equipment	Remarks
Baker 1977 [17] (Bak)	50000	3500	0.7	Tur.	1.10	5.7-6.0	Pulsed-wire	-
Chandrsuda and Bradshaw 1981 [37] (CB)	102000	400	0.04	Lam.	1.65	5.9	Hot-wire	Upper wall inclined 1.7° downward
Kim *et al.* 1980 [129] (KKJ)	30000, 45000	1300	0.30, 0.45	Tur.	1.33, 1.5	7 ± 1	Hot-wire	Measurements unavailable in recirculation zone
Eaton and Johnston 1980 [75] (EJ)	11000-39000	240-890	0.18-0.23	Lam., tra., tur.	1.67	6.97-8.2	Pulsed-wire	Three set-ups with the same ER and different inflow B. L.s
Adams *et al.* 1984 [6] (AJE)	26000	-	-	-	1.25	-	-	Parameters provided by Avva *et al.* [16] (incomplete)
Seegmiller and Driver 1984 [182] (SD)	-	5000	-	-	1.33, 1.5	5.0, 5.33	-	Private communication with Amano and Goel, information incomplete
Driver and Seegmiller 1985 [66] (DrS)	37500	5000	1.50	Tur.	1.125	6.26	LDV	Upstream Mach number 0.128
Vogel and Eaton 1985 [211] (VE)	28000	3370	1.07	Tur.	1.25	6.67	LDV	Heat transfer was studied
Durst and Schmitt 1985 [73] (DuS)	100000	4000	-	Tur.	2.0	8.4	LDV	Momentum thickness $\delta_2/H = 0.04$
Jovic and Driver 1994 [121] (JD)	5100	610	1.2	Tur.	1.2	6 ± 0.15	LDV	Double-expansion channel
Le *et al.* 1997 [144] (LMK)	5100	670	1.2	Tur.	1.2	6.28	DNS	No-stress upper wall to simulate double-expansion channel in [121]
Kasagi and Matsunaga 1995 [127] (KM)	5540	-	-	Tur.	1.504	6.51	PTV	Upstream B.L. state unknown

Reynolds-Averaged Navier-Stokes turbulence models that were tested for BFS flows in the literature are tabulated in Table (C.3). Each model is codified by the initials of its authors followed by its type, and in case of multiple models of the same type proposed by a group of authors, the year is added to distinguish among them.

The published numerical studies on turbulent BFS flows are summarized in (Table C.4). Bench-

mark case and model names are taken from Table (C.2) and Table (C.3). The spatial discretization scheme is presented if available (some were not explicitly mentioned by the authors, or mentioned without full detail).

C. Literature Review on Turbulent BFS Flows

Table C.3: RANS models tested on turbulent BFS flows in the literature.

Model	Type	Remarks
Daly and Harlow [61] (DH-RSM)	RSM	HRN model
Jones and Launder 1972 [120] (JL-KE)	$k-\varepsilon$	LRN model
Hanjalić and Launder 1972 [104] (HL-RSM-72)	RSM	HRN model
Rodi 1972 [174, 175] (Rod-ASM)	ASM	Standard ASM
Mellor 1973 [153] (Mel-RSM)	RSM	Wall function
Shir 1973 [188] (Shir-RSM)	RSM	HRN model, wall reflection effects
Launder and Spalding 1974 [141] (LSp-KE)	$k-\varepsilon$	Wall function
Launder and Sharma 1974 [140] (LSh-KE)	$k-\varepsilon$	Standard $k-\varepsilon$ model, LRN model
Launder *et al.* 1975 [142] (LRR-RSM)	RSM	HRN model
Hanjalić and Launder 1976 [105] (HL-RSM-76)	RSM	LRN model
Cormack *et al.* 1978 [56] (CLS-RSM)	RSM	HRN model
Gibson and Launder 1978 [95] (GL-RSM)	RSM	HRN model, wall reflection effects
Mellor and Yamada 1982 [154] (MY-RSM)	RSM	Wall function
Chien 1982 [47] (Chi-KE)	$k-\varepsilon$	LRN model
Sindir 1982 [194] (Sin-ASM)	ASM	Production term modified in ε-equation
Amano and Goel 1985 [11] (AG-RSM)	RSM	Hybrid RSM-eddy-viscosity model
So and Yoo 1986 [196] (SY-KE)	$k-\varepsilon$	Wall function
Speziale 1987 [200] (Spe-KE)	$k-\varepsilon$	Non-linear $k-\varepsilon$, wall-function
Shima 1988 [187] (Shim-RSM)	RSM	LRN model
Myong and Kasagi 1990 [162] (MK-KE)	$k-\varepsilon$	LRN model, damping function
Rubinstein and Barton 1990 [176] (RB-KE)	$k-\varepsilon$	Non-linear $k-\varepsilon$, RNG formulation
Durbin 1991 [69] (Dur-RSM-91)	RSM	LRN model, elliptical relaxation
Yakhot *et al.* 1992 [220] (YOTGS-KE)	$k-\varepsilon$	Re-Normalization Group (RNG) formulation
Yakhot *et al.* 1992 [220] (YOTGS-RSM)	RSM	Re-Normalization Group (RNG) formulation
Lien and Leschziner 1993 [146] (LL-KE)	$k-\varepsilon$	LRN model
Shih and Lumley 1993 [186] (SL-KE)	$k-\varepsilon$	LRN model, no wall model
Durbin 1993 [70] (Dur-RSM-93)	RSM	LRN model, elliptical relaxation
Menter 1993 [155] (Men-KW)	$k-\omega$	Shear Stress Transport (SST)
Yang and Shih 1993 [221] (YaSh-KE)	$k-\varepsilon$	LRN model, wall-normal vector
So *et al.* 1994 [197] (SASY-RSM)	RSM	LRN moel, wall-normal vector
Abe *et al.* 1994 [2, 3] (AKN-KE-94)	$k-\varepsilon$	LRN model, non-linear eddy-viscosity
Abe *et al.* 1997 [4] (AKN-KE-97)	$k-\varepsilon$	LRN model, non-linear Reynolds stress features
Sarkar and So 1997 [177] (SS-KE)	$k-\varepsilon$	Near-wall model, wall-function
So *et al.* 1997 [198] (SSGZ-KE)	$k-\varepsilon$	LRN moel, no wall-function
Yuan and So 1997 [224] (YuSo-RSM)	RSM	LRN model, wall-normal-free
Hanjalić and Jakirlić 1998 [106] (HJ-RSM)	RSM	LRN model, wall-normal vector
Craft 1998 [60] (Cra-RSM)	RSM	LRN model, wall-normal-free
Jakirlić and Hanjalić 2002 [106] (JH-RSM)	RSM	LRN model, wall-normal vector, homogeneous ε^h

C. Literature Review on Turbulent BFS Flows

Table C.4: Published studies on turbulent BFS flows in the literature.

Study	Benchmark cases	Models used	Discretization scheme	Remarks
Baker 1977 [17]	Bak	LSp-KE	1^{st}-order upwind FD	-
Sindir 1982 [194]	DrS	LSh-KE, Rod-ASM, Sin-ASM	-	-
Amano and Goel 1985 [11]	SD	Rod-ASM, AG-RSM	Hybrid central-4^{th}-order-power-law FD based on cell Reynolds number [10]	-
Celenligil and Mellor 1985 [34]	KKJ	MY-RSM	2^{nd}-order central FD (stream function method)	-
Amano and Goel 1986 [12]	CB	DH-RSM, HL-RSM-72, Shir-RSM, CLS-RSM	-	Hybrid RSM-eddy-viscosity models [11]
Avva *et al* 1988 [16]	DrS, AJE, KKJ, EJ	LSp-KE	2^{nd}-order deferred correction FD	Streamline curvature modification
Yoo *et al.* 1989 [223]	KKJ	LSh-KE, LRR-RSM, GL-RSM	-	ε modifications of HL-RSM-72 and Launder *et al.* [143] were used
Obi *et al.* 1991 [167]	KKJ, DuS	LSp-KE, LRR-RSM, GL-RSM	Collocated FV, upwind for convective flux, central-differencing for diffusive flux	-
Lasher and Taulbee 1992 [139]	KKJ, DrS, SD	HL-RSM-76, Shim-RSM	FD, Power law and QUICK for convective term	-
Thangam and Speziale 1992 [205]	KKJ	LSp-KE, Spe-KE	Central-differencing for mean-flow variables, fourth-order central scheme for Reynolds stresses	-
Steffen, Jr. 1993 [201]	DrS	JL-KE, Chi-KE, LSh-KE, SL-KE	2^{nd}-order TVD FV scheme of Chakravarthy and Osher [35]	-
Ko 1993 [132]	KKJ, DrS, JD, LMK	Dur-RSM-93	FV, 3^{rd}-order QUICK scheme	-
Abe *et al.* 1994 [2]	KKJ, EJ, KM, DrS, VE, DuS	AKN-KE-94	FD, 3^{rd}-order upwind for momentum, 1^{st}-order upwind for $k-\varepsilon$, central differencing for other terms	Focused on flow features
Lien and Leschziner 1994 [147]	DrS (6° upper wall)	JL-KE, YOTGS-KE, LL-KE, Spe-KE, RB-KE, GL-RSM	Collocated cell-centered FV, QUICK for main-flow variables and MUSCL TVD for turbulent model	LL-KE with Yap correction [222]. Different combinations and variants were used for some models, please refer to [147] for details
Hwang and Peng 1995 [112]	KKJ, DrS	LRR-RSM	Staggered FV, power-law differencing for convective and diffusive terms, central differencing for source term	LRR-RSM with near wall model of Chen and Patel [41]
Abe *et al.* 1995 [3]	KKJ, EJ, KM, DrS, VE, DuS	AKN-KE-94	FD, 3^{rd}-order upwind for momentum, 1^{st}-order upwind for $k-\varepsilon$, central differencing for other terms	Focused on heat transfer
Abe *et al.* 1997 [4]	KKJ, EJ, KM, DrS, VE, DuS	AKN-KE-97	FD, 3^{rd}-order upwind for momentum, 1^{st}-order upwind for $k-\varepsilon$, central differencing for other terms	-
So and Yuan 1998 [199]	JD, LMK	LSh-KE, Chi-KE, MK-KE, AKN-KE-94, YaSh-KE, SS-KE, SSGZ-KE, Dur-RSM-91, SASY-RSM, YuSo-RSM	-	-
Hanjalić and Jakirlić 1998 [106]	JD, LMK, KKJ, DrS, DuS	LRR-RSM, GL-RSM, HJ-RSM	Collocated FV, 2^{nd}-order upwind for HRN model, 2^{nd}-order deferred correction for LRN model	All models with Yap correction [222]
Craft 1998 [60]	LMK, DrS	Cra-RSM	Collocated cell-centered FV, QUICK for main-flow variables and MUSCL TVD for turbulent model	Iacovides and Raisee correction [113]
Probst *et al.* 2010 [172]	DrS	JH-RSM	Unstructured FV, 2^{nd}-order central scheme (DLR-TAU code)	Yap correction [222]
Smirnov *et al.* 2018 [195]	VE	Men-KW	QUICK scheme for SINF/Flag-S code, 2^{nd}-order upwind for ANSYS Fluent	-

Appendix D

Turbulent Equations and Boundary Conditions

D.1 Favre-Reynolds-averaged Navier-Stokes Equations and GLVY-RSM

Density-weighted Favre-averaging [81] for compressible flows variable

$$\begin{aligned} f &= \bar{f} + f' = \widetilde{f} + f'', \\ \widetilde{f} &= \frac{\overline{\rho f}}{\bar{\rho}} \end{aligned} \tag{D.1}$$

where $\bar{(\cdot)}$ is the Reynolds-averaging operator, $\widetilde{(\cdot)}$ is the density-weighted Favre-averaging operator, $(\cdot)'$ and $(\cdot)''$ are the respective fluctuating parts.

The Favre-Reynolds-averaged Navier-Stokes equations are the following

$$\begin{aligned} \frac{\partial \bar{\rho}}{\partial t} + \frac{\partial \bar{\rho}\tilde{u}_\ell}{\partial x_\ell} &= 0 \\ \frac{\partial \bar{\rho}\tilde{u}_i}{\partial t} + \frac{\partial}{\partial x_\ell}[\bar{\rho}\tilde{u}_i\tilde{u}_\ell + \bar{p}\delta_{i\ell}] - \frac{\partial}{\partial x_\ell}[\bar{\tau}_{i\ell} - \overline{\rho u_i'' u_\ell''}] &= 0 \\ \frac{\partial}{\partial t}[\bar{\rho}\breve{h}_t - \bar{p}] + \frac{\partial \bar{\rho}\tilde{u}_\ell \breve{h}_t}{\partial x_\ell} - \frac{\partial}{\partial x_l}[\tilde{u}_i(\bar{\tau}_{i\ell} - \overline{\rho u_i'' u_\ell''}) - (\bar{q}_\ell + \overline{\rho h'' u_\ell''})] &= S_{\breve{h}_t} \end{aligned} \tag{D.2}$$

where $\breve{(\cdot)}$ denotes the averaged variable which is neither a Favre-average nor a Reynolds-average, $S_{\breve{h}_t}$ denotes the turbulent source term introduced by the model. The GLVY-RSM [92] is used to close the system, where transport equations for the Favre-Reynolds-averaged Reynolds stresses $r_{ij} = \widetilde{u_i'' u_j''}$ and for the modified turbulence kinetic energy (TKE) dissipation rate $\varepsilon^* = \varepsilon - 2\breve{\nu}(\mathrm{grad}\sqrt{\mathrm{k}})^2$

are given by

$$\underbrace{\frac{\partial}{\partial t}\left(\bar{\rho} r_{ij}\right)+\frac{\partial}{\partial x_\ell}\left(\bar{\rho} r_{ij}\tilde{u}_\ell\right)}_{C_{ij}}=\underbrace{-\bar{\rho} r_{i\ell}\frac{\partial \tilde{u}_j}{\partial x_\ell}-\bar{\rho} r_{j\ell}\frac{\partial \tilde{u}_i}{\partial x_\ell}}_{P_{ij}}+\underbrace{\frac{\partial}{\partial x_\ell}\left(\breve{\mu}\frac{\partial r_{ij}}{\partial x_\ell}\right)}_{d_{ij}^{(\mu)}}$$
$$+d_{ij}^{(u)}+\Pi_{ij}-\bar{\rho}\varepsilon_{ij}+\cancelto{\approx 0}{K_{ij}} \tag{D.3a}$$

$$\frac{\partial \bar{\rho}\varepsilon^*}{\partial t}+\frac{\partial\left(\bar{\rho}\varepsilon^*\tilde{u}_\ell\right)}{\partial x_\ell}=\frac{\partial}{\partial x_\ell}\left[C_\varepsilon\frac{\mathrm{k}}{\varepsilon^*}\bar{\rho} r_{m\ell}\frac{\partial \varepsilon^*}{\partial x_m}+\breve{\mu}\frac{\partial \varepsilon^*}{\partial x_\ell}\right]$$
$$+C_{\varepsilon_1}P_\mathrm{k}\frac{\varepsilon^*}{\mathrm{k}}-C_{\varepsilon_2}\bar{\rho}\frac{\varepsilon^{*2}}{\mathrm{k}}+2\breve{\mu}C_\mu\frac{\mathrm{k}^2}{\varepsilon^*}\frac{\partial^2\tilde{u}_i}{\partial x_\ell\partial x_\ell}\frac{\partial^2\tilde{u}_i}{\partial x_m\partial x_m} \tag{D.3b}$$

$$P_\mathrm{k}:=\tfrac{1}{2}P_{\ell\ell}\ ;\ C_\varepsilon=0.18\ ;\ C_{\varepsilon 1}=1.44 \tag{D.3c}$$

$$C_{\varepsilon 2}=1.92(1-0.3\mathrm{e}^{-Re_T^{*2}})\ ;\ C_\mu=0.09\mathrm{e}^{-\frac{3.4}{(1+0.02Re_T^*)^2}} \tag{D.3d}$$

$$\mathrm{k}:=\tfrac{1}{2}r_{\ell\ell}\ ;\ Re_T^*:=\frac{\mathrm{k}^2}{\breve{\nu}\varepsilon^*}\ ;\ \breve{\mu}:=\mu_{\text{Sutherland}}(\widetilde{T})\ ;\ \breve{\nu}:=\frac{\breve{\mu}}{\bar{\rho}} \tag{D.3e}$$

and for a detailed description of the modeling terms ($d_{ij}^{(u)}$, Π_{ij}, ε_{ij}) in Eqn. D.3, we refer to the original publication [92] of Gerolymos-Lo-Vallet-Younis.

D.2 Boundary Conditions

The derivations of boundary conditions are given in Section. 2.7. Here, we only provide the exterior state of each boundary condition discussed in Section. 2.7 with addition turbulent variables including the four Reynolds stresses in 2D and the modified turbulent kinetic energy dissipation rate. For relatively simple boundary conditions, the expression of the Jacobian matrix $\underline{\underline{\mathbf{J}}}'_{ij}$ is also provided.

D.2.1 Adiabatic No-slip Wall

As mentioned in Section. 2.7.2, special care needs to be taken for no-slip wall BCs, since they require different treatments for the computations of $\underline{F}_{G_{ij}}^{\mathrm{BC,NUM}}$ and $\underline{F}_{G_{ij}}^{\mathrm{BC,APP}}$. For the high-order

boundary flux $\underline{F}_{G_{ij}}^{\mathrm{BC,NUM}}$

$$\underline{V}_j(\underline{V}_i, \underline{V}_{\mathrm{BC}}) = \begin{bmatrix} \rho_i \\ u_i \\ v_i \\ p_i \\ \widetilde{u''u''}_i \\ \widetilde{u''v''}_i \\ \widetilde{v''v''}_i \\ \widetilde{w''w''}_i \\ \varepsilon_i^* \end{bmatrix} \tag{D.4}$$

while for the first-order $\underline{F}_{G_{ij}}^{\mathrm{BC,APP}}$, the cell-averaged velocity components in the fictitious cell E_j $\langle u \rangle_{E_j}$ and $\langle v \rangle_{E_j}$, as well as all turbulent variables $\langle r_{ij} \rangle_{E_i}$ and $\langle \varepsilon^* \rangle_{E_i}$ are set opposite to those in cell E_i to ensure a zero-value approximation of the velocity vector and turbulent variables on edge G_{ij}

$$\langle \underline{V} \rangle_{E_j}(\langle \underline{V} \rangle_{E_i}, \underline{V}_{\mathrm{BC}}) = \begin{bmatrix} \langle \rho \rangle_{E_i} \\ -\langle u \rangle_{E_i} \\ -\langle v \rangle_{E_i} \\ \langle p \rangle_{E_i} \\ -\langle \widetilde{u''u''} \rangle_{E_i} \\ -\langle \widetilde{u''v''} \rangle_{E_i} \\ -\langle \widetilde{v''v''} \rangle_{E_i} \\ -\langle \widetilde{w''w''} \rangle_{E_i} \\ -\langle \varepsilon^* \rangle_{E_i} \end{bmatrix} \tag{D.5}$$

Based on Eqn. D.5, we obtain $\underline{\underline{\mathbf{J}}}'_{ij}$

$$\underline{\underline{\mathbf{J}}}'_{ij} := \frac{\partial \langle \underline{V} \rangle_{E_j}}{\partial \langle \underline{V} \rangle_{E_i}} = \begin{bmatrix} 1 & 0 & 0 & 0 & 0 & 0 & 0 & 0 & 0 \\ 0 & -1 & 0 & 0 & 0 & 0 & 0 & 0 & 0 \\ 0 & 0 & -1 & 0 & 0 & 0 & 0 & 0 & 0 \\ 0 & 0 & 0 & 1 & 0 & 0 & 0 & 0 & 0 \\ 0 & 0 & 0 & 0 & -1 & 0 & 0 & 0 & 0 \\ 0 & 0 & 0 & 0 & 0 & -1 & 0 & 0 & 0 \\ 0 & 0 & 0 & 0 & 0 & 0 & -1 & 0 & 0 \\ 0 & 0 & 0 & 0 & 0 & 0 & 0 & -1 & 0 \\ 0 & 0 & 0 & 0 & 0 & 0 & 0 & 0 & -1 \end{bmatrix}. \tag{D.6}$$

D.2.2 Isothermal No-slip Wall

For the high-order boundary flux $\underline{F}_{G_{ij}}^{\mathrm{BC,NUM}}$

$$\underline{V}_j(\underline{V}_i, \underline{V}_{\mathrm{BC}}) = \begin{bmatrix} \frac{p_i}{RT_w} \\ u_i \\ v_i \\ p_i \\ \widetilde{u''u''}_i \\ \widetilde{u''v''}_i \\ \widetilde{v''v''}_i \\ \widetilde{w''w''}_i \\ \varepsilon_i^* \end{bmatrix} \tag{D.7}$$

while for the first-order $\underline{F}_{G_{ij}}^{\mathrm{BC,APP}}$

$$\langle \underline{V} \rangle_{E_j}(\langle \underline{V} \rangle_{E_i}, \underline{V}_{\mathrm{BC}}) = \begin{bmatrix} \frac{\langle p \rangle_{E_i}}{R_g T_w} \\ -\langle u \rangle_{E_i} \\ -\langle v \rangle_{E_i} \\ \langle p \rangle_{E_i} \\ -\langle \widetilde{u''u''} \rangle_{E_i} \\ -\langle \widetilde{u''v''} \rangle_{E_i} \\ -\langle \widetilde{v''v''} \rangle_{E_i} \\ -\langle \widetilde{w''w''} \rangle_{E_i} \\ -\langle \varepsilon^* \rangle_{E_i} \end{bmatrix} \tag{D.8}$$

Based on Eqn. D.8, we obtain $\underline{\underline{\mathbf{J}}}'_{ij}$

$$\underline{\underline{\mathbf{J}}}'_{ij} := \frac{\partial \langle \underline{V} \rangle_{E_j}}{\partial \langle \underline{V} \rangle_{E_i}} = \begin{bmatrix} 0 & 0 & 0 & \frac{1}{R_g T_w} & 0 & 0 & 0 & 0 & 0 \\ 0 & -1 & 0 & 0 & 0 & 0 & 0 & 0 & 0 \\ 0 & 0 & -1 & 0 & 0 & 0 & 0 & 0 & 0 \\ 0 & 0 & 0 & 1 & 0 & 0 & 0 & 0 & 0 \\ 0 & 0 & 0 & 0 & -1 & 0 & 0 & 0 & 0 \\ 0 & 0 & 0 & 0 & 0 & -1 & 0 & 0 & 0 \\ 0 & 0 & 0 & 0 & 0 & 0 & -1 & 0 & 0 \\ 0 & 0 & 0 & 0 & 0 & 0 & 0 & -1 & 0 \\ 0 & 0 & 0 & 0 & 0 & 0 & 0 & 0 & -1 \end{bmatrix}. \tag{D.9}$$

Apart from the two no-slip wall BCs mentioned above, other BCs in the rest of this appendix treat the low- and high-order numerical fluxes with the same BC relations.

D.2.3 Riemann Invariant Inflow and Outflow

(1) Supersonic Inflow

$$\underline{V}_j^{(\texttt{supIn})}(\underline{V}_i, \underline{V}_{\texttt{BC}}) = \begin{bmatrix} \rho_\infty \\ u_\infty \\ v_\infty \\ p_\infty \\ \widetilde{u''u''}_\infty \\ \widetilde{u''v''}_\infty \\ \widetilde{v''v''}_\infty \\ \widetilde{w''w''}_\infty \\ \varepsilon^*_\infty \end{bmatrix} \tag{D.10}$$

Based on Eqn. D.10, we obtain $\underline{\underline{\mathbf{J}}}'^{(\texttt{supIn})}_{ij}$

$$\underline{\underline{\mathbf{J}}}'^{(\texttt{supIn})}_{ij} = 0. \tag{D.11}$$

(2) Supersonic Outflow

$$\underline{V}_j^{(\texttt{supOut})}(\underline{V}_i, \underline{V}_{\texttt{BC}}) = \begin{bmatrix} \rho_i \\ u_i \\ v_i \\ p_i \\ \widetilde{u''u''}_i \\ \widetilde{u''v''}_i \\ \widetilde{v''v''}_i \\ \widetilde{w''w''}_i \\ \varepsilon^*_i \end{bmatrix} \tag{D.12}$$

Based on Eqn. D.12, we obtain $\underline{\underline{\mathbf{J}}}'^{(\texttt{supOut})}_{ij}$

$$\underline{\underline{\mathbf{J}}}'^{(\texttt{supOut})}_{ij} = \underline{\underline{\mathbf{I}}}. \tag{D.13}$$

(3) Subsonic Inflow/Outflow

$$\underline{V}_j^{(\texttt{subIn})}(\underline{V}_i, \underline{V}_{\texttt{BC}}) = \begin{bmatrix} \rho_\infty \left(T_j/T_\infty\right)^{\frac{1}{\gamma-1}} \\ u_\infty + (V_{n_j} - V_{n_\infty})\mathrm{n}_x \\ v_\infty + (V_{n_j} - V_{n_\infty})\mathrm{n}_y \\ p_\infty \left(T_j/T_\infty\right)^{\frac{\gamma}{\gamma-1}} \\ \widetilde{u''u''}_\infty \\ \widetilde{u''v''}_\infty \\ \widetilde{v''v''}_\infty \\ \widetilde{w''w''}_\infty \\ \varepsilon^*_\infty \end{bmatrix} \tag{D.14}$$

$$\underline{V}_j^{(\texttt{subOut})}(\underline{V}_i, \underline{V}_{\mathrm{BC}}) = \begin{bmatrix} \rho_i \left(T_j/T_i\right)^{\frac{1}{\gamma-1}} \\ u_i + (V_{n_j} - V_{n_i})\mathrm{n}_x \\ v_i + (V_{n_j} - V_{n_i})\mathrm{n}_y \\ p_i \left(T_j/T_i\right)^{\frac{\gamma}{\gamma-1}} \\ \widetilde{u''u''}_i \\ \widetilde{u''v''}_i \\ \widetilde{v''v''}_i \\ \widetilde{w''w''}_i \\ \varepsilon_i^* \end{bmatrix}. \tag{D.15}$$

D.2.4 Reservoir Inflow

$$\underline{V}_j(\underline{V}_i, \underline{V}_{\mathrm{BC}}) = \begin{bmatrix} \rho_{\mathrm{BC}} \left(T_j/T_{\mathrm{BC}}\right)^{\frac{1}{\gamma-1}} \\ u_{\mathrm{BC}} + (V_{n_j} - V_{n_{\mathrm{BC}}})\mathrm{n}_x \\ v_{\mathrm{BC}} + (V_{n_j} - V_{n_{\mathrm{BC}}})\mathrm{n}_y \\ p_{\mathrm{BC}} \left(T_j/T_{\mathrm{BC}}\right)^{\frac{\gamma}{\gamma-1}} \\ \widetilde{u''u''}_{\mathrm{BC}} \\ \widetilde{u''v''}_{\mathrm{BC}} \\ \widetilde{v''v''}_{\mathrm{BC}} \\ \widetilde{w''w''}_{\mathrm{BC}} \\ \varepsilon_{\mathrm{BC}}^* \end{bmatrix}. \tag{D.16}$$

D.2.5 Pressure Outflow

$$\underline{V}_j(\underline{V}_i, \underline{V}_{\mathrm{BC}}) = \begin{bmatrix} \frac{p_j}{R_g T_i} \\ u_i \\ v_i \\ p_j \\ \widetilde{u''u''}_i \\ \widetilde{u''v''}_i \\ \widetilde{v''v''}_i \\ \widetilde{w''w''}_i \\ \varepsilon_i^* \end{bmatrix}. \tag{D.17}$$